Experimental and numerical analysis of chip formation in metal cutting

Von der Fakultät für Maschinenwesen der
Rheinisch-Westfälischen Technischen Hochschule Aachen
zur Erlangung des akademischen Grades eines
Doktors der Ingenieurwissenschaften
genehmigte Dissertation

vorgelegt von

Stefan Hoppe

aus

Gladbeck/Westfalen

Berichter: Univ.-Prof. Dr.-Ing. F. Klocke
Univ.-Prof. Dr.-Ing. Dr.-Ing. E.h. mult. H. K. Tönshoff

Tag der mündlichen Prüfung: 8. Dezember 2003

Diese Dissertation ist auf den Internetseiten der Hochschulbibliothek online verfügbar.

Vorwort und Danksagung

Die vorliegende Arbeit entstand während meiner Tätigkeit als wissenschaftlicher Mitarbeiter am Laboratorium für Werkzeugmaschinen und Betriebslehre (WZL) der RWTH Aachen.

Herrn Prof. Dr.-Ing. Fritz Klocke, dem Inhaber des Lehrstuhls für Technologie der Fertigungsverfahren, danke ich für die Diskussionsbereitschaft und die wohlwollende Förderung der Arbeit.

Ebenso bedanke ich mich bei em. Prof. Dr.-Ing. Dr.-Ing. E.h. mult. Hans Kurt Tönshoff, dem ehemaligen Leiter des Instituts für Fertigungstechnik und Werkzeugmaschinen der Universität Hannover, für die Übernahme des Korreferates.

Mein Dank gilt ebenfalls Herrn Prof. Dr.-Ing. Hubertus Murrenhoff, dem Leiter des Lehrstuhls für fluidtechnische Antriebe und Steuerungen der RWTH Aachen, für die Übernahme des Vorsitzes bei der mündlichen Prüfung.

Für zahlreiche anregende Diskussionen, Vorarbeiten und Ratschläge bedanke ich mich bei den ehemaligen und derzeitigen Kollegen Dipl.-Ing. Rainer Fritsch, Dr.-Ing. Tilo Krieg, Dr.-Ing. Hans-Willi Raedt und Dr.-Ing. Volker Zinkann sowie meinen Projektpartnern Dr.-Ing. Christoph Treppmann und Dipl.-Ing. Bernhard Müller. Für die kritische Durchsicht des Manuskriptes gilt mein besonderer Dank meinen Kollegen Dipl.-Ing. Gregor Messner und Dipl.-Ing. Ingo Essel.

Für ihren Anteil an der Entstehung der Arbeit bedanke ich mich bei allen ehemaligen und jetzigen studentischen Mitarbeitern, Studien- und Diplomarbeitern. Weiterhin gilt mein Dank den Mitarbeitern des Lehrstuhls, die durch ihre Mitarbeit zum Gelingen der Arbeit beigetragen haben.

Mein Dank gilt insbesondere meinen Eltern, Regina und Hans Hoppe sowie meiner Frau Christiane, die meinen beruflichen Werdegang zu jedem Zeitpunkt ermöglicht und unterstützt haben.

Aachen, im Januar 2004 Stefan Hoppe

für Katharina Marie

Contents

Contents i

List of symbols 1

1 Introduction and objective of the work 5

2 Plastic behavior of the examined workpiece materials 7

2.1 Flow stress curve 9

3 Elastic and thermo-mechanical properties of workpiece and tool 27

3.1 Young's modulus E 28

3.2 Poisson ratio ν 30

3.3 Coefficient of linear thermal expansion α_L 32

3.4 Coefficient of heat transfer h 33

3.5 Specific heat capacity c_p 34

3.6 Density ρ 35

3.7 Product of specific heat capacity c_p and density ρ 35

3.8 Thermal diffusivity a and thermal conductivity λ 36

3.9 Taylor-Quinney coefficient κ 37

3.10 Thermal contact conductance h_{tc} 38

3.11 Friction 40

4 Summary of material description 45

5 Experimental setups and results 47

5.1 External turning operation 48

5.2 Chip formation 65

5.3 Micrographs of chips 67

5.4 Chip thickness 74

5.5 Length of the contact zone 75

5.6 Chip root examinations 78

5.7 State of the art of the in-situ photograpy of the chip formation process 82
5.8 Design of a new setup for the in-situ photography of chip formation 84
5.9 Results of in-situ photography 93
5.10 Tool wear 102
5.11 Surface quality 108
6 Conclusions from experimental results 111
6.1 Chip formation 111
6.2 Resultant forces 113
6.3 Cutting temperatures 121
6.4 Tool wear 123
6.5 Surface quality 124
7 Modeling and simulation of the cutting process 125
7.1 Modeling of the cutting process – an overview 126
7.2 Setup of the model 135
7.3 Evaluation of material data 138
7.4 Numerical means to adapt the simulation to the cutting process 140
7.5 Application of design of experiments to the cutting simulation 142
7.6 Experimental verification of the simulation 150
8 Conclusions from cutting simulation 161
8.1 Simulation of continuous chip formation 161
8.2 Simulation of segmented chip formation 172
9 Conclusion and potential applications of the results 183
10 Literature 187
Curriculum vitae 199

List of symbols

symbol	explanation	unit
A	flexural strength	%
a	thermal diffusivity	m^2/s
A_c	cross-sectional area of the uncut chip thickness	mm^2
A_{ch}	cross-sectional area of the chip	mm^2
AISI	American Iron and Steel Institute	
Al	aluminum	
Al_2O_3	aluminum oxide	
ALE	arbitrary Lagrangian-Eulerian	
AlN	aluminum nitride	
a_p	depth of cut	mm
BN	boron nitride	
BUE	build up edge	
BUL	build up layer	
C	carbon	
CAD	computer aided design	
CMC	ceramic matrix compound	
CNC	computerized numerical control	
Co	cobalt	
c_p	specific heat coefficient	(N*m)/(kg*K)
CPU	central processing unit	
Cr	chromium	
Cu	copper	
d	diameter	mm
DOE	design of experiments	
E	Young`s Modulus	MPa
EDM	electronic discharge machining	
EDP	electronic data processing	
EDX	energy dispersive x-ray analysis	
f	feed	mm
$F_{\phi n}$	force component normal to the primary shear zone	N
$F_{\phi t}$	force component tangential to the primary shear zone	N
F_c	cutting force	N
Fe	iron	
FEM	finite element method	
F_f	feed force	N
F_m	inertia or mass force	N
F_p	passive force	N
F_{sh}	shear force	N
F_{su}	resultant shear force	N
F_z	resultant force	N
$F_{\alpha n}$	force component normal to the rake face	N
$F_{\alpha t}$	force component tangential to the rake face	N
G	degree of segmentation	
H	hydrogen	
h_c	uncut chip thickness	mm

symbol	explanation	unit
h_{ch}	chip thickness	mm
HPC	High Performance Cutting	
HSC	High Speed Cutting	
h_{tc}	thermal contact conductance	W/m^2K
HV	Vickers hardness	
IMC	intermetallic matrix compound	
$k_{c1.1}$	specific cutting force	N/mm
l	distance	mm
l_c	cutting distance	m
l_k	length of the contact zone	mm
m	strain rate coefficient	
Mg	magnesium	
MMC	metal matrix compound	
Mn	manganese	
N	nitrogen	
n	strain hardening coefficient	
n	revolutions per minute	min^{-1}
NC	numerical control	
NiO	nickel oxide	
O	oxygen	
P_c	cutting power	W
P_f	feed power	W
P_{fr}	power generated by friction	W
P_{sh}	shear power	W
P	phosphorus	
PC	personal computer	
PMC	polymer matrix composits	
p_n	normal pressure	MPa
Q	heat flux	W/m^2
R_a	arithmetic average height	µm
R_{kin}	kinematic roughness	µm
R_m	tensile strength	MPa
R_{max}	maximum roughness	µm
r_O	edge roundness	µm
$R_{p0.2}$	yield stress	MPa
R_z	five or ten point height	µm
r_ε	nose radius	mm
S	sulfur	
SEM	scanning electron microscope	
SHBT	Split-Hopkinson-Bar-Test	
Si	silicon	
SiC	silicon carbide	
T	temperature	°C
t	time	s
T_0	room or reference temperature	°C
Ti	titanium	
T_m	melting temperature	°C

symbol	explanation	unit
V	vanadium	
VB	flank wear	µm
VB_{max}	maximum flank wear	µm
VB_H	flank wear at the major cutting edge	µm
VB_N	Flank wear at the minor cutting edge	µm
v_a	cutting speed where full adiabatic shearing occurs	m/min
v_c	cutting speed	m/min
v_i	cutting speed where the inertia forces are equal to the shearing forces at conventional cutting speed	m/min
v_{konv}	conventional cutting speed	m/min
v_{sl}	sliding speed	m/s
WC	tungsten carbide	
W_N	parasitic force component normal to the flank face	N
W_T	parasitic force component tangential to the flank face	N
Z	necking	%
Zn	zinc	
Δt	time difference	µs
α_L	coefficient of linear thermal expansion	K^{-1}
α_O	rake angle	°
Ψ	temperature function	
ν	Poisson ratio	
μ	coefficient of friction	
δ_{slide}	sliding distance	mm
ε	strain	
ε_{el}	elastic strain	
ε_{kr}	creeping strain	
ε_{pl}	plastic strain	
ε_{th}	thermal expansion	
$d\varepsilon/dt$	strain rate	s^{-1}
$d\gamma/dt$	shear strain rate	s^{-1}
γ	shear strain	
γ_O	clearance angle	°
η	strain rate coefficient	MPa∗s
κ	Taylor-Quinney coefficient	
λ	thermal conductivity	W/(m∗K)
λ	wave length	mm
ρ	density	g/cm^3
σ	stress	MPa
σ_{eff}	v. Mises effective stress	MPa
τ	shear stress	MPa

1 Introduction and objective of the work

In the last decades the analysis of machining processes, the development of new cutting materials and tool geometries led to a significant increase of the productivity of machining operations. High performance technologies such as dry machining, hard machining and high speed machining became state of the art. The cooperation of tool producers and end-users supported by research institutes led to adapted solutions for nearly all machining operations. Actually, this cooperation is necessary, because the progress in tool materials is accompanied by the development of new workpiece materials. Examples are improved alloys of titanium and nickel for aerospace industries as well as metal matrix compounds for automotive applications. As the development of new cutting materials temporarily found its end by the application of cubic centered boron nitride and ultra fine grain cemented carbides, the focus of current research is on coatings. For an appropriate combination of the right machining operation, workpiece material, tool material, coating and lubrication strategy a deep understanding of the cutting process is necessary.

To obtain and transfer this understanding, many analytical, empirical and numerical models have been developed. All of them have in common that they are not capable of describing or predicting the cutting process in all its details. Even the actual possibilities of artificial intelligence and three dimensional finite element method (FEM) models are limited. Therefore, the current thesis shows an approach to describe the metal cutting process as follows:

First of all, the cutting process is described by measurements of resultant forces, temperatures and chip geometry. This is realized by the combination of conventional as well as newly developed measurement setups. They are necessary to verify the results of cutting models as well as to obtain information about whether proposed simplifications are legal. Three different workpiece materials (medium carbon steel AISI 1045 (C45E), aeronautical aluminum alloys AA 7075 (AlZnMgCu1.5) and Ti6Al4V are examined at conventional and high cutting velocities. To describe the particular setups the state of the art will be given at the beginning of every chapter.

In a second step, a FEM based model of dry cutting is presented. Keeping in mind its limitations, the model describes important mechanisms that are not measurable. Examples are shearing processes and gradients of temperatures, stresses, strains

and strain rates. As far as possible, the necessary workpiece and tool properties are determined and the results from modeling are verified by the experimental results. Finally, possible applications of the model are presented such as the prediction of tool load and wear. This information will allow to find adapted process conditions or tool-coating systems.

2 Plastic behavior of the examined workpiece materials

In the current work, the chip formation of the medium carbon steel AISI 1045 (Ck45 or C45E), the wrought aluminum alloy AA 7075-T351 (AlZnMgCu1.5) and the titanium alloy Ti6Al4V is described. The experiments comprehend micrographs of the chips, chip roots and machined surfaces of external turning as well as in-situ pictures of the orthogonal cutting process. Furthermore, temperature, resultant forces and tool wear are measured to describe the conditions under which chip formation occurs. It is distinguished between continuous and segmented chip formation.

The focus of this investigation is on the chip formation of the normalized medium carbon steel AISI 1045. This material is applied in the automotive as well as in the machine tool industry. The microstructure of AISI 1045 shows the typical black (perlite) and white (ferrite) structure of a medium carbon steel (**figure 2.1 left**).

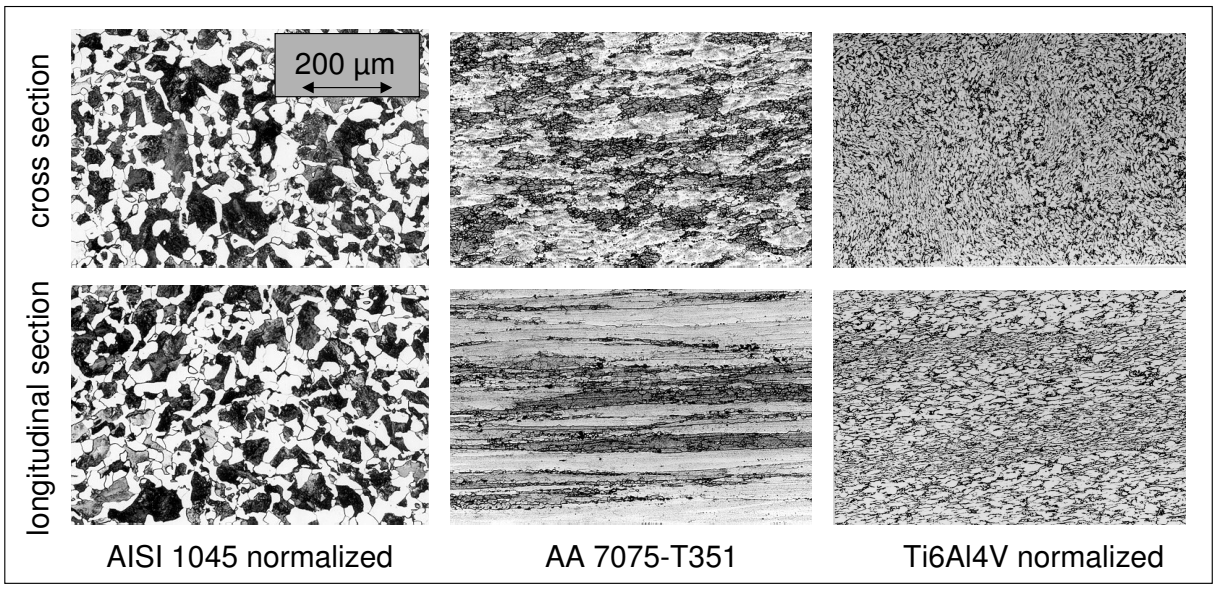


Figure 2.1: Microstructure of AISI 1045, AA 7075, Ti6Al4V

The chemical and mechanical properties can be taken from **table 2.1** to **2.4**. As a reference and to draw general conclusions from the experiments, the aluminum alloy AA 7075 and the titanium alloy Ti6Al4V are also examined. The heat treatment T351 of the aluminum alloy defines that the material is normalized, quenched, cold deformed and cold aged. The examined titanium alloy is forged and annealed. The microstructure of these alloys are also given in figure 2.1. In contrast to the steel

alloy, both microstructures show a significant dependency on the direction of the metallographic section (figure 2.1 center and right).

	C [%]	Si [%]	Mn [%]	P [%]	S [%]
AISI 1045	0.45	0.22	0.63	0.016	0.026

Table 2.1: Chemical composition of AISI 1045

	Si [%]	Fe [%]	Cu [%]	Mn [%]	Mg [%]	Cr [%]	Zn [%]	Ti [%]	Al [%]
AA 7075	0.067-0.087	0.14-0.2	1.34-1.49	0.027-0.028	2.57-2.9	0.188-0.19	5.74-6.05	0.017-0.02	balance

Table 2.2: Chemical composition of AA 7075

	C [%]	N [%]	Al [%]	O [%]	Fe [%]	H [%]	V [%]
Ti6Al4V	0.02	0.01-0.02	5.91-5.96	0.12	0.11-0.12	0.0027-0.0044	3.85-3.90

Table 2.3: Chemical composition of Ti6Al4V

	heat treatment	tensile strength R_m [MPa]	yield stress $R_{p0.2}$ [MPa]	flexural strength A [%]	necking Z [%]	hardness (Vickers)
AISI 1045	normalized	627	334	17	23.5	HV 30 169.5
AA 7075	T351	508-557	466-472	2.3-2.6	-	HV 5 185
Ti6Al4V	normalized	1219	1084	25	17.6	HV 10 350

Table 2.4: Mechanical properties of the examined materials

One major goal of this thesis is to simulate the chip formation using the finite element method. For the simulation, many material properties such as the flow stress curve,

thermal conductivity and density have to be determined. As this data strongly depends on the chemical composition, the heat treatment and the manufacturing of the workpiece, this data is described in the following. The information given in this chapter is also helpful to interpret the results of the cutting experiments.

2.1 Flow stress curve

Using FEM simulations to predict the cutting process it is important to implement a verified model of material behavior. The extreme conditions under which cutting operations take place require constitutive equations to allow the extrapolation of the flow stress curves up to strains, strain rates and temperatures which cannot be realized by an experimental setup. Moreover, the number of tests to determine the material behavior can be reduced significantly by applying constitutive material laws. Ideally, theoretical relationships derived from the physical processes at the atomic level should be used to describe the macroscopic flow behavior of materials. However, a soundly based theoretical approach of good accuracy is still some way from being realized /HARD89/. Consequently, it is inevitable that (semi-) empirical models are used to describe the constitutive behavior of the material /JASP02/.

The accuracy of these mathematical models mainly depends on the assumed boundary conditions (e.g. assumptions of plain strain or plain stress), the model of the material (e. g. assumption of material properties at very high strain rates and temperatures) and errors in numerical calculations (the accuracy how the material constants of the constitutive equation are fitted to the experimental results). Referring to Gronostajski /GRON00/ the equations describing changes in flow stress can be divided into two groups. The first group, which is applied in this work, describes directly the changes in the flow stress of materials depending on the deformation conditions such as temperature and rate of deformation. Usually, these models do not take into account the history of deformation. This can be accepted for the current work as material with a reproductive forming history is supplied to the cutting process. The second group takes the process of thermally activated softening into account. These processes are limited to temperatures below 0.2 of the homologous temperature /TREP01/, which is far below the temperatures that can be found in the shear zones of the cutting process as will be shown later. Thus thermally activated properties are not considered in the current work. The examined metals have in

common that they are inhomogeneous alloys as it can be easily seen in the micrographs, figure 2.1. The properties of these materials are determined by compression and tensile tests of specimen with a diameter of at least 4 mm. This is the reason why the influence of single grains on the flow stress is negligible and consequently the results of these tests describe a quasi homogenous material. The workpiece material behaves elastic-plastic. This means that under load it starts to behave elastic. If the flow stress is reached the material only behaves plastic. The flow stress is defined as the stress where the material deforms irreversible. This value can be obtained by different material tests and it strongly depends on the strain, strain rate and temperature. Approaches to obtain the flow stress data and to describe the flow stress curve by constitutive equations will be presented later. However, all flow stress data used in this work is based on the experiments and constitutive material laws by Treppmann /TREP01/.

2.1.1 Description of the flow stress curve by constitutive equations

In cutting operations, the values for strain, strain rate and temperature in the various shear zones are much higher than in forming operations. Klocke et al. /KLOC99/ calculated strain rates up to $d\varepsilon/dt = 10^7\ s^{-1}$ based on the measurement of the shear bands in chips. In this area the strain can increase up to $\varepsilon = 3$ and the temperature is estimated to rise up to the melting temperature. As a comparison the values in a conventional quasi-statical compression test are $\varepsilon = 0.7$, $d\varepsilon/dt = 10\ s^{-1}$ and $T = 1000$ °C /TREP01/. Because of the enormous range of values for strain, strain rate and temperatures which has to be delivered to the FEM, it is not suitable to rely only on test results. Therefore, constitutive equations for metal alloys are preferred to set up the simulation. However, a constitutive equation uses structural mechanical mechanisms to describe the material behavior. Main parts of such an equation are the strain, strain rate and temperature. These equations are fitted to experimental data by material dependent coefficients. This fitting is the main reason why different constitutive equations are suitable to describe the run of the flow stress curve of one material. Hamann et al. defined the rules to get reliable constitutive laws for cutting operations /MESL00/:

- The static and dynamic test benches must be equipped with a high energy heating device because dynamic testing at room temperature does not allow enough temperature increase for a reliable estimation of thermal softening.
- At least 4 testing conditions with crossing parameters should be performed, e.g. quasi static, low temperature; quasi static, high temperature; dynamic, low temperature; dynamic, high temperature.
- Quasi static conditions should be slow enough for the isothermal assumption to apply.
- Dynamic loading conditions should be high enough for the adiabatic assumption to apply.
- Careful microscopic observations of impacted specimen and chips are necessary to compare the response of the material.
- Higher loading conditions will preferably be done on “hat shaped” specimen (this type of specimen will be described later).

For low cutting speeds, where a rise in temperature can be neglected, Stevenson found that using constitutive relations obtained from conventional material testing for predicting resultant forces show a good agreement /STEV97/. As the temperature and high strain rates play a significant role in cutting with industrial relevant parameters, the statement by Stevenson has to be proved by own experiments. In literature, the following constitutive equations are used to predict the material behavior in cutting simulations.

A simple empirical description of the dependency of the flow stress on the strain was given by Hollomon, equation 2.1 /HOLL45/. In this equation the flow stress is calculated by a material constant K, the strain ε and strain hardening coefficient n. It is obvious that the flow stress description is not accurate for very low values of strain. However, its simple structure leads to a wide spread of this formulation. To overcome this problem Swift introduced an initial flow stress for $\varepsilon = 0$, equation 2.2 /SWIF52/.

$$\sigma = K\varepsilon^n \qquad \text{(eq. 2.1)}$$

$$\sigma = K(B+\varepsilon)^n \qquad \text{(eq. 2.2)}$$

Johnson-Cook /JOHN83/

Johnson and Cook assumed the von Mises flow stress σ to be independently affected by strain, strain rate and temperature, equation 2.3 and 2.4.

$$\sigma = [A + B\varepsilon^{n}][1 + C\ln\dot{\varepsilon}^{*}][1 - T^{*m}] \qquad \text{(eq. 2.3)}$$

$$T^{*} = \frac{T - T_0}{T_M - T_0} \qquad \text{(eq. 2.4)}$$

In these equations, ε is the equivalent plastic strain, dε*/dt the strain rate normalized to dε/dt = 1.0 s^{-1}. T* is the homologous temperature that is calculated by the absolute temperature T, the melting temperature T_m and the room temperature T_0. A, B, C, n and m are considered to be material constants which are determined by material testing. It is obvious that an interaction, such as the influence of the strain on the temperature is not considered in this model. For AISI 1045 **figure 2.2** shows the measured values for the flow stress dependent on the temperature and equivalent plastic strain /JASP02a/. The flow stress curve calculated by the application of the Johnson-Cook law can also be taken from figure 2.2**.** Dotted lines represent the model by Johnson-Cook, the markers are experimental data.

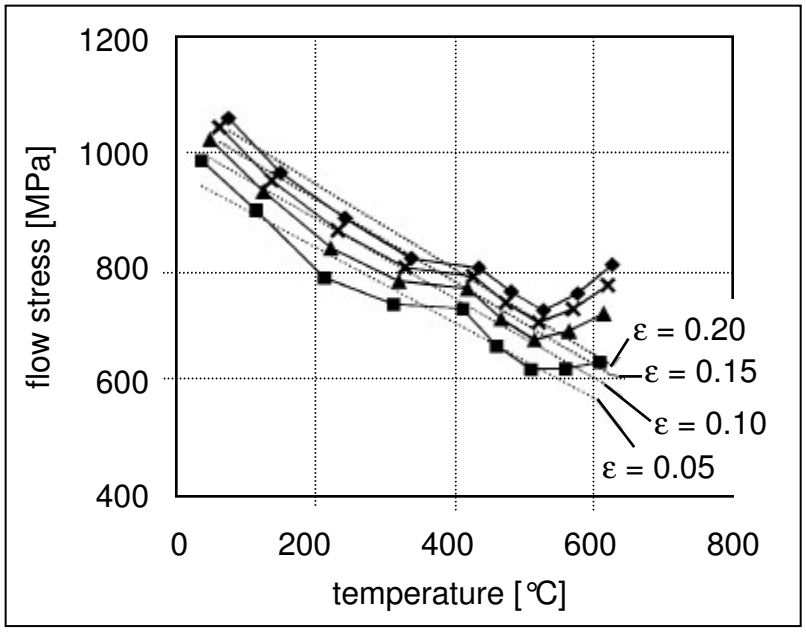


Figure 2.2: Flow stress versus temperature for AISI 1045 at a strain rate of dε/dt = 7.5 10^{-3} s^{-1} /JASP02a/

It is obvious that the model deviates from the measurement results. This is most significant in the temperature range where the blue brittleness of the material influences the flow stress curve (T ≈ 410 °C). To minimize this error, Altan et al. developed a modified Johnson-Cook equation (equation 2.5) that describes the material behavior more accurately /ALTA00/. In this equation an additional material constant a is needed.

$$\sigma = [\mathrm{B}\bar{\varepsilon}^{n}][1 + C\ln\dot{\bar{\varepsilon}}^{*}]\left[\left(\frac{T_M - T}{T_M - T_0}\right) + ae^{-0.00005(T-700)^2}\right] \qquad \text{(eq. 2.5)}$$

Description of the flow stress curve by Maekawa

Maekawa /MAEK96/ has identified a constitutive equation for a AISI4140 (42CrMo4) steel where interactions between temperature, strain rate and strain hardening are taken into account, equation 2.6. In this law the coefficients A and N strongly depend on the temperature.

$$\bar{\sigma} = \mathrm{A}\left(\frac{\dot{\bar{\varepsilon}}}{1000}\right)^{\mathrm{M}} \mathrm{e}^{\mathrm{aT}}\left(\frac{\dot{\bar{\varepsilon}}}{1000}\right)^{\mathrm{m}}\left(\int_{\text{strain path}} \mathrm{e}^{-\mathrm{aT/N}}\left(\frac{\dot{\bar{\varepsilon}}}{1000}\right)^{-\mathrm{m/M}} \mathrm{d}\bar{\varepsilon}\right)^{\mathrm{N}} \qquad \text{(eq. 2.6)}$$

Zerilli-Armstrong /ZERI87/

Applying the recent developments in dislocation-mechanics theory, Zerilli and Armstrong set up a more complex constitutive material law. This includes a distinction between face-centered cubic (f.c.c.), equation 2.7, and body-centered cubic (b.c.c.), equation 2.8, materials. In these equations C_0 - C_5 are material constants.

$$\sigma = C_0 + C_1 \exp(-C_3 T + C_4 T \ln\dot{\bar{\varepsilon}}^{*}) + C_5 \bar{\varepsilon}^{n} \qquad \text{(eq. 2.7)}$$

$$\sigma = C_0 + C_2 \bar{\varepsilon}^{0,5} \exp(-C_3 T + C_4 T \ln\dot{\bar{\varepsilon}}^{*}) \qquad \text{(eq. 2.8)}$$

It is remarkable that Zerilli-Armstrong assume that the flow stress curve of the face-centered metal is strongly affected by temperature and strain rate. According to them this is not the case for body-centered alloys. To compare the Zerilli-Armstrong model to that of Johnson-Cook, the flow stress data, model and constants are shown in **figure 2.3**. Dotted lines represent the model by Zerilli-Armstrong, the markers are

experimental data. Jaspers et al. compared both material laws to experimental results /JAS02b/ for an aluminum (AA6082-T6) and a steel alloy (AISI 1045). They found that for steel the Zerilli-Armstrong and for aluminum the Johnson-Cook model show the best results. This result makes obvious that the selection of the applied material law is very important and that an experimental verification must be conducted.

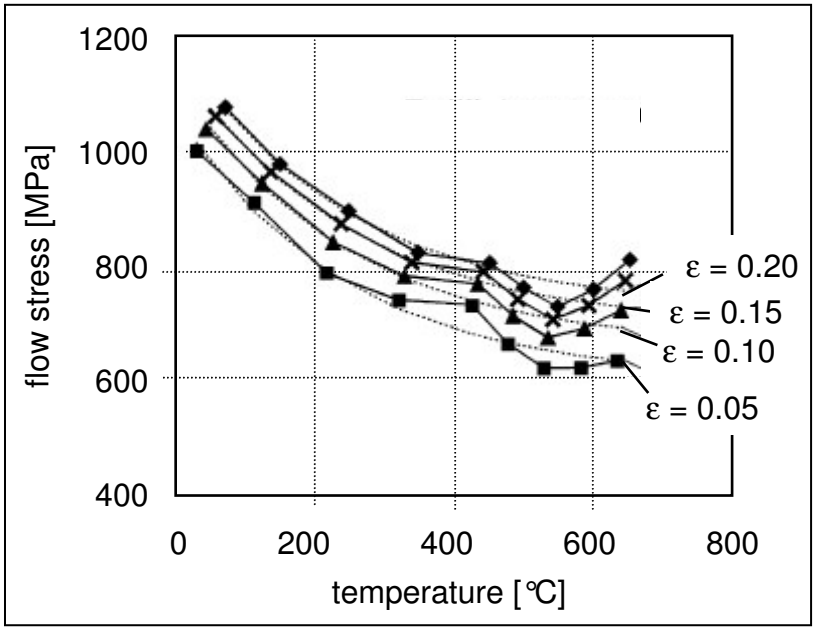


Figure 2.3: Flow stress versus temperature for AISI1045 at a strain rate of $d\varepsilon/dt = 7.5\ 10^{-3}\ s^{-1}$ /JASP02a/

Material law by Treppmann and El-Magd /TREP01/

Treppmann and El-Magd developed a transient equation (2.13) which covers the range of low, medium and high strain rates and thus creeping mechanisms as well as viscous damping, equations 2.9 to 2.11. Moreover, it considers the dynamical strain aging for the ferrous alloy AISI 1045. This equation was set up for the same metal alloys as used for machining tests in this work. Therefore, and because the author knows that the rules by Hamann mentioned above are fulfilled, this law is applied in this work.

$$\dot{\varepsilon} = (1-M)(\dot{\varepsilon}_{kr} + \dot{\varepsilon}_{pl}) + M \cdot \dot{\varepsilon}_{damping} \quad \text{(eq. 2.9)}$$

$$M = 1 - \exp\left(-\left(\frac{\dot{\varepsilon}}{\dot{\varepsilon}_G(T,\varepsilon)}\right)^{100}\right) \quad \text{(eq. 2.10)}$$

$$\sigma_G(T,\varepsilon) = \sigma_H(T,\varepsilon)\left(\frac{\dot{\varepsilon}_G(T,\varepsilon)}{\dot{\varepsilon}*}\right)^{m(T)} \quad \text{(eq. 2.11)}$$

$$\dot{\varepsilon}_G(T,\varepsilon) = \left(\frac{m(T)\cdot\sigma_h(T,\varepsilon)}{\eta}\right)^{1/(1-m(T))} \quad \text{(eq. 2.12)}$$

$$\dot{\varepsilon} = (1-M)\left(\left(\frac{\sigma}{\sigma_0(T,\varepsilon)}\right)^{N(T)} + \left(\frac{\sigma}{\sigma_H(T,\varepsilon)}\right)^{1/m(T)}\right)\dot{\varepsilon}* + M\left(\frac{\sigma-\sigma_G(T,\varepsilon)}{\eta} + \dot{\varepsilon}_G(T,\varepsilon)\right) \quad \text{(eq. 2.13)}$$

The values for the constants of the equations 2.9 to 2.13 for the three workpiece materials are taken from literature /TREP01/. Equation 2.13 can only be solved by using numerical methods. Therefore, simulations based upon a less complicated material description are also examined. If a term which describes the viscous damping is added to the approach by Swift, equation 2.2, the following equation 2.14 is obtained. It has to be considered that this approach is only valid for high strain rates and a limited range of temperature.

$$\sigma = (K(B+\varepsilon)^n + \eta\cdot\dot{\varepsilon})\Psi(T) \quad \text{(eq. 2.14)}$$

In this equation K, B, n and η are material constants describing the influence of strain and strain rate on the flow stress. To consider the thermal softening of the material two different equations can be examined, equation 2.15 and 2.16. The coefficients for equation 2.14, which will be used later, are given in **table 2.5**.

$$\Psi(T) = \exp\left[-\beta_1\frac{T-T_0}{T_m}\right] \quad \text{(eq. 2.15)}$$

$$\Psi(T) = \left[1-\beta_3\frac{T-T_0}{T_m}\right]^{\alpha} \quad \text{(eq. 2.16)}$$

To obtain and to verify the material dependent variables of the equations 2.13 and 2.14 a high amount of material testing was done. For the range of low and medium strain rates (10^{-3} s^{-1} < dε/dt <100 s^{-1}) conventional tensile and compression tests

were applied. To obtain the material behavior at strain rates up to $d\varepsilon/dt = 10^4\ s^{-1}$ a Split-Hopkinson-Pressure-Bar (SHPB) was applied, **figure 2.4**.

	K [MPa]	B	n	η [MPa∗s]	β_1 [-]	T_0 [°C]	T_m [°C]
AISI 1045	1390	0	0.21	0.02	1.43	20	1428
AA 7075	1036	0.01	0.2	0.004	2.57	20	625
Ti6Al4V	1806	0	0.24	0.06	1	20	1538

Table 2.5: Coefficients of equation 2.14

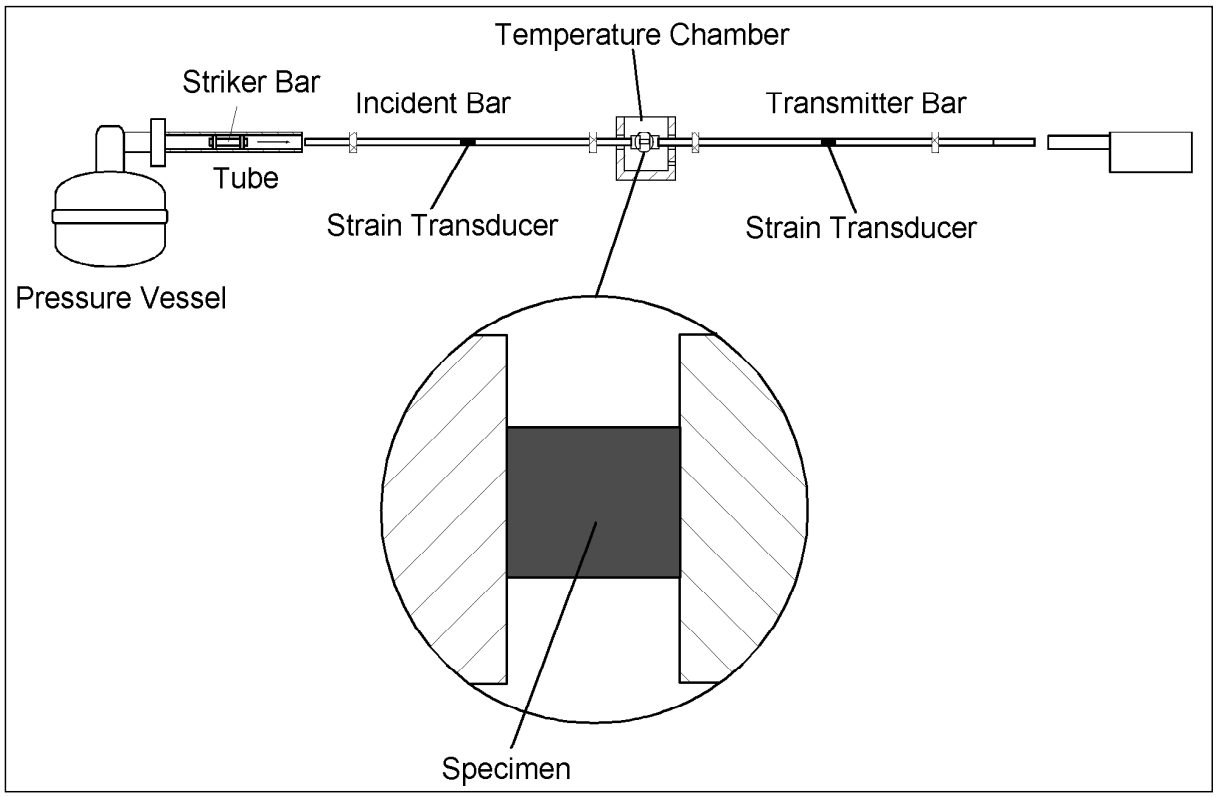


Figure 2.4: Split-Hopkinson-Pressure-Bar-Test /TREP01/

In this test a mechanical wave is applied in an incident bar by a projectile. At the end of the incident bar the specimen is located and glued onto a transmitter bar. The different diameters of the incident bar and the specimen result in a deformation of the specimen. The mechanical wave in the input bar is divided into two parts. The first one is reflected at the end of the incident bar because of its higher diameter. The second part runs through the specimen into the transmitter bar. Both parts of the mechanical wave can be measured by strain transducers on the incident and

transmitter bar. The results of these measurements contain information about the particle speed, the compressive strain and strain rate. Modifications of the SHPB allow to conduct tensile and torsion tests at high strain rates. To obtain flow stress data at increased temperatures, the specimen were heated up before testing. **Figure 2.5** shows the specimen after a SHPB-test for all examined materials.

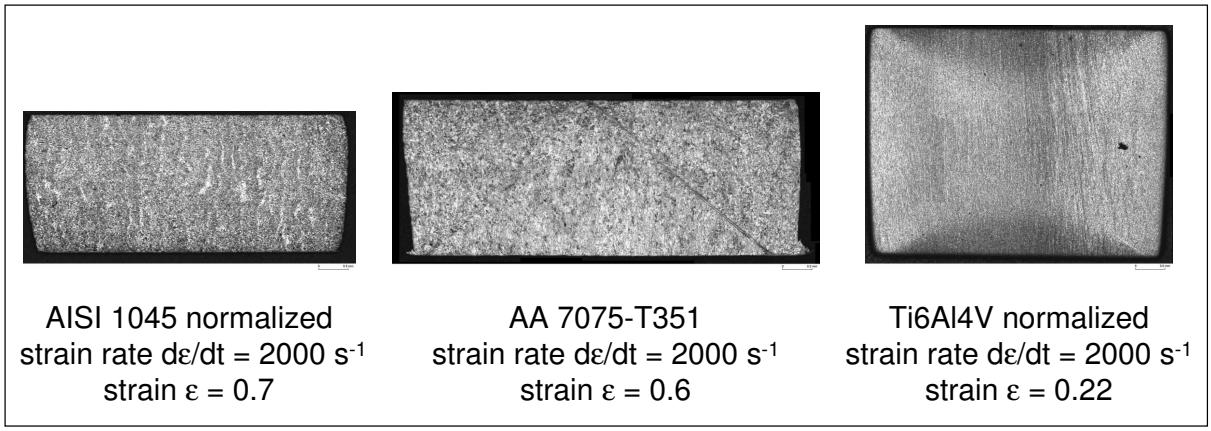


Figure 2.5: Obtained specimen of AISI 1045, AA 7075 and Ti6Al4V /TREP01/

It can be found that AISI 1045 shows no failure after a compression up to $\varepsilon = 0.7$ at a strain rate of $d\varepsilon/dt = 2000\ s^{-1}$. Compressing the aluminum alloy AA 7075 under the same conditions the material fails by catastrophic shearing. The titanium alloy Ti6Al4V does not allow such high values for strain. It fails at a strain of approximately $\varepsilon = 0.22$ due to the appearance of a shear band. To verify his material law Treppmann used the SHPB-test and hat-shaped specimen to achieve a shear localization with high values for strain and strain rate. **Figure 2.6** shows the specimen and the magnification of the sheared areas.

The shear strain and shear strain rate in the shear zone can be calculated by equation 2.17 where γ is the shear strain, $d\gamma/dt$ the shear strain rate, B the thickness of the shear zone and v the velocity.

$$\dot{\gamma} = v / B \text{ and } \gamma = \int \mathrm{vdt/B} \qquad \text{(eq. 2.17)}$$

The obtained results are average values and can significantly differ from the real local strains and strain rates. However, even the average values are much higher than those of dynamic compression tests. Treppmann simulated this experiment and was able to verify the constitutive material law of equation 2.13.

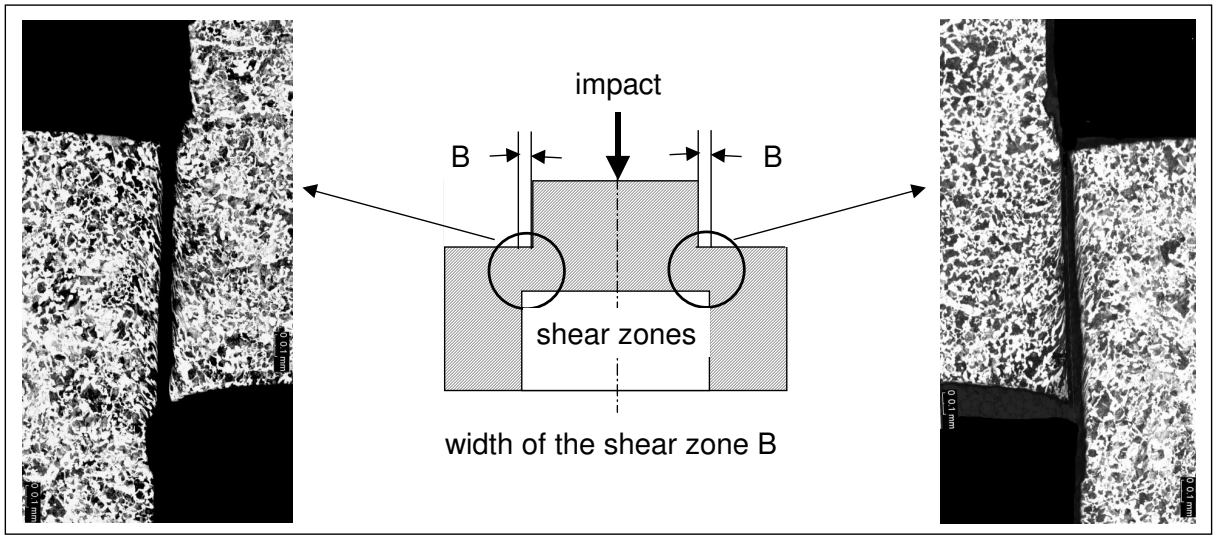


Figure 2.6: Hat-shaped specimen and microstructure of the shear zone /TREP01/

Figure 2.7 shows the obtained results by equation 2.13 for AISI 1045 at a constant strain of $\varepsilon = 0.1$. The line represents the results by equation 2.13, marker stand for the experimental data. It will be described later that the occurrence of shear bands or catastrophic shearing is an important mechanism in chip formation, too.

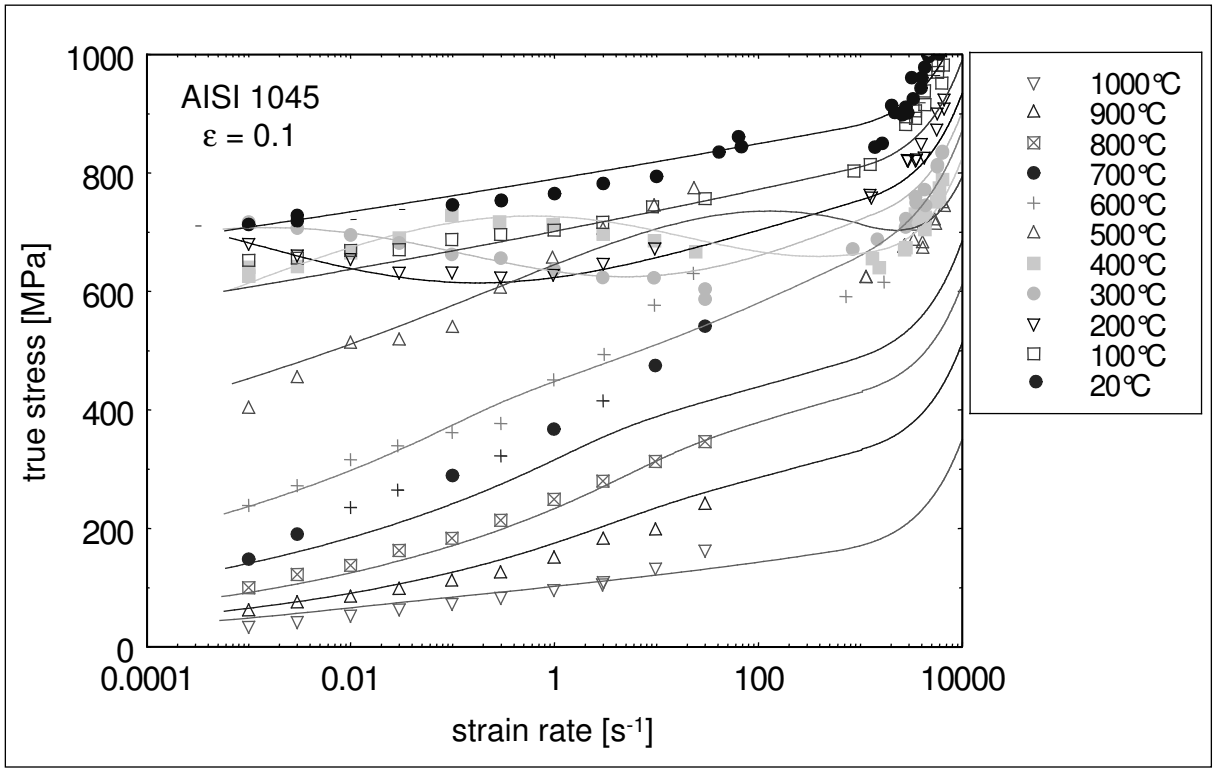


Figure 2.7: Flow stress versus strain rate for AISI 1045 at a strain of $\varepsilon = 0.1$ /TREP01/

For the evaluation of the flow stress curve by the results of the compression tests, the failure is not considered. Currently, an approach to simplify the equation 2.13 is examined by El-Magd /ELMA04/. In this equation 2.18 the flow stress is directly calculated and the number of material dependent parameters is reduced from about 25 to 10 parameters. For ferrous materials an additional term R (equation 2.20) that considers strain aging has to be added.

$$\sigma_0 = (\sigma_h \cdot \dot{\varepsilon}^m \cdot \varepsilon^n + \eta\dot{\varepsilon})\Psi(T) \qquad \text{(eq. 2.18)}$$

$$\sigma = \frac{\sigma_0}{\left(1 + \frac{(\sigma_0/\sigma^*)^v}{\exp(-T/T^*)} \cdot \frac{\dot{\varepsilon}^*}{\dot{\varepsilon}}\right)^{1/v}} \qquad \text{(eq. 2.19)}$$

$$R = 140 \cdot \exp\left[-\left(\frac{T-700}{130}\right)^6\right] \cdot \exp\left[-\left(\frac{\ln(\dot{\varepsilon}) - 0.023 \cdot T + 16.5}{9 - 0.01 \cdot T}\right)^2\right] \qquad \text{(eq. 2.20)}$$

Flow stress curve adapted to cutting by Marusich /ORTI95/

To simulate the workpiece behavior Marusich used a material law (equation 2.21) with a similar structure as Johnson-Cook. Both laws have in common that the flow stress is determined by the product of three terms which depend on the plastic strain ($g(\varepsilon^p,T)$), strain rate ($\Gamma(d\varepsilon/dt)$) and temperature ($\Theta(T)$). All three components of equation 3.20 are defined for two different areas.

$$\sigma(\varepsilon,\dot{\varepsilon},T) = g(\varepsilon^p,T) \cdot \Gamma(\dot{\varepsilon}) \cdot \Theta(T) \qquad \text{(eq. 2.21)}$$

For the strain dependent term $g(\varepsilon^p,T)$ Marusich defined one range of strain where the stress increases steadily due to strain hardening. In the second area $g(\varepsilon^p,T)$ is constant. The plastic strain that separates both areas is called cut of strain ε^p_{cut}. The function $g(\varepsilon^p,T)$ for both cases is defined in equation 2.22 and 2.23.

$$g = \sigma_0 \cdot \Theta(T)\left(1 + \frac{\varepsilon^p}{\varepsilon_0^p}\right)^{1/n} \text{, if } \varepsilon^p < \varepsilon^p{}_{cut} \qquad \text{(eq. 2.22)}$$

$$g = \sigma_0 \cdot \Theta(T)\left(1 + \frac{\varepsilon^p{}_{cut}}{\varepsilon_0^p}\right)^{1/n} \text{, if } \varepsilon^p \geq \varepsilon^p{}_{cut} \qquad \text{(eq. 2.23)}$$

In these equations σ_0 is the initial flow stress at room temperature T_0 and for ε^p and $d\varepsilon^p/dt$ equal zero (compare the approach by Swift), ε^p is the plastic strain, ε^p_0 a reference strain, n the strain hardening coefficient. The strain rate dependent part of the flow stress ($\Gamma(d\varepsilon/dt)$) takes the different areas of strain rate hardening into account. In the equations 2.24 and 2.25 $d\varepsilon^p/dt$ is the plastic strain rate, $d\varepsilon^p_0/dt$ a reference strain rate and σ the effective strain by von Mises. The value for $d\varepsilon^p_t/dt$ defines the strain rate for which equation 2.25 is valid. The existence of $d\varepsilon^p_t/dt$ was also determined by Treppmann /TREP01/. The strain rate hardening coefficients m_1 and m_2 are different in both areas.

$$\left(1+\frac{\dot{\varepsilon}^p}{\dot{\varepsilon}^p_0}\right)=\left(\frac{\overline{\sigma}}{g(\varepsilon^p)}\right)^{m_1}, \text{if } \dot{\varepsilon}^p \le \dot{\varepsilon}^p_t \qquad \text{(eq. 2.24)}$$

$$\left(1+\frac{\dot{\varepsilon}^p}{\dot{\varepsilon}^p_0}\right)\left(1+\frac{\dot{\varepsilon}_t}{\dot{\varepsilon}^p_0}\right)^{m_2/m_1}=\left(\frac{\overline{\sigma}}{g(\varepsilon^p)}\right)^{m_1}, \text{if } \dot{\varepsilon}^p > \dot{\varepsilon}^p_t \qquad \text{(eq. 2.25)}$$

The influence of thermal softening on the flow stress is realized by fitting equation 2.26 to the plot of the flow stress versus the temperature. Until the cut off temperature T_{cut} is reached the flow stress is nearly equal to the measurement values. At higher temperatures ($T > T_{cut}$) the flow stress is extrapolated linear until it reaches zero, equation 2.27. In equation 2.26 $C_0 – C_5$ are material constants and in equation 2.27 T_{melt} is the melting temperature of the workpiece.

$$\Theta(T)=C_0+C_1T+C_2T^2+...+C_5T^5 \text{ , if } T \le T_{cut} \qquad \text{(eq. 2.26)}$$

$$\Theta(T)=\Theta(T_{cut})-(T-T_{cut})/(T_{melt}-T_{cut}), \text{if } T > T_{cut} \qquad \text{(eq. 2.27)}$$

Flow stress curve adapted to cutting by Usui /CHIL98/

A major difference between the conditions of the compression tests and cutting operations is that compression tests use preheated specimen. The comparable long time from heating to the test allows the material's microstructure to come into thermal equilibrium. In machining, the heating from room temperature to the heated state takes only microseconds. As the microstructure has a strong influence on the chip formation process /SCHU01, SCH01b/ this is a possible error source. To prevent this Usui et al. chose another approach. They coupled a Split-Hopkinson-Bar-Test and an

inductive heating device. The fast heating prevents any annealing /CHIL98/. This allowed them to conduct dynamic compression tests with specimen of different forming histories. The results were fitted to equation 2.28. In this equation A is the thermal softening factor while M and N describe the strain rate and strain dependency. The factors a and m are history effect correction parameters, T the temperature [°C] and $d\varepsilon_0/dt = 1000\ s^{-1}$ a reference strain rate. Further results for different steel alloys and the titanium alloy Ti6Al4V can also be taken from /CHIL98/.

$$\sigma = A(\dot{\varepsilon}/\varepsilon_0)^M e^{aT}(\dot{\varepsilon}/\varepsilon_0)^m \left[\int_{strainpath} d^{-aT/N}(\dot{\varepsilon}/\varepsilon_0)^{-m/N} d\varepsilon\right]^N \qquad \text{(eq. 2.28)}$$

For AISI 1045 the coefficients of equation 2.28 are given as follows, **table 2.6** /CHIL98/.

A	$1350*\exp(-0.0011T) +167*\exp(-0.00006(T-275)^2)$
M	0.036
N	$0.17*\exp(-0.0017) +0.09*\exp(-0.000015(T-340)^2)$
a	0.00014
m	-0.0024

Table 2.6: Coefficients for the approach by Usui (equation 2.28) /CHIL98/

Description of the flow stress curve by cutting experiments – the Oxcut approach

Another approach to obtain the flow stress under cutting conditions is to conduct machining experiments and to use the measured resultant forces to determine the flow stress. To calculate the flow stress from the resultant force the analytical approach by Oxley was used by Altan et al. /ÖZEL00, KERK99, SHAT00, ALTA00/ and will be described later. The theory by Oxley links the flow stress in the primary shear zone to the resultant forces and tool geometry. To do so, the resultant forces and the geometry of the chip root (shear angle, length and thickness of the primary and secondary shear zone) have to be determined by cutting and quick stop experiments. Furthermore a constitutive material law, in this case the equation by Johnson-Cook, is needed and the coefficients are fitted by using a numerical routine

called OXCUT. This approach shows good results if the following demands are fulfilled, **table 2.7**.

Oxley`s assumptions	experimental requirements
1. cutting edge is acceptable sharp (very small edge radius)	1. tool wear is considerably small
2. chip formation is continuous type	2. vibration in the cutting operation is not too high to affect force data acquisition
3. the depth of cut is more than 10 times of the feed to satisfy plane strain conditions	3. no chip breakage during the cut
4. stresses and temperatures in the shear plane and the tool-chip interface are assumed as average values and uniform distribution	4. cut chip is continuous enough for measuring its thickness
5. passive forces can be neglected	5. quick-stop chip have less thinning and no severe broken chip is collected
6. no built-up-edge (BUE) appears on the tool	

Table 2.7: Demands for the application of the Oxley approach /ALTA00/

However, the approach by Oxley is limited to a continuous chip formation. Therefore, it cannot be applied to determine the flow stress curve of materials which show segmented chip formation. Examples are hard to machine alloys (titanium and nickel based alloys) and hardened steel at all cutting conditions and aluminum, magnesium and medium steels at higher cutting speeds and/or feeds. This limitation and the considerable effort to produce and evaluate the chip roots are the reason why this approach is not considered in this work.

2.1.2 Adiabatic and isothermal flow stress curve

In material science two kinds of flow stress curves are commonly used, the adiabatic and the isothermal type. In manufacturing technology and in the applied FEM code DEFORM the isothermal flow stress curve is applied, **figure 2.8 left**. The increase of the flow stress with the strain (strain hardening) is characteristic for an isothermal

flow stress curve. The temperature of the specimen is assumed to be constant for the whole test. This means, that the increase of temperature by deformation of the specimen is neglected. The adiabatic flow stress curve considers this increase. Especially at higher strain rates the temperature of the specimen is not equal to the environment. The resultant increase of the temperature leads to a decrease of the flow stress at high values for strain. An example of an adiabatic flow stress curve is given in figure 2.8 right.

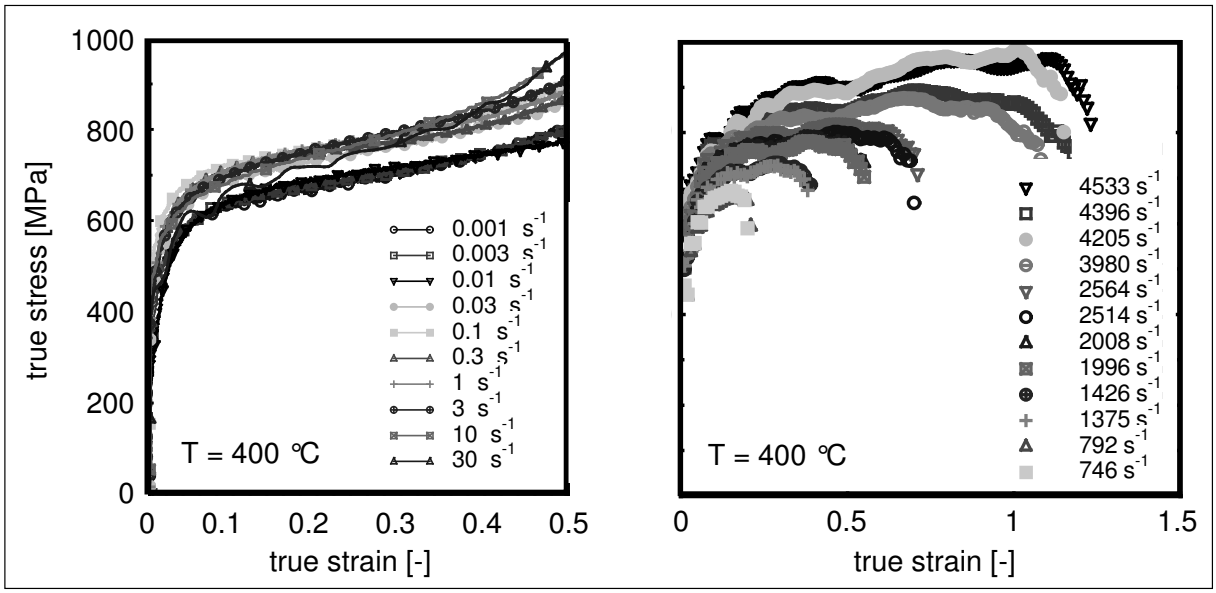


Figure 2.8: Isothermal and adiabatic flow stress curve for AISI 1045 at different strain rates /TREP01/

If for example compression tests at high strain rates are conducted, the resulting flow stress curve is an adiabatic one. At high strain rates the isothermal flow stress curve has to be calculated from the adiabatic /TREP01/. For both kinds of flow stress curves the increase of strain leads to a rise of the flow stress (strain hardening) which is decreased if the temperature is also increased (thermal softening). For AISI 1045 a temperature at which the strain hardening is fully compensated by the thermal softening has to exist. At this temperature a possible increase of the flow stress is only due to a rise of the strain rate (strain rate dependency) /TREP01/. Regarding the conditions under which cutting operations take place it is probable that the strain rate dependency may have an influence on the chip formation.

As mentioned above, the FEM-code DEFORM applied in the current work needs an isothermal flow stress curve as input data. The increase of temperature by

deformation is taken into account automatically if the thermo-mechanical calculation is activated. If an adiabatic flow stress curve is applied and the thermo-mechanical calculation is activated, then the temperature increase by the deformation of the material is considered twice and the simulation results are wrong.

2.1.3 Failure mechanisms

The determination of the flow stress curves mentioned above is based on the assumption that the workpiece material behaves ideally plastically. This is realized by evaluating the experimental results, e.g. the stress – strain curve in a tensile test, only until necking of the material starts. A procedure like this leads to the setup of constitutive material laws which describe the plastic behavior of the specimen. However, technical alloys do not show an ideal plastic behavior over the whole range of test conditions. In compression tests adiabatic shearing occurs. In tensile tests the specimen fail by necking, crack initiation and crack growth.

Failure by adiabatic shearing and cracking

In dynamical compression tests, such as the Split-Hopkinson-Pressure-Bar test, the evaluated force- time or force- distance signal is considered until the failure of the specimen occurs. Figure 2.5 shows the resulting specimen of such a test. For the aluminum and the titanium specimen adiabatic shearing can be found while the steel specimen does not show any failure under these conditions. The occurrence of shearing depends on the values for strain, strain rate and temperature but also on the heat treatment of the material. Brodmann found that a peak aged aluminum alloy AA 7075 fails in the Split-Hopkinson-Pressure-Bar test by severe adiabatic shearing while the same material in an overaged status does not show any shearing /BROD01/. Under impact loading, an adiabatic shear band can be defined as a stress localization phenomenon generally caused by a plastic instability. At strain rates above 10^3 s^{-1}, plastic deformation in the impacted material has not enough time to occur thoroughly /RECH64/. Therefore, the impact energy has to be dissipated rapidly by an elevation of temperature within the material. This adiabatic temperature rise in the material can be very high and, because of the short duration of the event, it is concentrated within narrow bands at locations of maximum stresses. As a consequence the material within the shear band can possibly melt or, more usually,

its microstructure will be changed dramatically with the formation of the transformed white phase. Dynamic impact material failure can thus differ from the other dynamic fracture modes of void formation and coalescence. The fracture surface is relatively smooth, with fine striations running parallel to the shear direction. Also, cracks and secondary micro-cracks can be found in the fracture surface, indicating the brittleness of the examined AA 7075 material /LEE00/.

Nominally the mechanism of adiabatic shearing can be simulated, because it only depends on the response of the materials flow stress on the strain, strain rate and temperature. In reality it is doubtful whether the adiabatic behavior of the material can be modeled because the important thermo-mechanical parameters such as thermal conductivity are hardly known for very high temperature gradients. But even if adiabatic shearing occurs it was found by Brodmann that the resulting loss of material strength cannot be explained by the thermal softening alone. An additive failure mechanism, the occurrence of fracture, is needed to obtain this loss. Industrially applied alloys fail by strain dependent fractures supported by inhomogenities such as inclusions, which allow the initiation of micro cracks and voids. For the aluminum alloy AA 7075 the fracture mechanism is also influenced by the strain rate. An increase of strain rate leads to the occurrence of fractures at lower values for strain. Additionally, a rise in temperature increases the strain loss which can be explained by a limited adhesion of the aluminum matrix and embedded particles. For the aluminum alloy AA 7075 Brodmann found that the Avrami-function can be applied to describe the flow of the stress of a specimen which fails by fracture /BROD01/. To describe fracture several approaches can be found in literature /ZITZ95/.

2.1.4 Important aspects about the flow stress curve in cutting

As described above several test setups were developed to describe the material behavior under cutting conditions. However, only the Oxcut procedure can claim to determine material data under real cutting conditions but is restricted by the simplifications of the Oxley theory /OXLE62, OXLE89/. The test conditions of the other setups differ from those in cutting by the geometry and stress conditions. Especially the multi-axial stress conditions in the test setups are different to those in cutting. Additionally the inhomogeneous nature of the workpiece is relevant for chip

formation /ZIEB96/. As this plays an important role in the case of failure it is obvious that the existing approaches to describe material behavior in cutting are limited. Furthermore the values for strain, strain rate and temperature which are obtained in the cutting process are far above those of material testing. Even if constitutive equations are applied which allow an extrapolation of the flow stress it is questionable if all relevant thermo-mechanical phenomena that take place at those extreme conditions are taken into account.

3 Elastic and thermo-mechanical properties of workpiece and tool

In the current chapter the elastic and thermo-mechanical properties of the workpiece and the tool materials which have to be given to the simulation are described. Under the applied cutting conditions the tool is regarded as ideally elastically and thus no flow stress data is given. However, the influence of plastic deformation can be considered if suitable flow stress data for a tool material exists as it is the case for tungsten carbide tools /LEE00a/. The main aspects for the choice of the tool material are a sufficient wear resistance and easy to determine material properties. For cutting the aluminum alloy AA 7075 an uncoated cemented carbide tool, for the steel alloy AISI 1045 and the titanium alloy Ti6Al4V at conventional and high cutting speed a SiC-whisker reinforced oxide ceramic tool was used. Furthermore, at very high cutting speeds the titanium alloy was also machined with a polycrystalline boron nitride tool. The chemical composition and some properties can be taken from **tables 3.1** to **3.3**.

	WC [%]	Co [%]	Young's Modulus [GPa]	Poisson ratio [-]	density [g/cm^3]	Vickers hardness HV 3
HW-K10	89.8	10.2	600	0.22	14.96	1563

Table 3.1: Properties of the HW-K20 cemented carbide tool /SAND03/

	Al_2O_3 [%]	SiC [%]	Young's Modulus [GPa]	Poisson ratio [-]	density [g/cm^3]	Vickers hardness HV 3
CC670	75	25	400	0.25	3.7	2000

Table 3.2: Properties of the SiC-whisker reinforced tool CC670 /SAND03/

	BN [%]	WC [%]	Co [%]	NiO [%]	AlN [%]	Young's Modulus [GPa]	Poisson ratio [-]	density [g/cm^3]	Vickers hardness HV 3
BN50	81.9	4.6	11.5	0.8	1.2	630	0.14	3.9	3400

Table 3.3: Properties of the PCBN tool BN50 /SAND03/

It has to be considered that, in contrast to the flow stress curve, this data is only available for low process times. Therefore, the dependency on the temperature is a quasi static one. It is questionable whether these material data describes the physical properties correctly if the temperature gradients are high. However, as no high speed data is available this quasi-static data is applied to the simulation.

3.1 Young's modulus E

The Young's modulus E is an elastic material property of solids. It can be calculated by the Hook law, equation 3.1 and describes the dependency of the elastic stress on the elastic strain. Young's modulus strongly depends on the temperature, **figure 3.1**, and the plastic strain of the material. Latter will be neglected in this work as well as the possibility to calculate the Young's modulus by the properties of the atomic lattice of the alloy /TROO80/. The Young's modulus is a quite important input value because for elastic objects it influences the value of the element stiffness matrix [K]. Assuming a square element with four nodes, the thickness t and the Poisson ratio ν the stiffness matrix is obtained, equation 3.2. The property of a finite element is given by equation 3.3 where {F} represents all external forces and torques and {U} is the strain matrix.

$$\sigma = E \cdot \varepsilon \qquad \text{(eq. 3.1)}$$

$$[K] = \frac{Et}{12(1-\nu^2)} \begin{bmatrix} 1 & -1 \\ -1 & 1 \end{bmatrix} \qquad \text{(eq. 3.2)}$$

$$\{F\} = [K]\{U\} \qquad \text{(eq. 3.3)}$$

It is obvious that if the Young's modulus gets zero or negative the stiffness matrix [K] also will. This is not realistic and it additionally leads to a crash of the simulation.

Unfortunately, it can be seen in figure 3.1 that Young's modulus for all examined workpiece materials is proportional to the temperature and has a negative slope if the temperature is increased. Moreover, it cannot be determined for such high temperatures as they occur in cutting /RICH91, RICH88/.

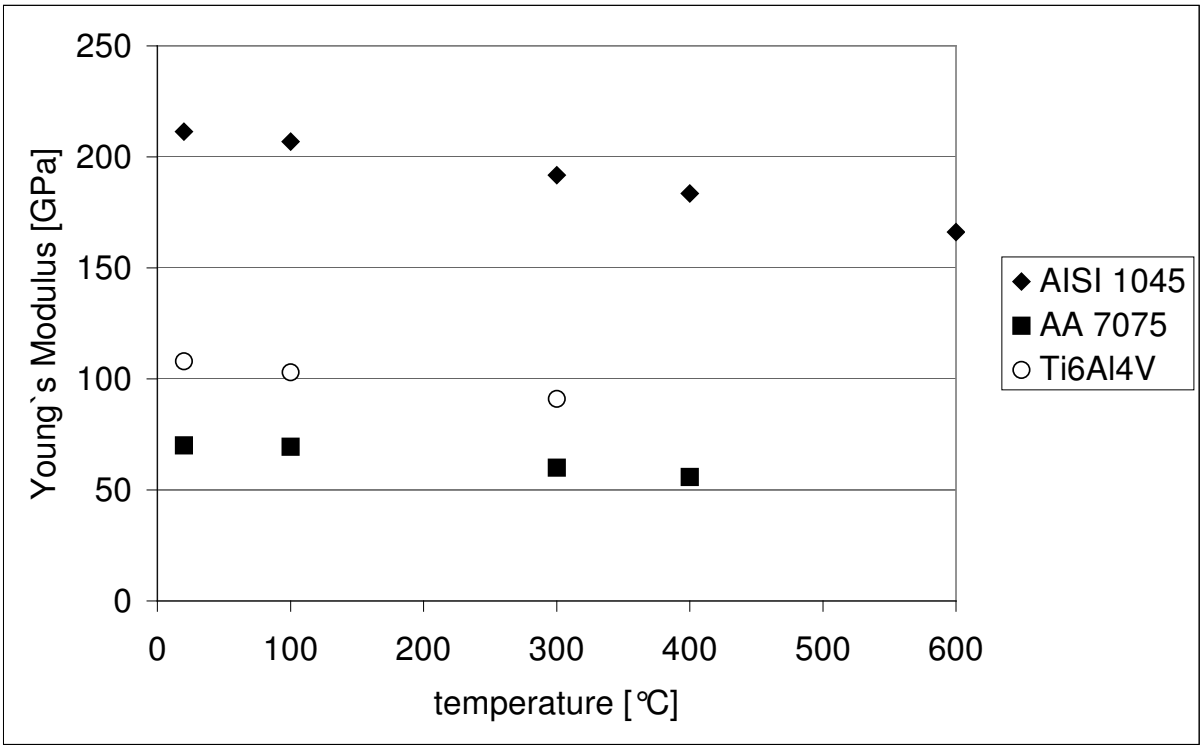


Figure 3.1: Dependency of the Young's modulus on the temperature for AISI 1045, AA 7075 and Ti6Al4V /RICH91, RICH88/

Therefore, if the values for the Young's modulus in figure 3.1 are put into the simulation, an extrapolation to negative values will be done by the program and it will shut down. To prevent this two approaches are possible. First, the temperature of the workpiece is limited to a value for which the Young's modulus is still positive. This approach is suitable for the simulation of the aluminum alloy as the melting temperature is about $T_{melt} = 600$ °C. If the maximum simulation temperature is not limited by the melting temperature, an elastic-plastic description of a liquid material would be the result, which cannot be accepted. The same approach is valid for steel as the linear extrapolation leads to a negative value for the Young's modulus if a temperature higher than $T = 2732{,}3$ °C and therefore far above the melting temperature of $T_{melt} = 1540$ °C occurs. However, for titanium this method is not suitable as the melting temperature and the temperature where the Young's modulus

will change the sign are in the same range. The second approach is to prevent the simulation from uncontrolled extrapolation. In this case it is assumed that higher temperatures do not lead to a further decrease of the modulus. This method is applied in this work for all materials and has the advantage that the user knows the direction in which he modifies the simulation results. As the behavior of the Young's modulus at high temperatures is unknown the assumption of a constant modulus at high temperatures leads to a constant value for the stiffness matrix and thus an estimation to higher values than they may occur in reality. The resultant stresses will be overestimated. If the simulation results are used for the calculation of the tool stresses, the changes in the design will always be put on the safe side. The influence of the Young's modulus will be examined later in the sensitivity analysis by applying experimental design (DOE).

For the applied cutting materials the Young's modulus also decreases if the temperature is increased. However, experimental values for the applied materials are not available and therefore the modulus is kept constant on the value at room temperature given in tables 3.1 to 3.3. This assumption is legal as comparable ceramics and cemented carbides do not show a significant decrease in the temperature area as they occur in cutting. So found Sarrafi-Nour et al. the Young's modulus of a SiC-whisker reinforced (33% SiC, 67% Al_2O_3) to be constant up to temperatures of T = 1000 °C /SARR01/ and Milman et al. measured only a low decrease of the Young's modulus of a WC-Co (Co content from 6 to 15%) cemented carbide up to temperatures of T = 600 °C /MILM02/.

3.2 Poisson ratio ν

Putting tensile loads on a bar it shows an axial elongation ε and a reduction of the radius ε_q, which can be calculated by the Poisson ratio ν [-], equation 3.4. It can also be obtained if Young's modulus E and shear modulus G are known, equation 3.5. As Young's modulus depends on the temperature, it is obvious that the Poisson ratio and the shear modulus also do, **figure 3.2**. Therefore, the same problem of extrapolation is found for the Poisson ratio as it was described for the Young's modulus and the same approach of a user extrapolation on a constant value is

suggested. However, as far as the Poisson ratio is not lower or equal minus one the stiffness matrix will not become negative or zero for any value, equation 3.5.

$$\varepsilon = -\nu\varepsilon_q \qquad \text{(eq. 3.4)}$$

$$G = \frac{E}{2(1+\nu)} \qquad \text{(eq. 3.5)}$$

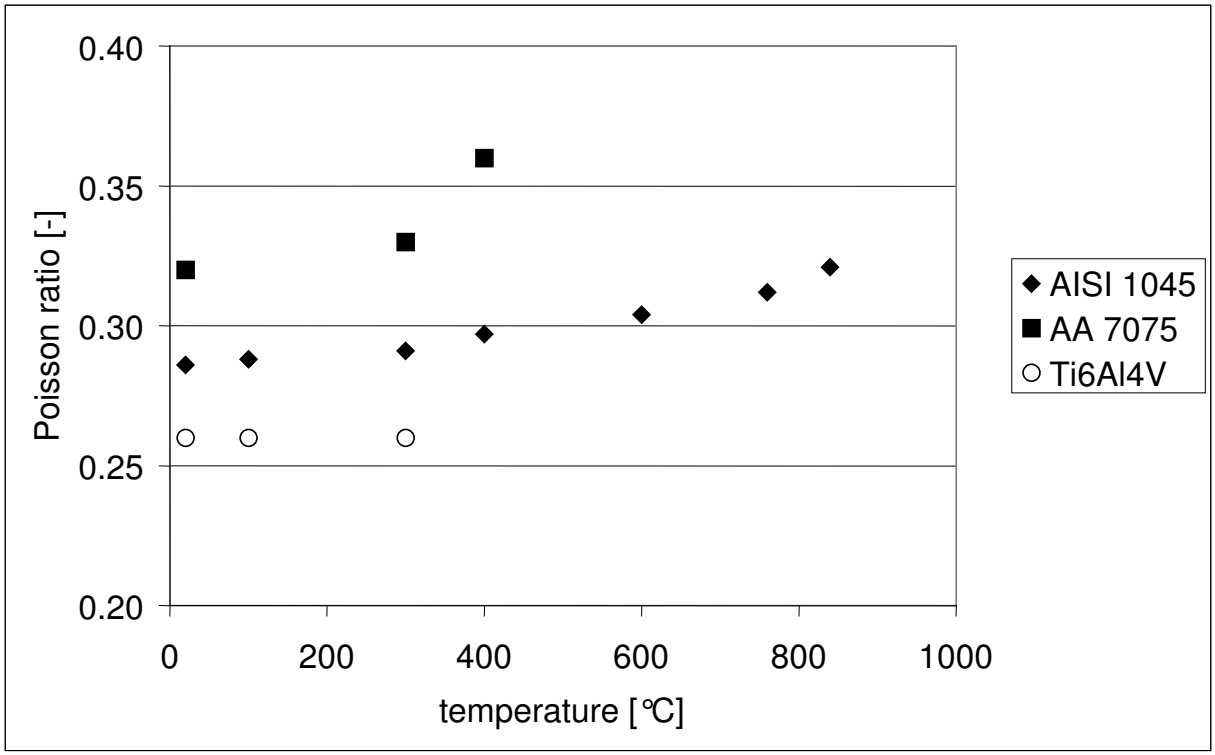


Figure 3.2: Dependency of the Poisson ratio on the temperature for AISI 1045, AA 7075 and Ti6Al4V /RICH91, RICH88/

3.3 Coefficient of linear thermal expansion α_L

The thermal expansion ε_{th} describes the change of the volume caused by the variation $\Delta\vartheta$ of the temperature. If the coefficient of thermal expansion α_L [K^{-1}] and the temperature variation $\Delta T = T - T_0$ are given, the thermal expansion of an elastic material can be calculated using equation 3.6.

$$\varepsilon_{th} = \alpha_L \cdot (T - T_0) \qquad \text{(eq. 3.6)}$$

The coefficient of thermal expansion shows a dependency on the temperature as can be seen in **figure 3.3**. For the cutting materials a constant (average) coefficient of thermal expansion is used. For the ceramic tool $\alpha_{L,CC670} = 6.8\ 10^{-6}\ K^{-1}$ is taken from /SCHN98/ and for the cemented carbide tool $\alpha_{L,H13A} = 6.0\ 10^{-6}\ K^{-1}$ from /SCHE88/, respectively.

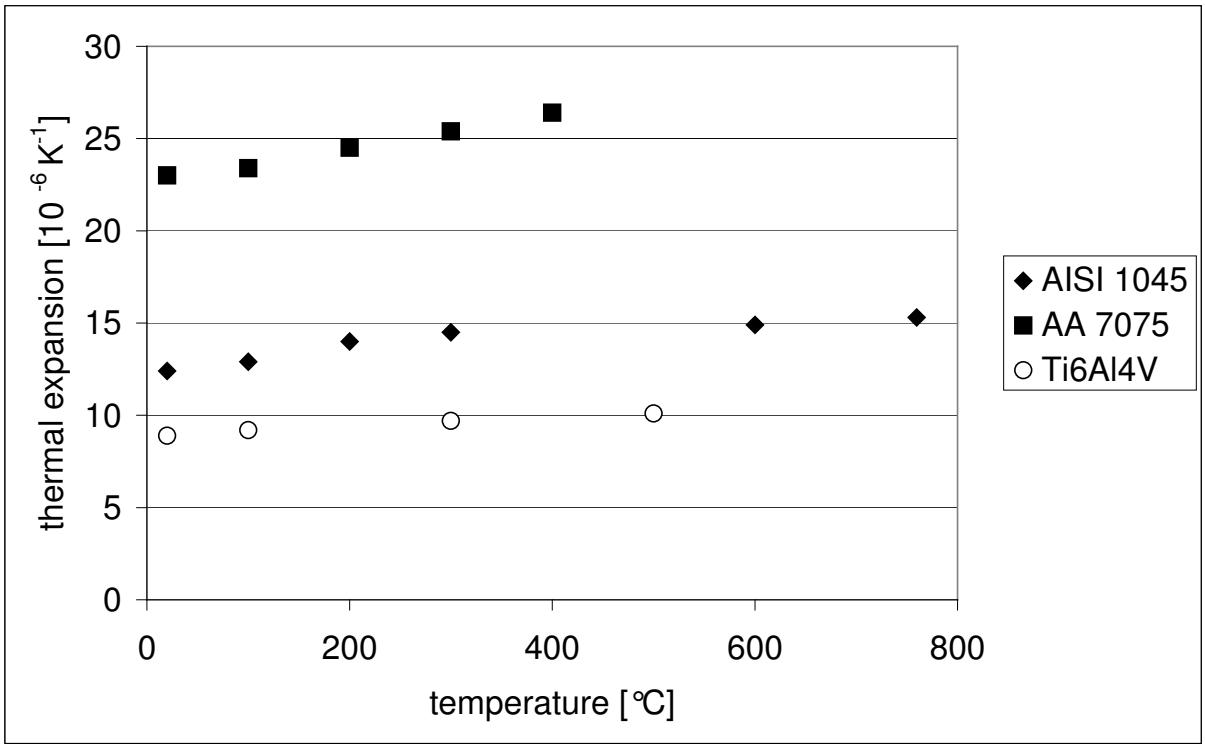


Figure 3.3: Dependency of the coefficient of thermal expansion on the temperature for AISI 1045, AA 7075 and Ti6Al4V /RICH91, RICH88/

The heat flow in a structure can be described by equation 3.7. In this equation $Q_{zu}(t)$ is the supplied heat flow (heat source), Q_L the heat flow in the structure (conduction), Q_K the heat flow via the surface of the structure (convection) and Q_{SP} the time

dependent change of the heat in the structure (capacity). The corresponding matrix is given in equation 3.8. For an element e with the length l, the diameter d and the plane A the vectors and matrix can be written as follows (equation 3.9 - 3.12). In these equations λ is the thermal conductivity, ρ is the density, c is the specific heat capacity, h the coefficient of heat convection.

$$Q_{zu}(t) = Q_L + Q_K + Q_{Sp} \qquad \text{(eq. 3.7)}$$

$$\{Q\ (t)\} = ([L] + [K^0]) + [C]\left\{\frac{\partial T}{\partial t}\right\} \qquad \text{(eq. 3.8)}$$

$$\{Q\ (t)\}^e = \begin{Bmatrix} Q(t)_1 \\ Q(t)_2 \end{Bmatrix} \qquad \text{(eq. 3.9)}$$

$$[L]^e = \frac{\lambda A}{l}\begin{bmatrix} 1 & -1 \\ -1 & 1 \end{bmatrix} \qquad \text{(eq. 3.10)}$$

$$[K^0]^e = hA\begin{bmatrix} 1 & 0 \\ 0 & 1 \end{bmatrix} \qquad \text{(eq. 3.11)}$$

$$[C]^e = \frac{\rho c A l}{6}\begin{bmatrix} 2 & 1 \\ 1 & 2 \end{bmatrix} \qquad \text{(eq. 3.12)}$$

3.4 Coefficient of heat transfer h

The coefficient of heat transfer h [N/Kms] describes the heat exchange of a solid with the surrounding fluid which can be a liquid or gas. It can be calculated by the Nußelt Nu number using equation 3.13 with the coefficient of thermal conductivity λ and a characteristic length l.

$$h = \frac{Nu \cdot \lambda}{l} \qquad \text{(eq. 3.13)}$$

The coefficient of heat transfer is influenced by the geometry of the part, the boundary layer development between surface and fluid, the properties of the fluid and whether it is laminar or turbulent. In cutting operations the relative velocity between surface and fluid is very high and the stream is assumed to be laminar. In this case the heat transfer is low.

3.5 Specific heat capacity c_p

The specific heat capacity c_p [J/kgK] of a material can be determined by measuring the temperature difference of the material and a reference material (e.g. steel) /HEMM89/. The heat capacity strongly depends on the temperature and is influenced by phase transformation of the material. In **figure 3.4** the specific heat capacities for AISI 1045, AA 7075 and Ti6Al4V are given. The workpiece material data is supplied by the Institute for Heat Transfer and Air Conditioning (WÜK) of the RWTH Aachen. The diagrams for AISI 1045 and Ti6Al4V show peaks where the phase transformations (ferrite-perlite to austenite for AISI 1045, $\alpha+\alpha+\beta\rightarrow\alpha+\beta$ (first peak Ti6Al4V) and $\alpha+\beta\rightarrow\beta$ (second peak Ti6Al4V)) take place. The peak in the diagram for AA 7075 results from the melting enthalpy. For AISI 1045 and Ti6Al4V the melting temperature was not reached in the experiments.

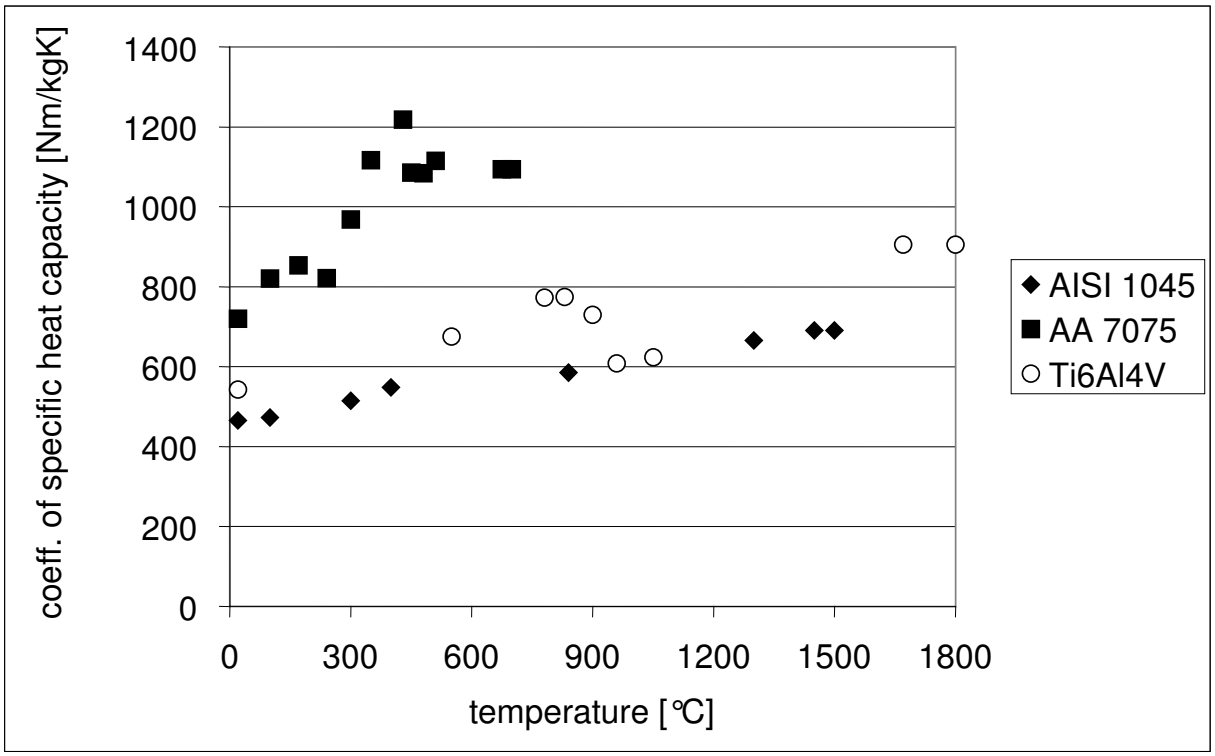


Figure 3.4: Dependency of the specific heat capacity c_p on the temperature for AISI 1045, AA 7075 and Ti6Al4V /MUEL00/

To calculate the thermal conduction by the density, the specific heat capacity and the thermal diffusivity the peaks of the c_p-measurements must not be considered. Moreover, if the exact mechanisms that cause the peaks are unknown (as it will be if alloys and not pure materials are examined), their influence on the specific heat

capacity are not known. Based on the assumptions by Höhne /HÖHN90/ the c_p-curve is "smoothed". The result is given in figure 3.4 which is the data that will be utilized for the simulation. It has to be remarked that the existence of two local minima for AA 7075 (at about T = 240 °C and ϑ = 480 °C) and for Ti6Al4V (at about ϑ = 1000 °C) may have strong influence on the simulation results.

3.6 Density ρ

The density ρ [kg/m^3] of all the examined metals shows a linear decrease if the temperature rises. Therefore, it can be calculated for the three alloys by applying the equations 3.14 - 3.16 /MATW02/. Because of the lack of data the density of the ceramic cutting material is assumed to be constant /SCHN98/ while that of the cemented carbide tool shows a declining flow of the curve /SCHE88/.

$$\rho_{AISI1045} = 7877\frac{kg}{m^3} - 0.35235\frac{kg}{°C \cdot m^3} \cdot \vartheta \qquad \text{(eq. 3.14)}$$

$$\rho_{AA7075} = 2814.5\frac{kg}{m^3} - 0.22429\frac{kg}{°C \cdot m^3} \cdot \vartheta \qquad \text{(eq. 3.15)}$$

$$\rho_{Ti6Al4V} = 4390.1\frac{kg}{m^3} - 0.17177\frac{kg}{°C \cdot m^3} \cdot \vartheta \qquad \text{(eq. 3.16)}$$

3.7 Product of specific heat capacity c_p and density ρ

One important input data for FEM simulations is the product of density ρ and specific heat capacity c_p to one input value (HEATCP in DEFORM). This product is plotted in **figure 3.5** /MUEL00, LEIT02, SCHN98, SCHE88/.

In the FEM code the temperature field in the object is calculated by equation 3.17.

$$\rho c_p \frac{\partial T}{\partial t} - \nabla(\lambda(T)\nabla T) = \dot{q}''' \qquad \text{(eq. 3.17)}$$

In this equation λ(T) is the temperature dependent thermal conductivity. The product of density ρ, specific heat capacity c_p and the temperature change has a strong influence on the heat source dq/dt and thus on the resultant temperature. It is always positive because the increase of the specific heat capacity with the temperature is higher than the decrease of the density.

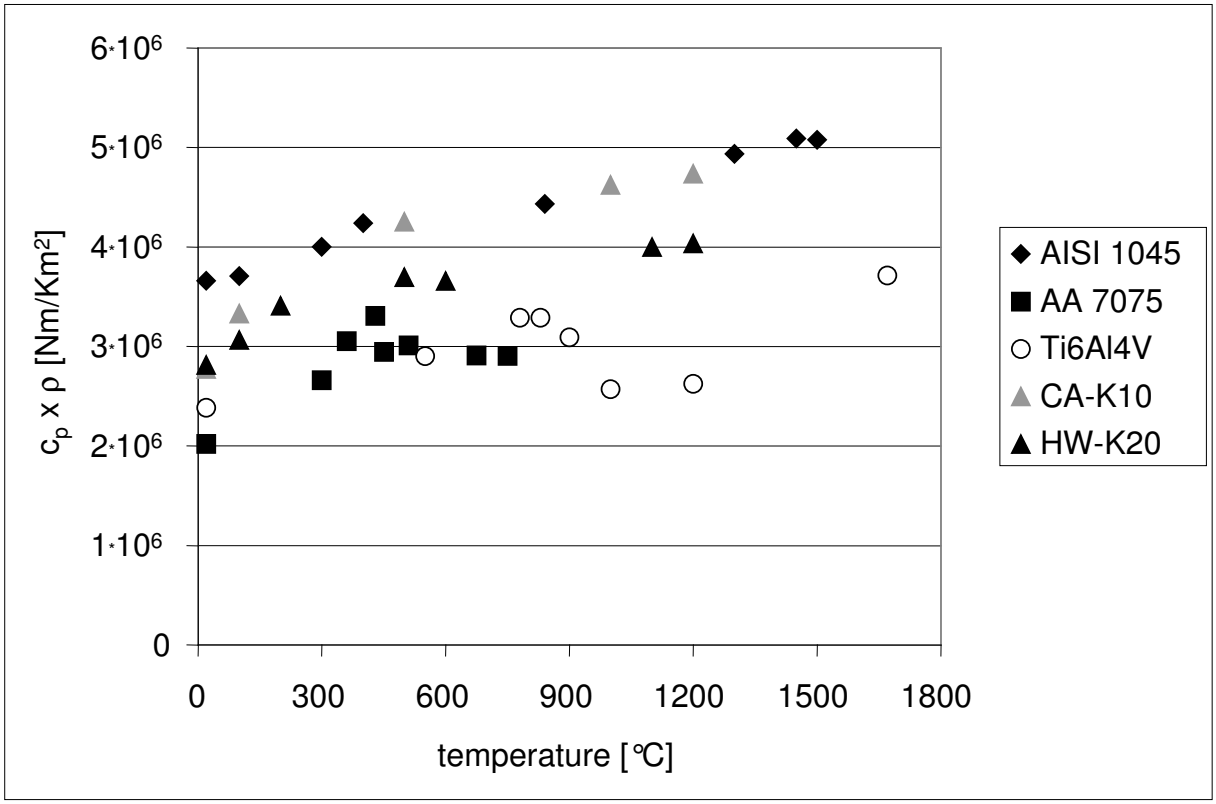


Figure 3.5: Product of specific heat capacity c_p and the density ρ vs. temperature for AISI 1045, AA 7075, Ti6Al4V, CA-K10 and HW-K20

3.8 Thermal diffusivity a and thermal conductivity λ

The thermal diffusivity a [m^2/s] is measured by applying a laser beam on one surface of the specimen. The instationary rise in temperature on the opposite surface is measured by a detector for infrared radiation /MUEL00/. The thermal diffusivity a and the thermal conductivity λ are linked by the product of the materials density and specific heat coefficient, equation 3.18.

$$a = \frac{\lambda}{\rho c} \qquad \text{(eq. 3.18)}$$

Plotting the thermal diffusivity a versus the temperature it can be found that the dependency is very low for the aluminum alloy AA 7075, **figure 3.6**. The steel and the titanium alloy show a stronger and quite different dependency on the temperature. As the heat capacity of Ti6Al4V rises when the temperature is increased, the one of AISI 1045 decreases. In the plots the influence of phase transformation (steel and titanium) and the melting of the aluminum alloy lead to

peaks in the flow of the curve. In contrast to the measurement of the specific heat coefficient the absolute measurement setup of the thermal diffusivity allows to consider these peaks. However, to get a stable convergence of the simulation it may be suitable to smoothen these curves, too. To avoid equation 3.18 from becoming zero, the extrapolation by the FEM code is manipulated by applying a slope of zero at high temperatures.

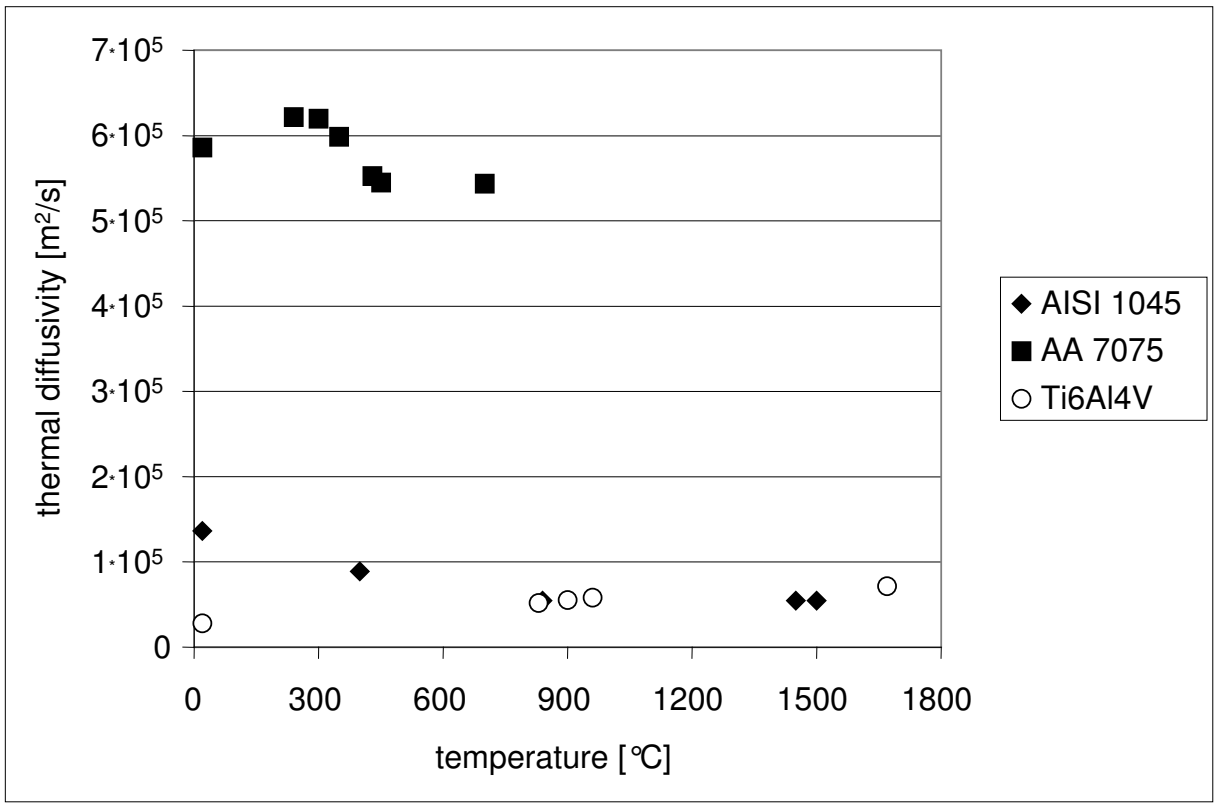


Figure 3.6: Dependency of the thermal diffusivity on the temperature for AISI 1045, AA 7075 and Ti6Al4V /MUEL00/

3.9 Taylor-Quinney coefficient κ

The mechanical deformation of a material may cause a change in temperature. When a specimen is compressed or a chip is formed, nearly all the work of plastic deformation is converted into heat. Only if the deformation takes place slowly ($d\varepsilon/dt < 10^{-2}\ s^{-1}$) the heat generated within the specimen can flow into the surroundings by means of natural cooling, and there will be no change in the temperature of the specimen itself. At higher strain rates there is no time for the heat to escape and the temperature will rise. For example, if the strain is sufficiently high,

a compression test can be assumed to be adiabatic. However, not all mechanical energy put into the process is transformed into heat. A part of it is stored as residual stresses or is lost by noise and vibrations. The fraction of the plastic work rate dW/dt converted to heating dQ/dt was defined by Taylor and Quinney /TAYL34/, equation 3.19.

$$\kappa = dP/dQ \qquad \text{(eq. 3.19)}$$

In forming operations the Taylor-Quinney coefficient κ (beside κ the variable β is common in literature to describe the Taylor-Quinney coefficient) is set to $\kappa = 0.9$. However, the constitutive equations of the material flow stress assume this coefficient to be one /TREP01/. Hamouda /HAMO02/ examined the Split-Hopkinson-Pressure-Bar-Test (SHPB) and found that about 7 percent of the input work is lost in a dynamic compression test. Consequently, the flow stress calculated by this test under the assumption of $\kappa = 1$ leads to values that are 7% too high. Rosakis et al. found the Taylor-Quinney coefficient to depend on the strain and strain rate /ROSA00/. The values he measured for an aluminum and a titanium alloy by applying a dynamic Kolsky-bar test are far below the values assumed by Taylor-Quinney and Hamouda. However, the determination of the Taylor-Quinney coefficient for cutting operations is not possible. As a consequence, this coefficient is considered as an unknown but quite important input value for the cutting simulation. The influence of the Taylor-Quinney coefficient on the simulation result is examined in chapter 7.

3.10 Thermal contact conductance h_{tc}

The thermal contact conductance h_{tc} [W/(m^{2}K)] describes the heat flux of two solids in contact and can be calculated by the quotient of the heat flux q and the temperature difference ΔT at the contacting surfaces A /ROSO03/.

$$h_{tc} = \frac{q}{\Delta T} \qquad \text{(eq. 3.20)}$$

$$q = \frac{d}{dA}\left(\frac{dQ}{dt}\right) \qquad \text{(eq. 3.21)}$$

It is hardly known for any combination of materials because of its strong dependency on the roughness, pressure, hardness and presence of a solid, liquid or gaseous

intermediary. Measurements for forming operations show the following dependency of h /ROSO03/:

- The thermal contact conductance increases with pressure and decreases with the surface roughness of the tool.
- For workpieces with a smooth surface the increase of the thermal contact conductance is more pronounced than for rough surfaces.
- If high pressures occur, a pressure dependent thermal contact conductance is suitable to describe the temperature in the tool and workpiece.
- For a tool steel-steel contact a value of h_{tc} = 600 kW/(m^{2}K) at a temperature of T = 200 °C and a normal pressure of p_n = 279 MPa is calculated. The arithmetical roughness of the workpiece is R_a = 0.27 µm.

The interface heat transfer in cutting operations, which takes place in the tool-chip and tool-workpiece contact, is assumed to be very high. This is reasoned as follows. When the chip or the machined surface are in contact with the tool, two shear zones, the secondary and the tertiary shear zone are created. They result of a velocity gradient from the chip/workpiece velocity to the material which nearly sticks on the tool in the contact zone. Additionally, very high pressures act on the shear zones. An infinite volume particle that can be found in the secondary or tertiary shear zone has suffered the following condition. First of all it passes the primary shear zone. Here it is strongly deformed and heated up. Arriving at the secondary or tertiary shear zone the particle is sheared again with a high velocity. As the particle is already heated up and sheared and the shear rate is high, a strain and strain rate hardened particle at high temperature is sheared again. The toughness of the material leads to the generation of heat. As a result the material behaves viscous and is able to level the roughness of the tool surface. This assumption can be evaluated by the examination of the bottom of a chip (the surface of the secondary shear zone), **figure 3.7**. The chip surface is influenced by the structure of the tool rake face. Moreover the high isostatic pressure and the slow but continuous relative motion prevent any presence of intermediate medium in the contact zone.

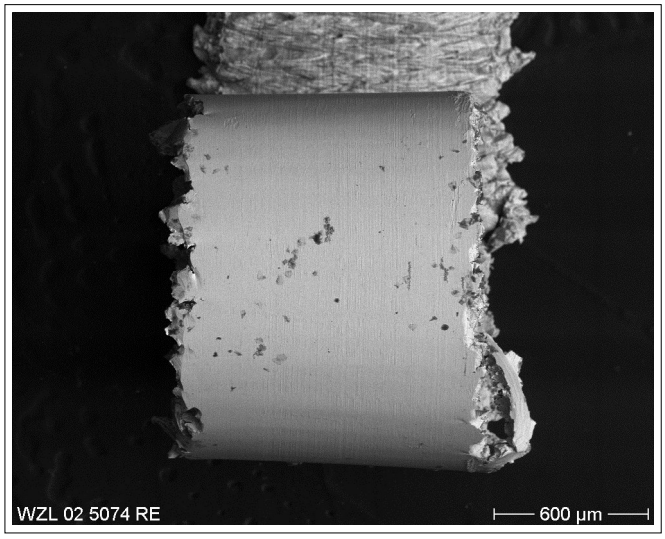


Figure 3.7: SEM picture of the bottom of an AISI 1045 chip at a v_c = 1000 m/min, f = 0.1 mm and a_p = 1 mm

3.11 Friction

In contrast to the heat-transfer coefficient h a huge amount of work has been done to describe the friction between the tool rake face and the bottom of the chip. However, the friction in cutting strongly depends on the occurring stresses and temperatures and was intensively examined in the past /SHAW53, KRON61, OXLE62, SCHI65, ZORE66, KHAR69, KOMA93, BENO96, MOUF98, SCHÄ99, GRZE00, CERE00, BALA00, WEST02, MOLI02, SUTT03/. In this chapter a general information is given about the existing approaches to describe the friction between two solids.

3.11.1 Coulomb friction

The friction law by Coulomb is valid for the elastic contact of two surfaces. It says that the friction (shear) stress τ_f is proportional to the normal stress σ_n, equation 3.22. The proportional factor μ is called the coefficient of friction. This approach overestimates the friction stress for very high normal pressures /KRAG83, RAED02/.

$$\tau_f = \mu \cdot \sigma_n \qquad \text{(eq. 3.22)}$$

3.11.2 Shear friction

The structure of the shear friction law is similar to the Coulomb law, equation 3.23. However, in this approach the friction stress τ_f is proportional to the v. Mises shear flow stress τ_v. The coefficient m is called the shear friction coefficient and σ_v is the effective flow stress. In contrast to the Coulomb law the shear friction law overestimates the friction stress for low normal stresses /PETE97/.

$$\tau_f = m \cdot \tau_v = m \cdot \frac{\sigma_v}{\sqrt{3}} \qquad \text{(eq. 3.23)}$$

3.11.3 Composite friction

The shortcomings of the Coulomb and the shear friction law led to a combination of both. In the range of low normal pressure the Coulomb law is applied while for high normal pressures the shear friction law is used /ÖZEL98, ZHAN94, BAY87, BAY00, CERR00/. The resultant friction law can be taken from equation 3.24 and 3.25.

$$\tau_f(x) = \mu\sigma(x) \quad \text{for } \tau_f < \frac{\sigma_v}{\sqrt{3}} \qquad \text{(eq. 3.24)}$$

$$\tau_f(x) = \frac{\sigma_v}{\sqrt{3}} \quad \text{for } \tau_f \geq \frac{\sigma_v}{\sqrt{3}} \qquad \text{(eq. 3.25)}$$

3.11.4 High speed friction

The Coulomb and shear friction law (equation 3.22 to 3.25) have in common, that the influence of the relative speed of the contact partners is not considered. This assumption is suitable for forming operations as well as under quasi static pin-on-disk tests to measure the friction. However, it is doubtful whether it can be applied in cutting.

Experiments with increased sliding speeds were conducted by Prakash et al. /RAJA99/. The maximum speeds up to v_{slide} = 3600 m/min were realized using a pressure shear plate friction impact test while for speeds up to v_{slide} = 600 m/min a torsional Kolky bar friction experiment was used. To compare the dynamic and static tests **figure 3.8** shows the range of examined normal stresses, sliding distances and sliding speeds of the three standard tests to detect friction.

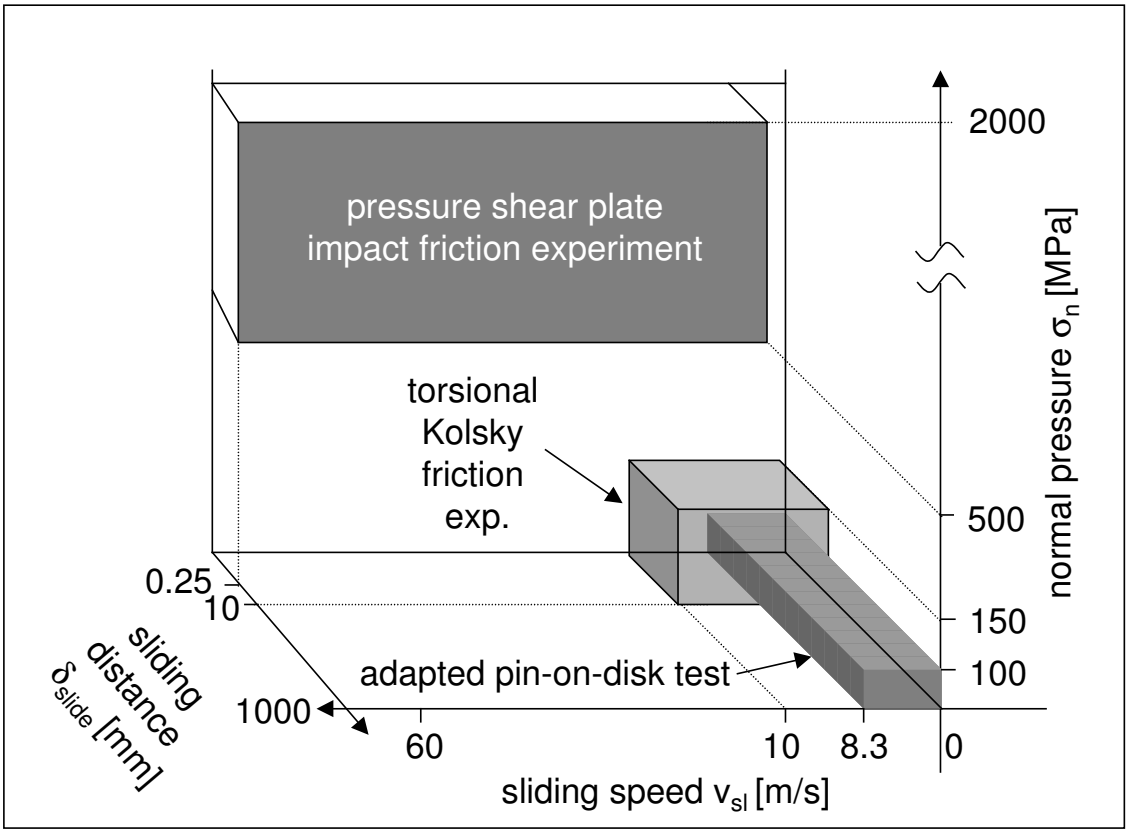


Figure 3.8: Comparison of three setups to measure the friction of two solids /KRIE01, RAJA99/

It can be found that the pressure shear plate friction impact test, where a specimen is shot on an inclined plate, allows the highest normal stresses and the maximum sliding velocity but the lowest sliding distance. The torsional Kolky bar friction experiment, which is similar to a torsional Split-Hopkinson-Pressure-Bar test with a friction couple, shows reduced speeds and pressures but enlarges the sliding distance. The adapted pin-on-disk test at the WZL allows the maximum sliding distance but is limited regarding the sliding speed and normal pressure /KRIE01, RAED02/. Prakash measured the normal and tangential stress and calculated a kinetic friction coefficient μ_k, equation 3.26.

$$\tau_f(t) = \mu_k(t) \cdot \sigma_n(t) \qquad \text{(eq. 3.26)}$$

For the pressure shear plate friction impact test the accelerated specimen was made of Ti6Al4V while the target was a work steel with a hardness of 62 HRC /RAJA99/. The realized values for sliding speed, sliding distance and normal pressure can be taken from figure 3.8. Under these conditions it was found that the high speed or

kinetic friction ($\mu_k = 0.14$) is lower than the static friction coefficient ($\mu = 0.36$) of this friction couple. This is due to the very high normal pressure in combination with a high sliding speed that results in high temperatures at the frictional interface. As the temperature gradient in this area is also very high, adiabatic conditions can be assumed. This leads to a thermal softening of the asperity-asperity junction, a reduced shear strength of the asperity and thus a low coefficient of kinetic friction /RAJA99/.

The conditions of the torsional Kolky bar friction experiment can also be taken from figure 3.8. The specimen was made of AA 7075-T6 aluminum and the contact partner was the same as for the pressure shear plate friction impact test /OKAD01/. The kinetic coefficient of friction calculated from the results of this test reaches a steady state value immediately after the arrival of the torsional wave. Depending on the roughness of the friction couple, the values for the kinetic friction coefficients were found between $\mu_k = 0.1$ and $\mu_k = 0.5$. Prakash pointed out that even large changes in sliding speed did not lead to significant changes of the kinetic friction coefficient /RAJA99/. Conducting pressure shear plate friction impact tests with the aluminum alloy he found that the aluminum alloy melts under these extreme conditions of high sliding speed ($v_{slide} = 6000$ m/min) and normal pressure ($\sigma_n = 1$ - 2 GPa) /OKAD01/. In this experiment the shear strength of the aluminum was $\tau_s = 100$ MPa which is similar to that of aluminum under hydrostatic pressures of approximately 1 - 3 GPa and shear strain rates of about $d\gamma/dt = 10^7\ s^{-1}$.

The friction data used in the current work is taken from the doctor thesis by Westhoff /WEST02/ who examined the same couple of workpiece and tool material. He found in pin on disc tests and cutting simulations that a Coulomb friction coefficient of $\mu = 0.2$ leads to good results for the combination of AISI 1045 and the CA-K10 oxide ceramic. Because of the described high speed friction tests the coefficient of friction is assumed to be constant even at high cutting speeds. Of course several friction approaches dedicated to cutting exist /MOUF98, CHIL00/.But either they are based on critical simplifications, e.g. the existence of the secondary shear zone is neglected by Moufki /MOUF98/. Or they need the determination of different material properties at different cutting speeds /CHIL00/.

4 Summary of material description

In the current work the three workpiece materials AISI 1045, AA 7075 and Ti6Al4V are examined. Their industrial application is very different. The medium carbon steel AISI 1045 can be found in several components of cars while several structures of airplanes are made of the wrought aluminum alloy AA 7075. The titanium alloy Ti6Al4V is often present in airplane turbines. The three materials strongly differ in chemical properties, mechanical properties and in the performance of the cutting process. All material properties needed to set up a FE simulation of the cutting process are described. Additionally, the available data and sources are given and possible error sources concerning the implementation of these properties into the model are described.

One important information is that the melting temperature of titanium is about 100 K higher than the one of steel and nearly 2.5 times higher than the one of aluminum. Further differences can be found in the temperature dependent mechanical properties. At 30 percent of the melting temperature the flow stress for aluminum and steel drops to 50 percent of the flow stress at room temperature. In contrast, for titanium about 60 percent of the melting temperature is needed to halve the flow stress. This warm toughness and a good chemical resistance are the reasons why parts made of Ti6Al4V can be found in thermally and mechanically stressed structures.

All examined materials show a strain rate sensitivity. This means that higher flow stress values are obtained when the strain rate rises. Beside the temperature dependency of the flow stress, the heat treated aluminum and the normalized steel have also similar values for tensile strength at room temperature. Regarding the thermal expansion, specific heat capacity and thermal diffusivity the values of aluminum are much higher compared to those of steel and titanium. These differences will be important for the interpretation of the experimental cutting results.

Concerning the plastic behavior under the extreme conditions of cutting, different approaches to calculate the flow stress curve were presented. These approaches are called constitutive equations if they are derived from structural mechanical principles. They have in common an extrapolation of the flow stress in ranges of strains, strain rates and temperatures that cannot be measured. To verify these extrapolations, the

constitutive equation used in the current work is proved in simulations of shearing operations with high strains and strain rates. However, to fit the constitutive equation to the available experimental results, a high amount of material dependent constants has to be determined by material testing.

To prevent the extrapolation, the cutting process itself can be used to obtain the flow stress curve. For this approach, the flow stress curve has to be calculated from the measured resultant forces. An analytical model, the Oxley theory /OXLE89/, exists that fulfills this demand. However, the advantage of the missing extrapolation is compensated by the simplifications of the analytical model concerning tool and chip geometry.

A solution is to use a finite element model instead of an analytical model. The main advantage is that the number of simplification is low compared to the analytical model. In this approach the flow stress data which is put into the simulation is iteratively modified. The result of the cutting simulation, e.g. the cutting force, is compared to the experiment. The modification of the material dependent parameters is repeated until the difference of simulation and experiment is low. This procedure is known as reverse engineering. But the chip formation is not only determined by the flow stress curve. The values of several thermo-mechanical properties and input parameters, e.g. friction, are also unknown at conditions as they occur in cutting operations. Therefore, an evaluation of the simulation result only by forces is not sufficient. In the next chapter different setups to determine cutting temperatures, resultant forces and chip geometry are presented. The aim is to evaluate the simulation results on more than one value. Only if at least two values, e.g. cutting force and temperature, of simulation and experiment show good agreement, the model is assumed to be accurate.

5 Experimental setups and results

The experimental results of the current work were obtained by using two different setups, **table 5.1**. The first is an external turning test on a high speed lathe. Using this setup the resultant forces and temperatures are measured and the produced chips are collected and examined. The average length of cut for aluminum and steel is l_c = 144 m and for titanium l_c = 62 m.

The second setup is an orthogonal cutting test with a setup that allows to take pictures of the chip formation during the cutting test. This setup delivers in-situ data about the chip formation mechanism as well as the contact length, chip thickness and chip velocity. In both setups conventional as well as high speed cutting conditions are examined.

	external turning			orthogonal cut		
	AISI 1045	AA 7075	Ti6Al4V	AISI 1045	AA 7075	Ti6Al4V
cutting speed v_c [m/min]	50 – 8000	250 – 8000	15 – 1500	100 – 1500	100 – 3000	50 – 1000
feed f [mm]	0.1 – 0.25	0.1 – 0.25	0.1	0.05 – 0.2	0.05 – 0.2	0.05 – 0.3
depth of cut a_p [mm]	1	1 – 2	1	1	1 – 2	1
resultant forces	yes	yes	yes	yes	-	-
cutting temperatures	yes	yes	yes	-	-	-
pyrometry	yes	yes	yes	-	-	-
thermocouple	work-piece	tool	tool	-	-	-
calorimetry	yes	-	-	-	-	-
in-situ photography	-	-	-	yes	yes	yes

Table 5.1: Cutting parameters and measurements of the two different setups

As cutting materials an uncoated cemented carbide tool (HW-K20), a SiC-whisker reinforced oxide ceramic (CA-K10) and a polycrystalline boron nitride tool (CB50) are used, **table 5.2**. The uncoated cemented carbide tool is chosen for turning aluminum because of its good wear resistance. Turning steel and titanium a SiC-whisker reinforced oxide ceramic is applied to realize a sufficient wear resistance at high cutting speeds as well as a high toughness. Latter is important for the experiments where the chip temperature is measured and a quartz fiber has to be clamped into a

hole of the insert. This setup is later described in detail. To increase the cutting velocity in external turning Ti6Al4V a polycrystalline cubic boron nitride with the same geometry as the ceramic tool is applied.

insert material	insert geometry	tool holder	turning operation	clearance angle γ_O [°]	rake angle α_O; land geometry [°]	inclination angle κ_O [°]	nose radius r_ε [mm]	edge roundness ρ_O [µm]	roughness R_z [µm]	roughness R_a [µm]
HW-K20	SPGN 120304	CSBPL 2525M12	ext.	5	6	75	0.4	18	9.93	1.5
CA-K10	SNGN 120408 T01020 CC670	CSRNL 2525M12	ext.	6	-6; 0.1mm x 20	75	0.8	-	1.6	0.2
CB50	SNGN 120408 T01020	CSRNL 2525M12	ext.	6	-6; 0.1mm x 20	75	0.8	-	6.49	0.88
HW-K20	N151.2-540-40-3B H13A	LF151.22-2525-40	ort.	10	0	90	0.4	5	11.8	2.0
CA-K10	150.23 0476 08T0102 0 CC670	LF150.23-3244-0476C	ort.	10	-6; 0.1mm x 20	90	0.8	-	5.6	0.66

Table 5.2: Geometry and surface quality of the examined tools

5.1 External turning operation

The cutting tool is mounted on a three-component piezoelectric force platform by the company Kistler. This setup is state of the art to obtain the resultant forces /DIML00, TOUN00, BLAN68, LANG72/. The experiments were conducted on tool a lathe by the company Index (Index GU 800) with a high speed spindle that allows a maximum of n = 12,000 revolutions per minute. For steel and aluminum the workpiece is designed as a disc with a diameter of d = 250 mm and a width of b = 20 mm. To minimize the radial run-out, the workpiece is clamped on a titanium adapter especially designed for this experiment. This was not necessary for machining the titanium alloy Ti6Al4V. Here, the cutting speeds are about one magnitude lower than for steel and aluminum. Hence, the titanium workpiece was a conventional rod with a

diameter of d = 100 mm. The length was about 400 mm and it was clamped by a conventional chuck and a tailstock.

5.1.1 Resultant forces

Using a dynamometer cutting force, feed force and passive or passive force are measured directly. The forces have their origin in shearing (all shear zones) and friction (secondary and tertiary shear zone) mechanisms that are needed to generate the chip (**Figure 5.1**).

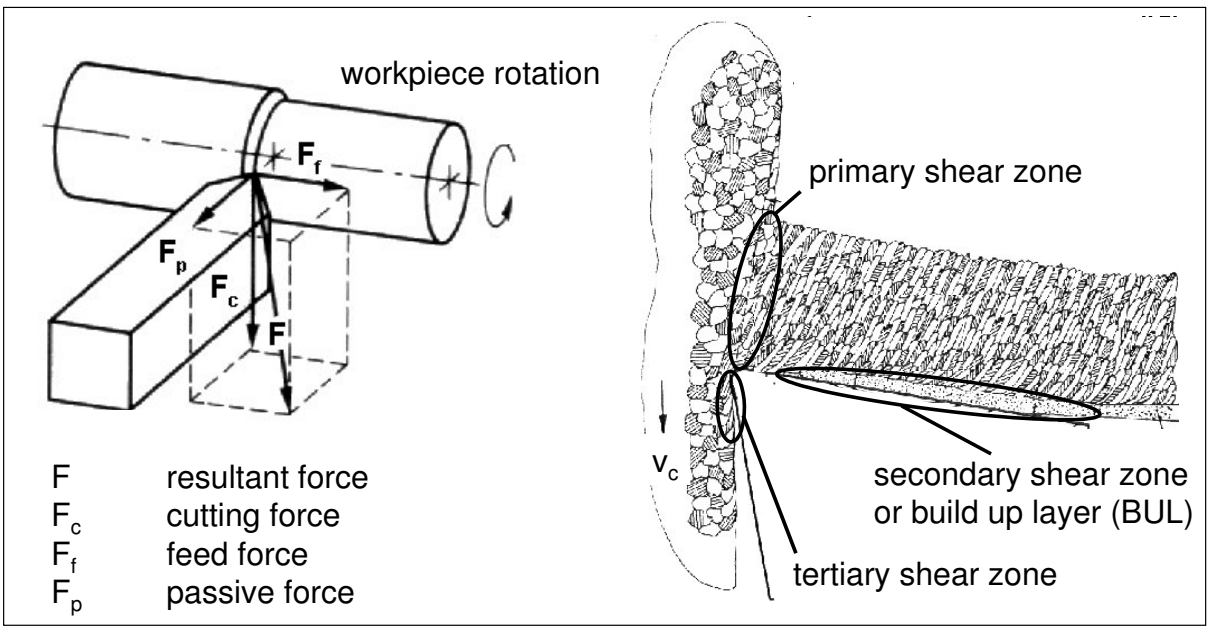


Figure 5.1: Forces and location of shear zones in metal cutting /KOEN97/

The force signals versus the cutting time are plotted in **figure 5.2** at a sampling rate of 5000 Hertz. The origin of the deviation or noise of the measured forces, which remains constant during the measurement, may lie in the unsteady chip formation, influences of the machine tool – workpiece – tool system and an electric or magnetic disturbance by the machine tool motors. At the beginning of the cut ($t < 0.2$ s) the forces strongly increase until the constant value of uncut chip thickness is obtained. Depending on the cutting conditions and the wear behavior of the tool the mean value of the force components does not change ($0.2\ s < t < 1.5\ s$). The increase of the tool wear leads to a steady rise of the forces ($1.5\ s < t < 4\ s$). This is followed by a stronger increase of the force components as the tool wear becomes significant ($t > 4$ s) and values four times of an unworn tool can be measured until the tool

breaks. To compare the forces for different cutting conditions, in the following experiments only the steady state signals are taken into account which are not affected by tool wear (0.2 s < t < 1.5 s in figure 5.2).

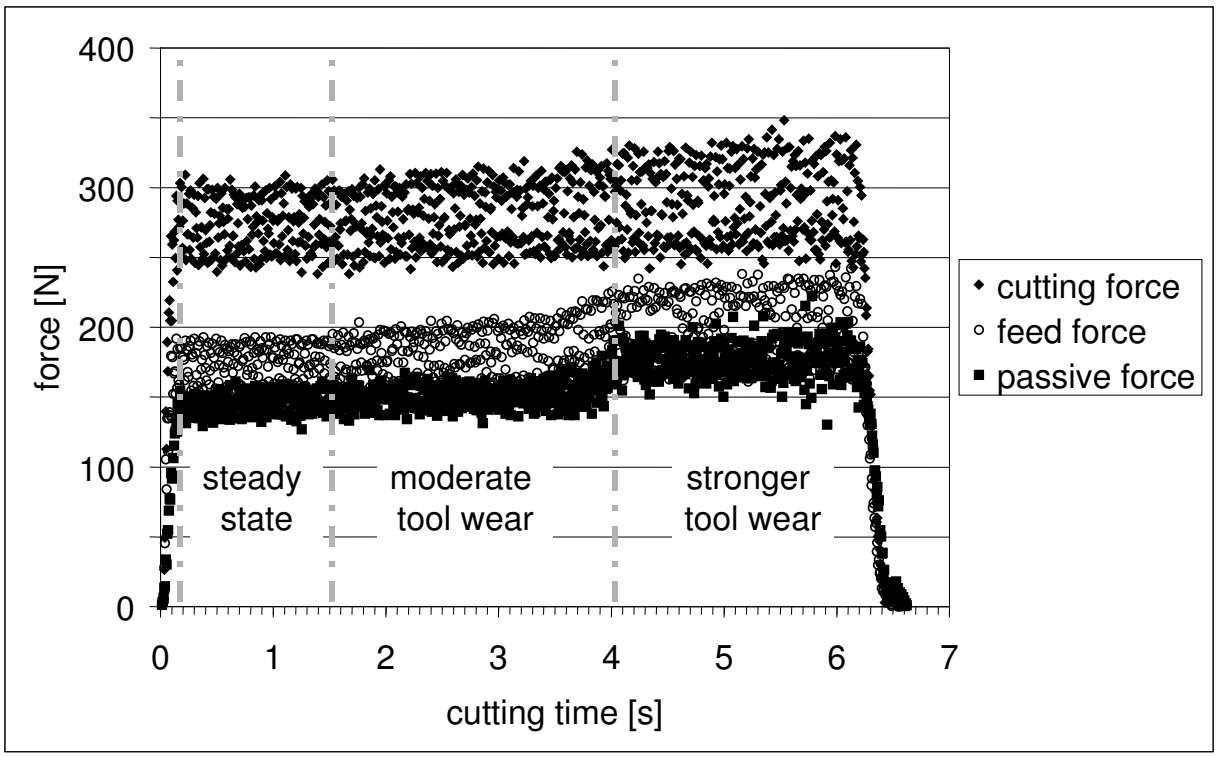


Figure 5.2: Dependency of the force components on the cutting time (AISI 1045, v_c = 3000 m/min, f = 0.1 mm, a_p = 1 mm)

As a result the cutting forces for turning AISI 1045 at different cutting conditions are plotted versus the cutting speed, **figure 5.3** and **5.4**. Increasing the feed from f = 0.1 mm to f = 0.25 mm the cutting forces are about two times higher. This well known dependency was described by Kienzle /KIEN52/, equation 5.1. In this equation F_c' is the cutting force related to the width of cut b = $a_p/\sin\kappa_r$, h = f*$\sin\kappa_r$ the uncut chip thickness, $k_{c1.1}$ the specific cutting force for b = h = 1 mm and (1-mc) a material dependent factor. Latter is the slope of F_c' in the double-logarithmic scale.

$$F_c' = k_{c1.1} \cdot h^{(1-mc)} \qquad \text{(eq. 5.1)}$$

Beside the influence of the uncut chip thickness, the comparison of the external and the orthogonal turning operation (figure 5.4) shows that the missing influence of the minor cutting edge in the orthogonal process also reduces the cutting forces. This can be explained by the reduced uncut chip volume and the lower friction.

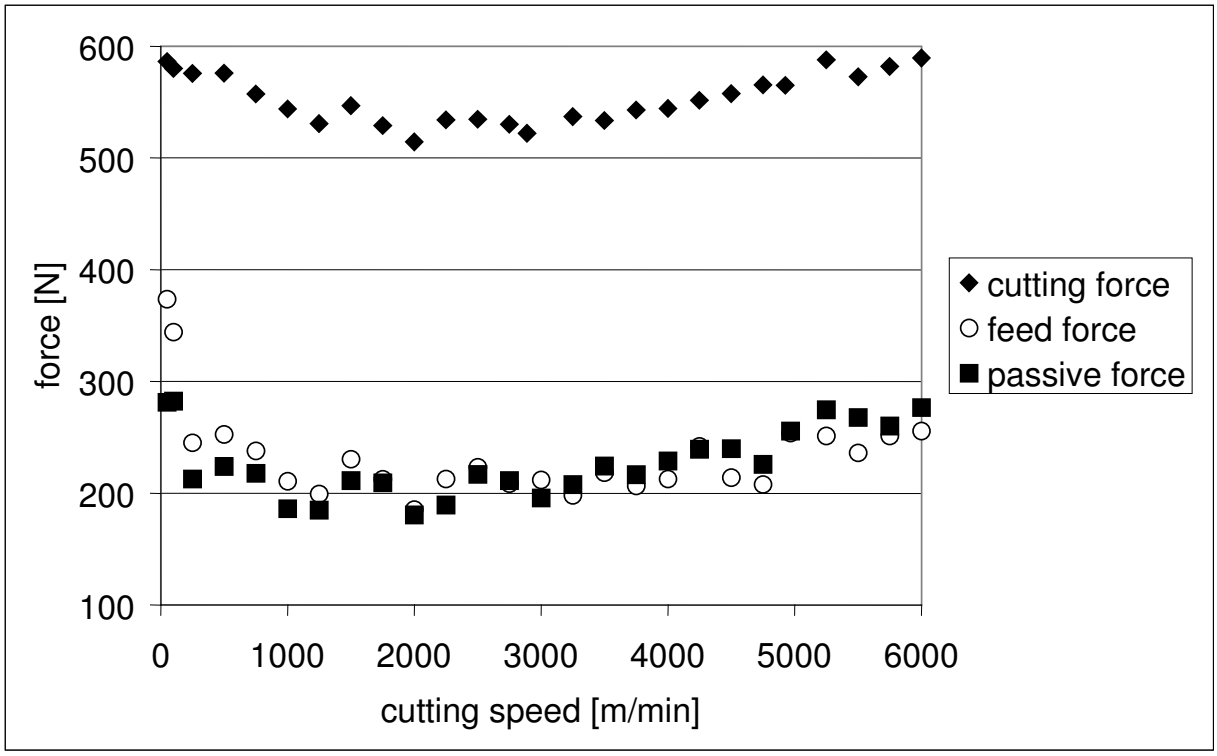


Figure 5.3: Dependency of the force components on the cutting speed (AISI 1045, f = 0.25 mm, a_p = 1 mm)

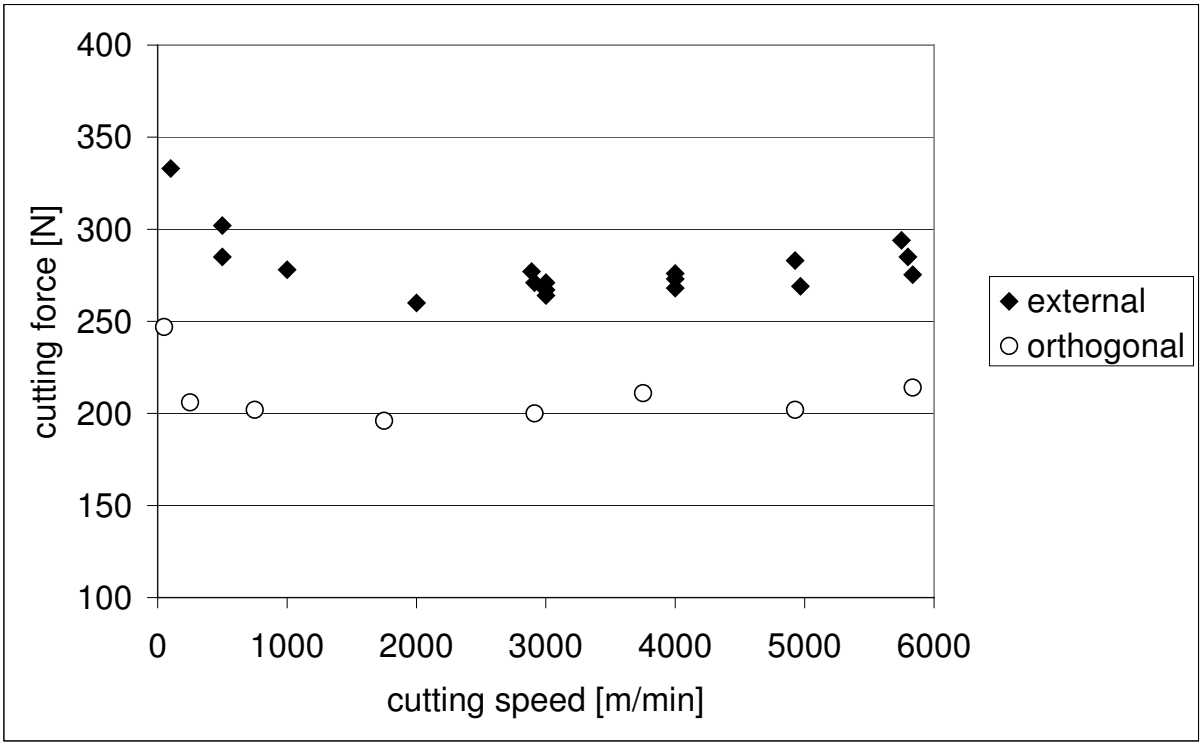


Figure 5.4: Dependency of the cutting force in external and orthogonal turning on the cutting speed (AISI 1045, f = 0.1 mm, a_p = 1 mm)

Increasing the cutting speed reduces the forces until a minimum value is reached. It is located at $v_c = 2000$ m/min for the different cutting conditions. At higher cutting speeds the cutting forces show an increase. For high uncut chip volumes the increase is more significant than for lower ones and all force components show the same tendency. The stronger increase in machining with high feed is due to the higher forces. Therefore, the signal can be separated from the noise of the measurement vales more easily. The described results are also valid for turning the aluminum alloy AA 7075, **figure 5.5** /KLOC02c/. The increase of cutting forces was also observed by Kusnetsov /KUSN60/ for aluminum and by Sutter /SUTT97/ for steel. Sutter further described that the geometry of the cutting edge, especially the rake angle, has a strong influence on the cutting force. Several scientists did not find the increase of resultant forces at high cutting speeds /TÖNS01, SAHM01, PLÖG02, BENA02/. The reason why they did not find the increase in their results as well as the mechanism that causes the increase will be given in chapter 6.

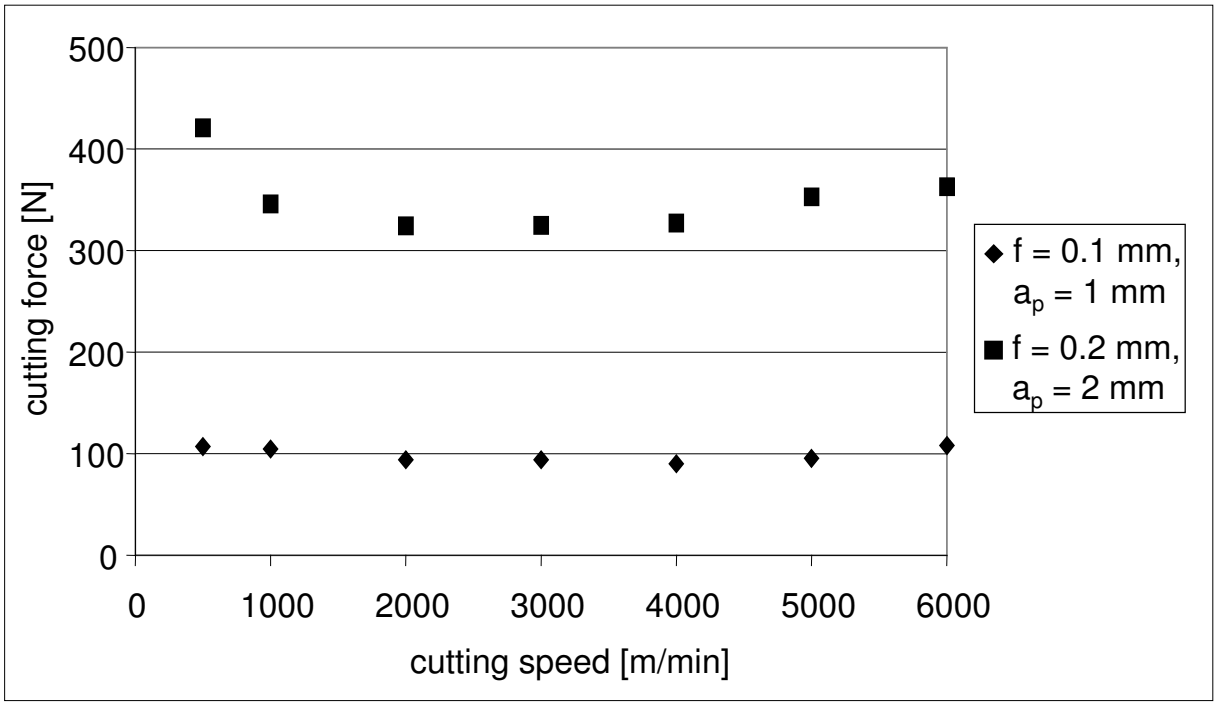


Figure 5.5: Dependency of the cutting force on the cutting conditions (AA 7075)

Turning the titanium alloy Ti6Al4V at moderate cutting speeds the decrease of the cutting forces can also be identified. Compared to the cutting of aluminum and steel the maximum cutting speed for titanium is limited. Using the SiC-reinforced oxide ceramic as cutting tool the maximum cutting speed is $v_c = 600$ m/min. At higher

cutting speeds it is not possible to identify a force value that is unaffected by tool wear. The application of the cubic boron nitride tool allows an increase of cutting speed up to $v_c = 1500$ m/min. At high cutting speeds, this causes a measurable increase of the forces. It can be supposed that titanium shows a similar increase at cutting speeds above $v_c = 2000$ m/min. Molinari has found this in ballistic tests /MOLI01/.

The lack of suitable cutting materials for high speed cutting titanium is the reason why the evidence of this theory cannot be brought by turning tests. The forces that are unaffected from the tool wear are plotted in **figure 5.6**. However, the cutting speeds are still too low to identify a possible increase of the forces at high cutting velocities.

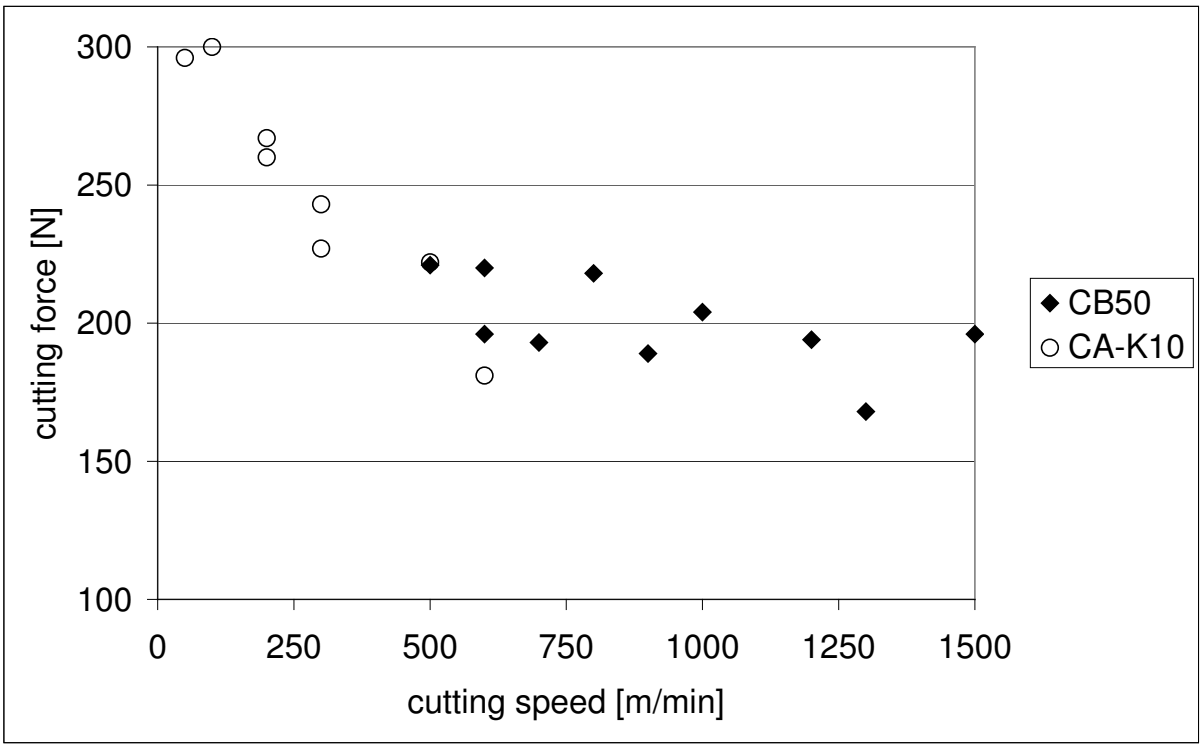


Figure 5.6: Dependency of the cutting force on the cutting speed (Ti6Al4V, $f = 0.1$ mm, $a_p = 1$ mm)

5.1.2 Cutting temperatures

Nearly all the mechanical work which takes place in the process of metal cutting is converted into heat. The basic mechanism is friction. Simply said, the total work carried out is divided into three quantities: (1) the work to shear (continuous chip

formation) or compress and shear (segmented chip formation) in the area of the primary shear zone to form the chip; (2) work to move the chip over the rake surface of the tool and resulting shear in the secondary shear zone; and (3) the work to move and shear the freshly cut surface over the flank face of the tool. The shearing can be regarded as internal friction and the sliding as external friction, respectively /BACC99/. The heat generated in the relevant areas of the chip formation zone has a strong influence on the chip formation process itself. It also influences the resultant forces, tool wear, chip formation and surface integrity and therefore all criteria of machinability /KOEN97/. This is the reason why many approaches to model and measure the occurring temperatures in cutting exist. The experimental setups to determine the cutting temperature can be distinguished by the applied physical principle. **Figure 5.7** contains an overview about measurement principles that have been examined in the past. In the current work temperature measurements using thermocouples and pyrometry were conducted. The other setups were not suitable because of the high efforts on specimen preparation (hardness distribution, thermo-sensitive paint, melting or phase transformation), the dynamic of the process (calorimetry), the poor local resolution (natural thermocouple and application of a wire) and the unknown coefficient of emission (thermography).

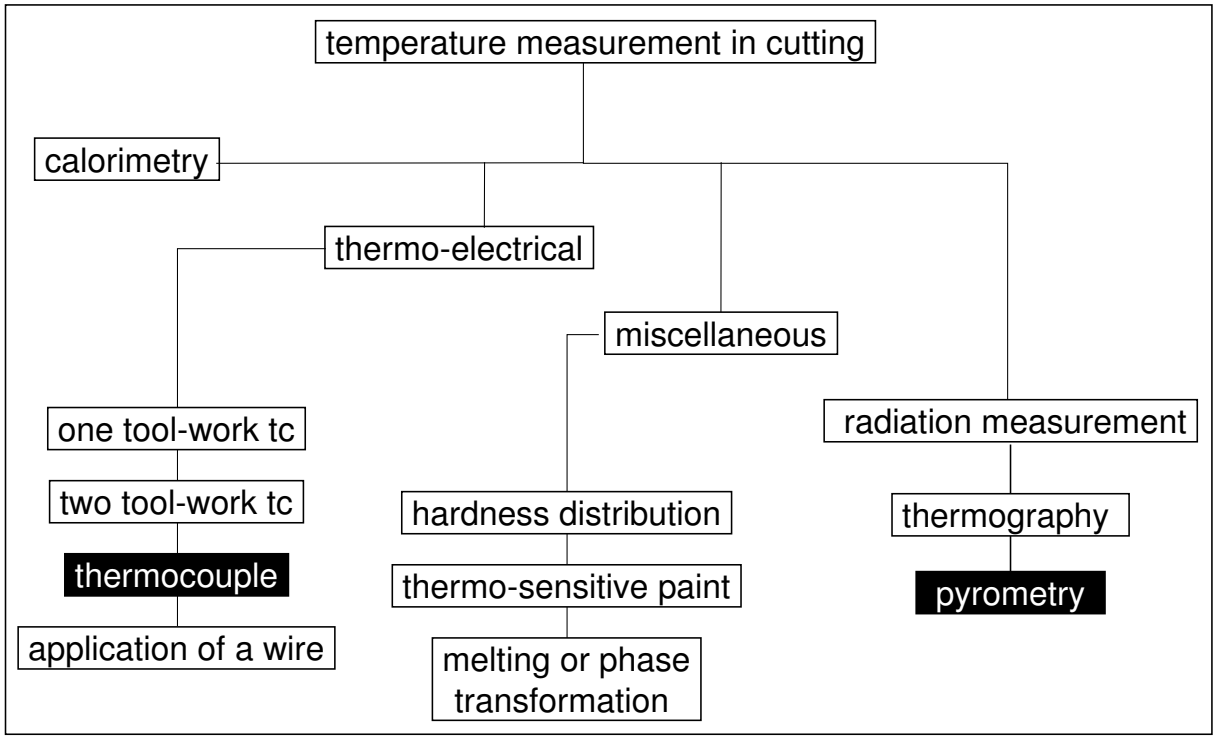


Figure 5.7: Measurement setups realized in cutting operations

Thermocouples

The most extensively applied principle is the thermo-electric effect /WEBE91/. Several ingenious setups to use or generate thermocouples during the cutting process were developed. The principle of the tool-work thermocouple is that the hot junction is formed by the contact zone, while an electrical conjunction to a cold part of the tool and the workpiece forms the cold part /SHAW84, HERB26/. Both, the tool and the workpiece have to be insulated from the machine tool. The major difficulty is the calibration of the tool and workpiece material as a thermocouple /BRAI68, ALVE70/. To overcome this problem a tool-work thermocouple with two tools was developed /SHAW84/. Two tools of identical geometry but different thermo-electrical properties machine one workpiece and the thermo-electric current between the tools is measured. A disadvantage of this setup is that the two tool-chip contact zones have to be identical. In general it is not known where and what temperature the tool-work thermocouple measures /BACC99, CHOI85/. It is assumed that the measured temperature is a mean temperature in the cutting process but not the mean temperature of the contact zone. This would be fulfilled if the temperature distribution in the contact zone is uniform. Moreover, it is obvious that the tool-work thermocouple cannot be applied if ceramic tools with their high electrical resistance are used. A variance to overcome this is to measure the temperature in the flank face of the tool with a wire of material different from that of the workpiece or tool /HIRA89/. This wire is insulated and clamped into the workpiece in a hole of a small diameter. When the workpiece is machined, the wire will also be cut and a thermocouple is formed between the wire and the tool. A similar result is obtained if the wire is inserted in the tool and contacts the chip on the rake face. The errors in this method arise from the uncertainty about the mechanisms in the cutting zone when it is touched by the thermocouple. Moreover, the duration of the contact is very short. **Figure 5.8** shows a sketch of the often applied natural thermocouples.

To avoid the described uncertainties of a natural thermocouple, commercial available thermocouples have been used. If the diameter of the thermocouple is low it is possible to clamp them into the insert or the workpiece. For turning and drilling experiments with a stationary tool the tool sided thermocouple leads to good results. In milling and drilling with rotating tools the thermocouple can be easily applied to the workpiece /KRIE01, EISE00/. A disadvantage of the tool sided measurement is that

the thermocouple is applied in a distance of 0.15 mm or 0.3 mm from the rake face. To evaluate the process by these measurements a stationary temperature field in the tool is needed.

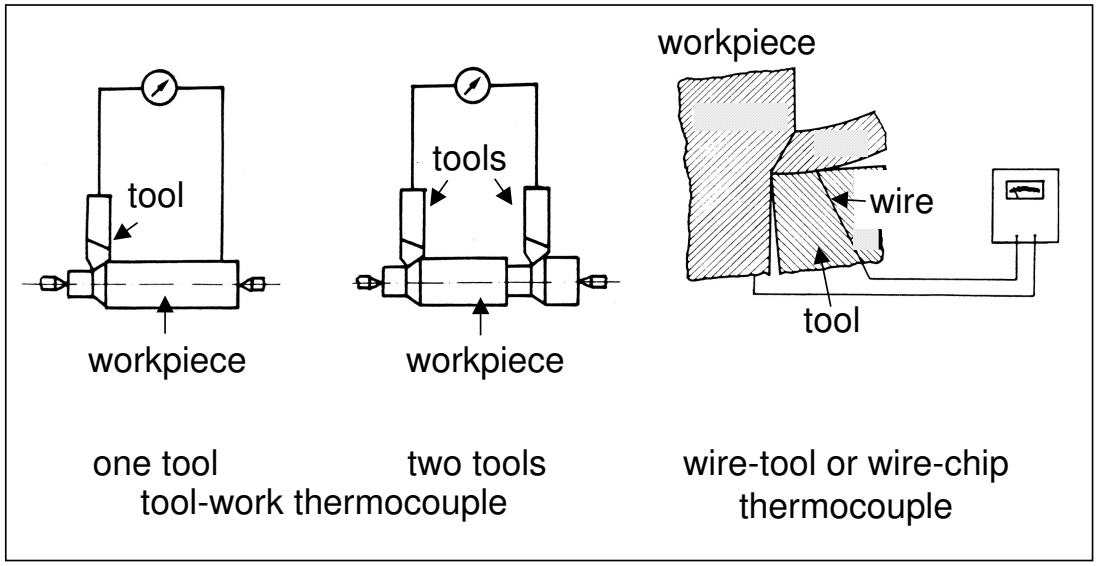


Figure 5.8: Recently applied natural thermocouples to measure the temperature in cutting /HERB26, SHAW84, HIRA89/

This is achieved after 8 to 10 seconds of cutting. In the current work a wide range of cutting speeds is examined. It can be taken from figure 5.2 that a significant tool wear occurs after approximately 4 seconds. Therefore, the measured temperature in high speed cutting will be affected by the tool wear and cannot be easily compared to those of low speeds. This is the reason why this method was not applied in the current work. The described problem can be overcome if the thermocouple is placed in the workpiece. The cutting tool can be regarded as a heat source that steadily removes material and therefore approaches the thermocouple. As a result an increasing temperature is measured until the thermocouple is machined. To transmit the signals of the thermocouple, a four channel telemetry unit is used. It is fixed inside the workpiece and clamped on the spindle, **figure 5.9**.

The advantage is the contactless transfer while the restricted sampling rate of 30 Hertz is a disadvantage. A sketch of the application of the thermocouple in the workpiece is shown in **figure 5.10**. The difficulty in this setup is to apply the thermocouples in an accurate distance from the surface. To ensure a good contact to the workpiece the thermocouple is clamped into a small but deep hole which is hard

to manufacture. Depending on the position of the thermocouple in the workpiece the temperature can be determined.

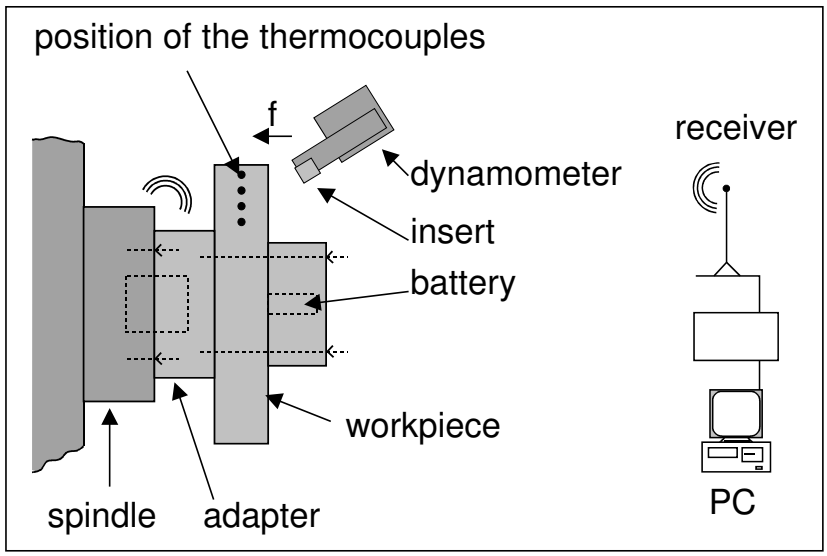


Figure 5.9: Sketch of the setup to measure the workpiece temperature using thermocouples and telemetry

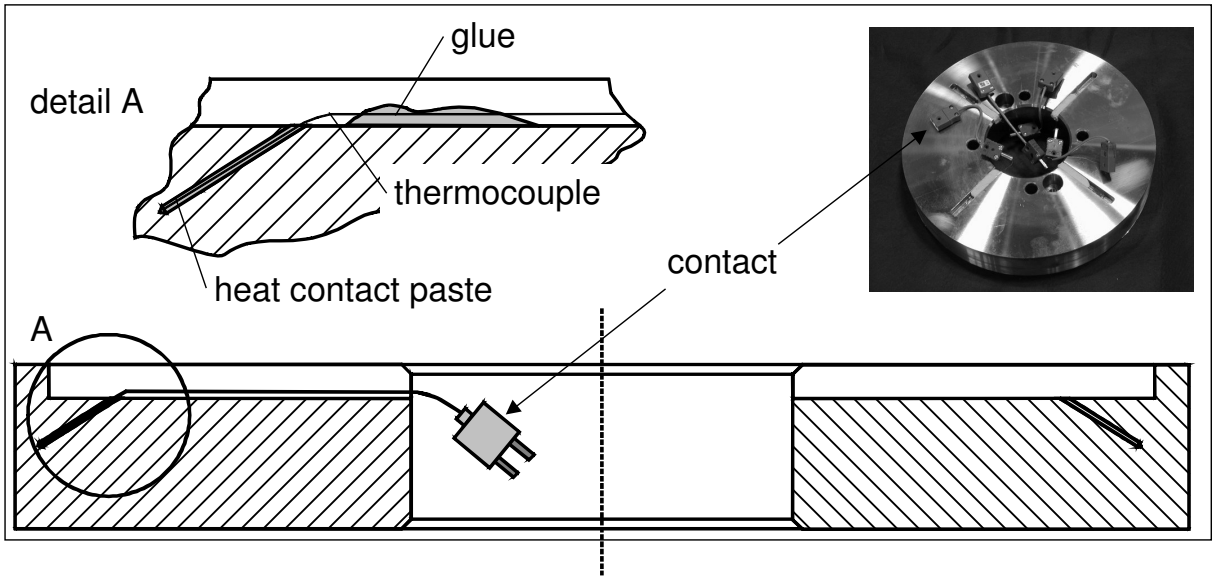


Figure 5.10: Application of the thermocouples in the workpiece

Figure 5.11 shows the obtained temperatures for two thermocouples in a distance of 1 and 2 millimeters from the surface and one near to the surface. At low cutting speed, as expected, the latter shows the highest temperature. At higher cutting speeds the measured temperature increases but the thermocouple near to the surface of the workpiece does not show the maximum temperature. Since it is

obvious that in the area near the surface and therefore near the cutting edge the temperature has to be maximal, an error must have occurred.

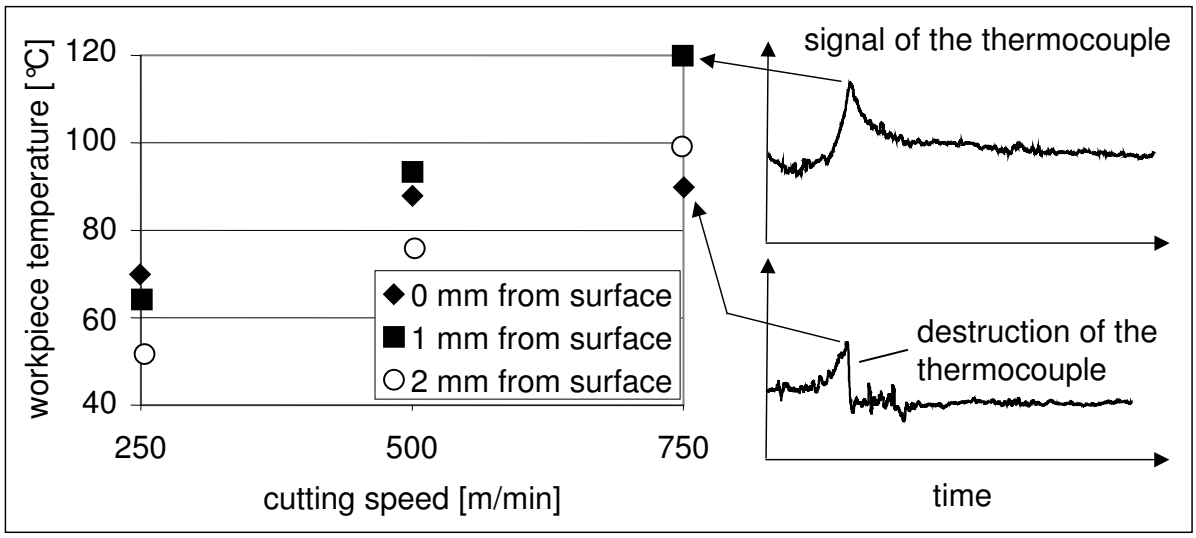


Figure 5.11: Temperatures at different cutting speeds and different distance from the workpiece surface

The origin of this error is found in the properties of the telemetry unit and the setup itself. As can be seen from the signal plots in figure 5.11 the signal breaks down when the thermocouple is destroyed by the cutting edge. Of course the last signal of the thermocouple would be a very high temperature. But at higher cutting speed the sampling rate of the telemetry unit is too low to send the maximum signal to the receiver. For example at a cutting speed of v_c = 500 m/min the sampling rate of 30 Hertz allows to send 10 signals per revolution. The relative position of the thermocouple and the tool tip cannot be determined and thus a temperature different from the maximum temperature is send to the receiver.

Measurement of thermal radiation

The results of the measurements using thermocouples showed that a high time resolution of the measurement setup is desirable. Due to their physical principle, setups measuring the heat radiation fulfil this demand. The heat radiation of the specimen is collected by an optical unit and led to a detector. Depending on the intensity of the radiation a high or low electric signal is produced. Via calibration of the measurement setup a temperature can be assigned to the signal. The contactless measurement allows to obtain the temperatures of areas in chip

formation that cannot be reached by other setups. In orthogonal cutting operations the temperature of the shear zone using thermography or pyrometry was measured /MUEL02, GENT02, SUTT03/. The method is referred to as pyrometry, if the temperature of only one point is measured. If the temperature of an array is measured the setup is called thermography. A further distinction is the type of the infrared detector used.

The main advantage of commercially available thermography devices are the high thermal resolution and the ability to measure low temperatures /MUEL96, BACC99, UEDA98, UEDA99, UEDA01, MUEL02/. On the other hand the time resolution is low and within the wide band width (about 2 µm) the coefficient of emission cannot be assumed to be constant. This coefficient depends on the wavelength, temperature, specimen material, surface quality and the angle between the object surface and the receiving optical device. In general the problem of the unknown coefficient of emission is valid for the pyrometer, too. However, within the lower band width (about 0.05 to 0.2 µm) of a pyrometer the coefficient can be assumed to be constant. If the ratio of the signals of two or more detectors at different wavelength and similar dependency of the emission coefficients is taken two advantages can be found /MUEL01, MUELx1/:

1. The measurement is nearly independent from the value of the emission coefficient.
2. If both signals are equally disturbed (e.g. by dust or dirt) the measured temperature remains unaffected.

A general disadvantage of a pyrometer is that either the intensity of the radiation or the coefficient of emission have to be high. This and the small band width limits the minimal temperature that can be measured. At least for the aluminum alloy the coefficient of emission and the occurring temperatures are low. Therefore, a two-color pyrometer developed for this application by the Institute of Heat Transfer and Air Conditioning (WÜK, Prof. Renz) at the RWTH Aachen was used. All results of this chapter were obtained in cooperation with the WÜK. A short description of the two-color pyrometer is given in this work. Further information such as the detailed experimental setup as well as the evaluation of the obtained data can be taken from literature /MUEL01, MUEL21, MUEL03, WUEK03, MUEL04/. **Figure 5.12** shows the

principle of the two-color pyrometer. The infrared radiation which is emitted from the object surface is collected and transmitted to the pyrometer housing by a quartz fiber. The diameter of the fiber can be varied from 0.2 to 1.0 mm. It is flexible and protected by a polyimide coating. The radiation is focussed by a lens and a dichroic beam splitter leads the radiation to two detectors.

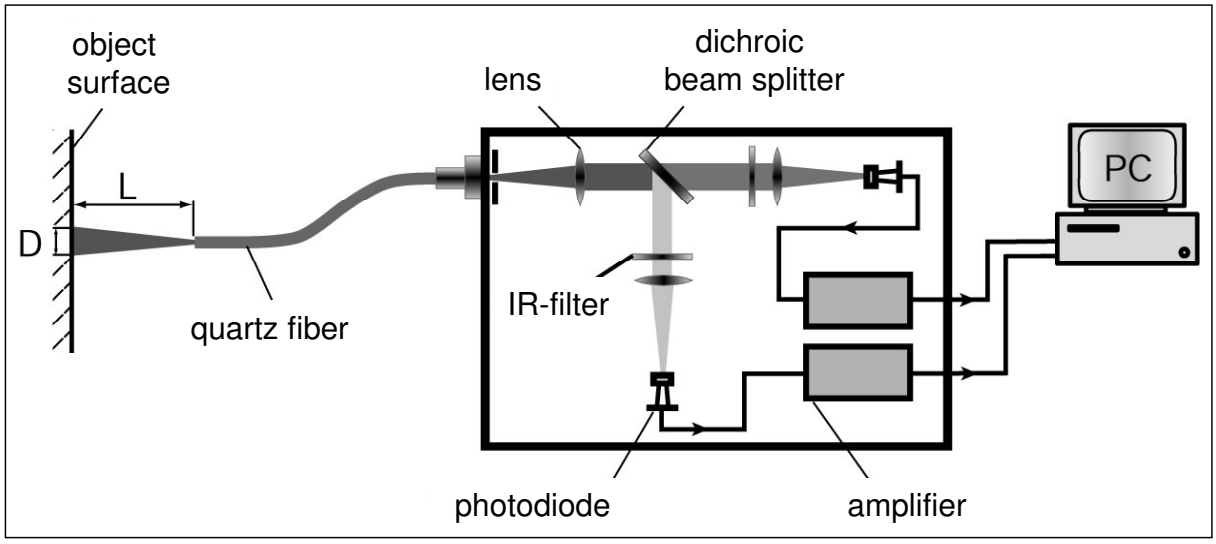


Figure 5.12: Principle of the two-color pyrometer /MUEL01/

The diodes are sensitive at a wavelength of $\lambda = 1.7$ µm and $\lambda = 2.0$ µm, respectively. The signals are amplified and filtered, before they are evaluated. The current pyrometer has a very high time resolution of $t = 2$ µs and allows to measure temperatures down to 250 °C at a coefficient of emission of 0.2 or higher.

The thin and flexible fiber can be clamped to nearly every position in the cutting operation. **Figure 5.13** shows a used cutting insert (left) and the fiber in the insert to obtain the temperature of the bottom of the chip (center) and the surface of the workpiece (right). As the magnification of the three pictures is the same, figure 5.13 also shows two different fiber diameters. At the bottom of the chip higher temperatures can be expected than at the manufactured surface of the workpiece. As a smaller fiber needs more radiation energy than a thicker one the bigger fiber (diameter 0.42 mm) is used to measure the surface temperature while the energy at the bottom of the chip is sufficient and the small fiber (diameter D = 0.26 mm) can be applied. The diameter of the measurement spot (figure 5.12) is determined by the opening angle of the fiber and the distance. The fiber is clamped into a hole in the insert. This hole in the cemented carbide tools for turning aluminum were

manufactured by electronic discharge machining (EDM). As the electronic conductivity of the ceramic tool is very low the EDM process does not work. To manufacture the holes in the ceramic insert a laser drilling process (percussion drilling) was applied. Neither the EDM nor the laser drilling process led to a strong decrease of the tool life. In addition to the measurement at the workpiece surface and the bottom of the chip, the temperature at the top of the chip was measured.

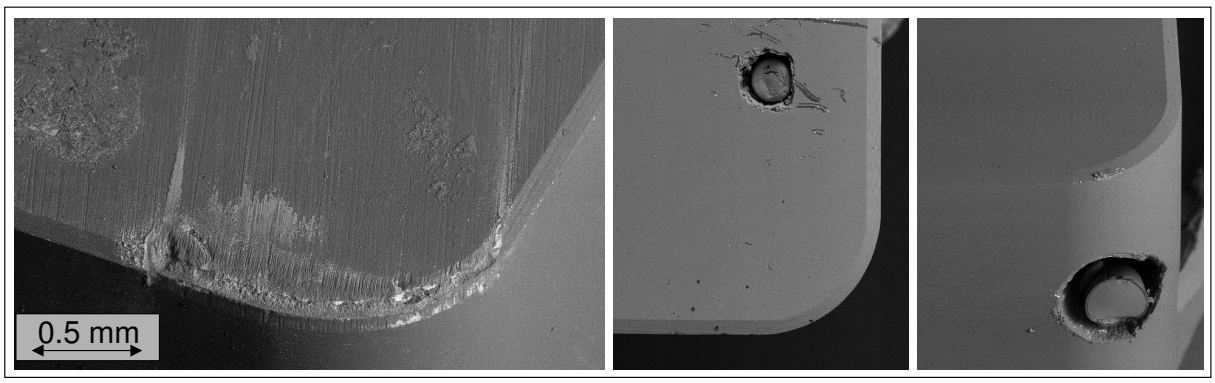


Figure 5.13: Different locations of the measurement spot (tool: CA-K10)

The focus of the experiments was on the bottom of the chip. The reason is that the highest temperatures occur in this area /VIER70/. The dependency of the chip temperature on the cutting speed and the machined material can be seen in **figure 5.14**. As the cutting conditions for steel and titanium were identical, a direct comparison of the results is possible. The aluminum temperatures were obtained with a different tool, tool geometry, feed and depth of cut.

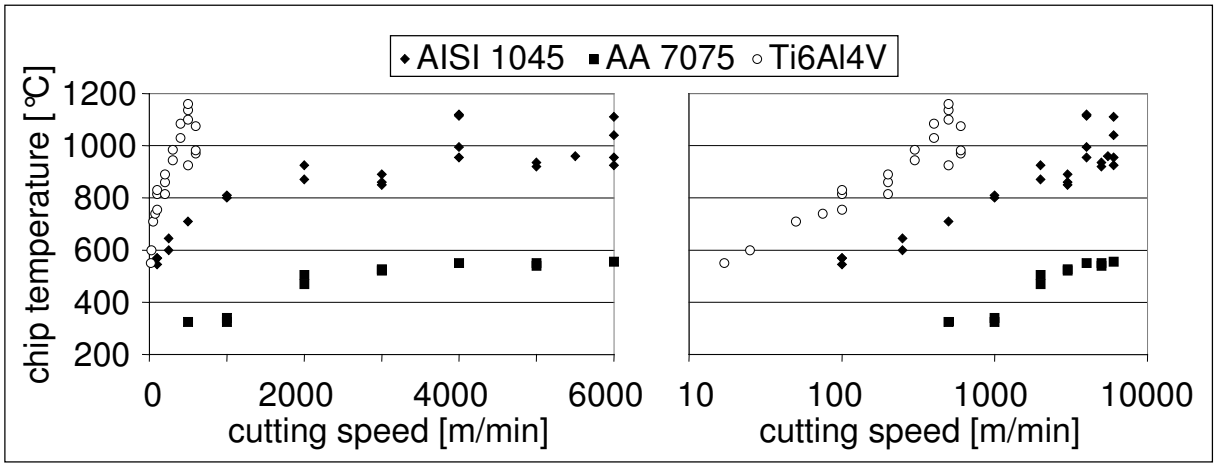


Figure 5.14: Chip temperature versus cutting speed (f = 0.1 mm, a_p = 1 mm for titanium and steel, f = 0.25 mm and a_p = 2 mm for aluminum) /MUELx1/

Therefore, the comparison of aluminum with steel and titanium is of qualitative nature. However, it can be found that the chip temperature of titanium at a cutting speed of v_c = 15 m/min is equal to that of steel at a cutting speed of v_c = 100 m/min. To obtain this temperature in turning aluminum the cutting speed has to be 70 times higher than for steel though in figure 5.14 the feed is 2.5 times higher for turning aluminum. Furthermore, the scatter of the values for titanium and steel at high cutting speed shows that temperature measurements under these extreme conditions are not easy and have to be repeated several times.

Examining the chip temperature in turning aluminum a strong increase can be found up to cutting speeds of v_c = 1000 m/min. A further increase of the velocity leads to a declining rise of the chip temperature. The maximum temperature is limited by the melting point of the aluminum alloy as can be seen in **figure 5.15**. The closer the fiber is located to the contact zone the higher the temperatures are. At very high cutting speeds the temperatures in the contact zone show no further increase and the temperature difference between the bottom of the chip and the contact zone is low. An equal dependency, the strong increase up to a cutting speed of v_c = 1000 m/min followed by a declining flow of the curve, can be found for turning AISI 1045.

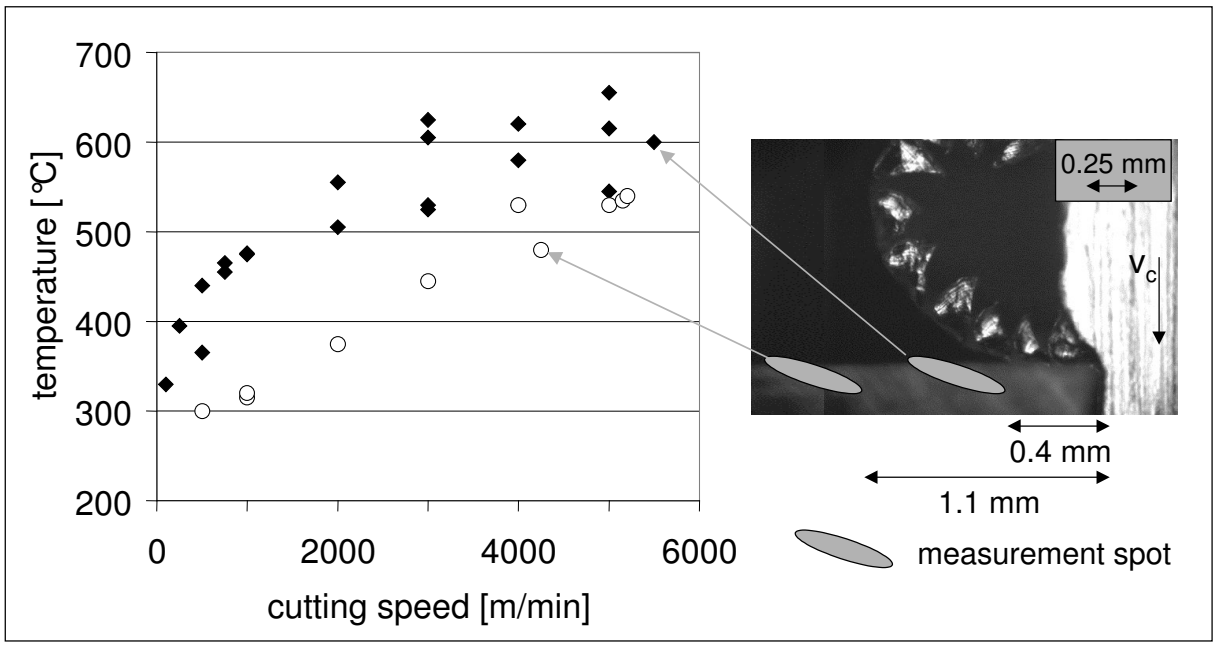


Figure 5.15: Dependency of chip temperature on cutting speed and measurement location (AA 7075, f = 0.25 mm, a_p = 2 mm) /MUEL04, MUE04a/

Because of the extensive tool wear it is not possible to position the fiber in the area of the contact zone. However, the similar dependency of steel and aluminum chip temperatures on the cutting speed lead to the assumption that the maximum temperature in high speed turning steel is the melting temperature, too. As the tool wear in turning titanium is even worse and the cutting speeds are comparable low no conclusion is drawn for a maximum temperature. To understand the mechanism that leads to the strong temperature increase at low cutting speeds the mechanism of chip formation plays a significant role. Therefore, it will be described in a separate chapter.

A further interesting measurement position is the top of the chip. For this measurement the fiber is clamped into a shaft and positioned in the area of the contact zone. Two limitations of the setup have to be mentioned. First, the shaft has to prevent the chip from curling until the measurement has been finished and thus influences the chip flow. Secondly, in contrast to the bottom the surface at the top of the chip is not smooth. Therefore, the obtained results give a mean value of the temperature. The comparison of the temperatures at the bottom and the top of the chip in turning steel can be found in **figure 5.16**. Despite the restrictions mentioned above, the lower temperatures of the top of the chip are obviously caused by the missing influence of the secondary shear zone.

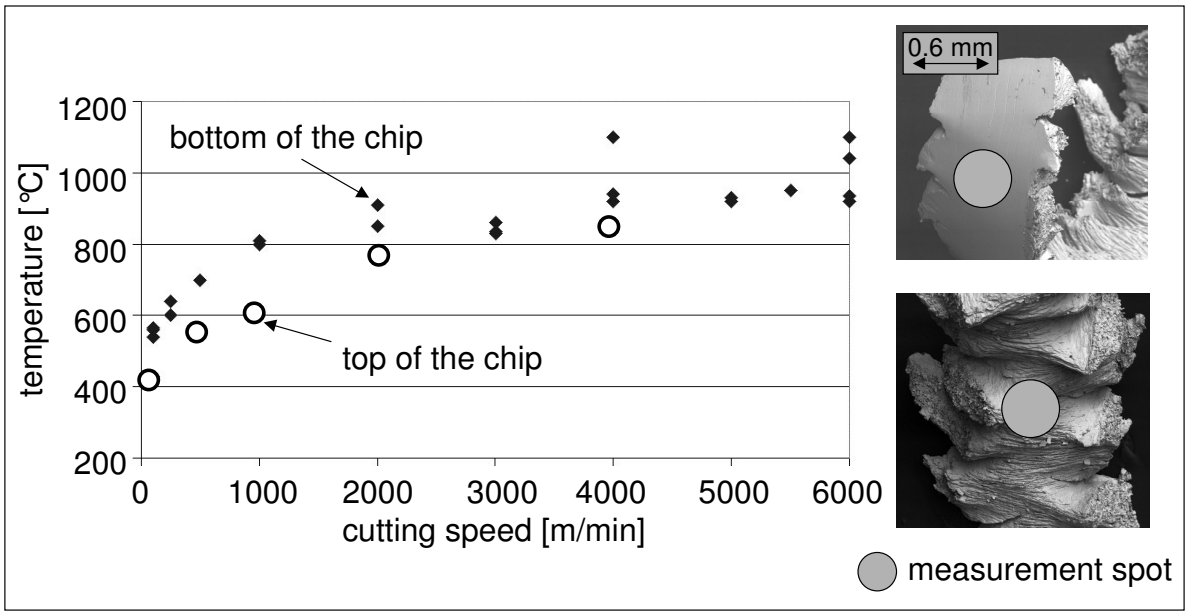


Figure 5.16: Comparison of the temperatures at the top and the bottom of the chip (AISI 1045, f = 0.1 mm, a_p = 1 mm) /MUEL04, MUE04a/

The knowledge of the chip temperature is important to estimate the heat flux and to identify the mechanism of crater wear on the rake face. To describe the temperature influence on the flank wear it is interesting to obtain the workpiece temperature near the cutting edge. Therefore, and because of the insufficient results of the telemetric measurements, the fiber is positioned as follows. To get close to the cutting edge, a hole is drilled into the ceramic insert. It is parallel to the flank face and has an inclination of 20° referring to the direction of cut. The distance from the cutting edge is about 1 mm and the temperature of the tertiary shear zone is measured. The obtained temperatures are proportional to the cutting speed, **figure 5.17**. The second measurement spot is located 4.5 mm below the cutting edge. The fiber is clamped underneath the insert. This setup has the advantage that no preparation of the cutting insert is necessary. Only the tool holder has to be modified. The obtained temperatures are also proportional to the cutting speed but the values and the slope of the resultant curve are significantly lower, figure 5.17. The temperatures are also much lower (30 to 50 percent). In contrast to the chip temperature none of both measurement results show a declining rise at high cutting speeds. However, the common opinion that the workpiece temperature decreases at high cutting speeds is obviously wrong.

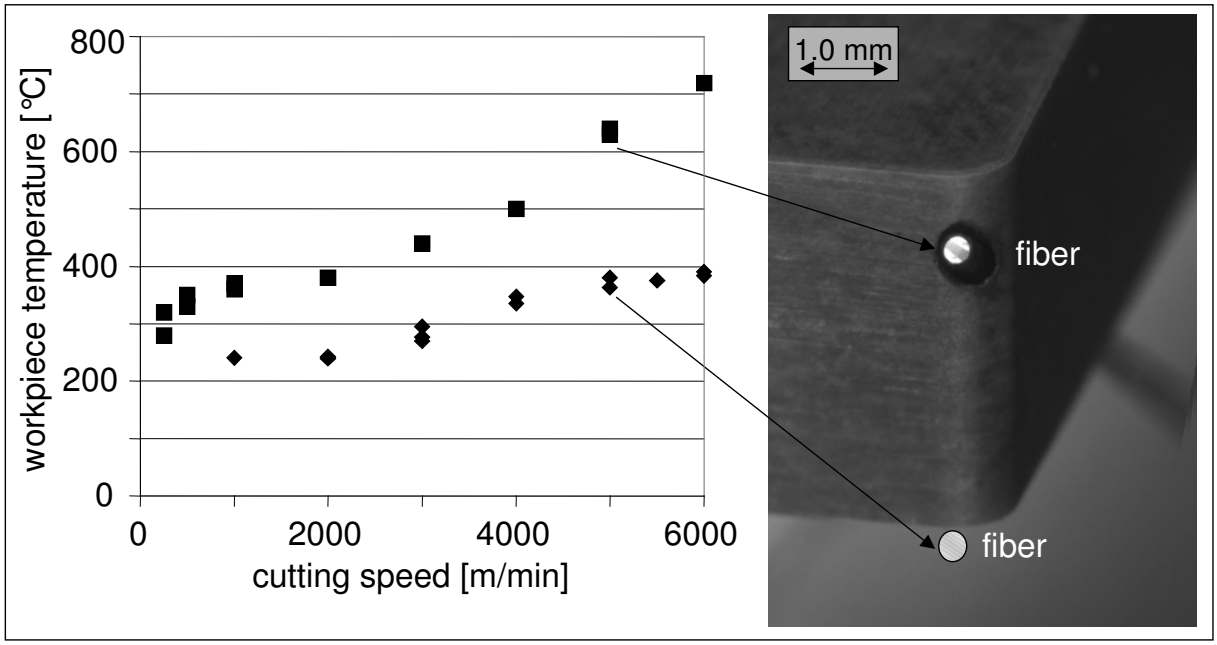


Figure 5.17: Workpiece temperature vs. cutting speed and measurement location (AISI 1045, f = 0.1 mm, a_p = 1 mm) /MUE01a, MUELx1, MUEL04a/

A reason why this was assumed in the past can be the high cooling rates. The rate at a cutting speed of v_c = 6000 m/min is about $8.5*10^6$ K/s, at v_c = 3000 m/min it is still $2*10^6$ K/s. To get the right temperature the measurement setup has to be very fast and must take place near to the cutting edge.

5.2 Chip formation

To describe the mechanism in external turning the produced chips were collected. The form and micro geometry of the chips are evaluated and linked to tool geometry and cutting conditions. Information about the chip form is important to judge the machinability. A short breaking chip is optimal because it does not affect the machined surface and can be easily transported out of the machine tool. The following pictures give an overview over how the chip formation is influenced by feed and cutting speed, **figure 5.18**. No chip breaker was used, so that the geometry of the tools is the same as described in table 5.2. At low feeds and cutting speeds a tangled chip is obtained and the chip formation is bad. High feeds lead to an improved chip breakage. At very high cutting speeds the shape of the chips is similar for both feeds.

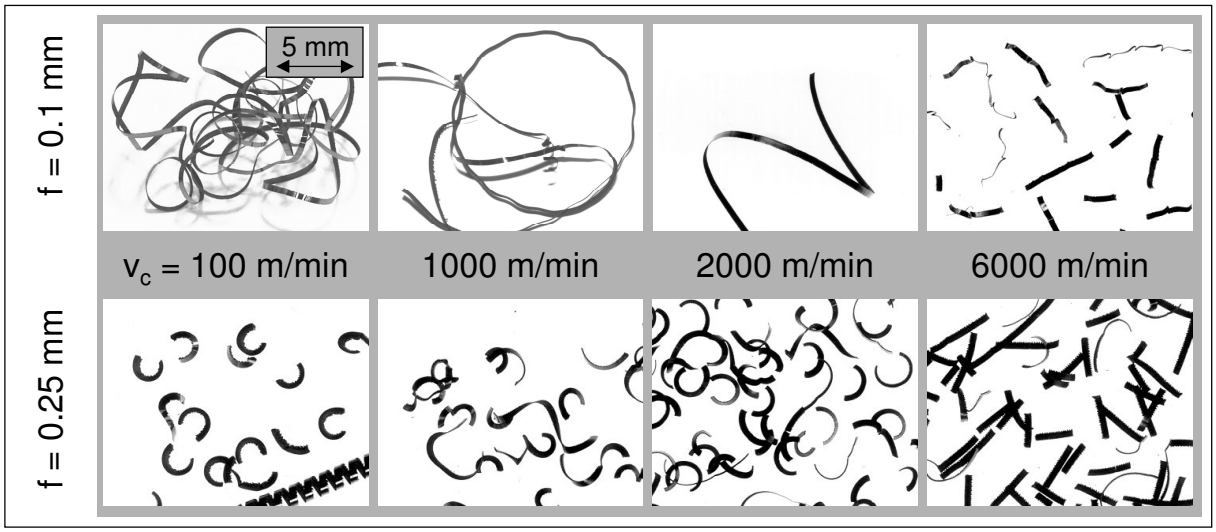


Figure 5.18: Chip form in turning AISI 1045 at variable cutting conditions (a_p = 1 mm)

At low cutting speed the wrought aluminum alloy AA 7075 shows a tangled chip, **figure 5.19**. The depth and width of cut hove no significant influence. This undesirable chip form is obtained for low feeds up to a cutting speed of v_c = 1000 m/min while the roughing conditions lead to a short breaking chip. Latter is

obtained for lower feeds at v_c = 2000 m/min and the chip type remains constant. However, for both cutting conditions the length of the chips is reduced by increasing the cutting speed.

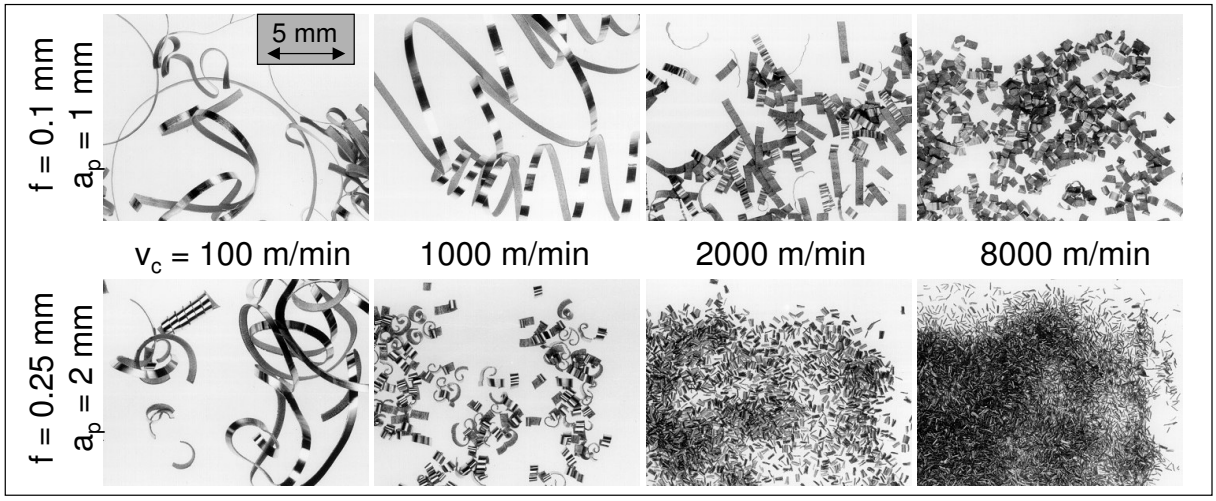


Figure 5.19: Chip form in turning AA 7075 at variable cutting conditions

Because of the high tool wear the maximum cutting speeds in turning Ti6Al4V are one magnitude lower than for steel and aluminum. As a result the cutting speed increments in turning Ti6Al4V are much lower and thus the different chip forms are not as different as for the other two metals, **figure 5.20**. Accordingly it can be found that for low and high feed the chip remains long for cutting speeds up to v_c = 300 m/min. A further increase in cutting speed has no significant influence on the chip formation. However, the chip curling is reduced if the cutting speed is increased.

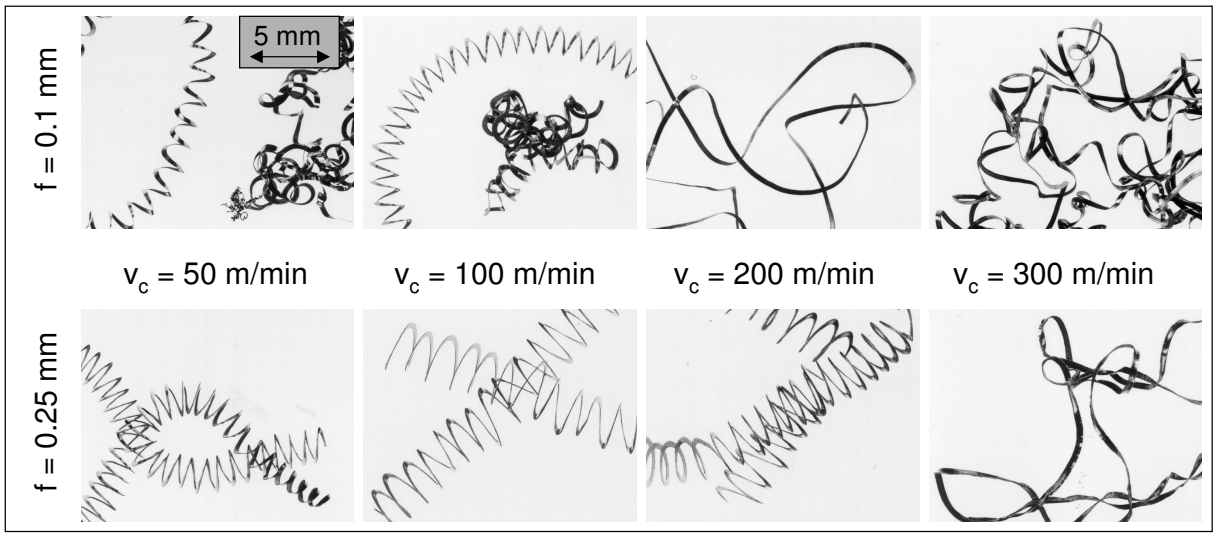


Figure 5.20: Chip form in turning Ti6Al4V at variable cutting conditions (a_p = 1 mm)

This can be found for the lower feed at a cutting speed of v_c = 200 m/min while the chip curling remains constant for the higher feed up to cutting speeds of v_c = 300 m/min. The occurrence of a tangled chip at high cutting speeds is accompanied by burning chips in the machine tool.

It can be summarized that an increase of the cutting speed leads to a better chip breakage for the aluminum alloy. A change of feed and depth of cut leads to lower cutting speed values at which the short chip is obtained. For steel the increase of cutting speed does not lead to a better chip breakage. A positive effect of the high cutting speed is that the tubular helical chip is prevented and therefore the chips can be easily taken out of the machine tool. For titanium a further increase in cutting speed leads to a change from corkscrew to a tangled chip. This is disadvantageous because the tangled chip tends to tie around the workpiece and may damage the machined surface and the tool.

5.3 Micrographs of chips

To obtain information about the chip formation process the analysis of the chip microstructure is a common mean. Therefore, the chips are collected after the machining operation, embedded, ground, polished and etched. The chip geometry, the occurrence of special phases such as martensite and the change of the hardness across the chips can be used to describe the complex mechanism of chip formation /HAFE01/. However, this procedure is very time consuming and the three dimensional structures are reduced to a plane. This is the reason why the chips have been also photographed using the very good depth of field of a scanning electron microscope (SEM) , **figure 5.21**. In these pictures, the influence of the external cut on the chip formation can be identified. The width of the chip can be divided into two areas. The first (A) starts at the surface of the chip that is parallel to the minor cutting edge. It ends where the influence of the corner radius r_ε gets significant. Therefore, this first area is dominant if the depth of cut is much higher than the corner radius. Consequently this area is very small for the experiments of this work where steel and titanium are turned with a corner radius of r_ε = 0.8 mm and a depth of cut of a_p = 1 mm. The second area (B) is produced by the minor cutting edge and the edge radius or, at low feed values and high corner radii, only by the edge radius.

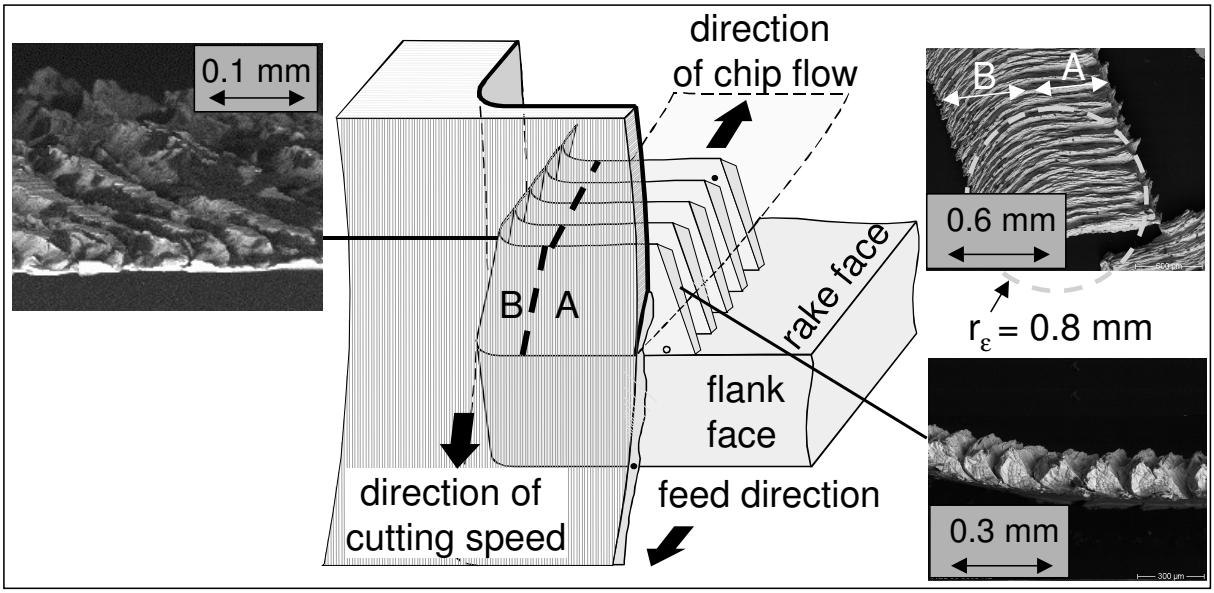


Figure 5.21: Chip formation in external cutting /GER98/

Because of the radius, the chip thickness is not constant along this area and thus decreases until zero. A bending of the second area with the same radius as the cutting edge can be found (figure 5.21). For the examination of micrographs it is obvious that the position of the longitudinal section has a strong influence on the obtained result, **figure 5.22**. In this example, segmented chip formation is found if the section is located in area A (figure 5.22 bottom). In area B the result is similar to a continuous chip (figure 5.22 top).

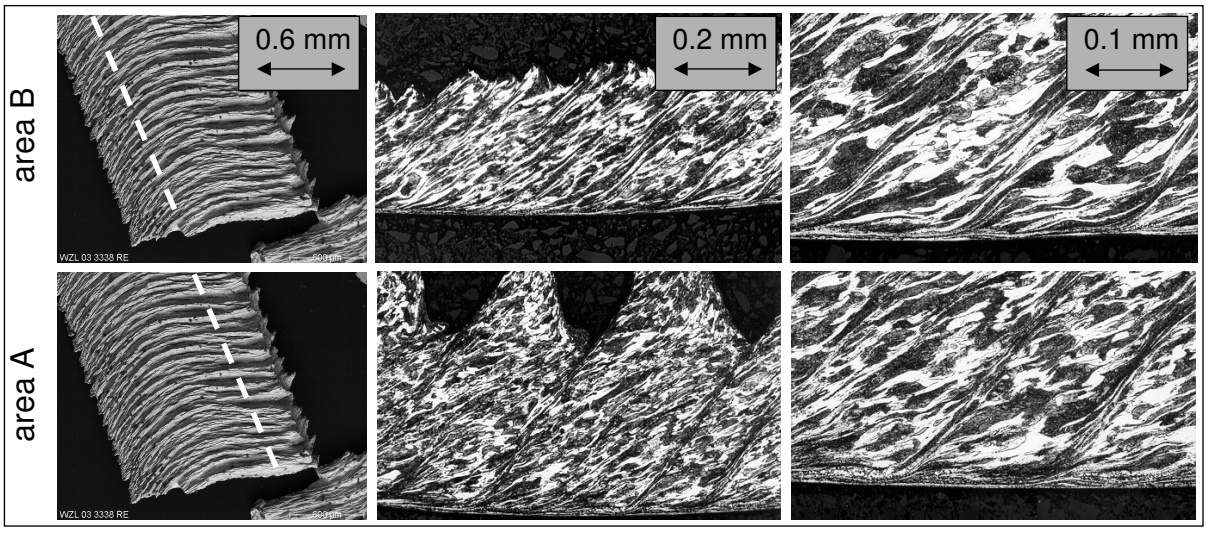


Figure 5.22: Influence of the position of the longitudinal section on the obtained micrograph (AISI 1045, v_c = 1000 m/min, f = 0.25 mm, a_p = 1 mm)

The bottom of the chip, the secondary shear zone, seems not be affected by the choice of the cross section location. The chip is thicker in area B than in area A, **figure 5.23**. Hence, the obtained chip thickness also depends on the location of the longitudinal section in the chip. To estimate the chip thickness, an orthogonal cut is preferred as the missing influence of the minor cutting edge leads to chips that only consist of area A. A straight distribution of continuous and segmented chip formation cannot be found in external turning. But in nearly every cutting operation with an industrial relevance at least one minor cutting edge is in contact with the workpiece. Consequently, the description of a real, three dimensional cutting process by segmented or continuous chip formation is not useful. However, the two chip formation mechanisms are described because of the different material behavior. In continuous chip formation continuous shearing occurs which has its origin in a different stress-strain relationship than the segmented chip formation which is dominated by adiabatic or catastrophic shearing (see chapter 2).

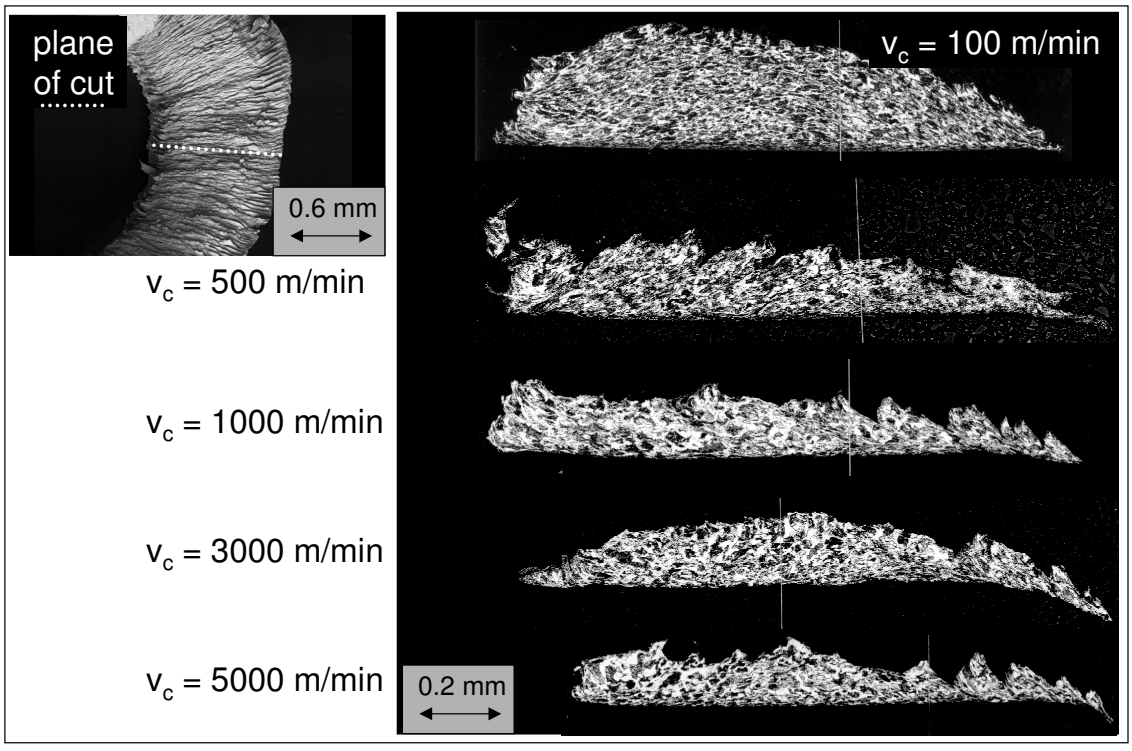


Figure 5.23: Cross section chip width AISI 1045 (f = 0.1 mm, a_p = 1 mm)

In the micrographs the ferrite-perlite structure of the AISI 1045 steel can be found in the chips. The comparison of chip and unmachined material (chapter 2) allows to estimate the deformation in cutting. At low cutting speeds (v_c = 100 m/min) the dominating chip formation mechanism is shearing, **figure 5.24**. In the past this led to

the assumption that chip formation is a result of the existence of a shear plane /MERC45/. For ductile materials such as mild steel and low uncut chip thickness this assumption is valid. The waviness of the top of the chip can be caused by a not constant uncut chip thickness as a result of the previous machining process. Vibrations of the machine tool or the run out of the workpiece may also have an influence. A secondary shear zone is created by the tool-chip contact. It is therefore located at the bottom of the chip. At low cutting speeds nearly every sheared area in the chip is connected to the secondary shear zone. It is obvious that the degree of shearing in the secondary shear zone is much higher than in those areas of the chip that are formed in the primary shear zone. An increase in cutting speed leads to the appearance of lower deformed structures in the chip.

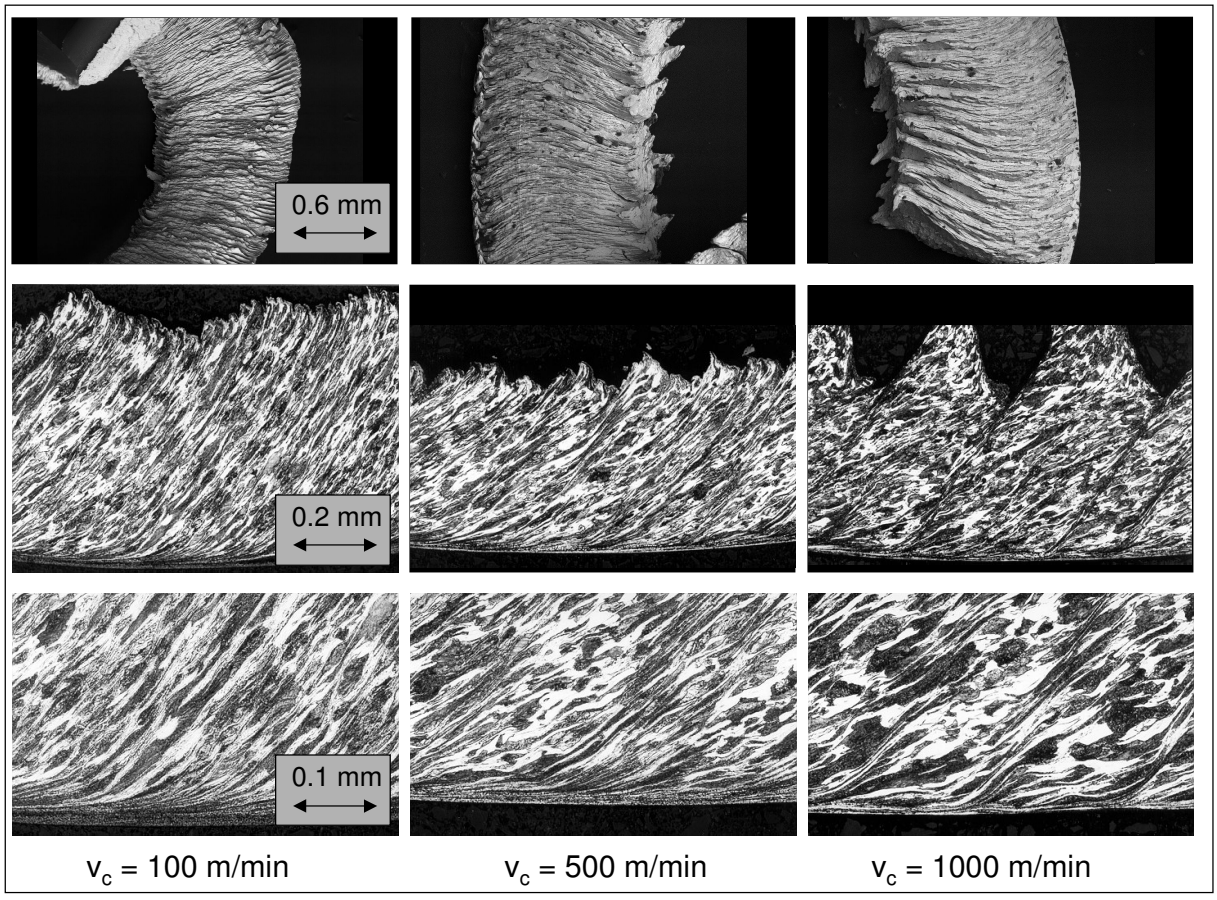


Figure 5.24: Micrographs and SEM pictures of AISI 1045 chips

These areas are embedded between two stronger sheared areas (shear bands) that are similar to the sheared chip at low cutting speed. The difference between continuous and segmented chip formation is therefore the existence of low sheared lamellae and not of shear bands. At a cutting speed of v_c = 500 m/min the two

different areas described above can be found. A further increase of cutting speed leads to a strong segmented chip formation in area A. In the micrograph the different extension of shearing that was found at v_c = 500 m/min is now more distinctive. In the chip three areas of different values for shear can be identified. The strongest shearing still occurs in the secondary shear zone. A shear band separates two low sheared areas, the lamella. Latter is embedded between the secondary shear zone and the medium sheared zones. The thickness of the secondary shear zone decreases as well as the mean chip thickness if the cutting speed rises. These general findings are valid for both variations of feed. A further increase of the cutting velocity does not lead to significant changes. The presence of the two areas A and B and therefore the mix of continuous and segmented chip formation in external cutting may be the reason why the obvious changes in chip formation have no strong influence on the chip form, figure 5.18. The chip formation of aluminum is similar to that of steel, **figure 5.25**.

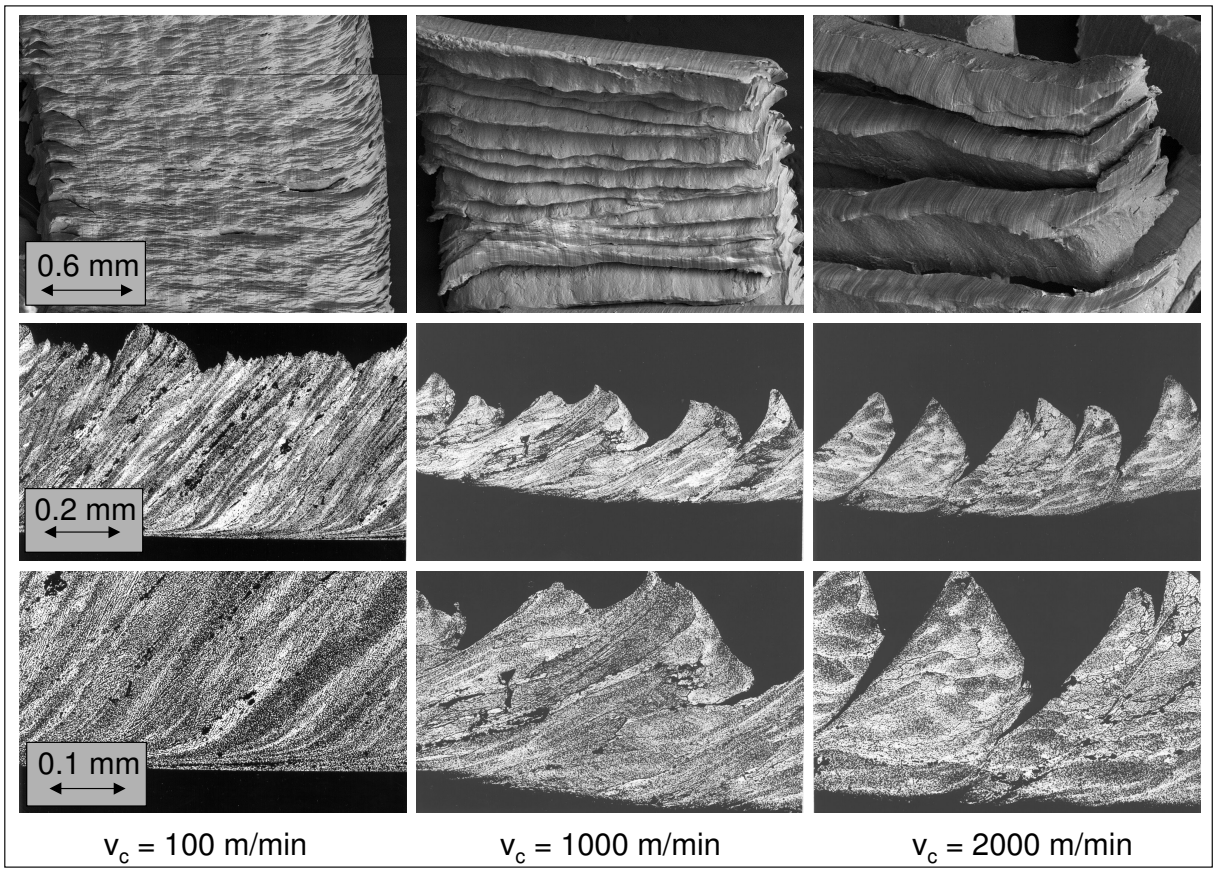


Figure 5.25: Micrographs and SEM pictures of AA 7075 chips

Again, a transition from a mainly continuous to a mainly discontinuous chip formation is found. At low cutting speeds the chip is formed by shearing and the secondary shear zone shows a higher degree of deformation. At a cutting speed of v_c = 500 m/min the transition from continuous to segmented chip formation is completed. In contrast to the steel chips it cannot be distinguished between strong and low sheared areas in the aluminum chips. At a cutting speed of v_c = 2000 m/min the chip is strongly segmented but no connecting shear bands can be found. This may be one reason why the segments of the chip at this and higher cutting speed are disconnected. The lack of the connecting shear bands has a strong influence on the chip form. It results in the improved chip breakage at higher cutting speeds, figure 5.19. A further increase of cutting speed leads to chips that are so strongly segmented that they only consist of one to five lamellae. These small structures cannot be embedded and prepared metallographically. Turning Ti6Al4V, no transition from continuous to segmented chip formation can be found, **figure 5.26**.

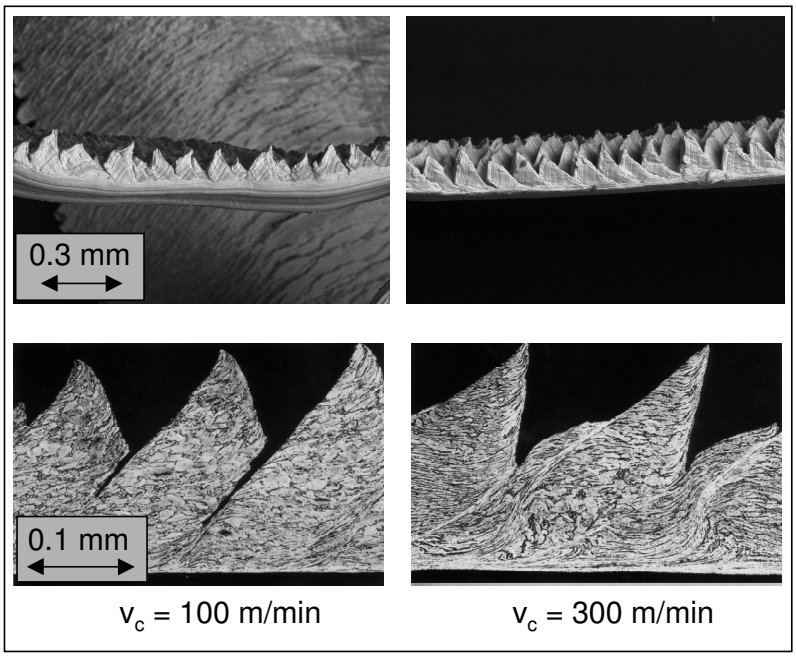


Figure 5.26: Micrographs and SEM pictures of Ti6Al4V chips (f = 0.1 mm, a_p = 1 mm)

Even at very low cutting speeds the segmented chip formation is dominant /RECH64, KREI73/. Similar to steel at high cutting speeds, a lamella is embedded between two strong deformed shear bands and the secondary shear zone. In contrast to aluminum, even a severe segmentation does not lead to chip breakage, figure 5.20.

Between two lamellae a gap or a small lamellae can be found. In orthogonal cutting tests Gente found that this is due to the fact that the shearing of one lamella consists of two phases /GENT02/. The first starts with a nearly brittle separation of the “unaffected” workpiece material, figure 5.26. This material shows only a low deformation. The second part is strongly deformed and heated up in front of the tool tip. This leads to a plastic flow of the material. At low cutting speeds this results in the stop of the gap or fracture. At high cutting speeds the high temperatures can even lead to the material flow of this material between two lamellae.

Regarding the varying dependency of the three workpiece materials on the cutting speed in external turning, it is quite interesting to note that the chip formation in orthogonal cutting shows many similarities, **figure 5.27**. The bottom of the chip is smooth for all materials. A low influence of the segmentation can be identified for the aluminum and titanium chips.

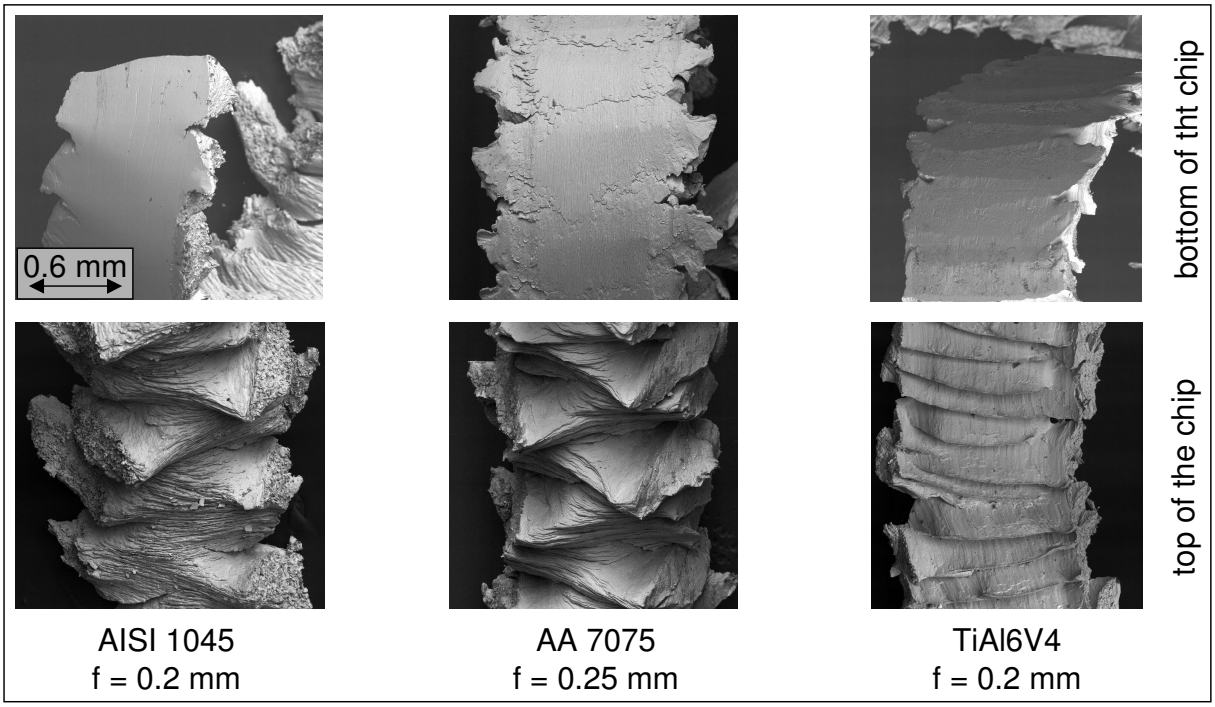


Figure 5.27: Comparison of steel, aluminum and titanium chips in orthogonal cutting (v_c = 100 m/min, a_p = 1 mm)

The top of the chips looks nearly identical for steel and aluminum. The height of the lamellae is not constant over the width of the chip and shows a regular alternation. One lamellae consists of several small sub-lamellae. These similarities of steel and aluminum are surprising because of the strong differences in the resultant forces,

chip temperatures and chip forms. For titanium, the lamellae height is nearly constant over the width of the chip. Moreover, the lamella seems not to consist of several sub-lamellae. It can be summarized that at least titanium shows a different chip formation mechanism compared to the other two materials.

5.4 Chip thickness

The chip thickness h_{ch} is one of the most important values in modeling continuous chip formation processes. The basic theories by Ernst, Merchant and Oxley always use measured values for the chip thickness to calculate the cutting forces /MATH82, PALM59, ARSE96, LIN82, ARSE95, LI95, STEV69, MANY86, YOUN87, LARS72, HU86, KAHL79, OXLE62, FANG01, MERC45, GENT02/. They assume the chip to be the product of continuous shearing with a rigid-ideal-plastic or plastic behavior. Moreover, a constant coefficient of friction was stated and implemented in the theory as the friction angle λ. These approaches do not consider the presence of a secondary or even tertiary shear zone. The constant friction law is in contradiction to the fact that adhesive mechanism take place in the real process of chip formation /SPAA71/. These simplifications are critical even for continuous chip formation in orthogonal cutting and lead to wrong results /KHAR69/. The assumptions are unacceptable for the current work where a segmented chip formation is found in the orthogonal cut for all examined materials. However, even when the chip thickness cannot be used to set up a model of segmented chip formation, its dependency on the cutting parameters improves the understanding of the process.

As already mentioned, the unsteady chip thickness in external cutting makes it hard to obtain comparable chip thickness by examining micrographs. Therefore, and to find similarities of the orthogonal and external cut, the chip thickness is measured in micrographs of the chip that are located near the free side (area A in figure 5.21) of the chip, **figure 5.28**. It is found that the chip thickness decreases when the cutting speed increases. At low speeds the chip does not show a significant maximum or minimum chip thickness. The value of cutting speed, at which a difference between maximum and minimum chip thickness is found, can therefore be assumed as the transition speed of continuous to segmented chip formation. This led to the introduction of a degree of segmentation (equation 5.2) /SCHU01/. The difference of

the maximum $h_{ch,max}$ and minimum $h_{ch,min}$ chip thickness is related to the maximum chip thickness $h_{ch,max}$.

$$G = \frac{h_{ch,\max} - h_{ch,\min}}{h_{ch,\max}} \qquad \text{(eq. 5.2)}$$

For G = 0 a smooth and continuous chip is obtained, while a thoroughly segmented chip has a degree of segmentation of G = 1. The degree of segmentation is used to describe the chip formation and to compare it for different cutting parameters. The choice of the plane where h_{ch} is measured is the reason why the degree of segmentation is not further investigated in this work. The mean chip thickness still decreases even in the area of segmented chip formation. At high cutting speeds the chip thickness can be assumed to be constant.

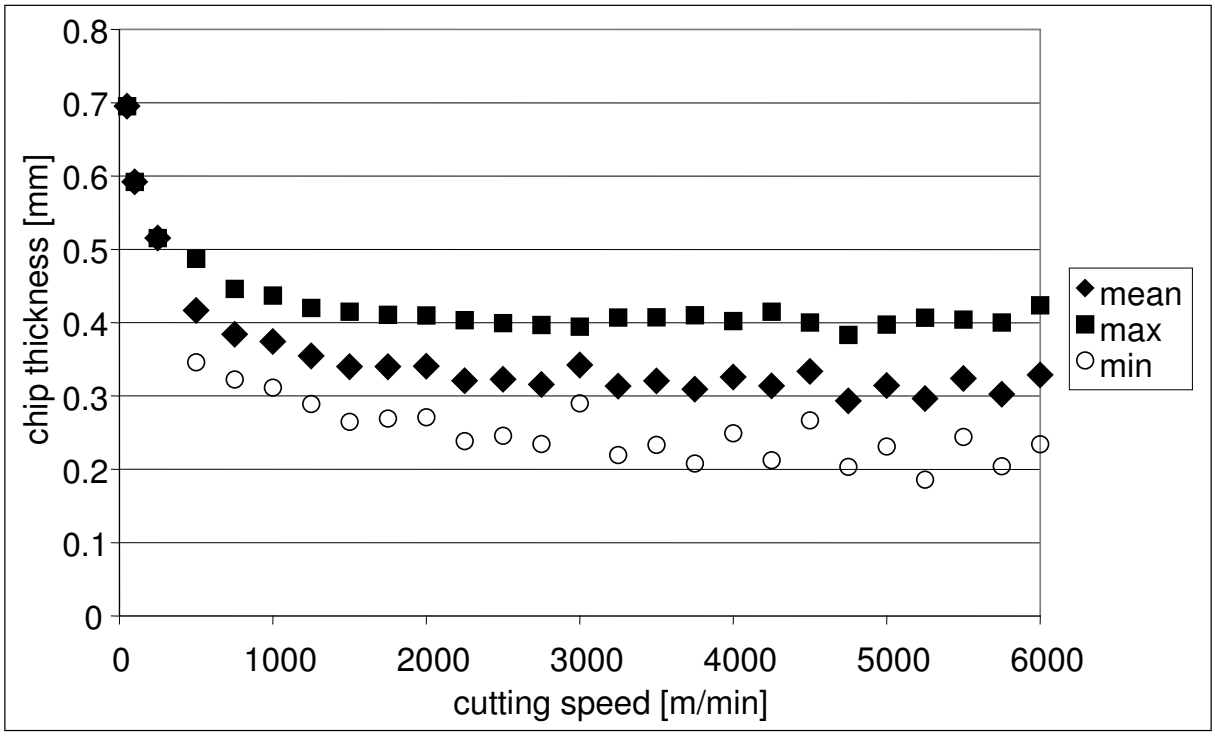


Figure 5.28: Thickness of AISI 1045 chips in external cutting (f = 0.25 mm, a_p = 1 mm)

5.5 Length of the contact zone

The contact zone length describes the area where the chip is in contact with the rake face. This implies that for tools with a high cutting edge radius ρ_O the length of the contact zone is the transition to the workpiece – clearance face contact zone.

Assuming a sharp tool, many measurements and assumptions have been made in the past to estimate the length of the contact zone. This can be reasoned by the fact that the length of the contact zone allows to describe chip formation mechanism, chip radius, chip breakage, crater wear and friction conditions in cutting. An overview about the different techniques was given by Spaans /SPAA71/. The earliest setup to measure the length of the contact zone is to analyze the rake face of the tool after the cut /ANDR58/. The contact of the chip with the tool leads to adhesion or abrasion. These mechanisms can be supported by the application of a coating that shows strong wear in contact with the chip material. These areas on the rake face can be measured using a light microscope or SEM. The **figures 5.29**, **5.30** and **5.31** show the length of the contact zone and the corresponding pictures of the rake face of the tools for turning AISI 1045, AA 7075 and Ti6Al4V.

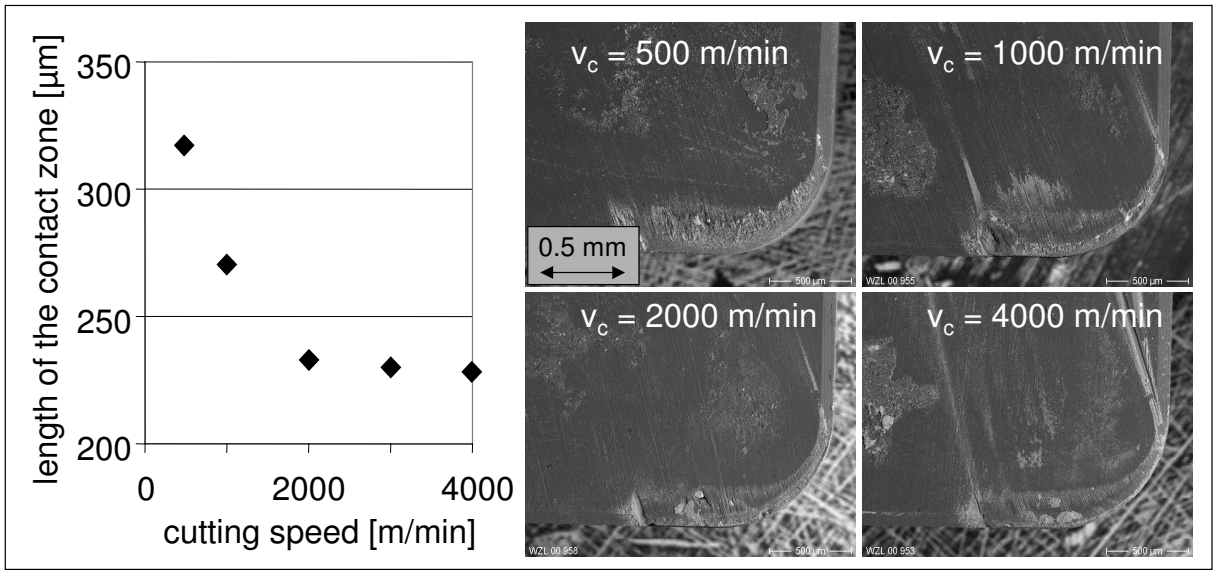


Figure 5.29: Inserts and length of the contact zone in external turning AISI 1045 (f = 0.1 mm, a_p = 1 mm)

For cutting aluminum, the contact length cannot be determined due to severe adhesion, figure 5.30. The pictures show the disadvantages of this measurement setup. First of all the influence of adhesion or tool wear cannot be neglected. Furthermore, the measurement of the length of the contact zone is limited to the area of intensive contact of tool and chip. Areas where the chip contact does not lead to significant tool wear are invisible. These disadvantages lead to the design of other setups.

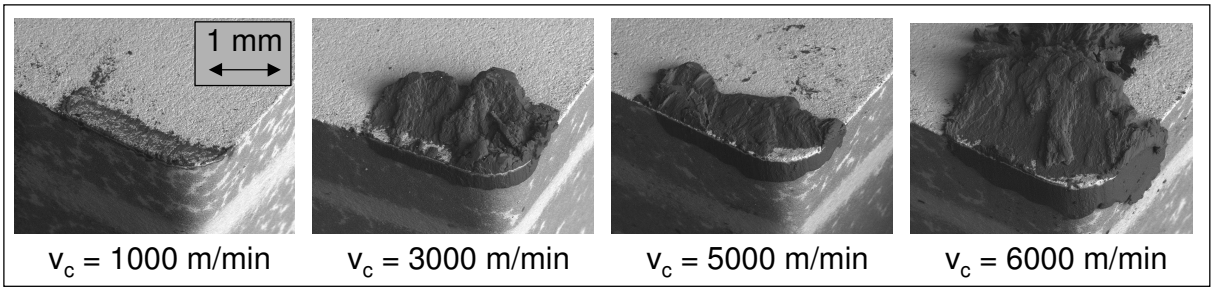


Figure 5.30: Cutting edges of uncoated cemented carbide tools in external turning of AA 7075 (f = 0.25 mm, a_p = 2 mm)

One approach to determine the contact length is the use of photo-elastic tool materials. The length of the contact zone is identified by the change of light breaking behavior of the tool under load /KATT57, ANDR58, PRIM69, LEOP80/.

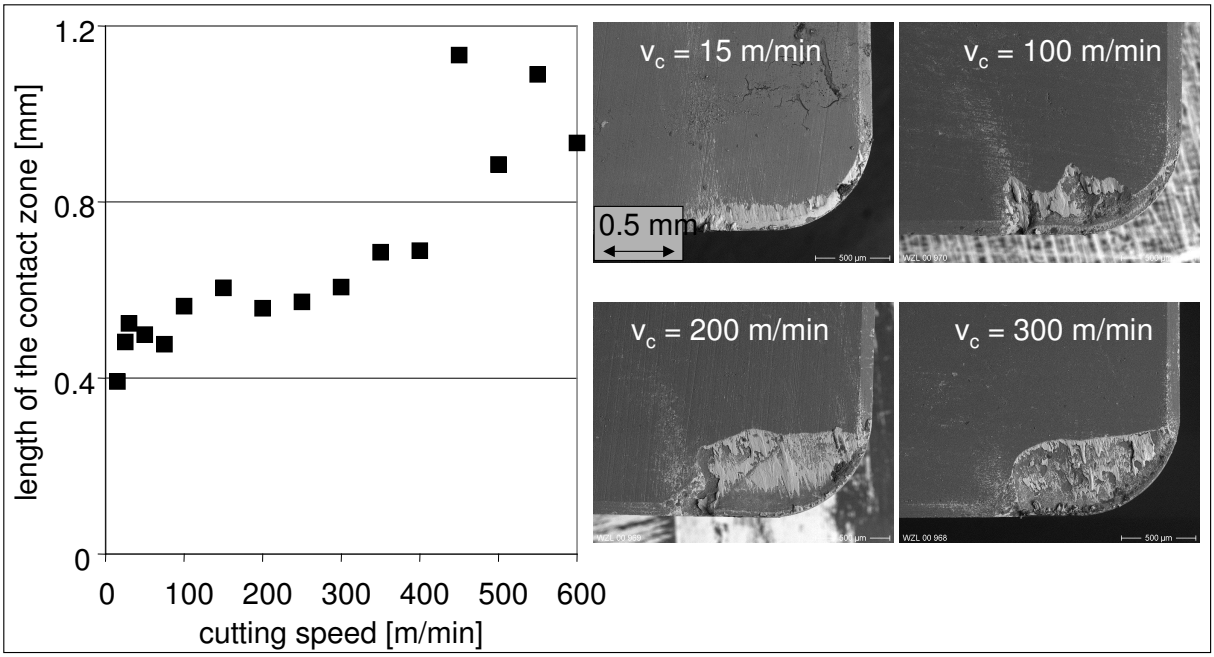


Figure 5.31: Inserts and length of the contact zone in external turning Ti6Al4V (f = 0.1 mm, a_p = 1 mm)

The main disadvantage of this setup is that the cutting conditions as well as the workpiece and tool materials cannot be compared to those of real processes. Applying a light source behind the tool in the area of the cutting edge was applied in another setup. A camera in front of the tool films the cutting process and the length of the contact zone can be estimated by the contrast of bright and dark areas /LATY63/. This setup, is only suitable for orthogonal or oblique cutting processes and the accuracy is limited by the picture frequency and the local resolution of the camera.

Modifications of the tool can also be used to measure the length of the contact zone. One example is the application of a tool with a restricted length of the rake face. The procedure is to start experiments with a tool where the rake face is very short and to increase the length of the rake face until no change to the previous experiment is found. A variation of the method is to use a clamped chip breaker and move it away from the cutting edge until no contact between chip and chip breaker is found /SATA63/. These setups are well suited to estimate the length of the contact zone. However, a high amount of experiments is necessary and several influences can lead to a strong scatter in the results.

Assuming the chip formation process to be continuous and steady state the length of the cutting zone can be calculated. Based on the theory by Merchant or Oxley the length is obtained, if the resultant forces and the shear angle are known. Applying a chip breaker and measuring the diameter of the chips can also be done in order to estimate the length of the contact zone /NAKA58, ZORE66, RUBE65/.

A very interesting approach is to use ultra sonic to measure the length of the contact zone during the cutting process /SPAA71/. An ultra-sonic device is clamped on the rake face of the tool in a distance from the cutting edge. The waves are reflected at the cutting edge and additionally at the rake face if a body is applied on it. The chip takes the role of this body in the cutting operation and because of the high frequency of the ultra-sonic wave, the contact length can be measured during the cut. A disadvantage of the setup was that the ultra-sonic device has to be placed far away from the cutting edge (about 90 mm) and therefore no insert but a cemented carbide plate was used in the past. Furthermore, the depth of cut has to be quite high (a_p = 15 mm) to obtain a good signal. However, using this device, a decrease of the length of the contact zone is found if the cutting speed increases.

5.6 Chip root examinations

The examination of chips gives hints about the chip formation process. Theories can be deduced whether the chip was formed by continuous shearing or compression and shearing operations. To obtain information about the mechanism at the cutting edge a very probable mean is the production of chip roots by interrupting the process. The so-called “quick stop technique” allows the examinations of the chip

root by etching and to measure the geometrical dimensions of the shear zones. Again the influence of the choice of the section plane has to be kept in mind. A very important issue in this process is that the cutting conditions stay the same; especially the cutting speed has to remain constant. To achieve this, different experimental setups exist, **figure 5.32**. In the setup with an accelerated tool, the latter is shot out of the cut. The tool is fixed in a bearing and on a pin with a notch. A gas gun shoots on the tool, destroys the pin and accelerates the tool out of the cut. Thereby the tool rotates around the bearing and is accelerated out of the cut. To guarantee that the tool speed is much higher than the cutting speed, the cutting velocity is limited up to v_c = 350 m/min. As this maximum speed only covers the relevant range for machining Ti6Al4V, in the current work the method is solely applied for this material. The resulting chip roots are shown in **figure 5.33** for four different cutting speeds.

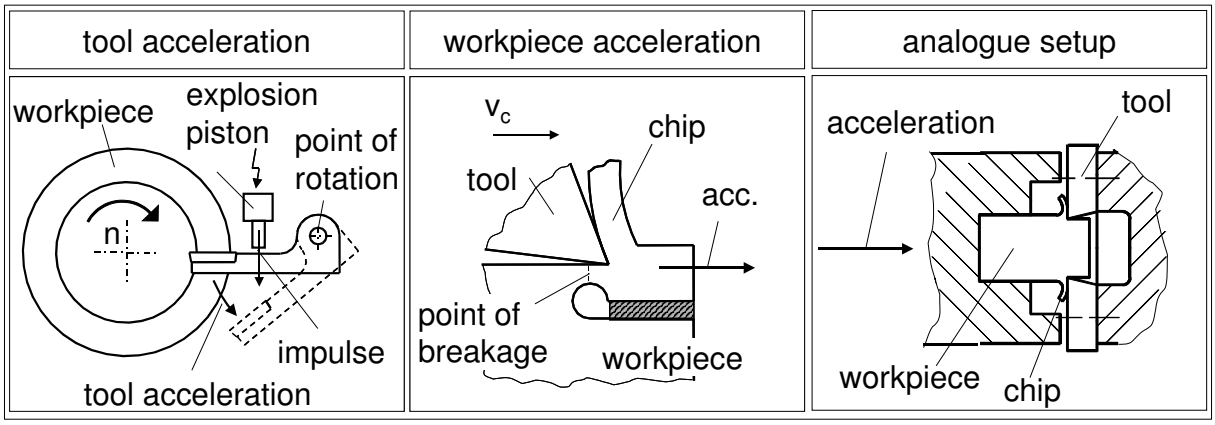


Figure 5.32: Principles of the quick stop setups in table 5.3 /BUDA68, BUDA72, ELMA01/

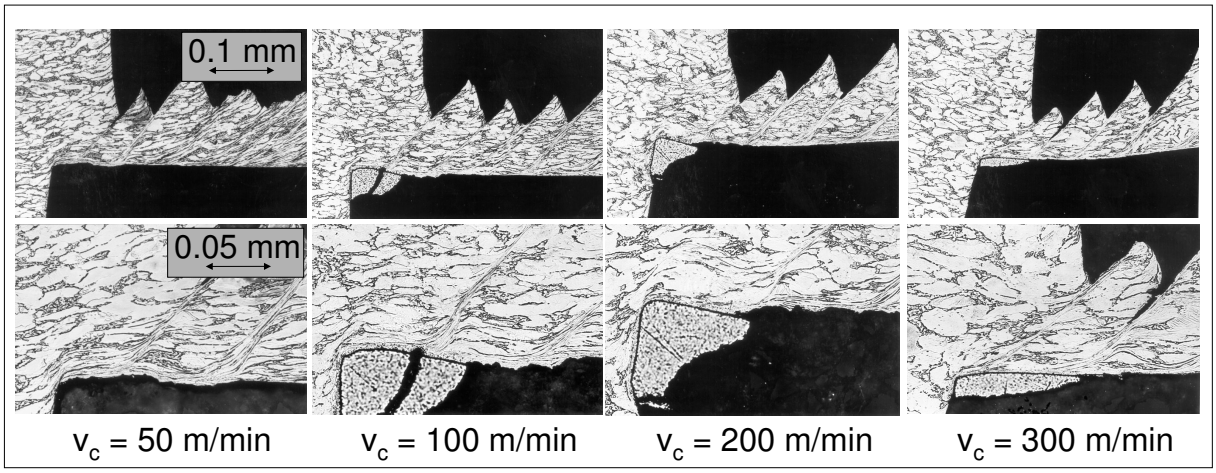


Figure 5.33: Chip roots of external turning Ti6Al4V (f = 0.1 mm, a_p = 1 mm)

The feed is f = 0.1 mm and the depth of cut a_p = 1 mm. As tool a cemented carbide was used. Fragments of the tool can be found at the secondary and tertiary shear zone. A deformation of these areas at all cutting speeds but v_c = 300 m/min shows the influence of the quick stop mechanism. The presented example of machining titanium shows that four different chip roots at four different cutting speeds freeze the process in four different stages. At the cutting speed of v_c = 300 m/min the shearing of one lamellae is just completed, the velocities v_c = 50 m/min and v_c = 100 m/min show the start of the compression phase while in the picture of v_c = 200 m/min the shearing is initiated. The conventional setup of accelerated tool was modified by Spaans /SPAA71/. He machined two disks that were clamped together. On one disk a grid is applied. This setup has two advantages. On the one hand the examination of the deformed grid allowed him to obtain streamlines, **figure 5.34**. This is similar to the visioplastic method used by Leopold /LEOP80/.

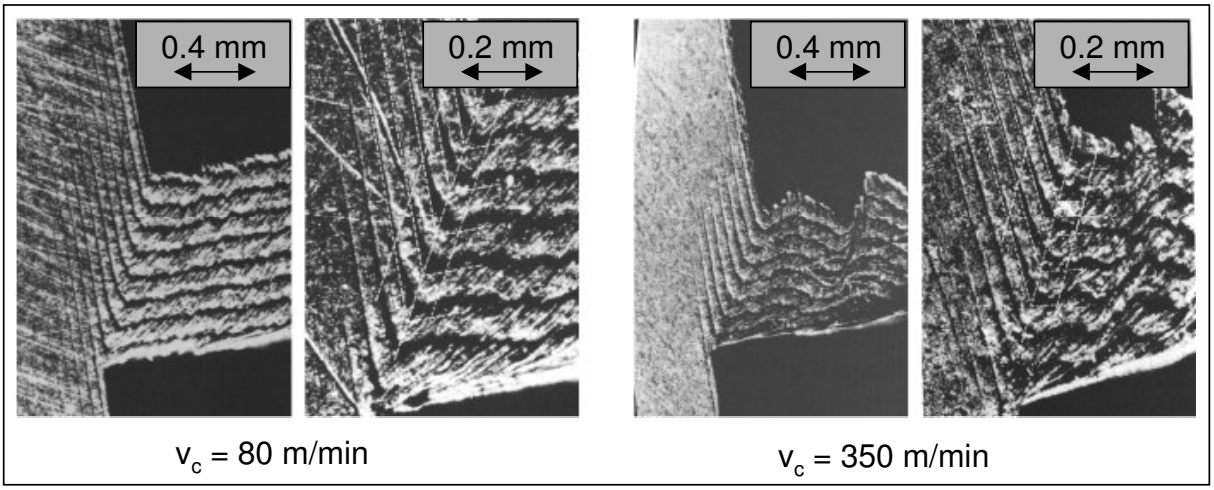


Figure 5.34: Chip roots by Spaans (AISI 1045, f = 0.4 mm, a_p = 5 mm) /SPAA71/

On the other hand, the material flow from the opposite disk into the grid leads to information about the hydrostatic stress conditions in cutting. The comparable high feed was necessary to obtain a dense grit into the specimen.

The principle to use the controlled breakage of the workpiece was first suggested by Buda /BUDA68, BUDA72/ in the sixties of the last century and is applicable for nearly all cutting processes (figure 5.32 center). Several other researcher have applied this method in the past /TÖNS99, ALTA00/. At the implemented breaking point the workpiece breaks and the chip root is accelerated out of the cutting zone. To obtain a series of chip roots, several breaking points can be implemented if the bending of the

workpiece near the breaking point is prevented by metal sheets. **Figure 5.35** shows the results of such a setup.

To obtain chip roots at very high cutting speeds, the Split-Hopkinson-Bar-Test (SPHT) described in chapter 3 /MOLI97/ was modified by Treppmann, figure 5.32 right /ELMA01/. At the end of the modified input bar, a specimen is fixed. The feed and width of cut is given by the geometry of the specimen. Clamped on the output bar it is moved onto two cutting inserts and two chips are formed. The movement is stopped in a few microseconds by two stoppers that are connected to the input bar.

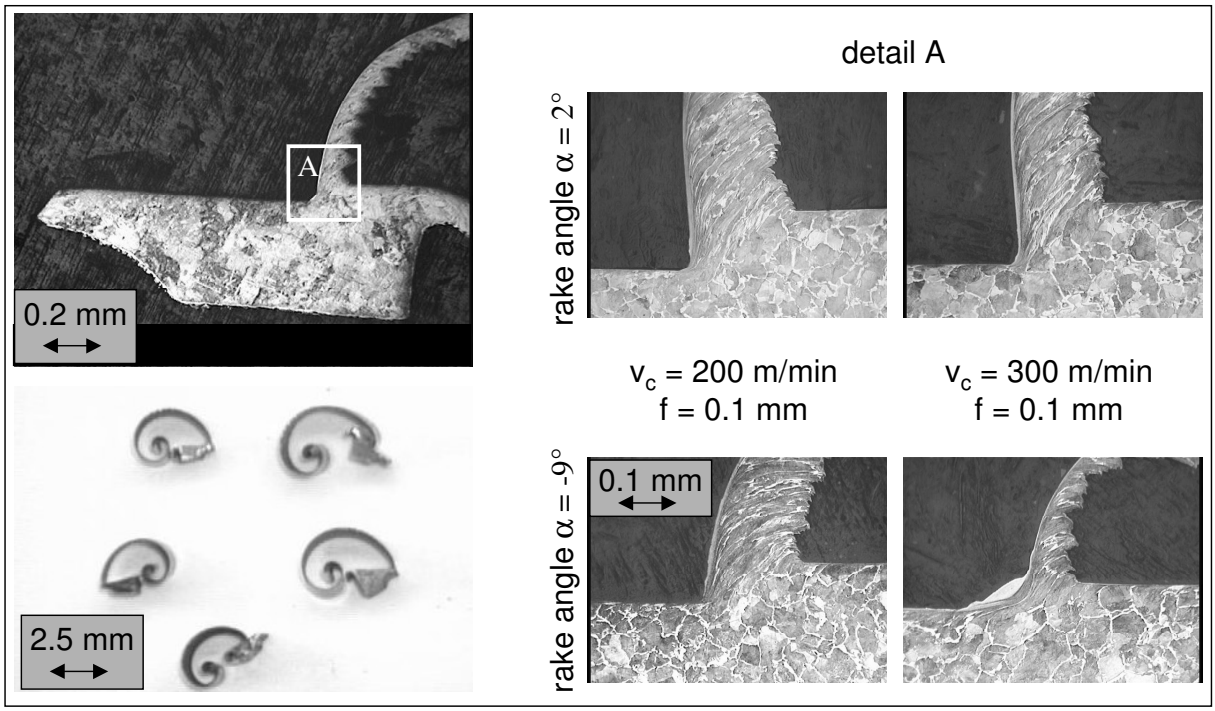


Figure 5.35: Results form the accelerated tool quick stop experiment of figure 5.32 center (AISI1045, a_p = 3 mm) /ALTA00/

An advantage of this setup is that the cutting forces can be obtained with a high time resolution (in this example 2 MHz) using strain gages, **figure 5.36**. This allows it for the first time to measure the forces of the compression and shearing phase of a lamella. The main disadvantage of this setup is that the specimens have to be manufactured with a very high accuracy and that for brittle materials the chip root is separated from the specimen because of the impact. A similar setup was realized by Gente /GENT02/.

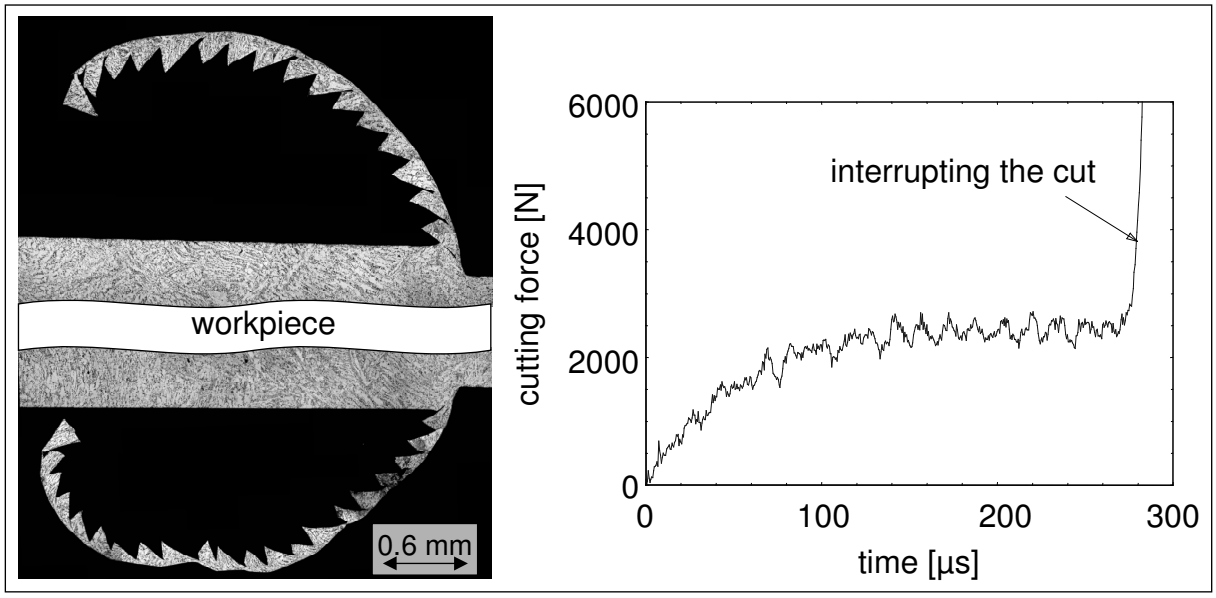


Figure 5.36: Results form the Split-Hopkinson-Bar quick stop experiment of figure 5.32 right (Ti6Al4V, v_c = 650 m/min, a_p = 4 mm, f = 0.2 mm) /ELMA01/

For all presented quick stop setups the main disadvantage is, that these tests do not „freeze“ the real process. The information about the conditions at the moment of chip formation such as the elastic stresses and the high temperatures in the specimen are lost. For example for the setup given in figure 5.36, Gente supposed the inertia forces to influence the chip radius /GENT02/. A further disadvantage is the uncertain point of time when the chip root is produced. If a continuous chip formation is obtained, this is not critical because the chip formation process can be assumed to be quasi stationary. In segmented chip formation several experiments have to be conducted to get chip roots at different states of chip formation, e.g. the compression and the shearing phase.

5.7 State of the art of the in-situ photograpy of the chip formation process

The disadvantages of the quick stop setups results in the idea to photograph the cutting process in-situ. In the past different approaches to achieve this aim were made /WARN73, CHIL71, KECE58/. The most influencing work in this area was done by Warnecke /WARN73/ in the seventies of the last century. He designed a machine tool to magnify and photograph the orthogonal cutting process with a high speed camera at a maximum picture frequency of 8000 s^{-1}. Because of the long exposure time the process parameters were limited to a cutting speed of v_c = 6 m/min. An

interesting invention by Warnecke was the use of an etched specimen instead of one prepared with a grid. This reduced the influence of the surface quality on the chip formation. Furthermore, it was possible to observe the deformation of the microstructure, e.g. the deformation of perlite components, **figure 5.37**. The workpiece was pressed against a lubricated window. This prevented the side flow of the chip and therefore forced him in the focus of the camera. The frequency of the camera and the cutting speed were suitable to examine the influence of the rake angle on the chip flow (figure 5.37 top left and center) and the mechanics of the build-up edge creation (figure 5.37 top right). Warnecke even filmed the segmented chip formation (pictures 1 to 3 in figure 5.37 bottom). The compression and shearing phase can be identified as well as the deformation of the uncut chip thickness. The crack initiation at the bottom of the chip is typical for cutting operations with very low cutting speeds and/or build up edge formation /IWAT76, FORM70/. The limitation of the cutting speed is caused by the long duration of the exposure time (figure 5.37 top right).

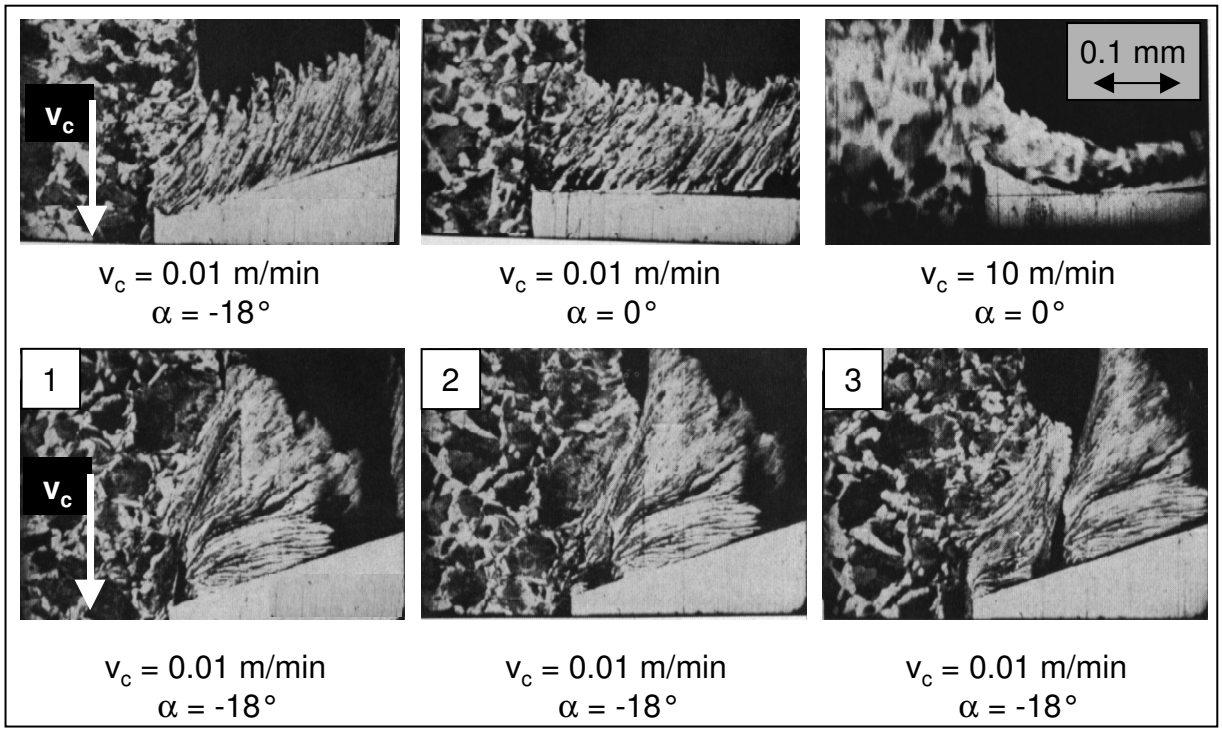


Figure 5.37: In-situ photography by Warnecke (AISI 1045, f = 0.05 mm) /WARN73/

In 1971 Childs /CHIL71/ published an experimental setup using a double exposure technique. The principle of this setup is to illuminate one picture twice. The time difference of the double exposure has to be short and known. These two pictures are

sufficient to describe the material deformation in the chip formation process. The information is quite accurate and even Warnecke, who obtained a film of the chip formation, hardly examined more than three pictures of one cut to describe the mechanism. Moreover, Childs used the two pictures of chip formation to get information about the streamlines in metal cutting operations. This approach is similar to the well known visioplasticity that is used in mechanical engineering /LEOP80/. The setup by Childs consisted of a microscope, a camera and two light sources. The specimen was prepared with a grid and pressed against a lubricated glass. The maximum magnification of 25 and an exposure time of twenty nanoseconds allowed him to validate his streamline theory. The quality of the obtained pictures was limited by the strong deformation of the grid.

While Childs and Warnecke realized photographs or films of the chip formation process the work by Damaritürk /DAMA90/ was focussed on the shape of the chip. Using a high speed camera, he obtained photographs at high cutting speeds. However, because of the low magnification and problems with the illumination his pictures did not lead to a further understanding of the high speed cutting process.

5.8 Design of a new setup for the in-situ photography of chip formation

The described shortcomings of the quick stop setups and the existent setups for in-situ photography lead to the design of a modified setup, **figure 5.38**.

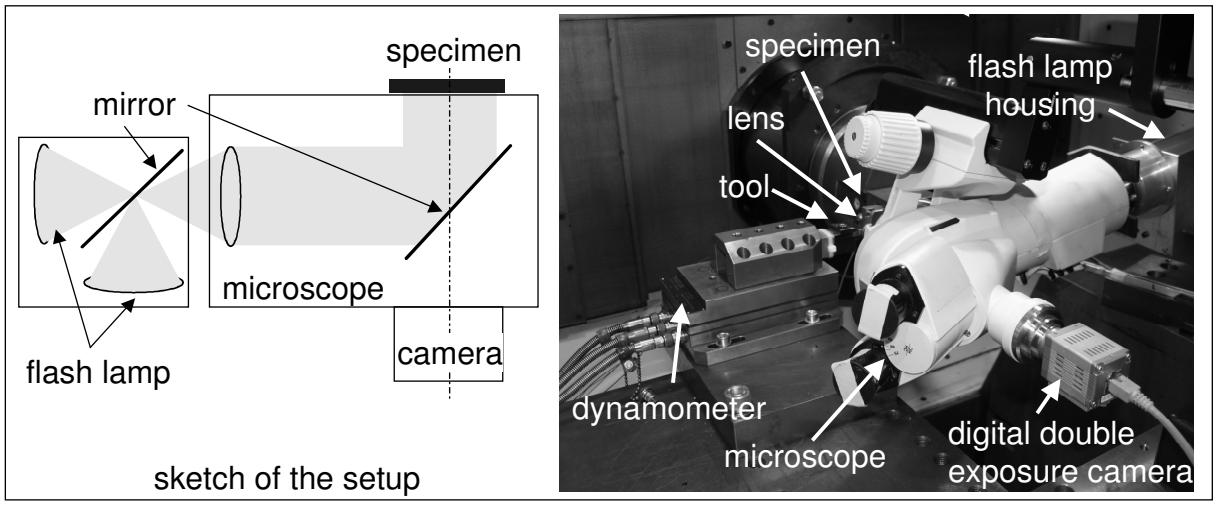


Figure 5.38: Modified experimental setup for in-situ photography

It allows to take pictures of the chip formation process for different materials up to cutting speeds of v_c = 3000 m/min. The double exposure technique by Childs is used, while the specimens were etched to obtain the advantages of the setup by Warnecke. The setup consists of a microscope /LEIC01/ with a possible magnification up to 500, two flash lamps /HSPS01/ with an illumination time of t_e = 20 ns and a digital camera /PCO01/ which allows the double exposure with a minimum time difference of Δt = 3 µs. This composition of flash lamps and double exposure camera is analogous to a setup to photograph the diesel injection process /SCHU00/. The specimen is illuminated by the flash lamps which are positioned in the optical axe. The picture is taken by the digital camera mounted on the C-mount adapter of the microscope. As long as the chip, the tool or the workpiece are in the area of the depth of field the picture is found to be sharp. For this purpose the specimen has to be perpendicular to the optical axe, figure 5.38 left. If this is not the case the illumination of the picture is insufficient. The chip formation as well as the tool wear and the three shear zones can be examined, **figure 5.39**.

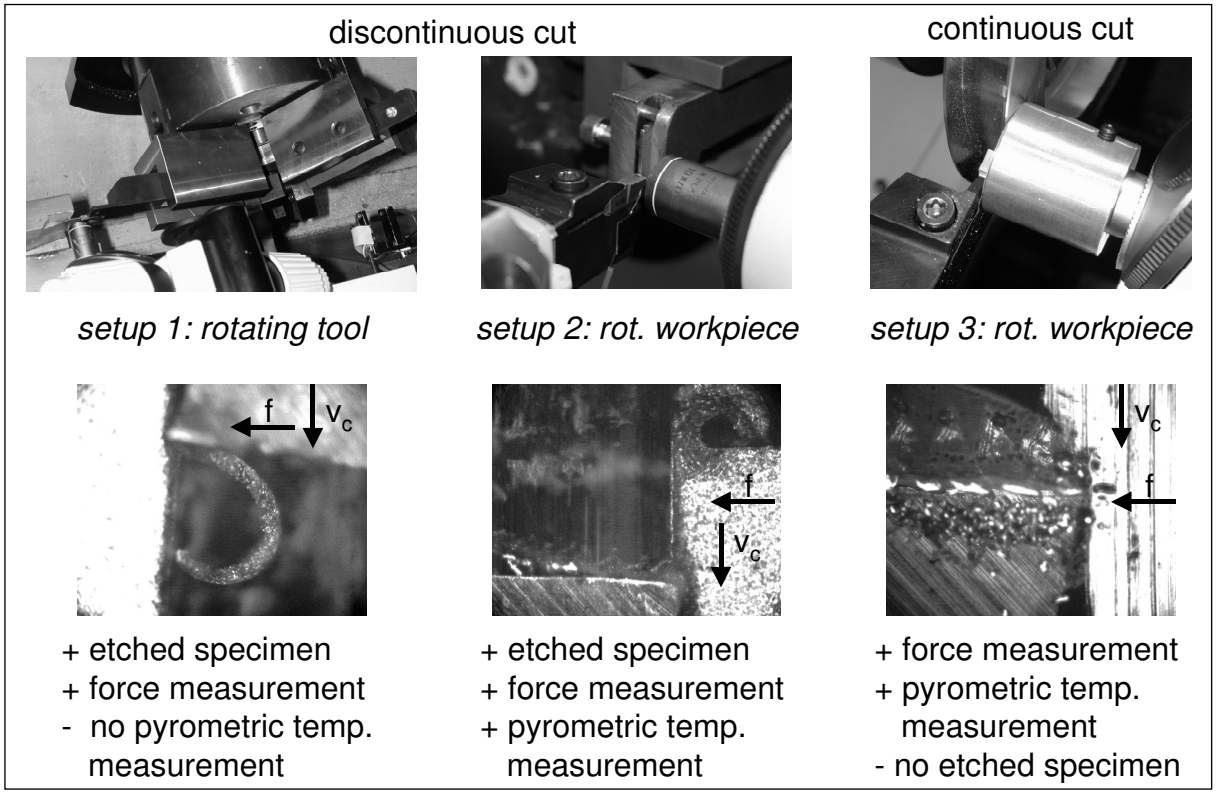


Figure 5.39: Advantages and disadvantages of the realized setups

Thereby, the material of the specimen can be chosen without restrictions. This setup allows to photograph the chip formation even of brittle workpiece materials such as

cast iron or inhomogeneous materials such as metal matrix compounds. The only requirement is that the material has to reflect the flash lamp. If this is given, even the chip formation of wood, stone, polymers, ceramics and glass can be examined. The current supply for the flash lamps is provided by two generators and the pictures are transferred from the camera to a conventional PC unit. The control of the time distance between the trigger signal, the camera, the first and second flash are realized by a delay generator /RISY01/. The setup was implemented in a conventional lathe (Frontor 1 CNC) by the company Weisser. This allows to photograph the cutting process under real world conditions. The high accuracy and stiffness of the machine tool lead to reproducible results.

The principle of the setup is similar to those of Warnecke and Childs. The chip is produced in an orthogonal cut. In contrast to the setups in the past, the protection window is not needed to lead the chip. However, a protection window was applied to prevent the optical device from any kind of damage or dust. As the setup for clamping the tool and workpiece material had to be designed anyway, three different setups were realized to obtain the maximum information about the cutting process.

5.8.1 Setup 1: Photography of the discontinuous cut with a rotating tool

In this setup (figure 5.39 left) the cutting tool is fixed in the clamping of the spindle and thus a cinematic similar to milling is designed. To reduce the run out three identical tool holders are implemented. The clamping adapters are suitable to fix all standard tool holders so nearly every tool geometry and inclination angle can be chosen. In the current setup the orthogonal cut was realized to obtain similar mechanisms as they can be found in the two dimensional cutting simulation. Therefore, a grooving tool was applied. To ensure the fixed position of the tool holders they are centered with two screws and the insert was ground evenly on the minor cutting edge exposed to the microscope. The clamping of the workpiece was designed to allow a solid fixture of the specimen and the protection window. The clamping also has to guarantee that the specimen is fixed exactly parallel to the optical axe. The specimen is ground, polished and etched to obtain a structured surface with a high reflection.

Because of the very short exposure time of the flash lamps the setup is suitable to obtain sharp pictures even at high cutting speeds. As in this setup the specimen is of limited size, on one hand the camera has to be triggered when a chip is produced. On the other hand the setup is designed to obtain two pictures in a defined time range. Moreover, it has to be considered that there is a delay in the triggering of the picture. This problem has been solved as follows. The trigger signal is produced by a light barrier which is interrupted by a thin sheet clamped to the rotating tool. This trigger signal which can also be produced by a piezo or strain gage signal is led to the delay generator /MUEL02/. This allows to trigger four devices with a high accuracy (time differences down to 5 nanoseconds are possible). One device is the PCI-board of the digital camera, the second and third are the flash lamp generators. In **figure 5.40** the tool, the workpiece, the objective and the light barrier are shown on the left. On the right a picture of the workpiece and the fixed tool is displayed.

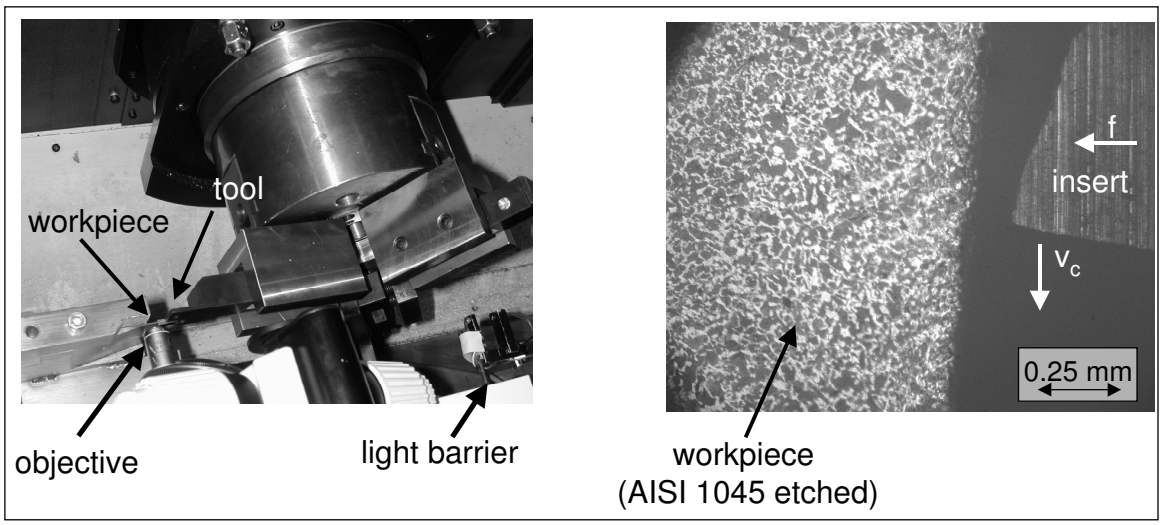


Figure 5.40: Setup with a rotating tool and fixed specimen (left), resulting picture (right)

It can be seen in figure 5.40 that the structure of the specimen is photographed. When the cutting process is started the resultant changes in the workpiece material, such as plastic deformation, become visible. This is quite important to estimate the influence of the cutting process on the surface integrity. A further application is the visualization of burr formation. Because of the limited depth of focus it must be decided whether the workpiece, the chip or the tool will be inside the focus. **Figure 5.41** shows photographs of the chip formation in cutting AISI 1045. The low magnification (figure 5.41 left) allows to determine the chip radius as well as the

length of the contact zone. A higher magnification (figure 5.41 center) visualizes the formation of different lamellae and, for moderate feeds, the length of the contact zone. If the magnification is further increased (figure 5.41 right), the formation of a single lamella can be photographed. Because of the lower depth of field the sharpness is not as well as for the lower magnifications. Nevertheless, fractures and the velocity of different areas in the lamellae can be identified. This is only possible because of the etched surface of the specimen. The different orientations of the microstructure lead to a different intensity of reflection and can therefore be found in both pictures. It can be summarized from figure 5.41 that the segmented chip formation is obtained by alternating compression and shearing mechanisms.

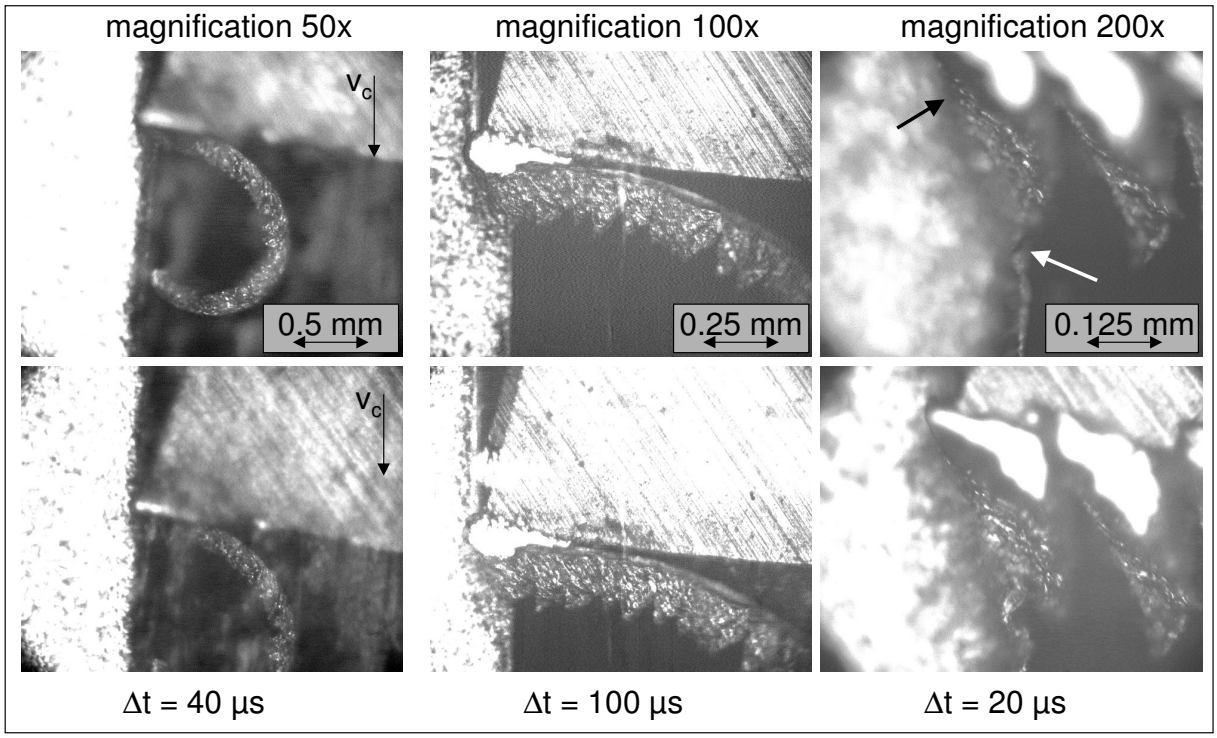


Figure 5.41: Photographs of cutting AISI 1045 at different magnifications
(v_c = 500 m/min, f = 0.1 mm, a_p = 1 mm)

The 100x and 200x magnification show a gap on the free side of the primary shear zone during the shearing phase. It is not possible to say whether a fracture at the top of the chip is necessary to initiate the shearing phase. In the picture with the 200x magnification some kind of scratch is found in that area where the shear zone is located (white arrow in figure 5.41 right top). Furthermore the initiation of shearing can also be started near the tool tip (black arrow in figure 5.41 right top). The

influence of the poor sharpness of these areas does not allow to draw general conclusions. In this work, the magnitude of pictures are taken with a 100x magnification to obtain information about chip formation, chip thickness, chip radius and contact length by a sufficient sharpness of the picture.

5.8.2 Setup 2: Photography of the discontinuous cut with rotating workpiece

This setup (figure 5.39 center) is similar to the first one concerning the triggering and geometry of the specimen. Here, feed and cutting speed are realized by the workpiece and the tool is fixed. The setup and a resulting picture are shown in **figure 5.42**. Because of the fact that the tool stays in the focus, the setup enables to examine the mechanisms at the flank and rake face of the cutting edge. As these mechanisms lead to the wear of the tool, this setup is very interesting. Even discontinuous wear mechanism such as tool breakage and delimitation of tool coatings can be examined. A further advantage of this setup is that the fixed tool allows the measurement of resultant forces and cutting temperatures while the pictures are made. Moreover, these measures can be triggered, too, so it is possible to obtain two pictures with the accurate values for temperatures and forces. Never before a test setup has been created that produces as many information about the cutting process. The results are presented later in this chapter.

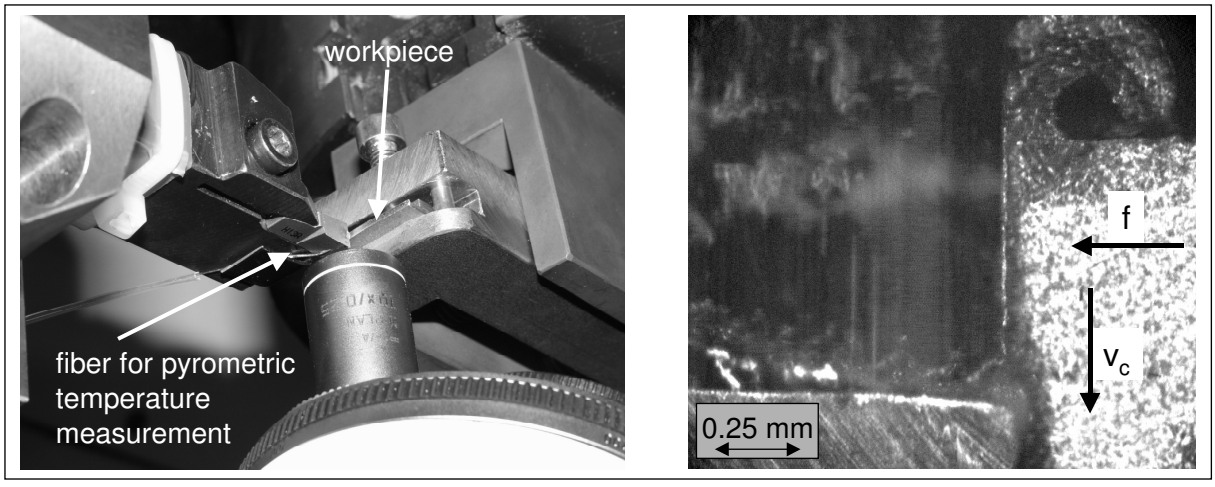


Figure 5.42: Setup with a rotating specimen (left), resulting picture (right)

5.8.3 Setup 3: Photography of the continuous cut with rotating workpiece

The two setups described above have in common that a specimen of limited size acts as workpiece. The reason for the limited size is that the specimen has to be etched. Therefore, a discontinuous cut, similar to a milling operation, was realized with those setups.

It is well known that the mechanisms of chip formation in milling and turning operations are quite different. Milling operations lead to small chips and an oscillating mechanical and thermal load on the cutting tool. In turning operations the chip breakage is an important criterion and the process can be assumed to be quasi stationary. This leads to higher temperatures because of the constant heating of the tool and thus to different wear mechanisms compared to milling operations. To examine this process the following setup was designed (figure 5.39 right). The tool is clamped as in setup 2. This allows the simultaneous measurement of temperatures and forces while the pictures were made. As workpiece a ring with a groove was used. The two remaining parts on the front and back of the ring are machined. The thickness, which is equal to the width of cut, is given by the width of the ring and the groove (**figure 43, left**).

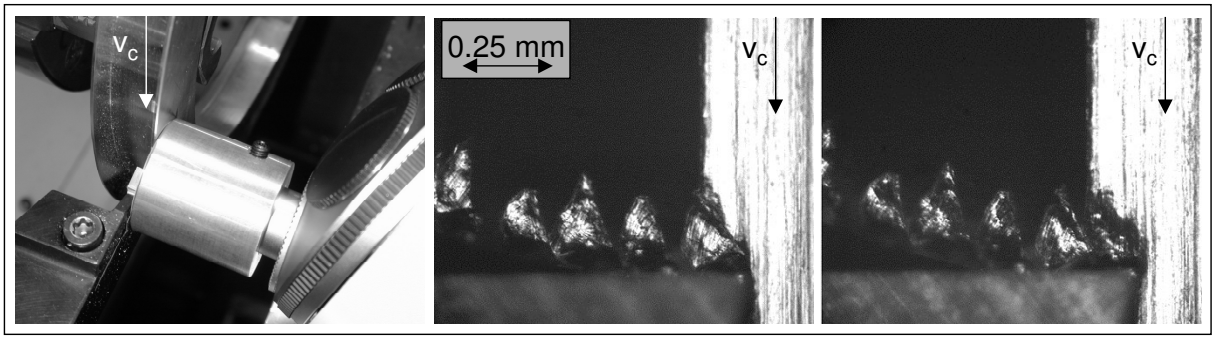


Figure 5.43: Setup to photograph the continuous chip formation (left) and resulting photos (AA 7075, v_c = 250 m/min, f = 0.2 mm, a_p = 1 mm, Δt = 60 µs)

The grooved workpiece was chosen in order to provide similar conditions as in the two dimensional cutting simulation. However, it is possible to take pictures of a facing operation with a grooving tool, too. As the protection window cannot be clamped to the tool or the workpiece it is fixed on the microscope. Therefore, a tube is designed which is clamped to the objective by a screw. At the end of the tube the protection

window is glued. Now the microscope is focussed on the area of interest which could be the surface of the workpiece, the tool or the chip, **figure 5.44**.

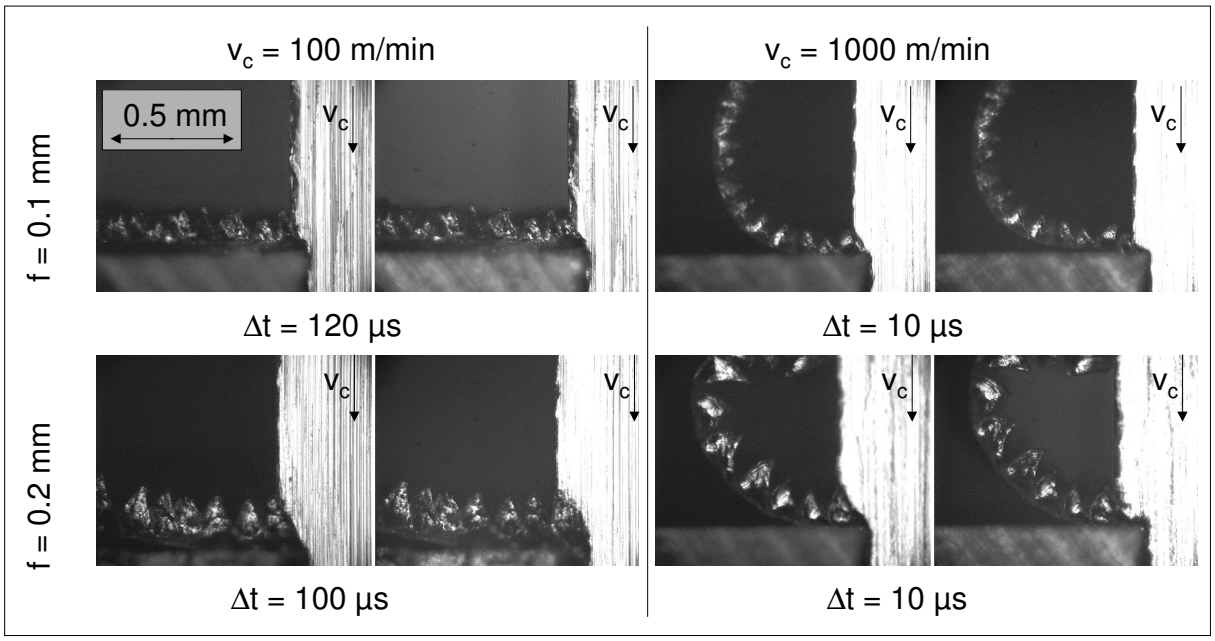


Figure 5.44: Chip formation in turning AA 7075 (f = 0.2 mm, a_p = 1 mm)

In order to photograph the chip, the microscope is focused on the surface of the protection window and the tube is clamped. The resulting pictures are shown in figure 5.43, right. If the chip is in contact with the protection window, adhesions can be found on the window (**figure 5.45 left**).

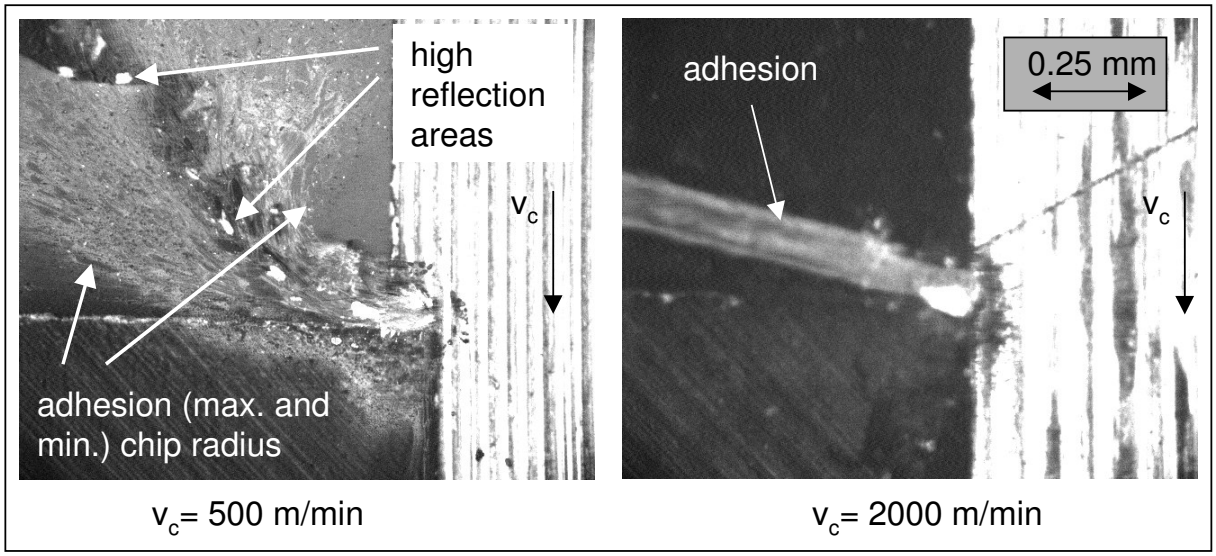


Figure 5.45: Highly reflective parts of the chip (left) and adhesion at different cutting speeds (right) (AA 7075, f = 0.25 mm, a_p = 2 mm)

The adhesions can be so thick that only the highly reflective parts of the chip can be photographed. This can be prevented, if the protection window is placed in some distance from the workpiece. On the other hand, these adhesions mark the area in which the chip radius varies as well as the maximum length of the contact zone. A minimum and maximum chip radius can be found as well as areas where the chip has never been (figure 5.45 right). This information is essential to design an optimized tool breaker geometry as well as to describe the influence of chip breaking elements in the material, e.g. lead.

For very high cutting speeds and brittle materials where the chip contains only of one or two lamellae it is hardly possible to force these lamellae in the depth of field. But the adhesions allow at least to determine important values such as contact length and chip thickness (figure 5.45 right). As mentioned above, the simultaneous measurement of resultant forces and temperatures is possible while taking the photos. A similar setup as described earlier in this chapter is suitable, **figure 5.46**. The length of cut for all three setups is long enough to obtain resultant force signals from a dynamometer. However, the photographs show that the segmented chip formation is dominant under the conditions of this work. Therefore, it would be desirable to correlate the force and temperature signal to the taken pictures.

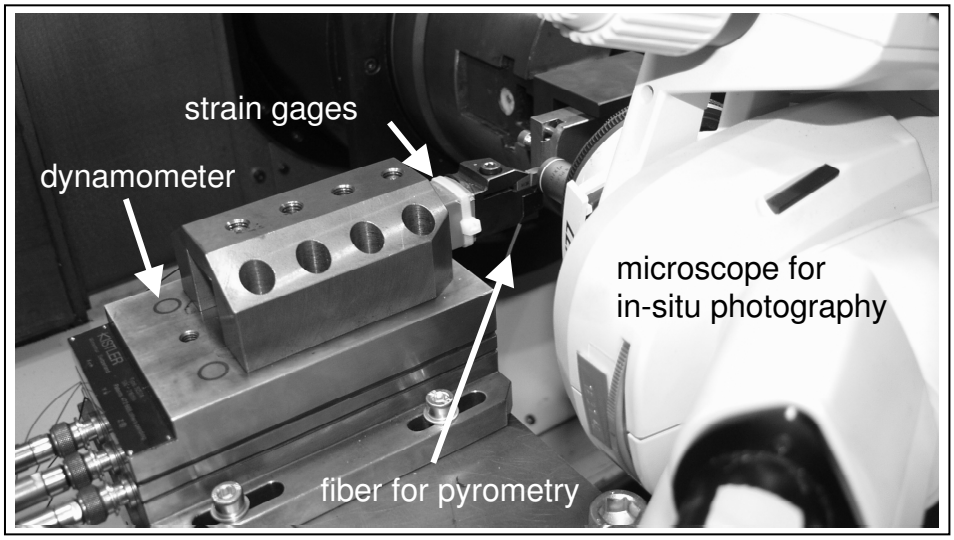


Figure 5.46: Combination of in-situ photography, resultant force and temperature measurement

The time resolution of the dynamometer is too low to obtain a value within the time window of the in situ photography. However, a quasi static value can be measured to

compare the results to those of the external turning experiment. To obtain highly resolved resultant forces, the application of strain gages on the tool is possible. This was shown by Treppmann and the result of such a measurement is given in figure 5.36. However, the tool in the in-situ setup is too stiff to obtain the force signals. A tool holder with a lower stiffness or much higher values for feed and depth of cut can solve the problem. In this work, the measurement of the dynamic forces was not conducted because the necessary changes of the tool and/or cutting parameters would have reduced the comparability to the external cutting results. The need of a very high time resolution temperature measurement leads to the application of the above mentioned two-color pyrometer in the setup, **figure 5.47**. To realize the three measurement positions bottom of the chip, top of the chip and machined surface a fixed tool is needed. Therefore, the temperatures in the first setup cannot be measured. Because of the similar mechanisms of chip formation in setup one and two no information is lost.

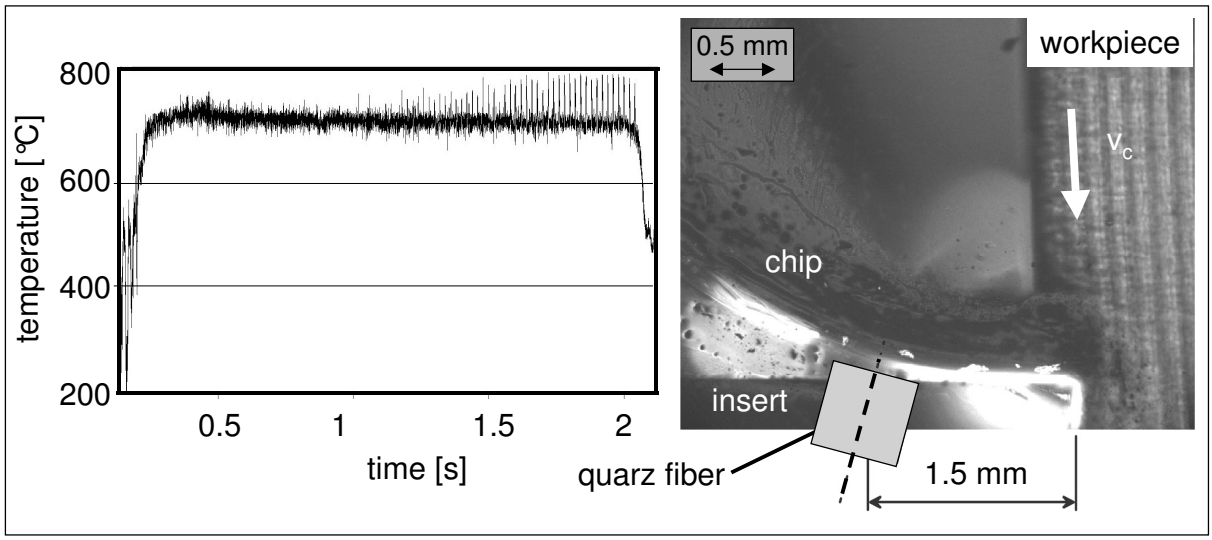


Figure 5.47: Results of a synchronized in-situ photography and temperature measurement

5.9 Results of in-situ photography

5.9.1 Chip thickness

The chip thickness shows a decrease if the cutting speed increases. **Figure 5.48** and **5.49** show the values for aluminum and steel. A similar dependency as in the external turning operation of steel is found (compare figure 5.28). For the segmented

chip the decrease can be found for the maximum and minimum chip thickness. Therefore, the segmented chip formation is quite stable in this range of cutting speed. This steady decrease of chip thickness with the cutting speed coincides with the strong temperature increase and the decrease of the resultant forces (compare figures 5.2-5.6, 5.14, 5.15).

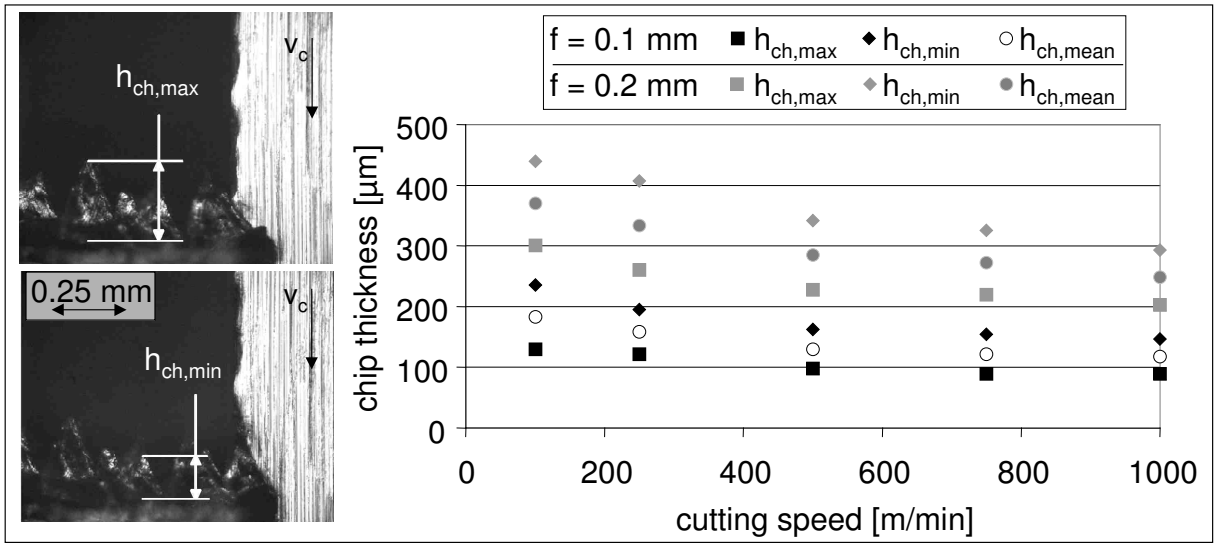


Figure 5.48: Chip thickness in orthogonal cutting AA 7075 (a_p = 2 mm)

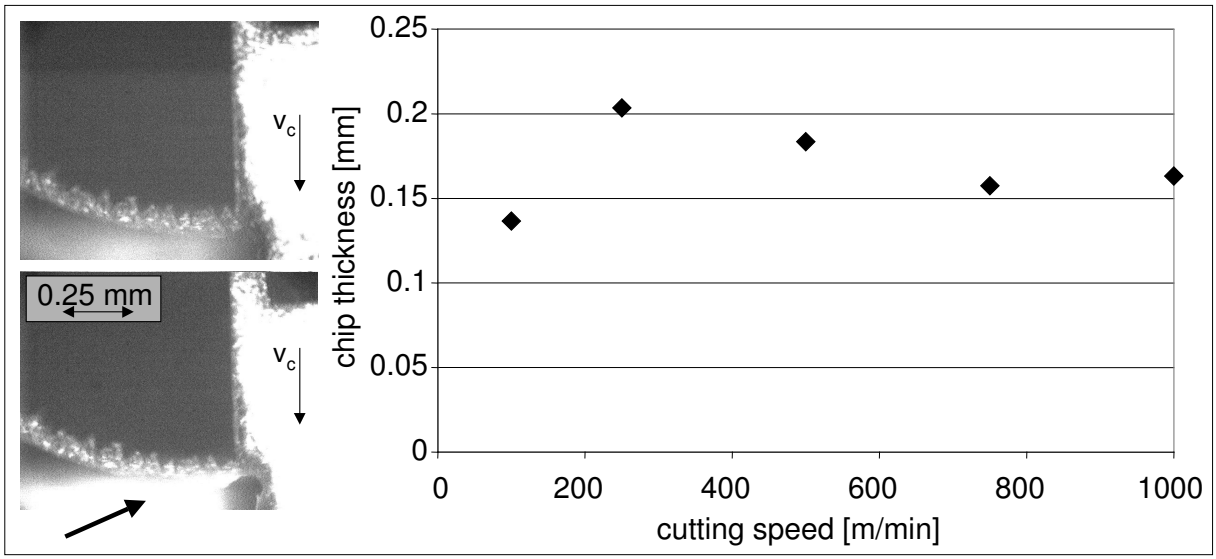


Figure 5.49: Chip thickness in cutting AISI 1045 with a glowing bottom of the chip (f = 0.1 mm, a_p = 2 mm)

Examining the in-situ pictures, it can be found that the high temperatures in turning steel lead to glowing of the chip (figure 5.49 arrow). This spoils the quality of the pictures. It is worse for the second picture as the camera shutter is open much longer

than for the first image. As a result, the scatter of the steel results is higher than for aluminum. However, using inverted pictures a reliable determination of the results is possible.

5.9.2 Chip radius

The chip radius is determined by the chip form and is therefore suitable to monitor the chip formation as a criterion of machinability. A lot of theories were developed to find the cause of the curling of the chip. The theories consider plastic bending /DAWE69/, residual stresses and temperature gradients /LENZ68/. Further possibilities are the presence of a build-up edge (BUE) or a build-up layer (BUL or secondary shear zone) /NAKA62, SPAA71/ and the curvature of the primary shear zone which leads to the assumption of a chip that is "born" curved. For continuous chip formation, the influence of BUE and BUL on the chip curl cannot be neglected. Also the curved shape of the primary shear zone may cause curved shear bands in the chip and thus creates a curved chip. All these assumptions and theories are created for continuous chip formation. It can be assumed that the mechanism of chip curling is different if a segmented chip formation is found, **figure 5.50**.

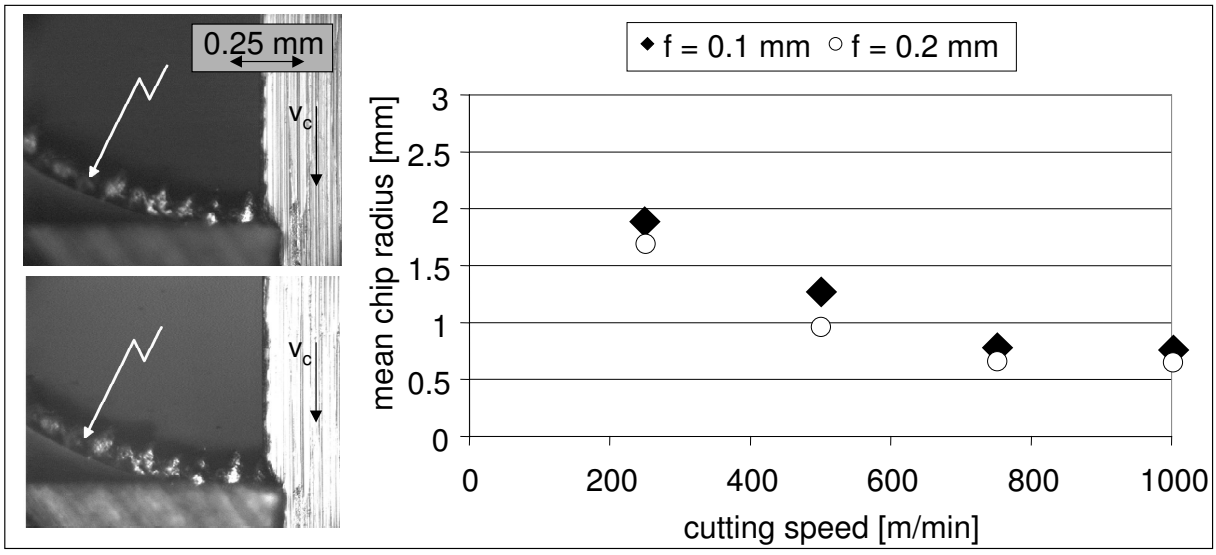


Figure 5.50: Chip radius in orthogonal cutting AA 7075 at different cutting speeds and feeds

One of the major advantages of the in-situ setup is the possibility to obtain the chip radius during the cut. This radius can be different from the one obtained from measurements of collected chips because of the thermal and mechanical conditions

the chip is subjected to on the way from the tool tip to the bottom of the machine tool. The aluminum alloy shows a decrease of the chip radius when the cutting speed rises. The chip radius in machining AISI 1045 shows a scatter of the values, **figure 5.51**. This is due to the chip hitting the unmachined workpiece and will be described later.

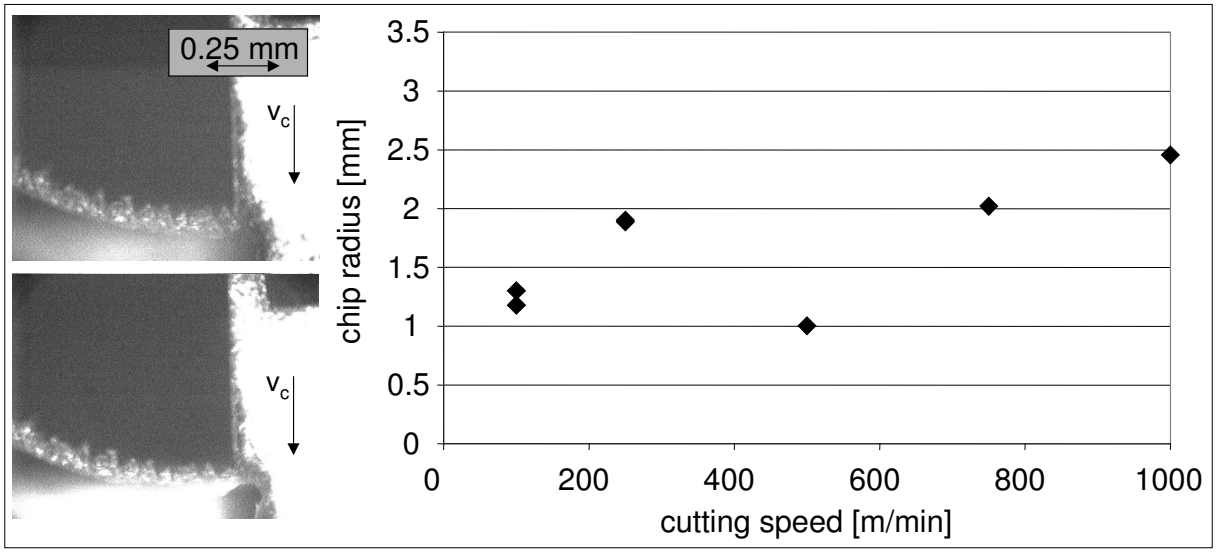


Figure 5.51: Chip radius in orthogonal cutting AISI 1045 at different cutting speeds (f = 0.1 mm, a_p = 2 mm)

The segmented chip formation, the absence of any kind of build-up edge and the constant thickness of the secondary shear zone (compare figure 5.24) propose that the earlier described theories for chip curling in continuous cutting are not valid. Using the in-situ photography and the SEM pictures of the chips an interesting phenomenon is found. When increasing the cutting speed, the segmentation becomes more severe and the shape of the lamellae changes. At low cutting speeds the flanks of the lamellae are straight, **figure 5.52**. At higher cutting speeds the straight shape disappears and a curved shape is found. To visualize the mechanism, two sketches of chip formation are given in figure 5.52. At low cutting speeds, the straight form of the primary shear zone produces a chip with a very high radius (figure 5.52 top). The change of the primary shear zone shape from straight to convex results in a chip with a low radius (figure 5.52 bottom).

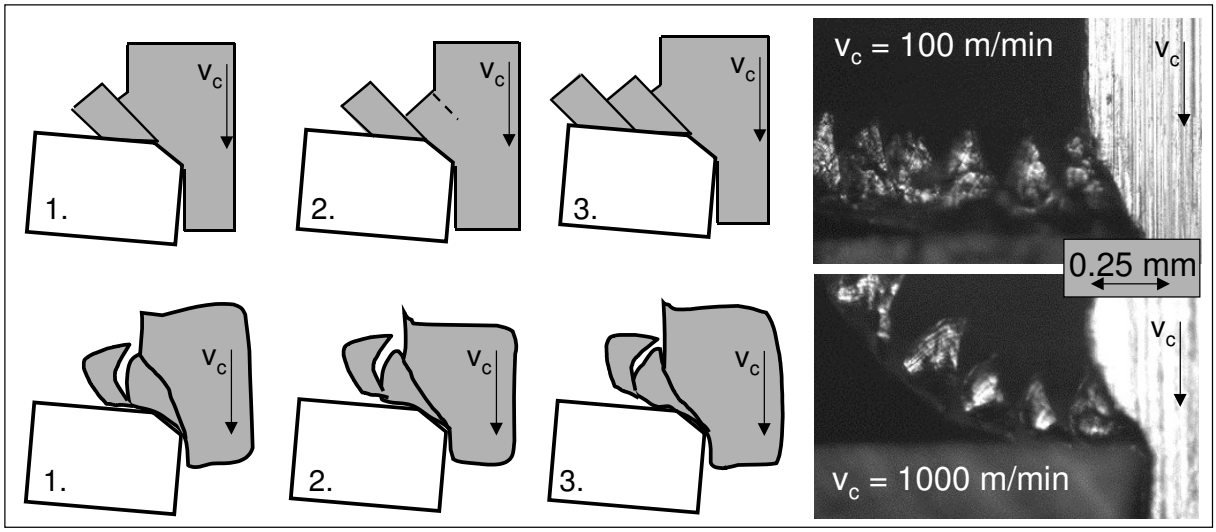


Figure 5.52: Influence of shear zone shape on cutting speed and chip radius

5.9.3 Length of the contact zone

The importance of the length of the contact zone and the overview about setups in the past were described earlier. The current in-situ setup allows to take the length of the contact zone directly from the pictures. For aluminum it is found that the length of the contact zone decreases if the cutting speed rises, **figure 5.53**.

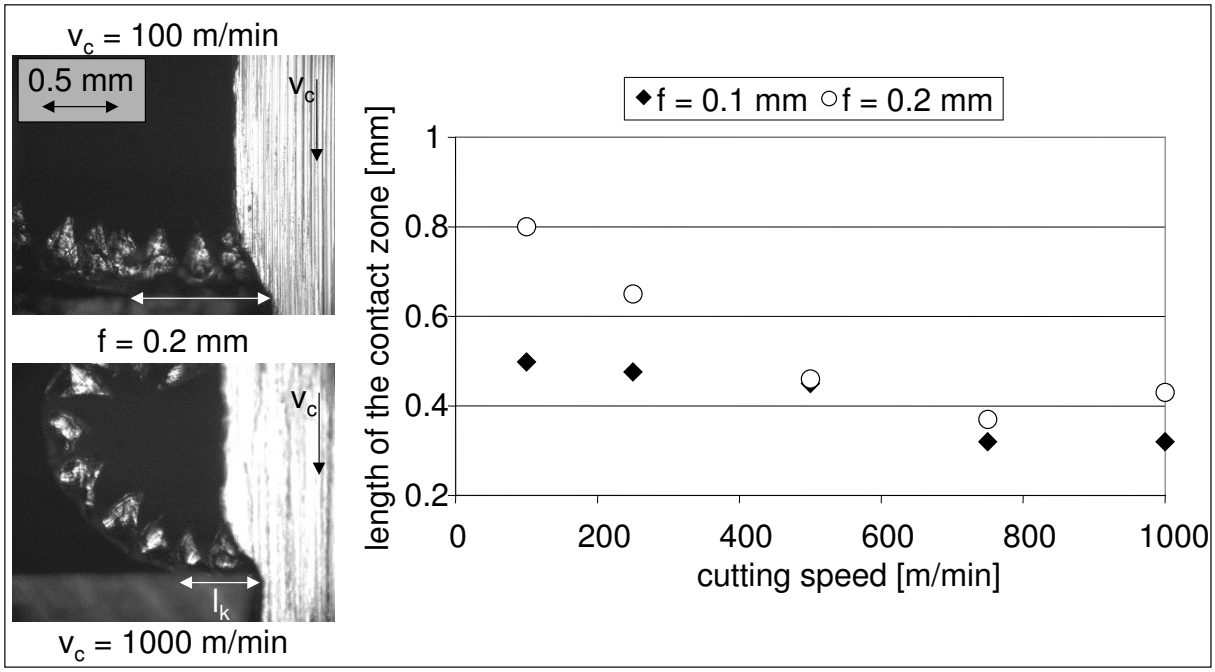


Figure 5.53: Length of the contact zone in cutting AA 7075 for different feeds and cutting speeds (a_p = 2 mm)

This is due to the change of the chip radius. The measurement results for steel show a strong chatter (**figure 5.54**). This is because of the lack of information about whether the chip contacts the uncut area of the workpiece or not. Figure 5.54 shows the length of the contact zone as well as a possible scatter reason. If the chip hits the workpiece it is bend and as a result the chip radius as well as the length of the contact zone increase. At a critical value for bending the chip breaks and the unbroken part of the chip bends strongly until it hits the workpiece again. This leads to a decrease of the chip radius as well as the length of the contact zone. The measured length of the contact zone is not comparable to the measurement results that were obtained by the SEM pictures of the inserts in the external turning operation. The reason is that the contact of tool and chip can be divided into two parts /ZORE66/. In the first one, the secondary shear zone, an intensive tool – chip contact is found. This creates the strong shearing of the bottom of the chip and causes the high temperatures on the rake face. The second part is of elastic nature. No shearing takes place and the contact conditions can be described by the friction law by Coulomb. Only this second area is affected by the bending of the chip and is assumed to be small compared to the zone of intensive shear.

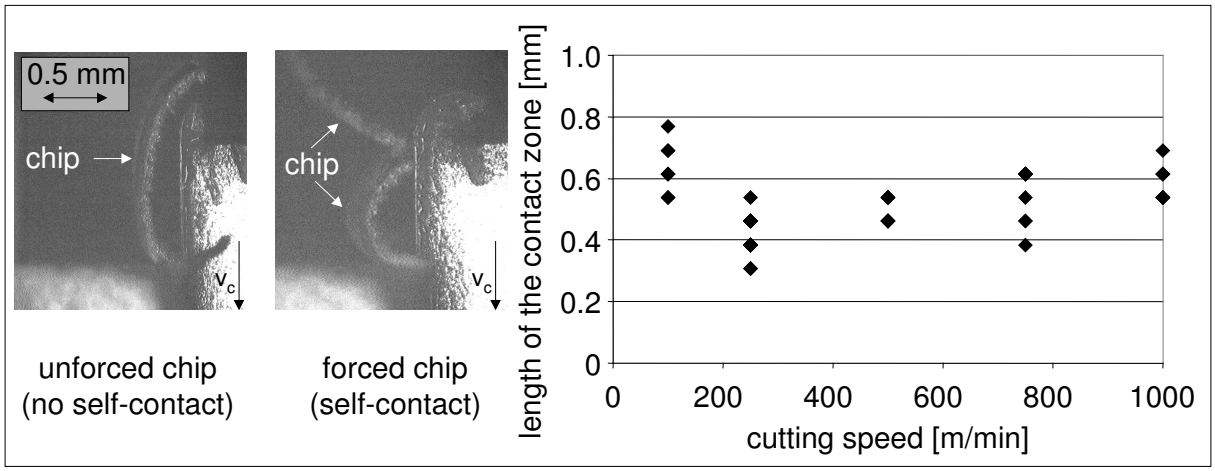


Figure 5.54: Length of the contact zone AISI 1045 and the forced ship as a possible error source (f = 0.1 mm, a_p = 2 mm)

5.9.4 Chip velocity

Several pieces of information can be obtained from the in-situ photography. Compared to chip root experiments, one advantage of the setup is the free to choose

state of chip formation that is photographed. The time difference between the two photographs can be chosen to take a picture of the compression and shearing of one lamellae, **figure 5.55**. Additionally the time interval that is needed to create one lamellae is determined. For the aluminum alloy AA 7075, figure 5.55 shows the mean time to create one lamella. Of course the process parameters such as feed and cutting velocity have a strong influence. As expected, an increase of the cutting speed leads to a decrease of the time difference because of the rise in chip velocity.

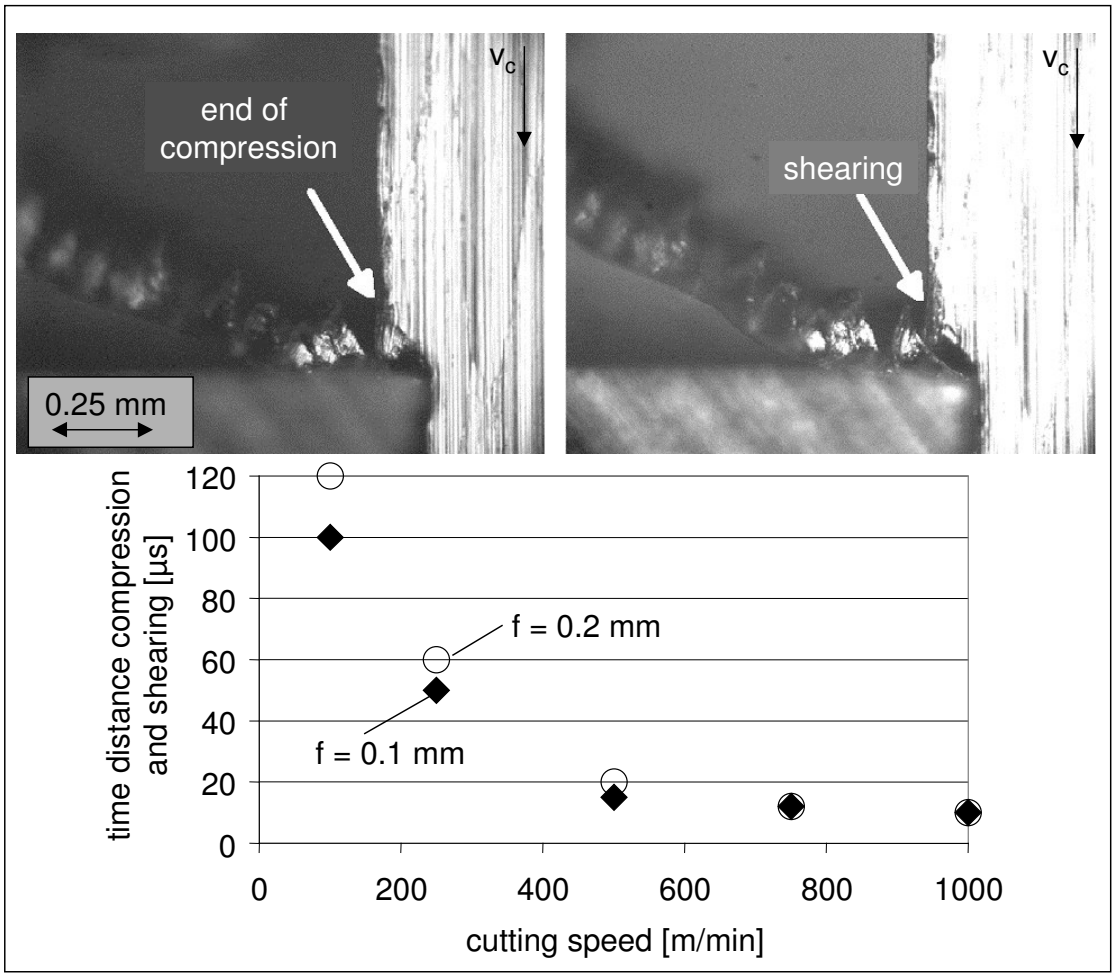


Figure 5.55: Dependency of the time between compression and shearing of a lamella depending on the cutting speed and feed (AA 7075)

Figure 5.56 shows the chip velocity at different distances from the cutting edge. The velocity of the chip is monitored in **figure 5.57**.

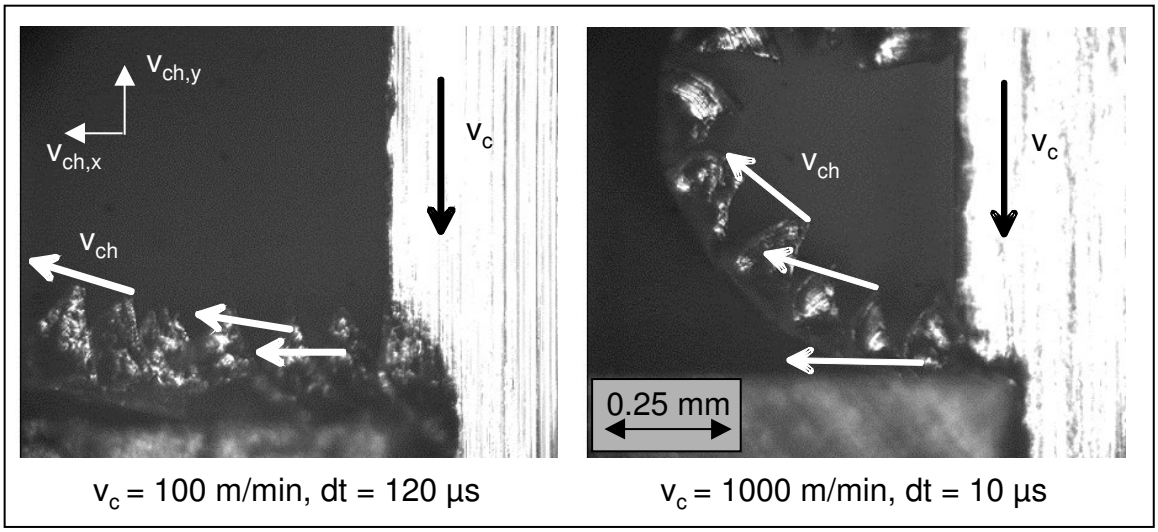


Figure 5.56: Dependency of chip velocity on cutting speeds (AA 7075, f = 0.2 mm, a_p = 2 mm)

Because of the mean chip thickness being higher than the uncut chip thickness, the chip velocity v_{ch} is always lower than the cutting speed. At low cutting speeds, the chip radius is large and therefore the value of the chip velocity ($v_{ch,y}$) in y-direction is low. This is not surprising in the area of the contact zone but even at a distance of the contact zone the velocity in y-direction can be neglected. At higher cutting speeds and the resulting lower chip radius the chip velocity in y-direction near and far from the contact zone becomes significant. **Figure 5.58** shows the dependency of the chip flow direction on the cutting speed for AISI 1045.

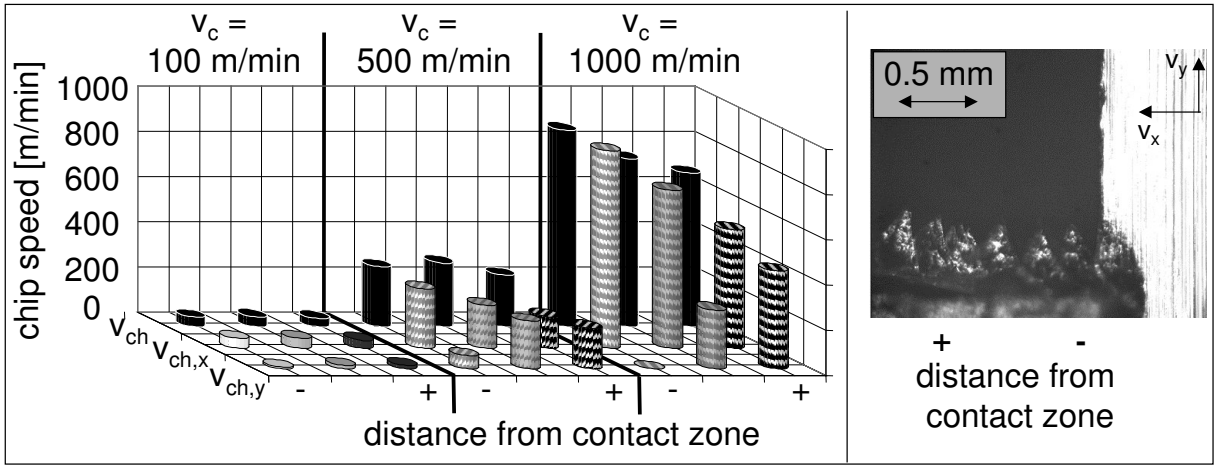


Figure 5.57: Dependency of x- and y-components on the chip speed on cutting speed v_c and position (AA 7075, f = 0.2 mm, a_p = 2 mm)

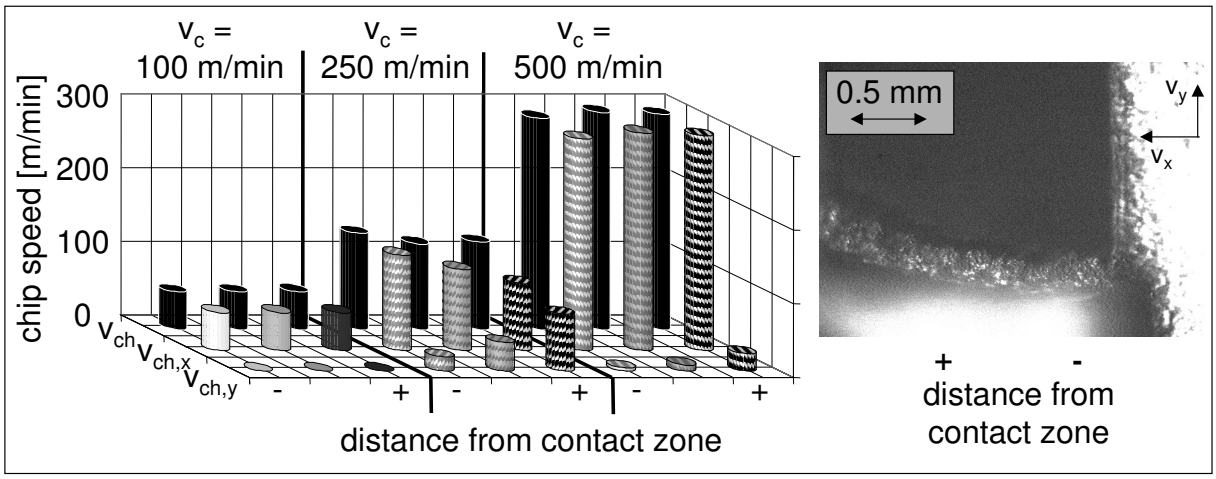


Figure 5.58: Dependency of x- and y-components on the chip speed on cutting speed v_c and position (AISI 1045, f = 0.1 mm, a_p = 1 mm)

It is similar to the results for aluminum. The higher chip radius of steel compared to aluminum leads to higher values of $v_{ch,x}$ and low values of $v_{ch,y}$. For aluminum the measured chip velocity of v_{ch} = 20 m/min is only 20% at a cutting speed of v_c = 100 m/min. At v_c = 500 m/min it is about 50% and more than 80% at v_c = 1000 m/min. These findings, especially at low cutting speeds, cannot be reasoned by change of the chip thickness as this decrease is too low. Even the flow of chip material in the direction of the depth of cut is not sufficient. At low cutting speed the chip width is about 30% higher than the depth of cut (compare figure 5.23). Consequently, the measured chip velocity is not constant as assumed in figure 5.57 and 5.58. In cutting aluminum at v_c = 100 m/min at a feed of f = 0.2 mm segmented chip formation is found (figure 5.48). The two pictures are taken in different stages of the compressing-shearing procedure. Therefore, the in-situ results can give an idea of the maximum and minimum chip velocities in segmented chip formation. But, as a consequence, the results also show that the chip speed calculated by measuring the chip thickness of chip roots or collected chips is only a rough assumption. If the variable chip speed becomes significant for the performance of the process, e.g. the chip removal in drilling, the examination of the collected chips may not be sufficient.

5.10 Tool wear

To describe the influence of tool wear on the cutting process and to find optimized process parameters, the mechanism of wear has to be understood. In metal cutting, four basic mechanisms of tool wear, namely abrasion, adhesion, diffusion and oxidation can be identified. A detailed description of these mechanisms and existing analogous processes are given by Gerschwiler /GERS98/.

Abrasion is found when the tool is scratched by hard particles of the workpiece. Results of pin-on-disk test show that the resistance of a solid to abrasion is proportional to its hardness /ARCH53/. A rise in temperature changes the hardness of both the workpiece and the tool material. Consequently, abrasive wear strongly depends on the temperature. Abrasive tool wear is the main cause for the flank wear of the major and minor cutting edge of the tool. The flank wear results in a flattening of the cutting edge, the effective clearance angle is reduced and the contact area of the flank face increases. This leads to rising resultant forces and temperatures. Moreover, the changed tool geometry at the minor cutting edge leads to a modified cutting process that may result in a lower quality of the machined surface. Typical phenomena are the increased surface roughness, a deformation of the workpiece of the rim zone accompanied by the change of residual stresses in that area and even changes of the microstructure by the increased temperature generation because of the tool wear. An example is the occurrence of a martensitic white layer on the machined surface /LIER97/.

To quantify the abrasive resistance of a tool material, several setups have been developed /GERS98/. For example a scratch test or a modified ball indenture test can be used. In the modified ball indenture setup a steel ball, rotating in a grinding paste with defined diamond grit size, grinds an indentation in the tool surface. The depth of indentation and the size of the indentation diameter after a specified grinding time can be used to compare the abrasive resistance of different tool materials. A disadvantage of this setup is its analogue character. Neither the combination of materials, nor the cinematic of a cutting process with defined cutting edge are realized in the modified ball indentation test. Therefore, the obtained results cannot be compared to the cutting process. In the past, several test setups were developed to overcome this problem. However, if the similarity of the analogous and real

process is high it becomes hard to model only one wear mechanism. An example of an analogous setup where the differences to the cutting process are low is the pin-on-disc test, described in chapter 3. If the pressures and relative velocities as they occur in cutting operations at the rake face are applied to the pin-on-disc test a superposition of abrasive and adhesive mechanisms is found.

The adhesive wear mechanism cannot be as easily described as the abrasive one. The first stage of adhesive wear is a mechanical clamping of workpiece material onto the tool. The clamping mechanism depends on the material combination and may consist of mechanical clamping of the soft material in the tool asperity, chemical and intermetallic bonding or diffusion processes. In the second stage, the adhesions lead to a change of tool geometry which spoils the surface quality. Moreover, increased cutting forces are obtained, resulting in a change of the stress distribution in the tool. This leads to microfractures in the tool surface as the bonding of the adhesion on the tool is often stronger than within the inhomogeneous tool. Because of these microcracks, small particles consisting of workpiece and tool material are separated from the tool. They act like grinding grids when they slide over the flank and rake face. Therefore, the adhesive wear attack results in an abrasive one. An eye striking example of adhesive wear in cutting operation is the build up edge mechanism /WARN73/. Here the adhesions create a “new” effective cutting edge. This edge is not stable and hard particles (in this case mainly strain hardened workpiece material) travel over rake and flank face and lead to an increased flank wear and surface roughness.

A prerequisite for the abrasive wear attack is the presence of hard particles in the workpiece or as a result of adhesive processes. For adhesive processes the described bonding mechanisms have to be effective. At low cutting temperatures these two wear mechanisms dominate the performance of a tool. At higher cutting temperatures, thermally driven wear mechanisms such as diffusion and oxidation become dominant /MOUF98, MOLI02/. Diffusion of tool material into the workpiece or chip is found in areas with a very high temperature and no atmosphere or lubrication between tool and workpiece. These mechanisms weaken the tool material by reducing the bonding which leads to an increased crater wear.

Oxidation requires high temperatures as well as an atmosphere containing oxygen. Two different types of oxidation lead to increased tool wear. On the one hand the

oxidation of tool material results in a reduced toughness of the tool material and therefore in lower abrasive wear resistance. On the other hand the oxidation of workpiece material in the areas where the cutting tool and the workpiece are just separated leads to hard oxide layers on the workpiece. These layers cause abrasive wear. The most obvious result of an oxidation wear attack on the tool is the notch wear. These notches are found at the minor and major cutting edge in that area where the tool-chip contact ends. Oxidation of the tool material as well as the abrasion by hard oxide layers on the workpiece are the main reasons for notch wear /GERS98/.

Further mechanisms such as the alternating mechanical and thermal load in interrupted cutting and when coolants are used will not be further described as they do not occur in the dry continuous external turning operations. Their influence on the results of the in-situ experiments (setup 1 and 2) is minimized by the low length of cut and a frequently change of tools.

In the experiments it was found that the tool wear mainly depends on the machined workpiece material. The influence of the cutting parameters is lower. Turning AA 7075 up to cutting speeds of v_c = 10000 m/min using uncoated cemented carbide does not result in significant tool wear. The maximum cutting speed is only limited by the machine tool. Even an increase of feed and depth of cut shows no significant influence on the tool. The resulting tool inserts after turning aluminum were already shown in figure 5.30.

To reduce the influence of the flank wear on the obtained results, a new cutting tool has been used for every single cutting test. Analyzing the cutting tool, no flank wear could be determined. Admittedly, at the flank and rake face of the tool severe adhesion of workpiece material at high cutting speeds could be found. This may be caused by the rough surface of the carbide tool (compare table 5.2) and can be reduced if a smoother tool or a coating is applied. For this tool a remarkable correlation of cutting speed and adhesion at the flank face is determined, which may be caused by the change in material properties at high cutting speeds. However, no increase of the resultant force during the cutting time was found in the measurement plots. Therefore, the adhesions seem to have no influence on the cutting process. The tool wear is low because the aluminum alloy AA 7075 does not contain hard

inclusions and the present adhesions do not lead to micro-cracks in the tool. Moreover, the cutting temperatures in turning aluminum are too low to result in severe diffusion or oxidation wear (compare figure 5.14).

For turning AISI 1045 steel up to $v_c = 6000$ m/min, highly wear resistant cutting materials are needed. As the cutting temperatures are very high at elevated cutting speeds, cemented carbide tools show plastic deformations. Therefore, a SiC-whisker reinforced aluminum oxide ceramic was used. Beside the good resistance against abrasive wear, the aluminum oxide shows a low tendency to diffusion and oxidation. This and the low roughness of the tool surface (compare table 5.2) prevent severe adhesion. The mean and maximum flank wear at different length of cut obtained by using a microscope can be taken from **figure 5.59**.

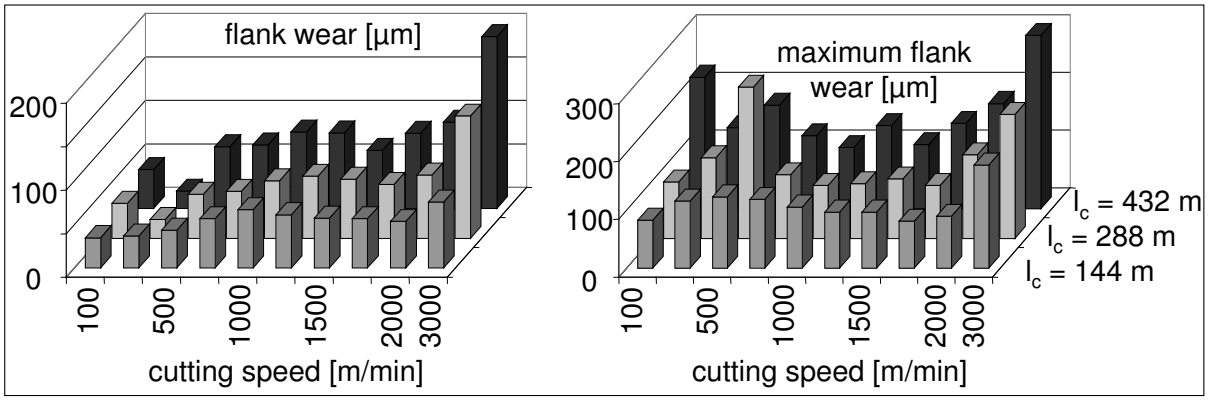


Figure 5.59: Flank wear of major cutting edge at different lengths of cutting distance (AISI 1045, f = 0.1 mm, a_p = 1 mm)

For a distance of cut of $l_c = 144$ m an increase of mean flank wear up to a cutting speed of $v_c = 1000$ m/min is followed by a slight decrease in the range of $v_c = 1250$ m/min up to $v_c = 2000$ m/min. At cutting speeds beyond $v_c = 2000$ m/min the tool wear increases. At higher values for the length of cut ($l_c = 288$ m and $l_c = 432$ m) the decrease is still present but not as obvious. When, examining the tool in the SEM, the results of figure 5.59 are supported (**figure 5.60**). The wear of the ceramic insert shows low deviations and a maximum at the minor cutting edge. A significant notch wear at the major cutting edge can be found. Furthermore, material is adhered on the rake face of the tool.

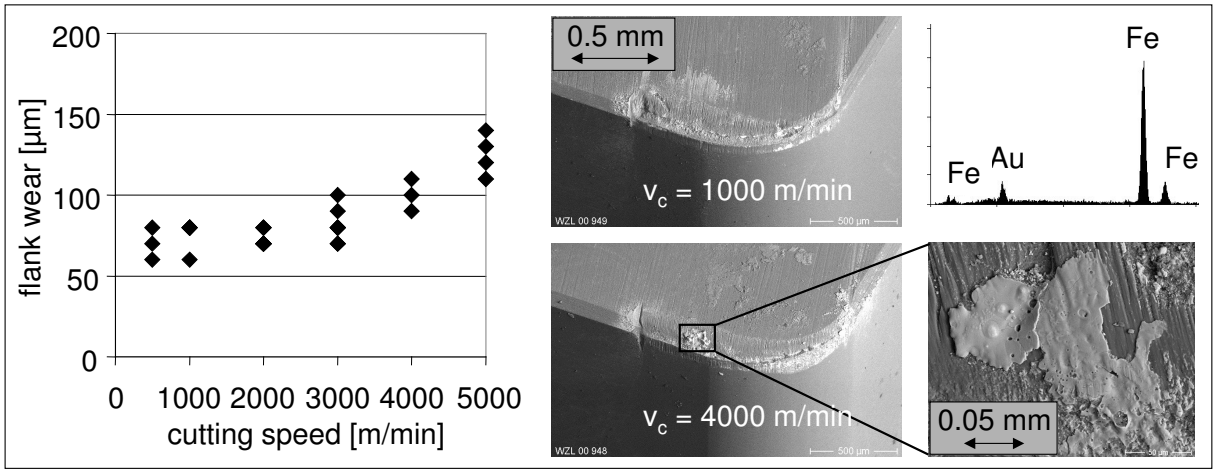


Figure 5.60: Flank wear at the major cutting edge and SEM pictures of worn inserts (AISI 1045, l_c = 144 m, f = 0.1 mm, a_p = 1 mm)

The magnification shows the typical spherical structures of molten metal. The energy dispersive X-ray analysis (EDX) assures that this material is similar to that of the workpiece. The presence of gold on the surface is caused by the preparation of the insert before it is put into the SEM. Increasing the cutting speed up to v_c = 5000 m/min the tool wear increases steadily, figure 5.60. The significant notch wear and the molten workpiece material at the rake face give a hint that the tool performance at high cutting speed strongly depends on the temperature. Comparing the diagrams of tool wear (figure 5.59) and workpiece temperature below the cutting edge (figure 5.17) it is obvious that the increase of tool wear up to v_c = 1000 m/min is accompanied by an increase of the workpiece temperature. In the range of v_c = 1000 m/min up to v_c = 2000 m/min the workpiece temperatures are nearly constant and show a strong increase for higher cutting speeds (figure 5.17). The correlation of temperature and tool wear suggests a thermal cause for the flank wear that becomes obvious for the maximum flank or notch wear. Compared to steel (figure 5.59 and 5.60), the tool wear in machining the titanium alloy Ti6Al4V is much higher. Even at values for cutting speeds one to two magnitudes lower than for steel this is valid, **figure 5.61**.

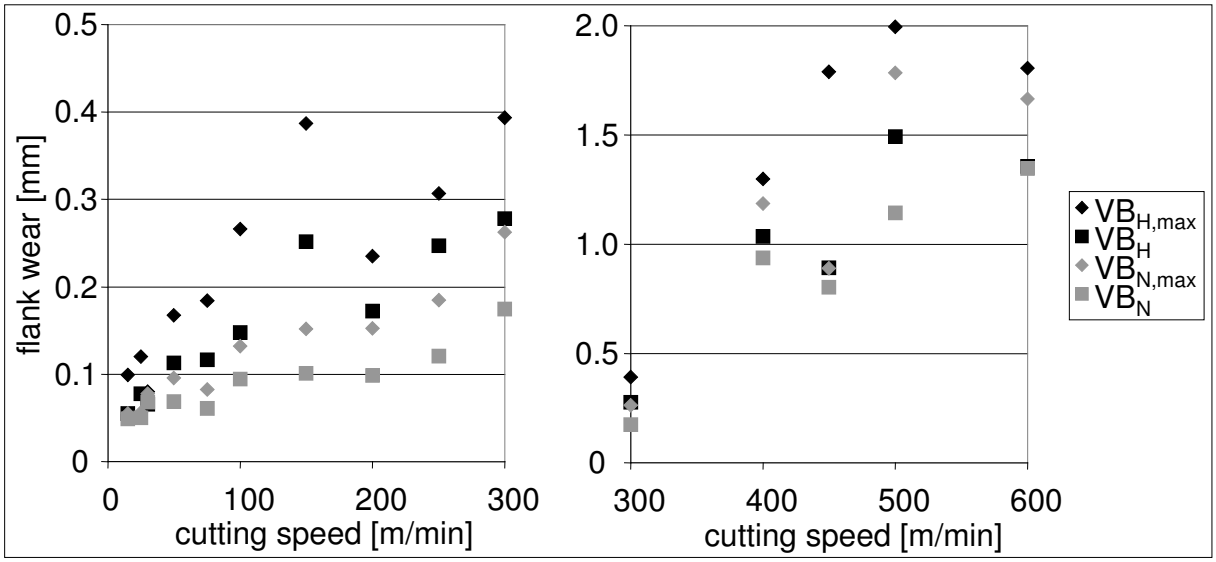


Figure 5.61: Flank wear dependency on cutting speed (Ti6Al4V, l_c = 62 m, f = 0.1 mm, a_p = 1 mm)

Using the same tool as for machining AISI 1045, the tool wear is quite different. At a cutting speed of v_c = 15 m/min after a length of cut of l_c = 5.6 m the start of crater wear on the rake face becomes visible, **figure 5.62**. At v_c = 100 m/min severe flank, notch and crater wear is found at the major cutting edge. Some workpiece material is sticking in the area of the crater wear. The maximum cutting speed with an acceptable value of flank wear of VB = 200 µm at a length of cut of l_c = 62 m is about v_c = 200 m/min.

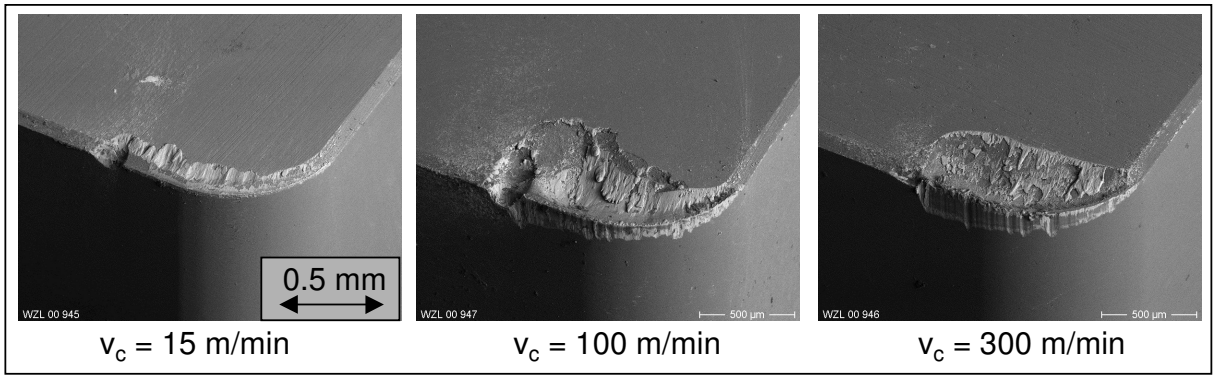


Figure 5.62: SEM pictures of worn inserts (Ti6Al4V, l_c = 62 m, f = 0.1 mm, a_p = 1 mm)

At cutting speeds higher than v_c = 300 m/min the wear is one magnitude higher and we are not longer talking about flank wear but tool breakage. All of the four wear mechanisms are active in external turning Ti6Al4V. The crater wear can be explained

by the very high chip temperatures (figure 5.14) and an affinity of titanium to the SiC-whisker of the tool. To prevent the latter a cubic boron nitride tool with the same geometry as the aluminum oxide tool was applied. This lead to a significant increase of tool life. At a cutting speed of v_c = 400 m/min a mean flank wear of VB = 140 µm was measured after a length of cut of l_c = 40 m. Especially the notch wear was lower than for the ceramic tool. As a consequence, the higher tool life enabled to increase the cutting speed range where resultant forces without any tool wear influence can be measured up to v_c = 1500 m/min (figure 5.6). The higher red hardness and chemical stability of the boron nitride tool are the cause for the higher tool life. Especially in dry cutting operations it may be an economical alternative to cemented carbide or ceramic.

5.11 Surface quality

The surface roughness of the workpiece after a turning operation can be approximated by the kinematic roughness R_{kin}, equation 5.3. High values for feed lead to an increase of surface roughness while it can be reduced by the increase of the nose radius of the tool. This relationship is used in actual wiper geometries where the high nose radius allows to obtain smooth surfaces even at high values for feed.

$$R_{kin} = \frac{f^2}{8 r_\varepsilon} \qquad \text{(eq. 5.3)}$$

Especially for low values of feed and nose radius the roughness of the tool tip, and here mainly that of the minor cutting edge, gains significance. Examining the obtained surfaces from turning AISI 1045 steel perpendicular to the cutting speed (**figure 5.63** bottom left) the strong influence of the feed strikes to the eye. The distance between two peaks is equal to the feed (f = 0.2 mm) and the application of equation 5.3 results in a kinematic roughness of R_{kin} = 6.25 mm. This value is close to the measured mean roughness R_z for cutting speeds below v_c = 3000 m/min, figure 5.63.

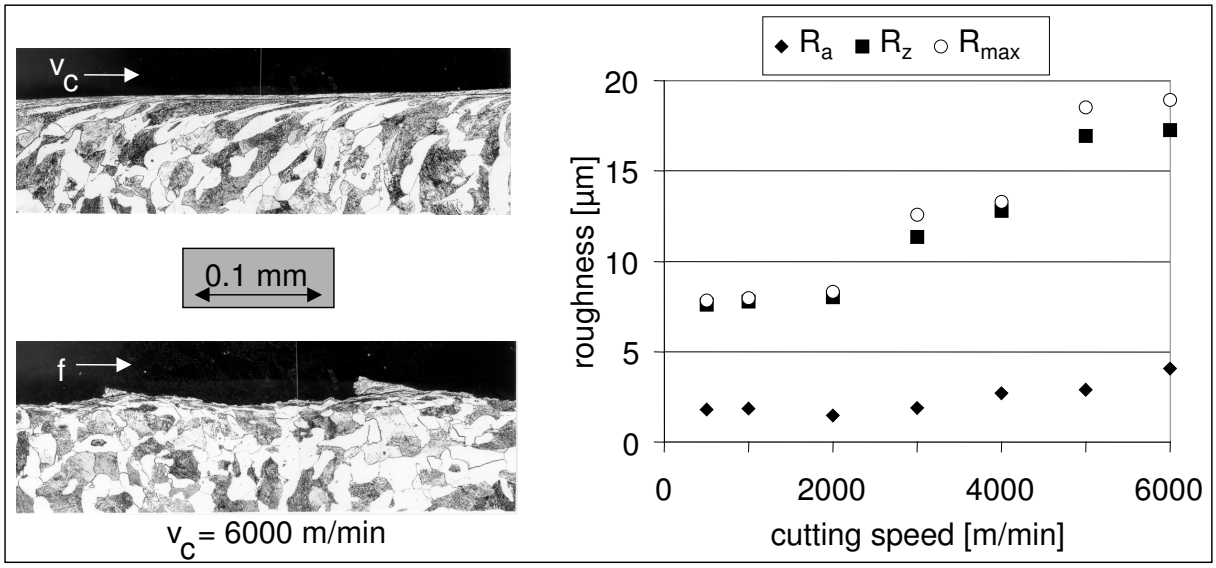


Figure 5.63: Micrographs of the workpiece rim zone and measured surface roughness vs. cutting speeds (AISI 1045, f = 0.2 mm, a_p = 1 mm)

For lower cutting speeds Plöger found a decrease of roughness in the area of v_c = 50 m/min up to v_c = 750 m/min. The cutting conditions, tool and workpiece material of Plöger were similar to those of the current work. Consequently, both examinations lead to similar results in the range of v_c = 1000 m/min and v_c = 3000 m/min /PLÖG02/. At a cutting speed of v_c = 3000 m/min the measured roughness values show a strong increase. Keeping the dependency of the tool wear in mind (figure 5.59 and 5.60) the higher flank wear may be a reason for this phenomenon. The tool wear increases the roughness of the minor cutting edge. As this edge creates the machined surface its roughness increases, too. Furthermore, the micrographs of the workpiece rim zones at cutting speeds higher than v_c = 2000 m/min show a significant difference from those at low speeds. The peaks are not as regular shaped. The material seems to be bend and thrown up to the direction opposite to the feed, **figure 5.64**. This results in a visible rise of the roughness and can be explained as follows. The workpiece material at cutting speeds higher than v_c = 2000 m/min shows an increased temperature as can be taken from figure 5.17. This leads to a thermal weakening and a stronger plastic flow of the workpiece material in the direction opposite to the feed. Here the material is not supported by the bulk material, **figure 5.65**. Furthermore, the deformation of the workpiece rim zone in cutting speed direction is higher in that range of cutting speed

(figure 5.64) which means that the thickness of the tertiary shear zone increases when the cutting speed rises.

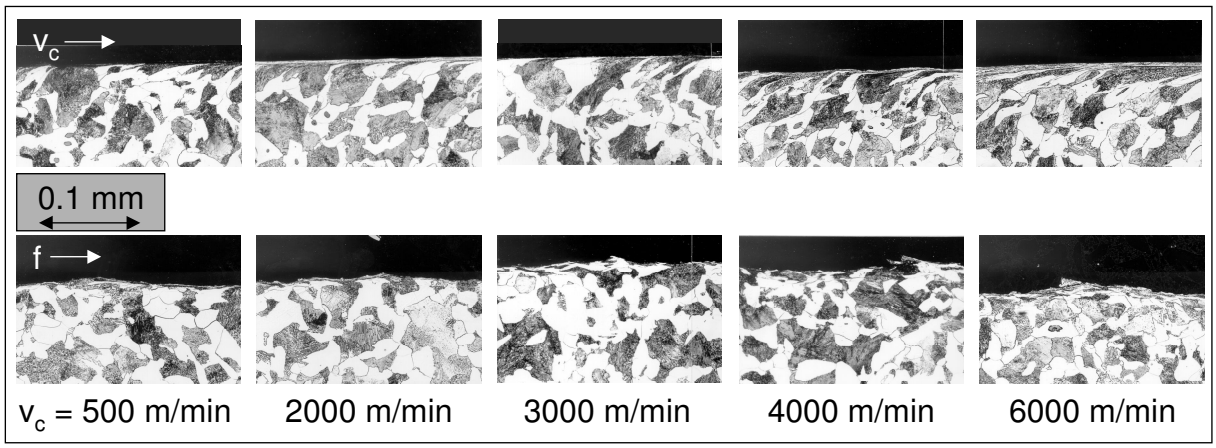


Figure 5.64: Micrographs of the workpiece rim zone at different cutting speeds (AISI 1045, f = 0.2 mm, a_p = 1 mm)

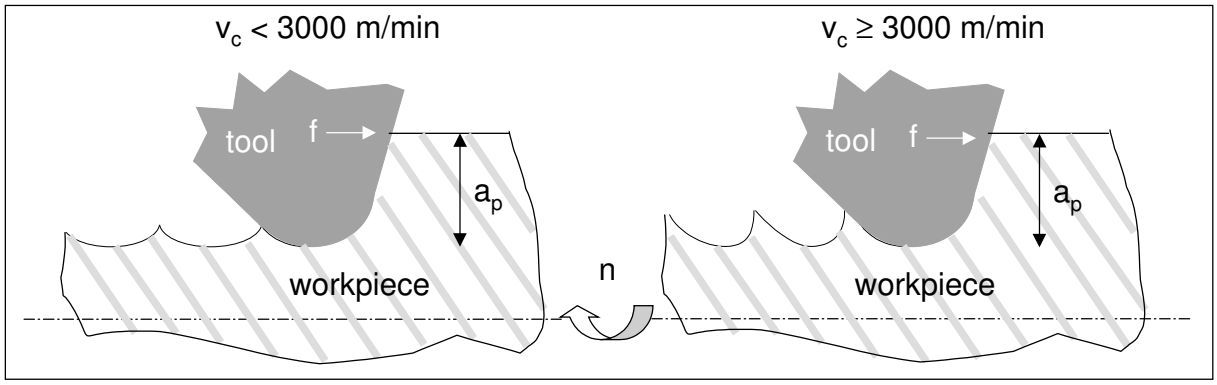


Figure 5.65: Sketch of the cause for the deformation of the roughness peaks

This influences the residual stresses in the workpiece. In his experiments Plöger found that the tensile residual stresses increase in and perpendicular to the cutting direction /TÖNS01, PLÖG02a/. He states that high temperatures and high temperatures gradients lead to a more extended tensile stress affected zone. The latter rises from about 5 µm at a cutting speed of v_c = 150 m/min up to 15 to 30 µm at a cutting speed of v_c = 3000 m/min.

6 Conclusions from experimental results

In the following the experimental results in cutting AISI 1045 steel in a wide range of cutting speed are interpreted. The results of machining aluminum (AlZnMgCu1,5) and titanium (TiAl6V4) are taken to differ between general mechanisms in metal machining and material dependent behavior. Furthermore, some information taken from literature are shortly described to complete the understanding of the results obtained from the experiments.

6.1 Chip formation

Cutting AISI1045 in an external turning operation, the formation of a continuous or segmented chip depends on the cutting speed and the feed. Furthermore, the diameter of the machined part and the heat treatment of the workpiece material influence the chip formation /SCHU01/. For example turning a bar with a diameter less than 50 mm shows segmented chip formation, while continuous chip formation occurs for internal turning /OKOS67/. At low cutting speeds the continuous chip formation dominates. As the chip is created by the major and minor cutting edge chip width as well as uncut chip thickness are not constant. This leads to different cutting conditions and subsequently the chip shows a structure with both, continuous and segmented chip areas. Latter may be prevented by the examination of an orthogonal cutting process, where only the major cutting edge is in contact with the workpiece. Admittedly, it has to be noted that for the range of cutting conditions examined in this investigation no ideally continuous chip is formed even in the orthogonal cutting tests. In external cutting at low cutting speeds the chips created by the tool nose radius and the minor cutting edge show a continuous structure. The workpiece material is sheared continuously in the primary shear zone and the contact of the tool with the chip and freshly generated surface creates the secondary and tertiary shear zone. At higher cutting speeds the chip formation turns from continuous to discontinuous. The segmented chip formation is characterized by alternating compression – shearing mechanisms. During the compression stage no shearing occurs and consequently, no primary shear zone exists. This leads to the conclusion that the chip formation models existing in literature are not accurate enough to describe the mechanism of segmented chip formation. As a result, the resultant forces that are calculated based on the assumption of a steady shearing operation will not provide accurate data.

Subsequently, the current work does not give a detailed description of these models. Furthermore, if the chip formation process is photographed by in-situ photography some kind of gap propagating from the free chip surface to the cutting edge can be found. As the local and time resolution of the in-situ setup is too low to determine the beginning and end of the shearing process it cannot be indicated whether or not a crack at the free chip surface is the cause for segmented chip formation. However, in the photographs no crack at the bottom of the chip near the cutting edge was found which is in contrast to the findings by different authors /SPAA71, WARN73, USUI76, FORM70/ at low cutting speeds. This indicates that the cutting speed has an influence on the chip formation as well as on the failure mechanisms of the chip.

As the height of the lamellae in segmented chip formation is regular, a mean chip thickness can be taken from the photographs of the chips. It is found that for all examined materials the mean chip thickness decreases as the cutting speed rises. This decrease takes place in continuous as well as in segmented chip formation. At a material dependent cutting speed the decrease approaches a constant value. The decrease of the chip thickness coincides with a strong increase of cutting temperatures and a reduction of the resultant forces. They show a rise at high cutting speeds, while the cutting temperatures and the chip thickness do not change significantly. Furthermore, the length of the contact zone as well as the chip radius decrease at higher cutting velocities. Because of these findings, the following theory of chip formation for a wide range of cutting speed is proposed.

6.1.1 Theory of chip formation at low and high cutting speeds

At conventional cutting speeds the chip temperature is low and the chip is formed by shearing. Here, the narrow area of the primary shear zone is strongly deformed. This leads to an increase of the material strength in the primary shear zone because of strain hardening. This again results in shearing of the material beside the primary shear zone and therefore a continuous shearing is obtained. In the secondary and the tertiary shear zones the material in front of the tool tip is sheared because of the speed gradient between the tool surface and the chip or workpiece surface, respectively. The low cutting temperatures lead to a comparably thick secondary shear zone. The tertiary shear zone strongly depends on the sharpness of the cutting

edge and is thin if the original tool geometry is still present. This is the case at comparably low cutting speeds with low tool wear.

An increase of the cutting speed leads to segmented chip formation. The shearing process is no longer stable, because the strain hardening of the material is overcompensated by the thermal material softening. The chip formation is defined by a fast but low compression of the chip material that will be the lamella. This stage is followed by a fast shearing process. The compression phase starts again during the shearing process. The assumption that the compression or deformation of the lamella is low can be derived from the examined chips. The lamella width is not much larger than the uncut chip thickness. The higher temperatures do not only lead to a modification of chip formation. The increased temperature is also found in the secondary shear zone. The result is soft material with a lower resistance against forming. This material can stand high values of strain and therefore the secondary shear zone is thinner at high cutting speeds. The phenomenon of lower chip thickness by increasing the cutting speed can also be explained by the temperature influence. As this decrease seems not to depend on the chip formation mechanism it is obvious that only the higher temperature and thus the lower resistance against forming causes a lower compression and results in the lower chip thickness. The cutting speed also influences the radius of the chip and as a result the length of the contact zone. As described above, the shape of the primary shear zone changes from straight to curved.

It was observed that the cutting speed has a strong influence on the chip formation, chip thickness, chip radius and length of the contact zone. Furthermore, the temperature seems to play the major role in this change. But how do these changes in chip formation influence the other criteria of machinability such as resultant forces, tool wear and surface quality? This question will be answered in the following chapters.

6.2 Resultant forces

Regarding the results of the resultant force measurements, three stages can be identified. First of all, the well known decrease of resultant forces as the cutting velocity increases. In this range of cutting speed, the chip formation changes from continuous to segmented. However, no signal in the force plot indicates the

beginning or influence of this change. Therefore, it can be concluded that the influence of the chip formation on the resultant force is negligible, or in other words the mechanisms that lead to the resultant force decrease are similar in continuous and segmented chip formation. One indication is the continuous increase of chip temperature in or near the secondary shear zone. Since the decrease of resultant forces is not influenced by the change of chip formation, this is also valid for the measured temperature. Even the shape of the secondary shear zone in the chip is not highly affected by this change. The only measurable difference is a decrease of the secondary shear zone thickness. This can be explained by the lower flow stress of the material at elevated temperatures. So, why do the resultant forces decrease? One part of the answer was already given above. The increase in chip temperature at higher cutting speeds leads to material softening and thus a lower compression of the chip. On the other hand, the increased temperature in the tool – chip interface leads to modified friction conditions. The secondary shear zone is created by shearing mechanism in the chip that are caused by the friction between tool and chip. A rise of temperature in the tool-chip contact zone reduces the friction as well as the resistance of the chip material against shearing. A reduction of friction and resistance against shearing will mainly lead to a decrease of the feed force component. In fact, the feed force decrease stronger in the range where the chip temperatures rises is significant ($v_c < 1000$ m/min in figure 5.14). This is not the fact for the cutting and passive forces (compare $v_c < 500$ m/min in figure 5.3). The softening of the workpiece material in the primary shear zone will primarily affect the cutting force. Since the resultant force components decrease when the cutting speed is increased, it is obvious that both mechanisms have a strong influence.

A cutting force minimum is found at elevated cutting speeds. In this range of cutting velocity, no significant increase of chip temperature is found (figure 5.14). This may be surprising, as the power consumed by the process is approximately equal to the result cutting force multiplied by the cutting speed, as will be shown in chapter 6.3. In this range of cutting speeds nearly all important values in cutting remain constant. The chip formation (figure 5.18), chip thickness (figure 5.28), and length of the contact zone (figure 5.29) do not change and even the tool wear is stagnating (figure 5.59). Furthermore, a constantly low roughness of the workpiece is found (figure 5.63). The only explanation for this stable equilibrium is that a new factor

becomes significant and compensates the continuously increasing cutting power. Regarding the flow stress curves described in chapter 2, it is obvious that the strain rate sensitivity of the material is this factor (figure 2.7). In the range of $d\varepsilon/dt = 10^3$ the strain rate starts to cause a significant increase of the flow stress. However, the thermal softening can compensate the strain rate sensitivity so that the resulting forces and also the chip formation and surface quality remain constant.

In the resultant force measurements, a third stage can be identified at very high cutting speeds. In this area ($v_c > 3000$ m/min) resultant forces rise up to values that are measured at low cutting speeds. This increase can also be described by the material behavior under the extreme conditions in (high speed) cutting. The strain rate increases steadily with the cutting speed. Very high values for strain rate are achieved in the shear bands if segmented chip formation occurs. But even the lamellae in the segmented chip formation are compressed so fast, that the strain rate sensitivity is highly relevant. At the same time, the temperature shows no further increase. This is because a material dependent limit, the melting temperature of the workpiece material, is reached in the secondary shear zone. Also the influence of strain hardening is low. The maximum increase of flow stress due to strain hardening is found at strains up to $\varepsilon = 0.1$ (compare figure 2.8). This value is reached in every part of the chip even at low cutting speeds. It therefore has no influence on the resultant forces at high cutting speeds.

Moreover, it is found that mechanisms that cause instabilities gain significance. Examples are adiabatic shearing, melting of areas within chip and at the bottom of the chip. The remaining material, which is the low but fast deformed material of the lamella, has to carry the load. Because of the strain rate sensitivity, this material has a high strength. This strain rate sensitivity of the lamella leads to the increase of the resultant forces.

In several publications the described increase of resultant forces is not mentioned /TÖNS01, SAHM01, PLÖG02, BENA02/. This is surprising as the phenomenon was found by different authors and also for different workpiece materials, tool geometries and experimental setup /KUSN60, SUTT97, MOLI01, KLOC01a, KLOC02, GENT02/. This may have different reasons.

First of all, the resultant force minimum extends from $2000 < v_c < 4000$ m/min. Ben Amor /BENA02/ conducted experiments up to a cutting speed of $v_c = 4000$ m/min. At this speed the resultant forces are hardly different from those at $v_c = 3000$ m/min. This result, which is similar to that given in figure 5.4, led Ben Amor to the assumption, that the cutting forces approach a constant value at high cutting speeds. As a consequence, he based his definition of a high cutting speed (v_{HSC}) on this assumption.

Furthermore, the increase of resultant forces is more distinctive if the uncut chip thickness is higher than $h_c = 0.1$ mm (compare figure 5.3) and the forces are measured at the cutting tool. For example, the results of figure 5.4 and Ben Amor /BENA02/ are similar up to a cutting speed of $v_c = 4000$ m/min. It is likely that if he had increased the cutting speed and feed he would have found an increase of resultant forces, too. But regarding the fact that the application of high cutting speed has an industrial relevance only for finishing operations, the combination of comparable high cutting speed, feed and depth of cut was not of major interest in the past. This plausible reason led to the wrong assumption that the resultant forces remain constant at high cutting speeds.

A further reason might be the location of the resultant force measurement. The force should be measured on the tool side. If feed and depth of cut are low and the forces are measured on the workpiece, the increase of resultant forces hides within the dynamics of the process. This is the reason why the force increase is hardly found in high speed milling operations with workpiece sided force measurements and finishing conditions /SAHM01/. Additionally, the range of cutting speeds in which the forces, tool wear and roughness increase were up to now not relevant for practice applications.

The last reason is the simplest one. To obtain the increase in resultant forces in a turning operation, very high cutting speeds and considerable feed and depth of cut have to be realized. A disk with a diameter of 200 mm has to rotate at $n = 8000$ to 12000 min^{-1} to obtain cutting speeds above $v_c = 5000$ m/min. As these are values of an airplane turbine and the rotating mass is quite high it is obvious that machining under these conditions is not state of the art. Safety aspects and efforts to reduce the run out of the workpiece will limit the application.

Beside these aspects it is often argued that at such high cutting speeds effects gain significance that can be neglected in conventional machining. This is not the case in high speed machining. As the tool travels along at high cutting speed remarkable tool wear occurs in turning steel and titanium. To keep this influence out, all tests were conducted with new, sharp tools. Furthermore, only that range of the cutting force plot is evaluated that is not affected by the tool wear ("steady state" area in figure 5.2). And finally, the resultant forces in turning aluminum with no visible tool wear (compare figure 5.30) show an increase similar to that of steel (compare figure 5.3 and figure 5.5).

However, the fact that forces strongly increase with tool wear is of importance. Furthermore, a cutting tool is never perfectly sharp. In cutting with a round cutting edge workpiece material remaining static or moving only at very low speed can be found in front of the edge. An extreme example for this is the build-up edge (BUE) formation. This material sticks to the cutting edge, increasing the friction and pushing the tool out of the cut. In the case that the build-up edge does not create a positive rake angle it also leads to an increase of resultant forces. Within the range of cutting speed examined in this work build-up edge formation is not probable. However, the influences of the chamfer (CA) or roundness (HW) of the applied tools (compare table 5.2) as well as the tool wear are summarized in the commonly called parasitic force W, equations 6.1 and 6.2 /SPAA71/. **Figure 6.1** shows the area where the parasitic forces act if a chamfered tool is applied.

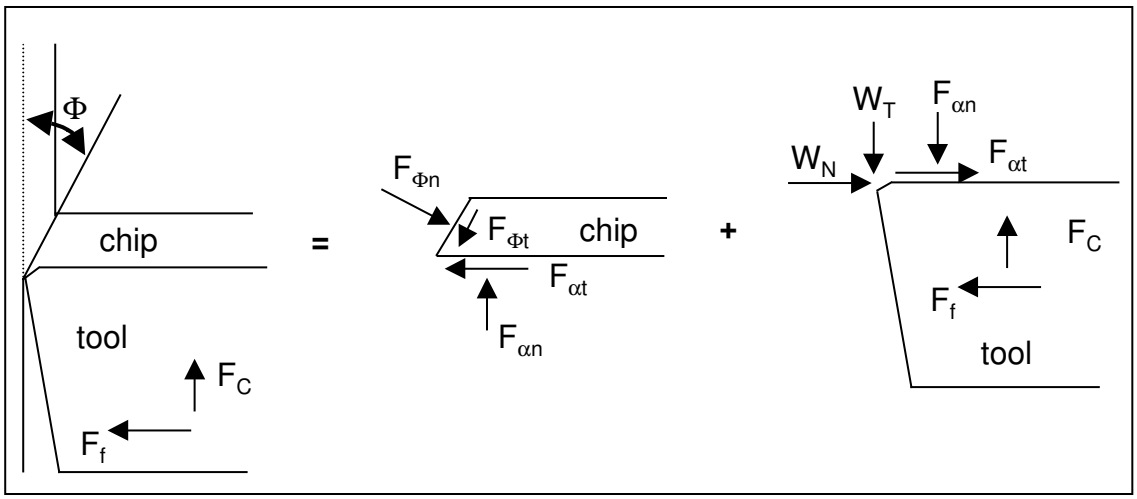


Figure 6.1: Principle of the parasitic forces in orthogonal cutting /SPAA71/

Therefore the measured cutting and feed forces consist of three components. F_α is the resulting force caused by the contact of the chip with the rake face. The force F_ϕ results from shear and normal stresses in the shear zone. It will remain constant if the tool is worn or rounded, because the location of the shear zone does will not be affected. This is different for the parasitic force W.

$$F_c = W_T + F_{\alpha n} + F_{\Phi t}\cos\Phi + F_{\Phi n}\sin\Phi \qquad \text{(eq. 6.1)}$$

$$F_f = W_N + F_{\alpha t} + F_{\Phi t}\sin\Phi + F_{\Phi n}\cos\Phi \cdot \qquad \text{(eq. 6.2)}$$

In experiments with artificial flank wear and chamfered tools Spaans showed that the resulting increase of forces is only due to the parasitic forces W /SPAA71/. Consequently, approaches to calculate the friction in cutting operation with rounded or chamfered tools neglecting the parasitic force, e.g. by Gente /GENT02/, are questionable.

Beside the tool wear, the inertia forces of the chip and other dynamic influence may cause the resultant force increase. These effects have been evaluated in the past. In the seventies of the last century, measuring resultant forces in high speed cutting processes was one of the main focuses of investigations. Using ballistic set-ups, cutting speeds up to 200000 m/min have been realized in these times. The workpiece was designed as a projectile and shot onto a fixed cutting tool. The resulting forces at the tool were measured. Arndt /ARND72/ presented a theory for the cutting speed dependency of resultant forces based on own experimental results, **figure 6.2**.

For low-melting materials such as aluminum alloys the resultant forces depend on the cutting speed. In figure 6.2, the decrease of forces at conventional cutting speeds is found in the range of $0 < v_c < v_{conv}$. F_{sc} is the resultant (shear) force at conventional cutting speeds (e.g. for aluminum v_c = 2000 m/min) and F_{sh} is the shear force. F_m is the inertia or momentum force which can be neglected at conventional cutting speeds. At high cutting speeds the value of F_m increases. Therefore, the resultant (shear) force F_{su} at high cutting speeds rises when increasing the cutting speed. For low melting materials, adiabatic shearing occurs at the cutting speed v_a. At the cutting speed v_i the momentum force F_m is equal to F_{sc}. Following this theory F_{sc} is achieved

at conventional cutting speed (v_{conv}), at speeds above v_a and at v_i. As a consequence, Arndt predicted two force minima in the machining operation.

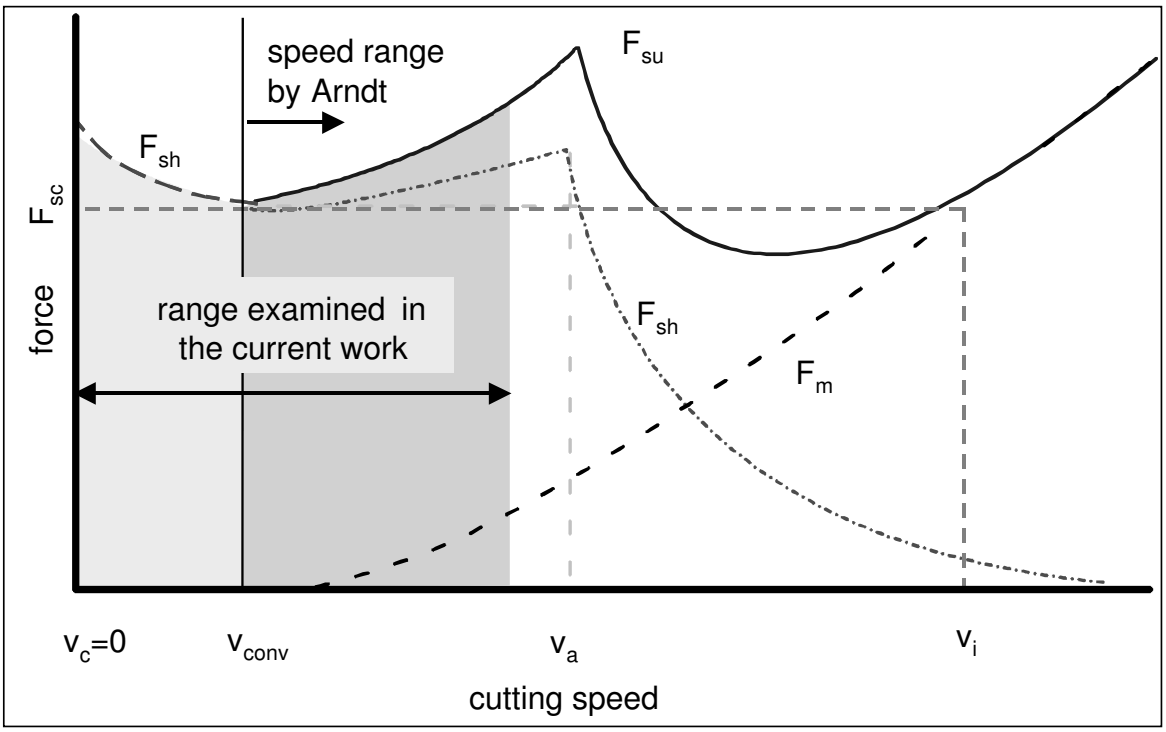


Figure 6.2: Theoretical behavior of resultant and component forces at ultra-high cutting velocities /ARND72/

Arndt involves the velocity dependant material hardening, too. Thus the resultant force F_s increases until the velocity of adiabatic shearing v_a is reached. Neglecting the well known decrease of the resultant forces at conventional cutting speeds ($v_c < v_{conv}$), he predicted an increase of resultant forces at high speeds. Arndt assumed that strain hardening and strain rate sensitivity of the workpiece material cause an increase of the forces in the primary shear zone. The resulting shear resistance of the workpiece consequently increases with the cutting speed. A further increase of cutting speed causes higher temperatures in the shear zone and starts a thermally caused reduction of the shear resistance. Mechanisms are adiabatic shearing and finally melting of the workpiece material. Now the resultant forces solely consist of the dynamic forces. These dynamic or inertia forces have been calculated by Bredendick in 1959 /BRED59/. He described the variation of the dynamic forces as a function of the cutting speed, using a conventional dynamic approach, **figure 6.3**.

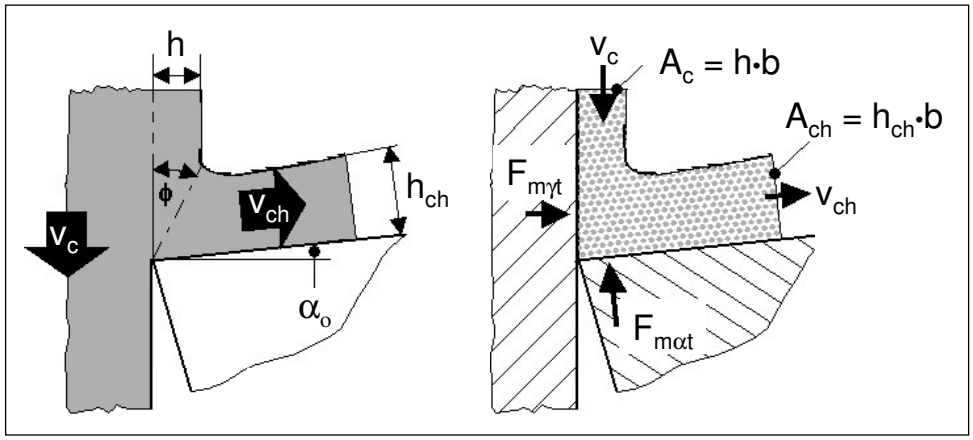


Figure 6.3: Determination of the inertia forces in cutting by Bredendick /BRED59/

He transformed the chip and uncut chip material into mass points, assumed the volume constancy (equation 6.3) and calculated the reaction force on the tool, equation 6.6 and 6.7. In these equation $F_{m\alpha p}$ is the resultant inertia force tangential to the rake face and $F_{m\alpha n}$ the normal force, respectively.

$$\rho \cdot A_c \cdot v_c^2 = \rho \cdot A_{ch} \cdot v_{ch}^2 \cdot \qquad \text{(eq. 6.3)}$$

$$A_c = h_c \cdot a_p \qquad \text{(eq. 6.4)}$$

$$A_{ch} = h_{ch} \cdot a_p \qquad \text{(eq. 6.5)}$$

$$F_{m\alpha n} = (\rho \cdot A_c \cdot v_c^2 + \rho \cdot A_{ch} \cdot v_{ch}^2 \cdot \sin\alpha_o) / \cos\alpha_o \qquad \text{(eq. 6.6)}$$

$$F_{m\alpha t} = F_{m\alpha n} \cdot \sin\alpha_o + \rho \cdot A_{ch} \cdot v_{ch}^2 \cos\alpha_o \qquad \text{(eq. 6.7)}$$

Figure 6.4 shows the cutting force component normal to the rake face for a feed of f = 0.25 mm and a depth of cut of a_p = 1 mm. Also the values obtained by subtracting the inertia forces are given. At a cutting speed of v_c = 6000 m/min the level of the inertia forces is about 3% of the cutting forces and the inertia independent forces ($F_{c\alpha n}$ - $F_{m\alpha n}$) still increase.

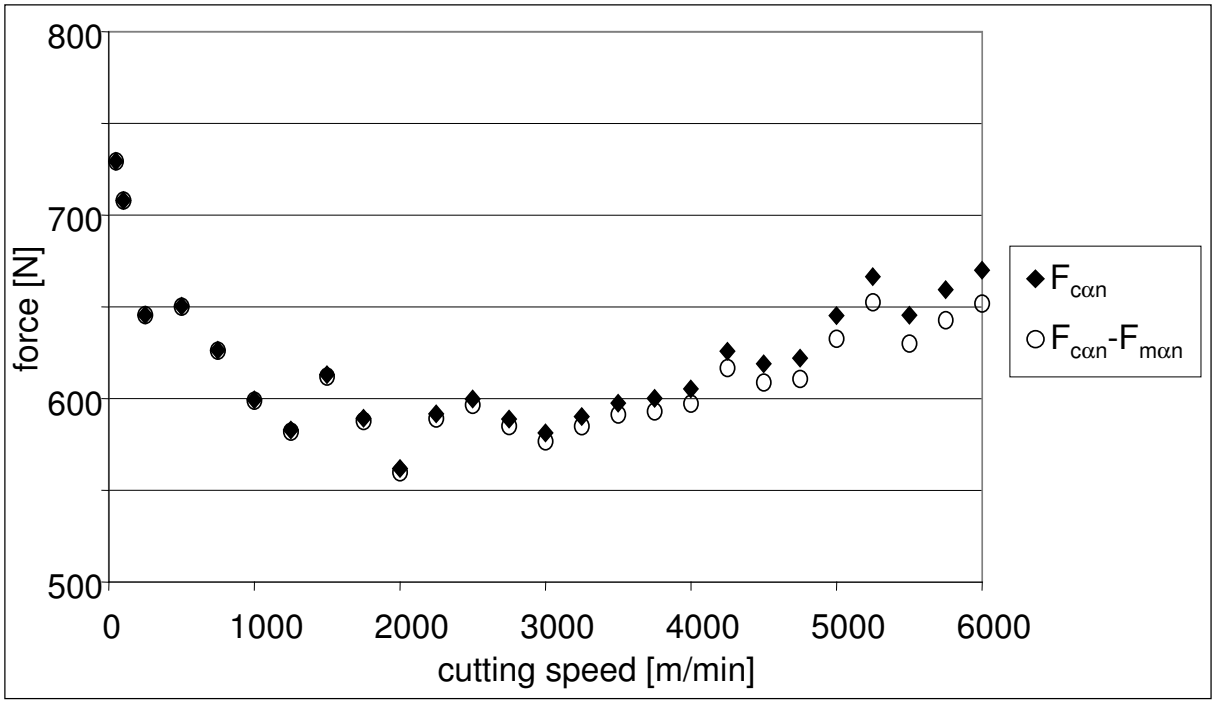


Figure 6.4: Influence of the inertia forces on the measured forces (AISI 1045, f = 0.25 mm, a_p = 1 mm)

Assuming the chip geometry not to change, for the cutting speed v_i by Arndt, where the inertia forces are equal the shearing forces, the calculation gives v_i = 36500 m/min. Because of the lower density, the velocity v_i for titanium and aluminum is much higher. Therefore, it can be said that the current work deals with conventional and high cutting velocities. The ultra-high machining range of cutting speed ($v_c > v_a$) is not subject of the current investigation.

6.3 Cutting temperatures

It can be summarized that the dependency of the force components on the cutting speed is caused by the change in chip formation, the material properties at high strain rates and the temperature. But why do the temperatures show the strong increase at moderate cutting speeds and a declining rise up to the melting temperature at high cutting velocities (compare figure 5.14)?

The similarity of chip temperature dependency at moderate cutting speeds for all examined workpiece materials leads to the first assumption. The chip formation mechanism seems not to be dominant. The chip formation for steel and aluminum, dominated by continuous chip formation at low speeds and segmented at high cutting

speeds, is different from the segmented chip formation of titanium. However, all three materials show the described increase. The temperature rise is caused by the increased power put into the process by the higher cutting speeds. Assuming the power in feed direction (P_f) and the friction (P_{fr}) to be small, the power generated in the primary shear zone (P_{sh}) can be calculated by the product of cutting forces and cutting speed (P_c), (equation 6.8). The assumption is valid as the friction coefficient and thus the friction forces are small (compare chapter 3). Also the feed velocity v_f is about 10^{-4} (for f = 0.1 mm and d = 200 mm) times lower than the cutting speed v_c. The mass flow dm/dt is the product of uncut chip plane A_c and the cutting speed v_c (equation 6.9). The quotient of equation 6.8 and 6.9 shows that the power increases with the mass flow, if the quotient of uncut chip plane A_c and mass flow dm/dt is constant. This is the case in the range of cutting speed where the resultant forces show a minimum.

$$P_{sh} = P_c + P_f + P_{fr} \Rightarrow P_{sh} = P_c = F_c \cdot v_c \qquad \text{(eq. 6.8)}$$

$$\dot{m} = A_c \cdot v_c \qquad \text{(eq. 6.9)}$$

$$\frac{P}{\dot{m}} = \frac{F_c \cdot v_c}{A_c \cdot v_c} \Rightarrow P = \frac{F_c \cdot \dot{m}}{A_c} \Rightarrow \frac{dQ}{dt} = \frac{F_c \cdot \dot{m}}{\kappa \cdot A_c} \qquad \text{(eq. 6.10)}$$

As the mass flow increases with the cutting speed and assuming a constant percentage of the power converted into heat (e.g. the Taylor-Quinney-factor $\kappa = 0.9$, chapter 3) the delivered heat dQ/dt and therefore the temperatures in cutting have to rise. At cutting speeds where the resultant force minimum is found, the power rises proportional with the cutting speed. At higher cutting speeds the rising forces cause an unproportional rise of the power and thus the heat brought into the process. The declining flow of the chip temperature at high cutting speeds as it was found for aluminum and steel can be reasoned as follows. For aluminum the melting temperature of the workpiece material is reached in the contact zone (figure 5.14 and 5.15). This is similar for steel as the molten material on the rake face at a cutting speed of v_c = 2000 m/min (figure 5.60) indicates. The differences between the chip temperature and the melting temperature of steel (figure 5.14 and 5.16) will be described later in this chapter. Assuming the melting temperature to be reached the pyrometer does not measure the maximum temperature but the temperature of the not molten material. But because of the high pressures in the contact zone and the

relative motion between chip and rake face the liquid material is accelerated away from the bottom of the chip. The limitation of the maximum chip temperature by the melting temperature as it can be found for steel and aluminum is a further proof of the theory that the liquid material limits the maximum temperatures in cutting (compare figure 5.14). Additionally, Müller found that the influence of melting and transformation enthalpy (e.g. transformation from ferrite to austenite) on the chip temperature is low /MUEL04/.

The fact that the measured temperatures in machining Ti6Al4V are lower than the melting point seems to contradict the theory given above. But the measured temperature strongly depends on the location of the measurement (compare figure 5.15 for aluminum). As a consequence the measurements in turning titanium were not close enough to the tool tip. This is due to the fact that it has to be prevented that the hole for the fiber weakens the tip of the ceramic tool. The theory of molten material limiting the maximum temperatures is supported by the obtained temperatures of the workpiece surface (compare figure 5.17). Here the temperatures are proportional to the cutting speed and show a strong increase. But even at a cutting speed of v_c = 6000 m/min they are far from reaching the melting temperature. This is caused by the heat flow from the freshly machined material into the cold bulk material. Some kind of self quenching process is active. In contrast the chip material is hot because of the deformation in the primary shear zone. Therefore, a self quenching cannot take place as no cold bulk material is present.

6.4 Tool wear

The tool wear mechanisms adhesion, diffusion and oxidation but also the abrasive wear attack are strongly affected by temperature. If the temperature in the cutting operation does not exceed the red hardness of the tool material, no significant wear is obtained. This was the case in turning AA 7075 that contains no hard inclusions and has a melting temperature below 600 °C.

If the cutting temperature is moderate, as it can be found for AISI 1045 steel and Ti6Al4V at low cutting speeds, the tool wear is dominated by the abrasive attack of hard inclusions in the workpiece. At increased cutting speeds the temperature rises and reaches values close to or above the red hardness of the tool. Now strong adhesive, diffusive and oxidation mechanisms are added to the abrasive wear attack.

Furthermore, the workpiece material stops softening and the toughness even increases because of the strain rate sensitivity (chapter 3). The fact that this happens under conditions where the area of the contact zone is small compared to the one at low cutting speeds, the tools fail because of the following mechanisms.

1. Comparably cold abrasive particles are continuously delivered to the cutting zone and cause higher forces due to the change of tool geometry by flank wear.
2. The high temperatures are in the range or above the red hardness of the tool. The tool tip is weakened by increased notch wear caused by oxidation.
3. Diffusion mechanisms gain significance and reduce the red hardness and toughness of the tool tip.

So the development of cutting tools devoted to high speed cutting of steel and titanium has to result in highly temperature resistant materials. The red hardness and chemical resistance of these tool materials have to be above those of currently available ceramic or boron nitride tools. Adapted coating systems or cooling strategies may be approaches to achieve high cutting speeds for high melting materials such as steel and titanium.

6.5 Surface quality

For a given tool geometry, the surface quality in turning strongly depends on the cinematic roughness, the cutting temperatures and the tool wear. If the cutting temperatures are too high at high cutting speeds a thermal softening of the surface occurs. This leads to a plastic flow of the asperities. Consequently, the surface roughness increases. Furthermore, the deformation of the rim zone increases and therefore the depth of the tertiary shear zone. The combination of deformation and high surface temperatures causes tensile residual stresses in the rim zone /TÖNS01, PLÖG02a/. The thickness of the area where tensile residual stresses are found, increases with the cutting speed. As tensile stresses support the initiation and propagation of fractures the surface integrity is lower compared to conventional cutting speeds. The mentioned mechanisms are amplified if the tool wear increases /JOCH01/. This causes higher temperatures and therefore a higher roughness and deformation of the surface.

7 Modeling and simulation of the cutting process

The results of several experimental setups presented in chapter 5 allowed to explain the dependency of resultant forces, chip formation, surface quality, tool wear and cutting temperatures on the cutting parameters and workpiece materials. A wide range of cutting speeds was being examined and the influence of feed and depth of cut became also visible. Furthermore, a setup was being developed that allows to obtain the chip geometry and chip velocity by in-situ photography. The presented results are suitable to optimize the turning process for the examined workpiece and tool materials. However, if only one aspect is changed - e.g. the heat treatment of the workpiece material, the machining process from turning to drilling or the application of a coated tool - the experimental information will not be suitable to optimize these processes. The consequence is to carry out an enormous number of machining experiments again. An alternative is to create a model of the cutting process. This was done in the past by different researchers. The resulting approaches are presented and judged in a CIRP keynote paper by van Luttervelt et al. /LUTT98/. Three conclusions were given:

1. “While significant effort has been made towards understanding the complex interactions in the basic mechanism, the validity and completeness of such (cutting) models and the means of transforming these models into practical models for the much more complex practical machining operation remain highly questionable.”
2. “A vast majority of past efforts deals with developing analytical models with very limited experimental validation of the models under only a few selected cutting conditions, tool geometries and work materials. Quantitative analysis of such models seems to suffer from the lack of adequately acceptable methodologies for applications under a wide range of conditions.”
3. “... the inaccuracies involved in the use of the thermal and mechanical property variations of the work and tool materials at high cutting temperatures characterized by large strains and strain rates are compounded by the limitations of the modeling technology.”

The first and second conclusions illustrate the main disadvantage of analytical and empirical models. These models do not allow to predict the process performance.

Empirical models (e.g. by Taylor and Kienzle) cannot be transferred to different tool-workpiece combinations without conducting experiments. This is the reason why empirical models are not described in the current work.

Analytical approaches such as shear plane and shear zone models are limited to simple orthogonal or oblique cutting processes. This is due to the fact that they strongly depend on the geometrical values such as chip thickness, rake angle and uncut chip thickness. Numerical models, as they will be presented in detail in this work, are not affected by the first and second conclusion. However, for this kind of model (and the analytical models) the third conclusion is valid. To understand why the numerical model is chosen, a short introduction to the existing analytical approaches is given.

7.1 Modeling of the cutting process – an overview

Referring to Beno the basic approach to describe the cutting process using an analytical model can be found in the essay by I.A. Thime from St. Petersburg who defined in his work “Resistance of wood and metal in cutting“ the shear plane and the shear zone /BENO96/. Today these definitions are still used to describe the cutting process. This highlights the pioneer work of Thime. Furthermore, his model was valid for metal as well as wood cutting. Without the modern techniques to evaluate machining experiments he assumed shearing processes to be of major importance in continuous chip formation. Based on his definition a high amount of analytical models were set up. A summary of the existing analytical models to describe the chip formation is given as they are in direct concurrence to the models based on FEM.

At moderate cutting speed and feed, ductile materials such as medium carbon steel and aluminum alloys show a continuous chip formation. These cutting conditions were the common parameters in the beginning and the middle of the last century. Therefore, it is not surprising, that the first approaches to describe the mechanism of chip formation by Ernst and Merchant /MERC45/ deal with the continuous chip formation. After a nearly constant uncut chip thickness is reached the process can be considered as time independent. The chip is being created by shearing the workpiece material off the uncut chip thickness. This shearing takes place in the primary cutting zone (primary shear zone) which is located between the front of the

tool edge and the area of the free surface. Thus the primary shear zone is the border between chip and uncut workpiece material, **figure 7.1**.

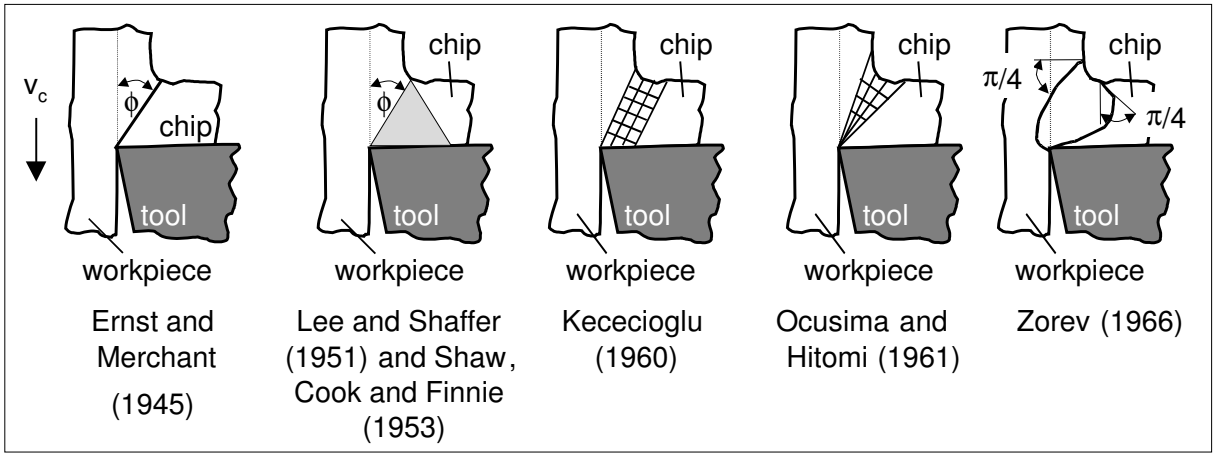


Figure 7.1: Shear zone and shear plane models for orthogonal cutting by Astakhow /ASTA97, MERC45, LEE51, SHAW53, KECE60, OCUS61, ZORE66/

In this area, the workpiece material with the cutting velocity v_c is being deflected tangentially to the rake face. Because of the continuous supply of workpiece material no back flow is possible. The area where the free surface of chip and uncut chip thickness is found is the only area where the material is allowed to move to. These boundary conditions determine the shear angle Φ between the primary shear zone and the direction of the cutting velocity v_c. Assuming the primary shear zone to be an infinitely thin plane, Merchant and Ernst published a shear plane model /MERC45/. The material of the uncut chip thickness flows into this shear plane and the velocity is instantaneously being changed from the cutting speed v_c to the chip speed v_{ch}. Ernst and Merchant introduced the following assumptions /MERC45/:

- The material in front of and behind the shear plane is ideally rigid.
- The material in the infinitely thin shear zone is ideally plastic (no strain hardening or strain rate sensitivity).
- The material velocity along the shear plane is constant (a straight continuous chip is assumed).
- At the rake face a constant friction coefficient (Coulomb friction law) exists.
- The tool is ideally sharp.

These assumptions allowed to calculate the cutting forces by the determination of the shear angle. The shear plane model was often modified and at present, more than 50 shear angle relationships are known /LUTT98/. Astakhov summarized several different shear plane and shear zone theories (figure 7.1).

The approaches have in common that they assume all shearing processes to take place in the shear plane. But the area of material that is regarded to behave plastically is extended normal and parallel to the shear plane. The flow of the material was calculated using the slip line field model. However, the agreement of calculated and experimental measured dependencies of the shear angle Φ, the rake angle α and the friction angle λ is poor. Oxley gives a good introduction to the different approaches and their shortcomings /OXLE89/. He found that the assumption of an ideally plastic material behavior is the main reason for the failure of the shear plane models. Based on the experimental determination of slip line fields by using visioplasticity, Palmer and Oxley obtained a new model /PALM59/. They found that the strain hardening properties of the workpiece material have a significant effect on the (hydrostatic) stress in the chip formation zone. However, because of a visioplastic evaluation of the data the realized cutting speeds were low. To apply these findings to cutting processes at higher cutting speeds Oxley and Welsh introduced a shear zone model /OXLE62/.

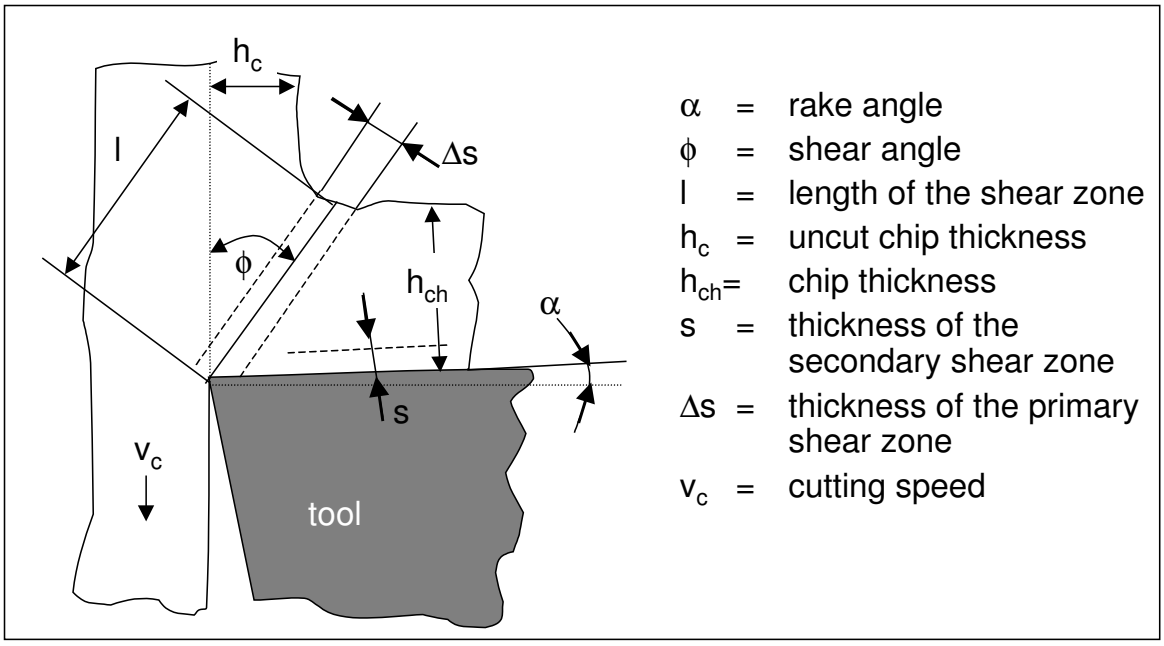


Figure 7.2: Geometry and parameters for the theory by Oxley /OXLE89/

In this model the shear zone has a finite thickness (**figure 7.2**). The boundaries of the shear zone are still parallel and chip curling is neglected. Using this model Oxley was able to consider the strain hardening as well as the strain rate sensitivity of the workpiece material. Latter enabled him to describe the influence of the cutting speed on the shear angle. Because of the considerable influence of the secondary shear zone on the shear angle relationships, Oxley modified his shear zone model. He found a good agreement of modeled and measured cutting forces in orthogonal cutting. His approach was suited to be adapted to the oblique cutting process as well as to comprise the influence of the tool nose radius, a restricted tool-chip contact, build-up edge formation /ARSE96/ and curled chips /FANG01/.

However, the described approach is only valid for continuous chip formation. If a segmented chip formation occurs, the shear plane model has to be modified. The shear zone has to be able to move during the cutting process. Pekelharing suggested a model of an oscillating shear zone /PEKE74/, **figure 7.3 left**. In this approach the shear plane moves downwards with the speed v_h. Three situations were distinguished:

1. $v_h < v_c$ undercritical

2. $v_h = v_c$ critical

3. $v_h > v_c$ overcritical

Especially the overcritical situation leads to a good comparison with in-situ photography of chip formation at low cutting speeds.

Disagreeing with the assumption of an oscillating shear plane van Luttervelt /LUTT77/ suggested a split shear zone, figure 7.3 right. The first shear zone is the boundary between the rigid workpiece and the rigid intermediate element. The latter moves with a velocity v_e which is not parallel to the rake face of the tool. Consequently, a second shear zone is necessary between this intermediate element and the chip. The second shear zone and the chip move with speed v_{ch} parallel to the tool face. Between the intermediate element and the tool face a solid build-up edge (dead zone) is present and the element slides over this dead zone. The speed difference between the intermediate element and the dead zone causes the formation of a third shear zone. A fourth shear zone is the boundary between workpiece and dead zone. Examining the chip formation in orthogonal cutting the

titanium alloy Ti6Al4V Gente proposed a model similar to that by van Luttervelt /GENT02/. His approach and the one by Pekelharing allow to model the continuous, the wavy and the segmented chip formation.

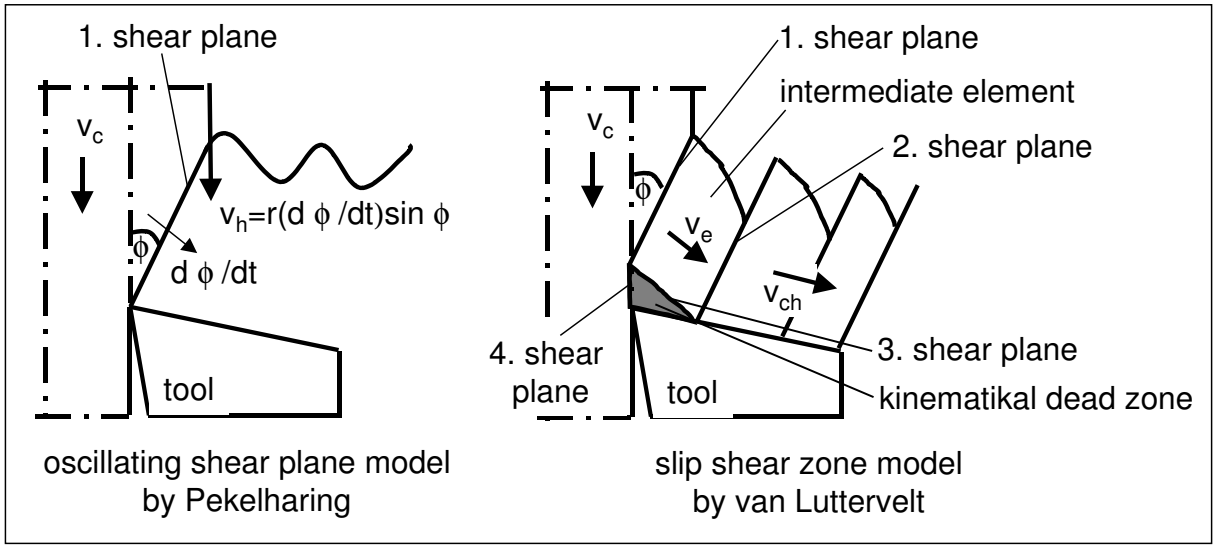


Figure 7.3: Theory of oscillating and split shear zone by Pekelharing and van Luttervelt /LUTT77/

The main disadvantage of the two approaches to model segmented chip formation is that they are only of kinematic nature. As a consequence they cannot be used to predict cutting forces.

As described in the approaches by Oxley and van Luttervelt a second shear zone is observed. The chip material which is near or in contact with the rake face of the tool has a lower speed than the rest of the chip. The area where the gradient of chip velocity is compensated by elongation and shearing is called the secondary shear zone. If the tool is ideal sharp every piece of the material in the secondary shear zone has passed the primary shear zone. Thus, the material found in the secondary shear zone of the chip has suffered two shearing operations in different directions.

As the secondary shear zone can be found by considering friction in the tool-chip contact zone, the application of a round cutting edge leads to a third or tertiary shear zone. This is the only shear zone that does not belong to the chip but to the workpiece material below the uncut chip thickness. The creation mechanism is similar to that of the secondary shear zone. The contact of the workpiece material and the flank face of the tool leads to a decrease of the material velocity in this area.

This gradient is compensated by an elongation and shearing of the workpiece material. Economically the tertiary shear zone is the most important one because it forms the surface of the machined workpiece and is therefore responsible for the quality of the machined part.

The tertiary shear zone is not directly implemented into the theory by Oxley. Admittedly, his model considers build-up edge (BUE) formation and the stress distribution in the area of the shear zone. Therefore, it describes mechanisms that are able to spoil the surface quality.

The existence of a realistically shaped, round tool edge leads to a compression area in front of the tool tip. In this area, the material velocity is minimized. In the direction of the cutting speed it is slowed down from the cutting velocity v_c to zero and accelerated in the direction of the feed. Next to this area the material flows into the three shear zones mentioned above. Thus the compression area is the link between the different shear zones. Under these conditions, strain hardened material may stick to the cutting edge and create the build-up edge. In cutting operations the BUE is not stable and therefore parts of it leave the area of the compression zone towards rake or flank face. The latter is worse as these parts reduce the surface quality and increase the flank wear. If the temperatures are high, the strain hardening of the workpiece material is overcompensated and the BUE disappears. The high temperatures can be achieved by high cutting speeds, high uncut chip thickness, dry cutting, the application of coatings and the change of the tool geometry.

- Regarding the described analytical models for chip formation as well as common empirical models, van Luttervelt /LUTT98/ came to the conclusion that those models could not serve the needs of industry:
- “The empirical models were never able to predict the influence of work material or tool material on the values of the constant in the equations.”
- ”The analytical models were never able to predict what type of chip formation would occur at specified conditions or even in the case of a continuous type of chip formation process; also they were never able to predict the actual behavior in the chip formation zone accurately enough.”

- ”The analytical models could never bridge the gap between the simplified fundamental case studied and actual three-dimensional cutting operations. The empirical models did not bridge the gap between pure empirical and fundamental scientific quantities.”
- “The introduction of new machining methods such as circular milling, high speed machining, dry machining, which bring in new problems needed to be addressed but in which knowledge obtained earlier did not apply.”
- “The fast introduction of new tool materials and new tool designs, including indexable inserts with chip forming geometry and coatings cause new phenomena, which were unknown before.”
- “The introduction of an ever widening spectrum of work materials including refractory materials and hardened steels has similar effects.”

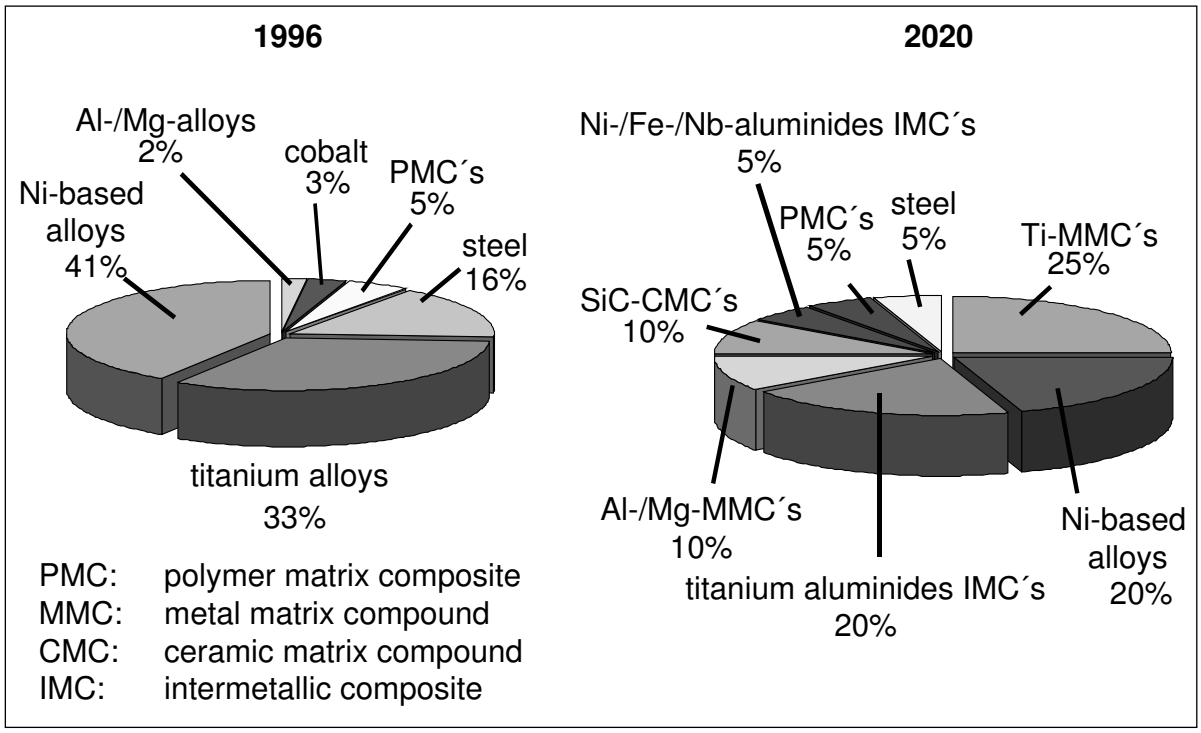


Figure 7.4: Workpiece materials in the aeronautic industry /source: Marsh 1993, Pratt & Whitney 1999, Schwatz 1996/

An example is the variety of workpiece materials in the aeronautic industry, **figure 7.4**. The amount of adapted alloys and materials increase while that of conventional material (with a well described machinability) decreases. This tendency,

that is mainly driven by consequent light weight designs, can also be found in the automotive industry and its supplying industry.

The shortcomings of analytical and empirical models in combination with the challenges of manufacturing technology in the future requires the search for alternatives. This alternative model should fulfill at least some of the following demands:

- The geometry of the chip formation zone as well as the chip must not be prescribed to allow modeling of segmented chip formation as well as chip breakage.
- It has to consider mechanical, thermal and fracture mechanisms to model tool wear, shearing processes and chip breakage.
- The model has to be based on fundamental physical laws to be not limited to orthogonal or oblique cutting operations. In addition the model has to be suitable for three dimensional processes.
- The setup of the model and the results have to be based on data of cutting processes. Thus process parameters (geometry, cutting speed, feed etc.) will be given to the model and the criteria of machinability (forces, wear, chip formation, surface quality) have to be obtained.
- The model should be implemented in a user friendly software that can be used by an engineer without too much modeling knowledge.

With these objectives in mind in the current work FEM was applied. The reason is that modeling of cutting processes using the finite element method (FEM) fulfills the mentioned demands to a large extend. First of all, the structure of FEM allows to predict all criteria of machinability. The reason is that the resultant forces, tool wear, chip formation and surface quality are determined by the combination of stress, strain, strain rate, temperature and geometry. These values are the results of a FEM simulation with a Lagrangian code. In this code the mesh is connected to the material. If the material is deformed, the mesh is deformed, too. If an Eulerian code is applied the geometry of the chip is determined with the setup of the model. The material is assumed to flow through a fixed mesh. So every mesh element has the information of the material without any deformation. The chip geometry can be

modeled if the Eulerian and Lagrangian approach are linked in the Arbitrary-Lagrangian-Eulerian code (ALE) /KALH00/. However, only the chip curvature but no segmented chip can be modeled using the ALE code.

In a Lagrangian code two different approaches, the implicit and the explicit code, can be used. The length of a time step in the implicit finite element code is only limited by accuracy requirements. On the other hand, a set of coupled equations has to be solved. Therefore, an optimum of high accuracy (high mesh density) and realistic computational time (limited number of elements for which the equations have to be solved) has to be found. The explicit algorithm is faster, but the limit on the time step is related to the time it takes for an acoustic wave to pass through the smallest element /KALH00/. It has been used with success for solving strongly non-linear problems where inertia is negligible by artificially increasing the density and thereby make it possible to implement larger time steps.

The application of FEM to model the cutting process is promising as the use of CAx technologies gains importance in all areas of manufacturing technology. The tools, workpieces and machine tools are designed by computer aided design (CAD) tools. Tools and workpieces are manufactured by transferring the CAD data into computer numerical control (CNC) data. Planning tools for factory, process chain and workpiece quality layout are also available in electronic data processing (EDP) systems. As the CAD data is the geometry input for two or three dimensional FEM software, the application of FEM instead of analytical or empirical models shows high potentials. The way how forming simulations are used to design and set up forming operations is a first example of the combination of CAx systems and FEM simulations /WIDD00/.

The possibility to consider many input variables such as friction, geometry, thermo-mechanical behavior of tool and workpiece material is a further reason for increasing activities in cutting simulation. This is also supported by the improved reliability of the FEM software accompanied by decreasing computation time. Additionally, the early results of two-dimensional cutting simulations were promising /MARU95, LEOP95, ORTI95, LUTT98, ÖZEL00, KLOC00, WEUL00, OLOV00, CERE00, MARU01, LEOP01, KLOC01, KLOC01a, LEOP01a, BEHR01, SÖHN01, WEST02, GENT02, ALTA03/. To gain significance in the industrial setup of cutting operations a three-

dimensional simulation is necessary. A capable model has to enable the user to predict the important criteria of machinability based on the geometrical and material input data. The amount of experiments to evaluate the simulation results will be minimized. The low computing time as well as the good comparability of two dimensional cutting simulation and the orthogonal cut are the cause why the majority of cutting simulations is still two dimensional. These advantages are used in this work to obtain input data that will lead to a good agreement of simulation and experiment.

7.2 Setup of the model

Several publications dealing with continuous chip formation are known /ÖZEL00, LEOP95, WEUL00/. This process can be described by assuming a quasi-stationary chip formation. Therefore, the Lagrangian, the Eulerian and the combination of both, the Arbitrary Lagrangian-Eulerian (ALE) approach can be used /OLOV00/. The chip formation is simulated by indicating a fracture in front of the tool tip /MARU95/ or by continuous remeshing /KLOC00/. Fractures occurring in front of the tool would mean that tensile stresses could be found in this area. This may be probable for cutting processes of brittle materials with very sharp tools. In the set-up described in this paper a ceramic tool with a strongly negative effective rake angle is used. Thus high compressive stresses can be found in front of the tool tip and the propagation of fractures is unlikely, **figure 7.5**.

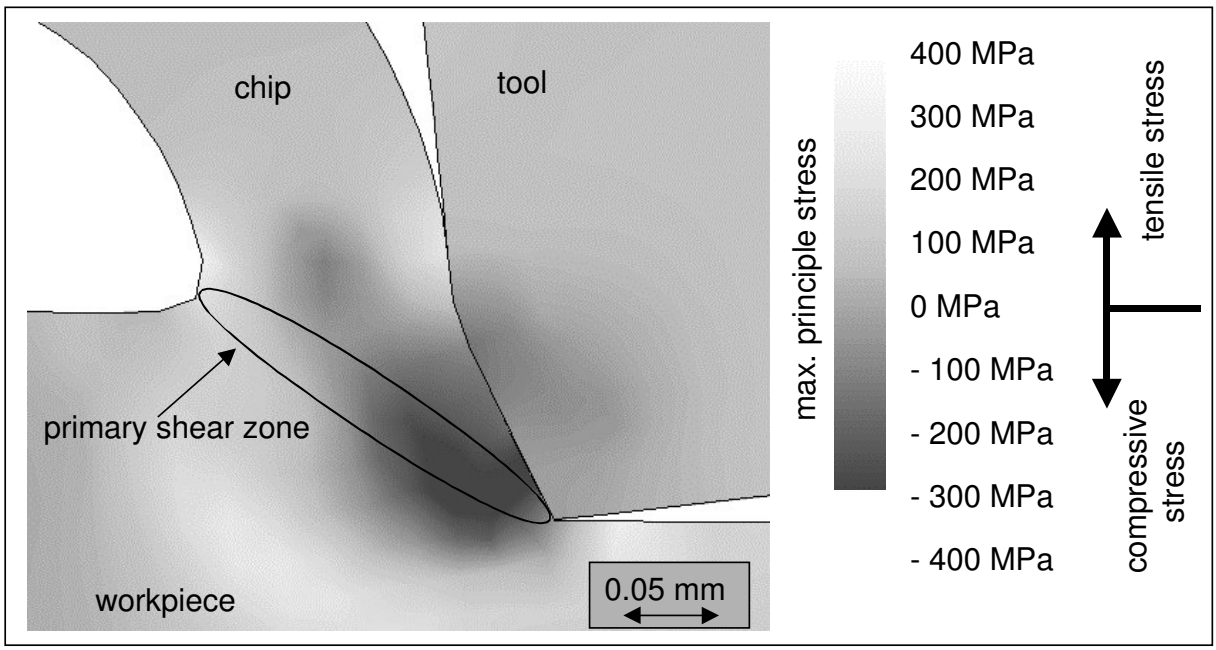


Figure 7.5: Distribution of the maximal principle stresses in the primary shear zone

In this area the models mentioned above indicate fractures to achieve the separation of chip and undeformed workpiece surface. Realizing the chip formation by continuous remeshing, as it is done in this work, the cutting process is modeled as a forming operation /SCHÄ99/. No fracture is needed in front of the tool tip but the “separation” is realized by the workpiece material flowing around the cutting edge. To simulate the segmented chip formation, only the Lagrangian approach is valid. Because of the non-quasi-stationary chip formation no constant boundary geometry can be realized as is needed for the Eulerian and ALE approach. Using the Lagrangian code two approaches for modeling segmented chip formation are suitable. Both models use continuous remeshing. The approaches, which will be described later in this chapter, are the implementation of a failure criteria and the specific extrapolation of flow curves to high values of strain /SCHÄ99/.

7.2.1 FE-Model

In this work, a two-dimensional cutting model is presented. For simulation the commercial software DEFORM 2D is used. This implicit Lagrangian code offers a very stable remeshing routine and the user is enabled to modify the input data. This ability is very important to create a model which is valid for the extreme conditions under which the cutting process takes place. Beside the implementation of own material data, which is described in chapter 2, the numerical settings are very important.

7.2.2 FE-Mesh

In simulations based on a Lagrangian code the mesh is moved and the geometry of the meshed body results out of the kinematic conditions and the element geometry. In DEFORM elements with four nodes are used. To get the maximal information the workpiece as well as the cutting tool are provided with a mesh. The cutting tool is considered as elastic while the workpiece material is regarded as rigid-plastic. The elastic formulation of the cutting tool allows to calculate the stress and temperature in the tool tip as well as the resultant force. The tool temperature and the resultant force are values which can be compared to experimental results. The stress distribution in the tool is important when a mechanical optimization of the tool is interesting.

The plastic formulation of the workpiece material allows to calculate the distribution of strain, strain rate, stress, temperature and velocity. The simulation is very stable because of continuous remeshing offered by the software DEFORM. If an element is critically deformed, a new undeformed mesh is generated for the geometry of the workpiece. The properties of the elements, e.g. the distribution of the strain rate, are transferred from the old to the new mesh as well as the boundary conditions. This remeshing can be started automatically or at a limit of strain or temperature set by the user. But the interpolation from the old to the new mesh leads to an accuracy loss. If the mesh density is not high enough, gradients of distribution may be smoothed. To minimize this error and to improve the convergence of the simulation, the mesh density in areas with high gradients of temperature, strain, strain rate and stress has to be increased. In the presented simulation a gradient mesh is used. The highest mesh density is set in that part of the workpiece where the primary and secondary shear zone will be located. In these areas the maximum gradients of temperature and strain rate distribution occur. The minimum distance of two nodes is about 3 µm, **Figure 7.6**.

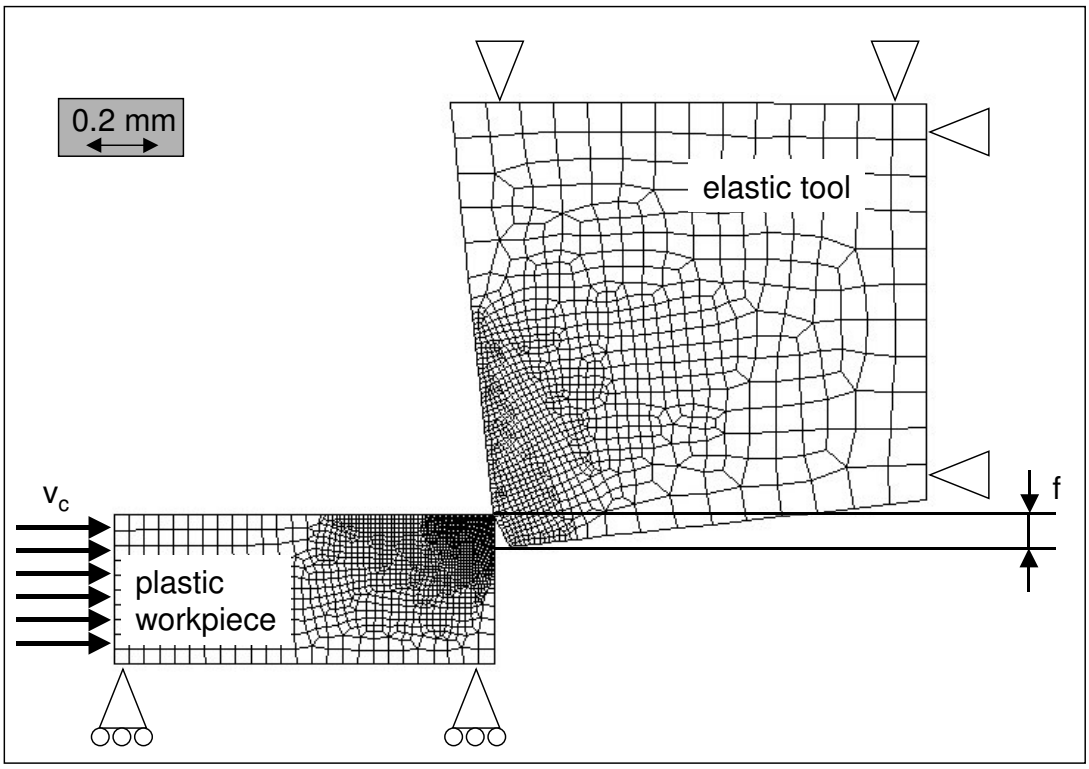


Figure 7.6: FEM model with a graded mesh

7.2.3 Boundary Conditions

In the current simulation, the two-dimensional orthogonal cutting process is modeled. The geometry of the cutting tool is based on the one used in the turning experiments (chapter 5). The clearance angle is $\gamma = 6°$, the rake angle $\alpha = -6°$ and because of a chamfer with an angle of 20° and a length of 0.1 mm an effective rake angle of $\alpha = -26°$ is achieved. In orthogonal cutting processes the feed f = 0.1 mm is equal to the undeformed chip thickness h_c and the depth of cut is $a_p = 1$ mm. Similar to the turning process, the workpiece is moved against a stationary cutting tool. Therefore, the process duration is limited by the length of the workpiece which has to be meshed completely. It is obvious that for a process time comparable to the experiment the workpiece has to be very long. The fact that every element of the mesh has to be calculated in every step leads to a limited length of the workpiece in order to reduce the computing time. Because of this contradiction the simulation routine within DEFORM 2d was modified. Later in this chapter it is described how comparable process times of simulation and experiment could be achieved without extensive computing time.

7.3 Evaluation of material data

The purpose of the simulation is to gain information about the material behavior as a result of the tool penetration. The material input data was described in the chapters 2 and 3. On the one hand, the obtained data contains values for stress, strain, strain rate, resultant force and temperature. A comparison of experimental and numerical results can be achieved for the temperature and the resultant force. On the other hand, a chip shape different from that at the start of the simulation is achieved by a Lagrangian simulation. This obtained geometry, in the current model the shape of the chip, can be also used for the comparison of simulation and experiment. The chip shape is a result of various parameters. One is the geometry of the applied finite elements. As DEFORM uses rectangular quadratic elements, the shape of the modeled chip in the current investigation is smoothened. A strong influence on the shape of the chip is gained by the cutting parameters such as tool geometry, feed and depth of cut /XIE96/. The influence of these parameters is not further examined in this investigation. The most influential parameter on the behavior of the workpiece material and of course on the chip shape is the flow stress curve /ELWA01/. In the

current work, the constitutive material law by Treppmann and El-Magd is used (compare equation 2.13) /TREP01/. DEFORM allows several ways to implement flow stress data into the simulation. A material can be chosen from a material database. As this material data is limited to low values of strain and strain rate it is not suitable for this work. A second way is to type the data into a table sheet. Because of the high amount of data caused by the remarkable range of strain, strain rate and temperature this function is also ignored. A third approach is the implementation of the constitutive equation into a user subroutine. However, the flow stress curve used in this work is obtained by numerically solving a transient problem. Therefore, the fourth opportunity is chosen. The equation is solved by an additional program. Then a text file is generated and copied into the keyword file of the actual simulation.

Beside the flow stress curve many material properties have to be provided as input to the simulation which are for example the Young's modulus E, the Poisson ratio ν, the heat capacity c_p and the density ρ. On the one hand, this data depends at least on the temperature and must be measured for each (workpiece and tool) material. On the other hand, the achieved results cannot be easily implemented into the simulation. The thermal dependency may lead to poor convergence or even wrong results as it is described in chapter 3. That is the reason why in the current simulation the temperature dependent material properties are regarded as temperature independent. The error of this assumption will be quantified later in this chapter.

To achieve a stable and economical machining operation the properties of tool and workpiece have to be different. The hardness and thermal stability of the tool has to be higher than those of the workpiece material. In consequence, inter-object properties such as friction and heat transfer between tool and workpiece are totally different than between workpiece and workpiece. It occurs when the generated chip contacts the surface of the workpiece, e.g. for strongly curled chips.

Details about friction and heat transfer between cutting tool and workpiece material is hardly known. Because of the difficult tribological system with a lot of unknown influences such as surface roughness and thin liquid or oxidation layers on the tool surface, no analytical description of the inter-object properties is known /KRIE01/. In the current simulation, the friction coefficient by Coulomb is set to $\mu = 0.2$. This assumption is based on the findings by Westhoff /WEST02/ and the high speed

friction experiments described in chapter 3. The value of $\mu = 0.2$ might be overestimated. The temperature measurements (figure 5.14) well as the findings in high speed friction (chapter 3.11.4) suggest a lower coefficent of friction due to liquid workpiece material present in the interface of chip and rake face.

The coefficient for the heat transfer from the chip to the tool is assumed to be very high (compare chapter 3). This assumption is based on the experimental results as temperature measurements, examinations of the chip surface at the secondary shear zone and the rake face of the tool (chapter 5). The temperature measurements show a very high temperature at the rake face of the tool and the surface of the chip is determined by the rake face surface structure. Because of the high temperatures and high pressures on the rake face a very good heat transfer from the chip to the tool is probable. Even if the rake face of the tool is very rough, softened workpiece material is pressed into the valleys of the rake face and an optimal heat transfer is achieved.

7.4 Numerical means to adapt the simulation to the cutting process

A tremendous amount of work has been done in the finite element simulation of the cutting process since the application of finite element methods to the analysis of plastic metal forming processes first appeared in the 70s of the last century. While early researchers had to focus on the sheer problem of running a stable simulation /STRE85/, with the advances in software technology the finite element cutting simulation in 2D with thermo-mechanical coupling can be regarded state of the art /LUTT98/.

Lagrangian and Eulerian codes are both employed in order to simulate the machining process, however, Lagrangian codes seem to dominate. The reason for this is the availability and previous experience with Lagrangian codes on the side of the researchers. The Lagrangian approach leads to the following problems: the mesh needs continuous remeshing due to the high mesh distortion which is generated by high plastic strains /KLOC01/. This problem can be overcome by sufficiently stable remeshing procedures and it is already solved in leading software products available on the market. Another drawback of the Lagrangian method is that the whole object on which chip formation simulation will be performed must be present as meshed object in the simulation right from the start. This limits the length of cut that can be

simulated. The length of cut is typically ten to thirty times the cutting depth. Depending on the cutting speed, the simulated process time can be only a few milliseconds. Then the length of the workpiece provided initially in the simulation is used up. Additionally, the contact of the chip with the workpiece normally leads to problems as well, as the chip starts curling up. If thermal issues are to be analyzed in the cutting simulation, time for heat transfer and thermal conduction are very short so that equilibrium conditions are certainly not reached in this short time and the whole process is still highly transient.

Therefore, a procedure has been developed at WZL in order to allow for potentially endless continuous cutting simulation in the commercial Lagrangian FEM system DEFORM 2D /KLOC01/. This “Konti-Cut” procedure is active during the remeshing procedure and the reapplication of boundary conditions onto the new mesh, **figure 7.7**.

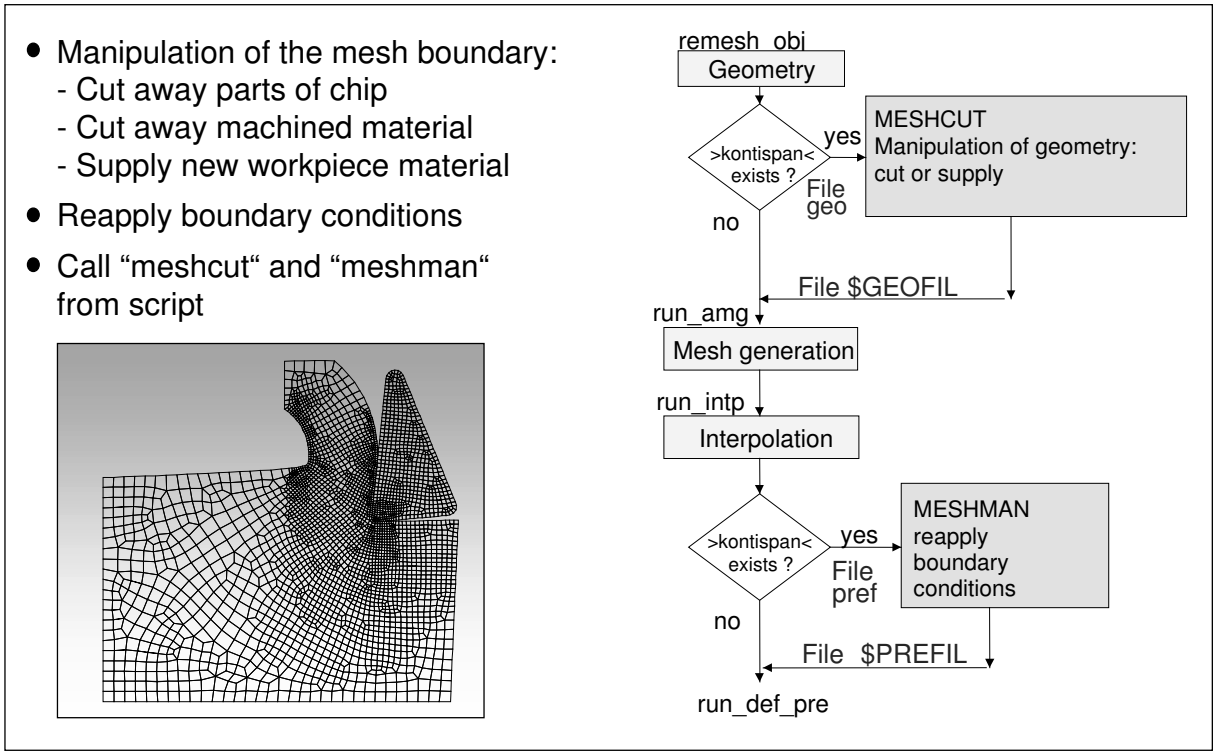


Figure 7.7: Procedure Konti-Cut within DEFORM 2D /KLOC01/

The remeshing procedure starts with the extraction of the boundary of the deformed mesh. The boundary geometry is fed into the remeshing program as a list of points that define a closed loop. If a file called «kontispan» exists in the working directory, the new program «MESHCUT» reads the old boundary, cuts of parts that are not

interesting any more in the simulation, like the remaining surface and parts of the chip, and adds new parts of the workpiece, that will take part in the chip formation a few time steps later. The location of these parts is provided in the file «kontispan».

The new boundary loop is then fed into the remeshing program. As the boundaries of the new mesh are now in a different location than they were before the remeshing, the automatic reapplication of the boundary conditions (velocity, constraints) cannot work properly. Therefore, the program «MESHMAN» is called from the remeshing script. Depending upon the geometric values that are provided in the file «kontispan», the boundary conditions as specified in this file are reapplied properly onto the new mesh. The remeshing script then calls the DEFORM pre-processor that converts the data into the database format that the simulation uses and finally calls the simulation engine. This procedure is repeated for every remeshing step that is necessary during the whole simulation. The mesh, that is reached finally, is shown in figure 7.7 and does not significantly change during the further course of the simulation.

Thus, the process time that can be simulated using the Konti-Cut procedure is not dependent on the length of the initial workpiece or a possible contact of the chip with the workpiece, but only on the available CPU time and disk storage space.

In 2D, potentially endless cutting simulations become possible using this procedure. The application of this procedure to 3D simulations is currently under development. In the simulation of 3D chip formation procedures, either in cutting with geometrically defined cutting edges, or in grinding, the number of available elements determines the stability and feasibility of such a simulation. The Konti-Cut procedure therefore will render 3D simulations more easy to handle.

7.5 Application of design of experiments to the cutting simulation

The simulation of metal cutting processes should be suitable to enlarge the understanding of the chip formation mechanism. To achieve this aim the simulation results have to be verified by experimental values such as resultant forces and temperatures. As these values strongly depend on the input values of the two dimensional simulation the current chapter examines the influence of different input

parameters on the simulation results. To obtain as much information as possible the design of experiments (DOE) is applied to the simulation process.

Design of Experiments (DOE) or Experimental Design was defined by Montgomery /MONT85/ as follows: Experimental Design consists of purposeful changes of the inputs (factors) to a process in order to observe the corresponding changes of the outputs (responses). The process is defined as some combination of machines, materials, methods, people, environment and measurement which - when used together - perform a service, produce a product or complete a task.

A further advantage of applying experimental design is that more information can be gathered by conducting fewer experiments. This advantage was first used in agriculture where experiments would last several months. Thanks to the improvement of computing systems, the duration of a cutting simulation is reduced from weeks to several hours. Nevertheless, because of the high amount of input variables and assumption that have to be made, many simulations have to be conducted to identify the influences of the variables. The process is considered as “black box”, only the inputs and outputs are known (**figure 7.8**). In the current work the simulation is this “black box” which means that all numerical iterations and calculations are assumed to be unknown. Therefore, the design of experiments (DOE) is applied to identify the influence of input variables on the simulation result (figure 7.8 right). These inputs can be of numerical nature as well as physical properties of the examined materials. In the current investigation, the numerical inputs were kept constant and only the influence of the physical properties on the simulation result was considered.

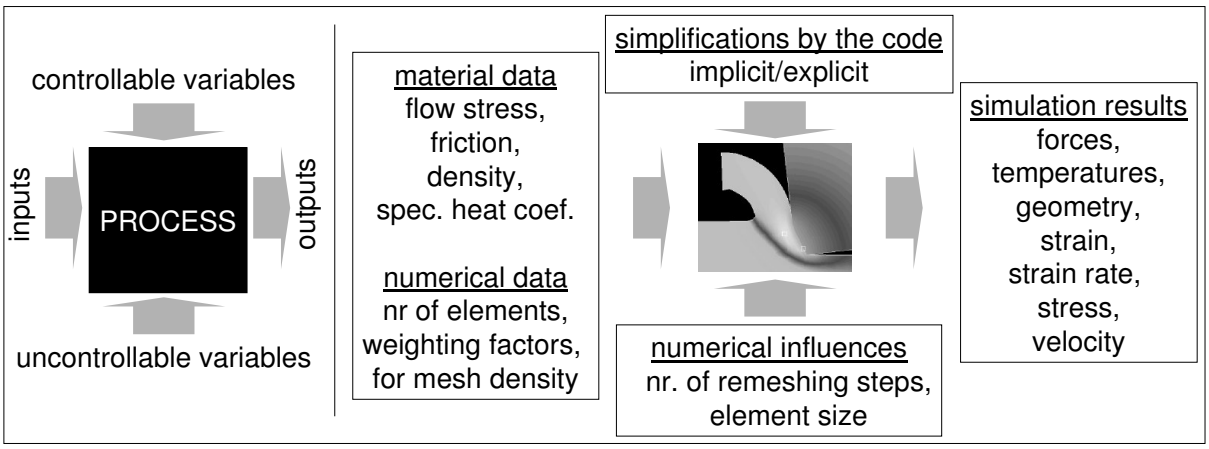


Figure 7.8: Design of experiments and its application to the (cutting) simulation

It may seem astonishing that physical values are set on two levels and were not implemented as temperature dependent variables. Of course better simulation results can be expected when the input parameter is given as a function of the temperature. On the other hand the assumption of constant values on two levels has three advantages:

- The DOE can be applied to identify the significant inputs. The number of inputs has to be reduced because of the high efforts that are necessary to obtain them.
- The direction of the output change (e.g. increase in temperature) can be assigned to the high or low level of the input.
- Some inputs are not defined or cannot be measured over the whole range of temperature.

This leads to extrapolations by the user or the FEM system and can even cause poor convergence of the simulation. An example is the Young's Modulus. This parameter can only be measured when the material is supposed to be elastic. Therefore, it cannot be determined at high temperatures where the material reacts plastically even at low stresses. Furthermore, the Young's Modulus decreases when the temperature is being raised. An extrapolation by the FEM system will lead to a negative stiffness matrix and the simulation breaks down.

The input variables can be distinguished as inputs, controllable variables and uncontrollable variables. They can also be set on reproducible levels and be of quantitative or qualitative nature. An example of a quantitative input in the simulation is friction which can be set on a low level $\mu = 0.2$ or a high level $\mu = 0.25$ (Coulomb friction coefficient). The flow stress curve is a qualitative input which can be selected freely (e.g. different constitutive approaches, compare chapter 2) but not set on a level.

For numerical inputs an example for a qualitative input is the weighting factor which determines the mesh density. The controllable variables with an influence on the simulation result, such as the applied implicit code or the geometry of the elements are known but cannot be chosen freely. Examples for the uncontrollable variables in the current simulation are the number and size of the elements and the number of remeshing steps. Usually the occurrence of uncontrollable values requires the

randomized repeat of the experiments. In the simulation the influence of the uncontrollable values can be neglected because of the identical input values and numerical routines.

As output variables the chip geometry, chip temperature and the reaction force on the cutting tool are chosen. The values for strain, strain rate and nodal velocity are neglected because they cannot be easily verified by experimental results. The inputs which are regarded as factors were described in chapter 3. They will be examined concerning their influence on the outputs. On the one hand, these factors have in common that they are physical variables which have to be given to the software and which can be measured for the examined materials. On the other hand, they are not measurable under the extreme conditions which occur in cutting operations. Especially the very short times in chip formation and the very high cutting temperatures lead to extrapolations or assumptions. The influence of a change in material on the simulation result is given in **figure 7.9**. The distribution of the effective strain and the chip geometry of two simulations are shown. On the left, the material properties are taken from literature and a smooth, continuous chip is obtained. In the right picture the product of density and specific heat capacity and the thermal conductivity were reduced to model quasi-adiabatic behavior. The result is a segmented chip with a strong shear localization between the lamellae.

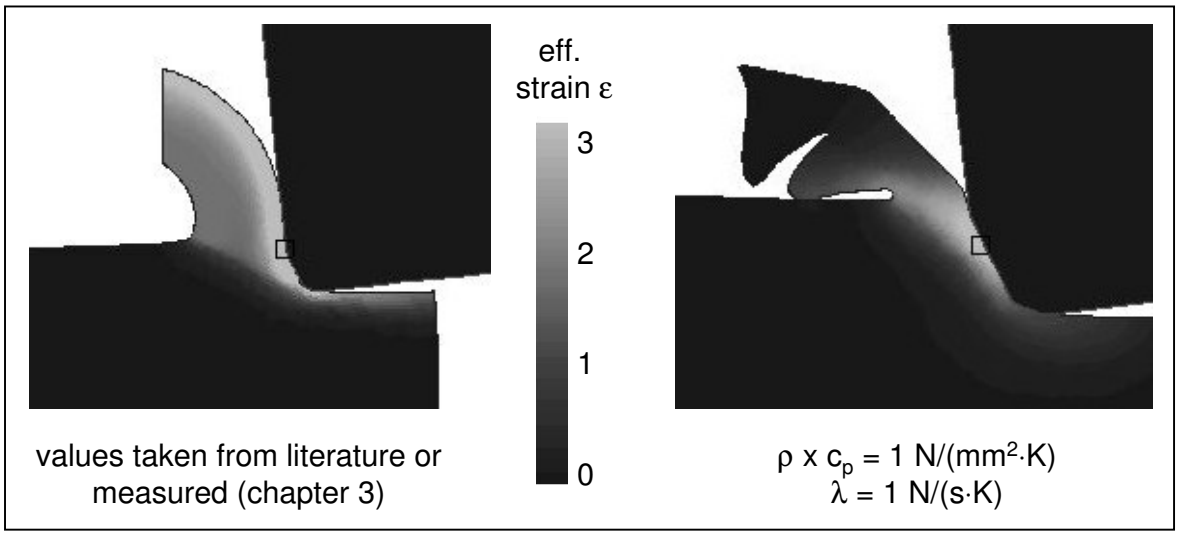


Figure 7.9: Influence of the input data on the simulation of chip formation (AISI 1045, v_c = 1000 m/min, f = 0.1 mm, a_p = 1 mm)

This strong dependency of the input data on the simulation result leads to the choice of the input parameters as factors shown in **table 7.1**. The other input data described in chapter 3 were kept constant. As flow stress curve the material law by Treppmann is implemented. Within the design of experiments only this flow stress curve is examined. To monitor its influence, the simulation results of different flow stress curves will be presented later.

As shown in table 7.1, eight input variables are chosen to be factors. The values for the different levels are taken from literature, were measured or assumed (compare chapter 3). The result of this examination will show which inputs have a strong influence on the simulated result and therefore have to be measured. The maximum difference between the upper and lower level of the factors is about 35 percent. If the difference between the two levels is too low, the influence on the result can be underestimated. If it is too high, it is possible that a maximum or minimum is located between the two levels and therefore the influence is underestimated. This is worse because the choice of only two levels allows only the description of a linear dependency.

factor	**symbol**	**unit**	**high level**	**low level**
convection coefficient h	A	N/(s·mm·K)	0.025	0.02
thermal expansion α_L	B	K^{-1}	$15.3 \cdot 10^{-6}$	$12.4 \cdot 10^{-6}$
Taylor-Quinney coefficient κ	C	-	1	0.8
friction coefficient μ	D	-	0.25	0.2
product of specific heat capacity and density $c_p \cdot \rho$	E	$N/(mm^2 \cdot K)$	5.0	3.7
thermal contact conductance h_{tc}	F	N/(s·mm·K)	1250	1000
thermal conductivity λ	G	N/(s·K)	41.27	28.8
Young's Modulus E	H	MPa	211400	166100

Table 7.1: Factors and levels for the DOE (AISI 1045)

To consider a non-linear dependency, a third level can be introduced and leads to more experiments. But even if the eight factors are examined on two levels, a 2^n-factorial design would lead to $2^8 = 256$ simulations. To prevent this, a fractional factorial design of $2^{8-4} = 16$ simulations is chosen. In this design only main effects and interactions of the first order are examined (**figure 7.10**). A main effect is defined as an input value that, if it is changed, has a significant effect on the interesting result.

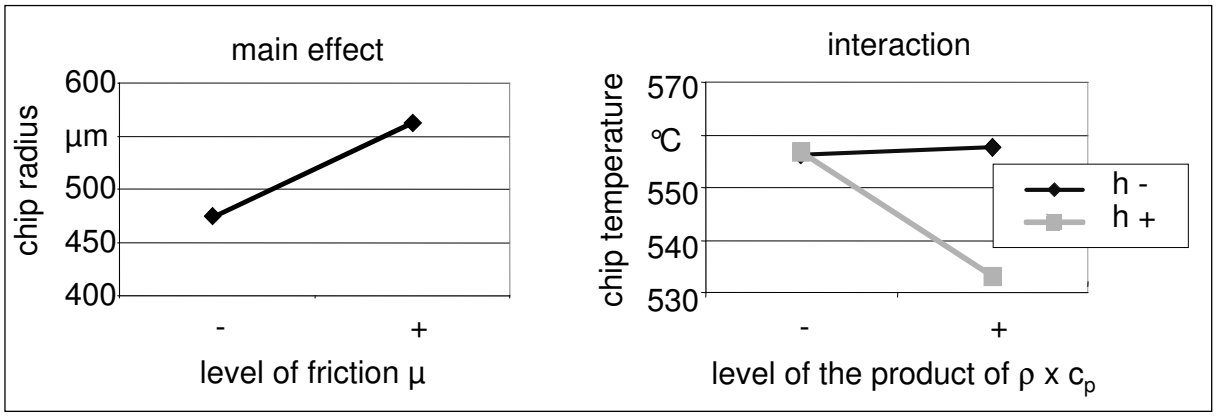


Figure 7.10: Examples of examined effects and interactions

An interaction is present if the effect of the interesting result depends on the combination of two input values. In figure 7.10 the level of friction has a significant effect on the result of interest, the simulated chip radius. The interaction of the product of density and specific heat capacity with the convection coefficient leads only in one of four possible combinations to a significant effect on the simulated chip temperature. The advantage of this factorial design is the reduction of simulations from 256 to 16. A disadvantage is that a factor, e.g. the friction coefficient, is set on the same input levels as the interaction. As the influence of interactions of more than two factors are often negligible, the chosen design will be suitable to identify factors with a high effect on the output /PFEI93/.The described approach leads to the following design. The interactions are not shown (**table 7.2**).

The level of the factors (given by the signs A-H) are shown by the numbers “-1” (low level) and “1” (high level). In the column “T_{sim}” the simulated chip temperature for each simulation is shown. The next column (T_{exp}) shows the chip temperature which was measured in the cutting process using the two-color-pyrometer described in chapter 5. It is the reference value for all 16 simulations. It can be found that all

simulations overestimate the chip temperature. The column ΔT shows that one combination of the factor levels leads to a good agreement (simulation number 2), while the most combinations lead to a larger error up to a 45 percent deviation (simulation number 14 and 15).

nr.	main effect								T_{sim} [°C]	T_{exp} [°C]	ΔT
	A	B	C	D	E	F	G	H			
1	-1	-1	-1	-1	-1	-1	-1	-1	1007	810	-24%
2	1	-1	-1	-1	1	1	-1	1	842	810	-4%
3	-1	1	-1	-1	-1	1	1	-1	1007	810	-24%
4	1	1	-1	-1	-1	-1	1	1	901	810	-11%
5	-1	-1	1	-1	1	-1	1	1	979	810	-21%
6	1	-1	1	-1	-1	1	1	-1	881	810	-9%
7	-1	1	1	-1	-1	1	-1	1	1111	810	-37%
8	1	1	1	-1	1	-1	-1	-1	1020	810	-26%
9	-1	-1	-1	1	-1	1	1	1	945	810	-17%
10	1	-1	-1	1	1	-1	1	-1	864	810	-7%
11	-1	1	-1	1	1	-1	-1	1	726	810	10%
12	1	1	-1	1	-1	1	-1	-1	1007	810	-24%
13	-1	-1	1	1	1	1	-1	-1	1007	810	-24%
14	1	-1	1	1	-1	-1	-1	1	1171	810	-45%
15	-1	1	1	1	-1	-1	1	-1	1171	810	-45%
16	1	1	1	1	1	1	1	1	1007	810	-24%

Table 7.2: Simulated and measured chip temperature for turning AISI 1045 at a cutting speed of v_c = 3000 m/min and a feed of f = 0.1 mm

In **figure 7.11** the main effects are shown. The value for the low level of each effect is the mean value of all simulation results where this effect is set to the low level and vice versa for the high level.

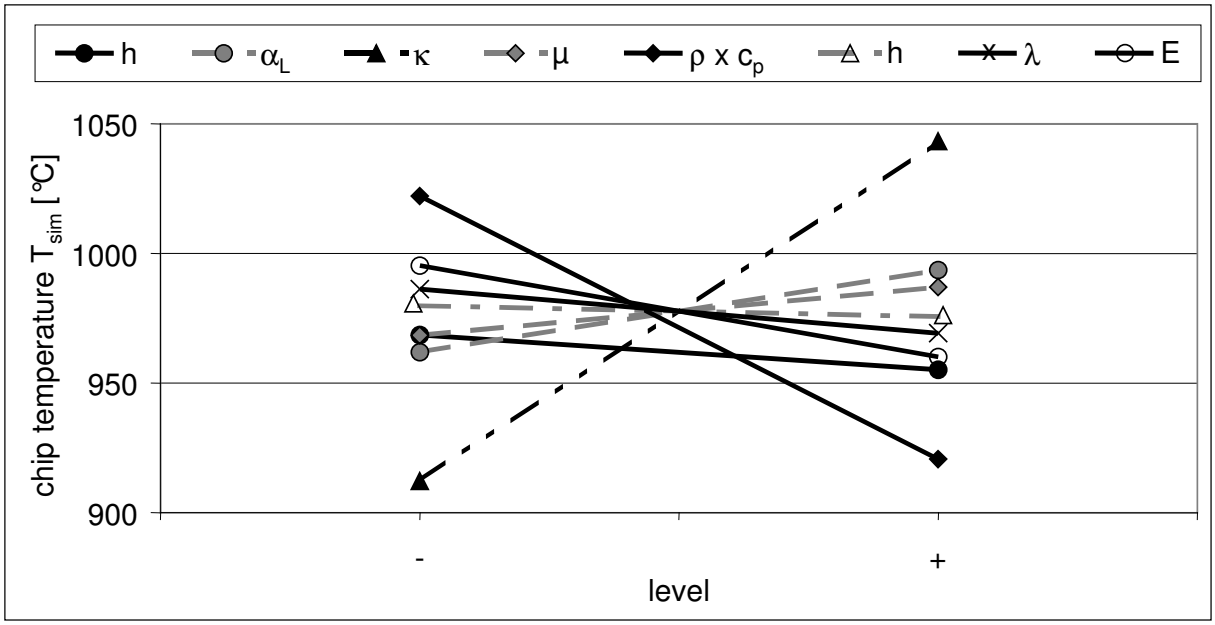


Figure 7.11: Main effects on the chip temperature for turning AISI 1045 at a cutting speed of v_c = 3000 m/min and a feed of f = 0.1 mm

It can be found that the inputs Taylor-Quinney coefficient κ (C) and the product of density and specific heat capacity ρ x c_p (E) have the strongest influence on the chip temperature. A 30 percent change of these inputs leads to a deviation of 130 °C and 1000 °C, respectively. This is not surprising as the quantity of mechanical work transformed into heat is given by the Taylor-Quinney coefficient (compare equation 3.17 and 3.19).

Based on these results the main result of the DOE is that the other inputs have a lower or nearly no influence on the simulated temperature. Of course this conclusion is only valid for the choice of factor levels given in table 7.1. A change of the levels and especially a bigger difference between the low and high level may lead to different results.

However, the current findings allow on the one hand the simulation setup without an exact determination of these six inputs which is significant because they cannot be determined without a huge amount of effort and extrapolation. On the other hand, the result of the DOE demands an intensive examination of the influence of the two significant inputs. One possibility is to check the interactions of these inputs with other inputs. Of course, the interaction of the two important inputs has the strongest influence on the chip temperature (**figure 7.12**).

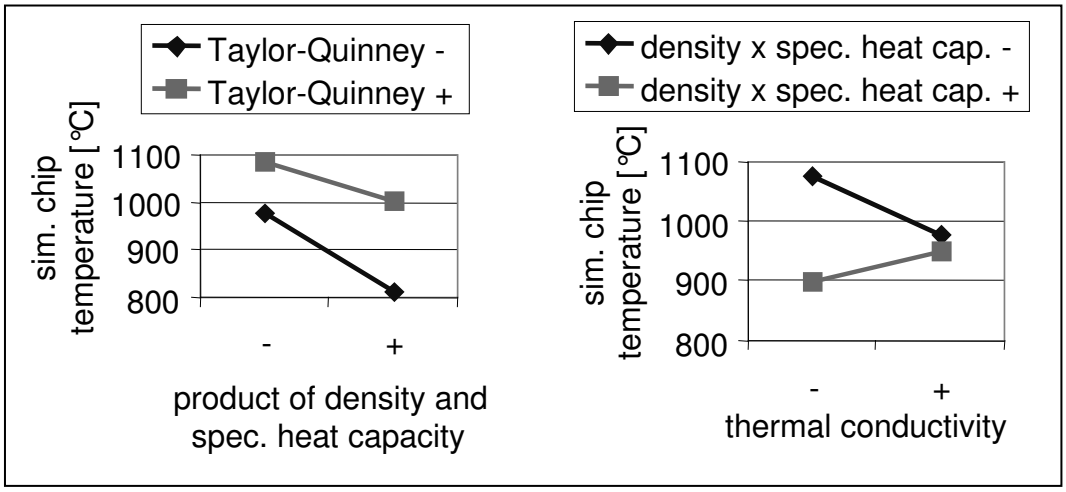
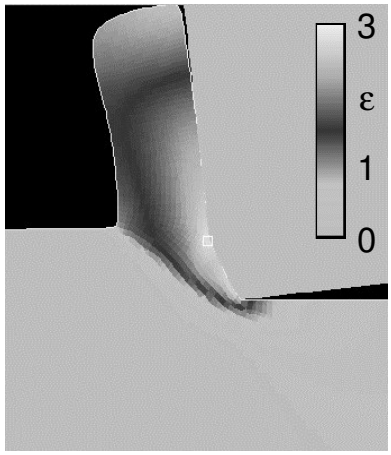


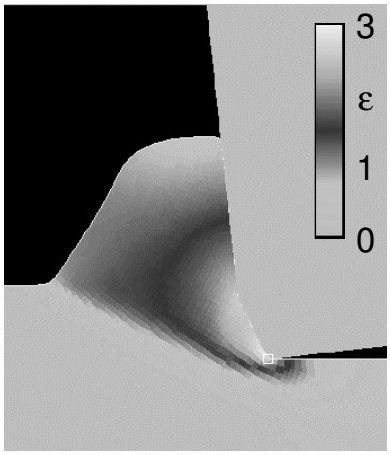
Figure 7.12: Influence of interactions on the chip temperature

Depending on the combination of all three, a temperature of T = 811 °C or T = 1083 °C is simulated. But also the interaction of a high and a low significant main effect can lead to remarkable temperature deviations (figure 7.12). The interaction of the thermal conductivity and the product of density and specific heat capacity can both be found in equation 3.17. As can be seen from this analysis, the experimental design leads to the reduction of the number of inputs which are not easy to measure. Then the focus is on the important inputs while their interaction with other, less important inputs, must be kept in mind. In the further examination, the input parameters with the best results (e.g. 2nd experiment in table 7.2) were taken as input values for the simulation.

7.6 Experimental verification of the simulation

In figure 7.9 the influence of two inputs on the chip geometry were shown. As mentioned above, the flow stress curve has a high influence on the results of the cutting simulation, too. It influences the simulated cutting forces as well as the chip geometry. The major problem is the unknown workpiece behavior at cutting conditions. In the primary and secondary shear zone high values for strain ($\varepsilon > 3$), strain rate ($d\varepsilon/dt > 10^5\ s^{-1}$) and temperature (near melting temperature) coincide. Under these conditions, the flow stress cannot be measured (chapter 2). Thus an extrapolation of the flow stress curve is necessary. **Figure 7.13** shows the influence of two different constitutive equations on the chip geometry.





$$\sigma(\varepsilon;\dot{\varepsilon},T)=(K\varepsilon^{n}+\eta\dot{\varepsilon})\exp\left(-\beta_1\frac{T-T_0}{T_m}\right)$$

$$\sigma(\varepsilon;\dot{\varepsilon},T)=(K\varepsilon^{n}+\eta\dot{\varepsilon})\left(1-\beta_3\frac{T-T_0}{T_m}\right)^{\alpha}$$

Figure 7.13: Influence of flow stress curve on chip geometry (AISI 1045, v_c = 100 m/min, f = 0.1 mm, material laws compare chapter 2)

It can be found that the different thermal softening leads to differences in chip thickness and the length of the contact zone. The equations are given in chapter 2 (equation 2.14 and 2.15). Beside these uncertainties, the chip geometry is a difficult parameter for the evaluation of the simulation results. This is due to the fact that most cutting operations lead to a segmented chip formation, e.g. high speed cutting of aluminum, magnesium and steel alloys as well as hard to machine and hardened materials. Even in orthogonal cutting, the segmented chip formation cannot be reduced to a two dimensional mechanism (compare chapter 5). However, the main motivation for simulating the chip geometry is to optimize chip breakage. To implement this into the model some kind of failure criterion has to be found. Approaches to achieve this will be given later in this chapter. For the following comparison of cutting forces and temperatures the differences in chip formation are neglected. This simplification is reasoned as follows. The segmented chip formation is due to alternating compression and shearing mechanisms. The compressed material is cold compared to that of the shearing area. Moreover, the volume of compressed material is much higher than that of the sheared one. The influence of the small volume of sheared material on the resulting cutting force is assumed to be low. As a consequence, the shearing process is neglected regarding the obtained cutting forces. Based on this assumption the simulated chip thickness, chip radius

and length of contact zone are described. These values are compared to the results of the external cutting and the in-situ photography of chapter 5.

7.6.1 Resultant forces in turning AISI 1045

In the past, the simulation was verified very often by the measured cutting forces /MARU95, KLOC01/ because they are easy to obtain by using a dynamometer. Using the constitutive material law by equation 2.14 gives the following results (**figure 7.14**). The differences between measurement and simulation at low cutting speeds are acceptable. When increasing the velocity, the agreement is very poor. This can be explained by the influence of the strain rate on the flow stress. In equation 2.14 the coefficient η is a constant. Therefore, an increase of strain rate results in a higher flow stress. Ongoing examinations show that the coefficient η decreases at high temperatures /ELMA04/.

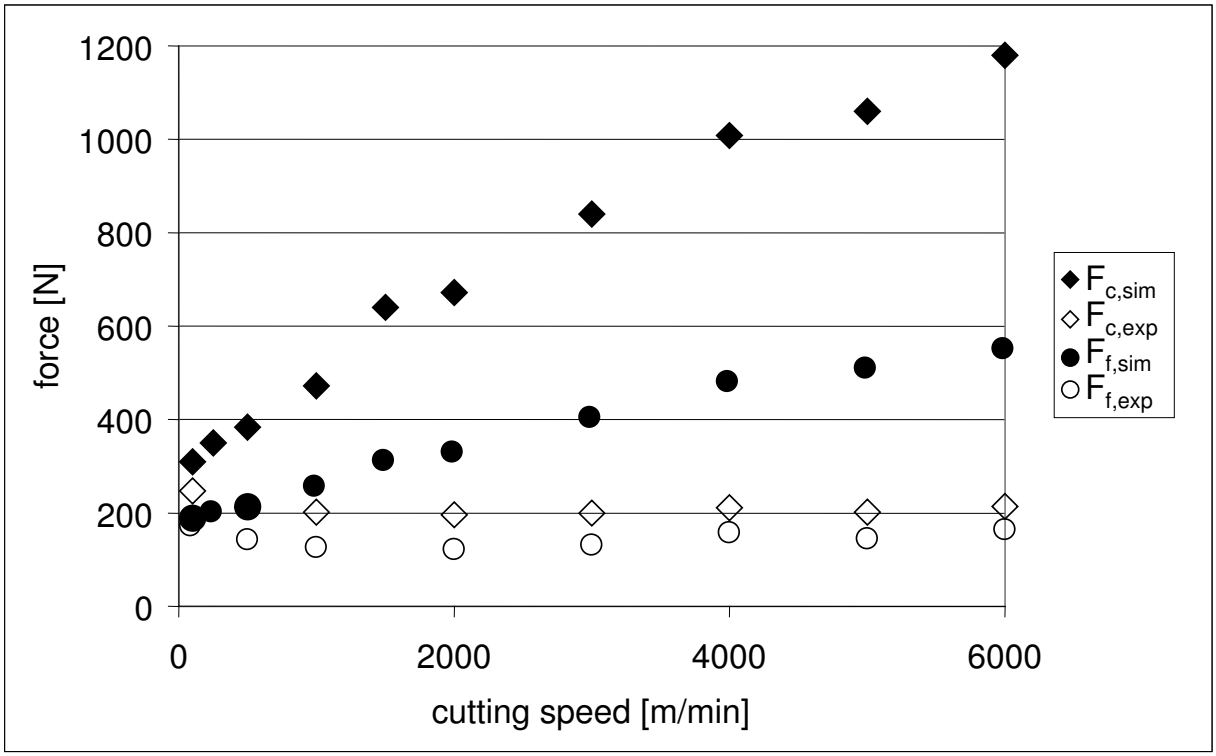


Figure 7.14: Simulated and measured cutting and feed forces (AISI 1045, material law: eq. 2.14, f = 0.1 mm, a_p = 1 mm)

If this will be implemented in the flow stress curve the agreement of simulated and measured resultant forces will be improved. The low agreement using equation 2.14 leads to the application of equation 2.13 for simulating the chip

formation of AISI 1045. The disadvantage of equation 2.13 compared to equation 2.14 is its transient nature. However, based on this constitutive law by Treppmann (equation 2.13) the comparison of simulated and measured cutting forces shows a good agreement. It can be found that the simulation tends to overestimate the cutting and feed forces at high cutting speed and underestimates them at low cutting speed (**figure 7.15**). The strong influence of the strain rate sensitivity is therefore still a problem. The described ongoing investigations on a temperature dependent strain rate coefficient η, however, will lead to further improvement. Furthermore, Gente found a strong dependency of the friction coefficient in this range of cutting speed /GENT02/. The friction coefficient decreases from μ =0.3 at v_c = 250 m/min to μ = 0.18 at v_c = 1000 m/min. It is obvious that in this range of cutting speed future simulations have to consider the strong increase of cutting temperature (figure 5.16).

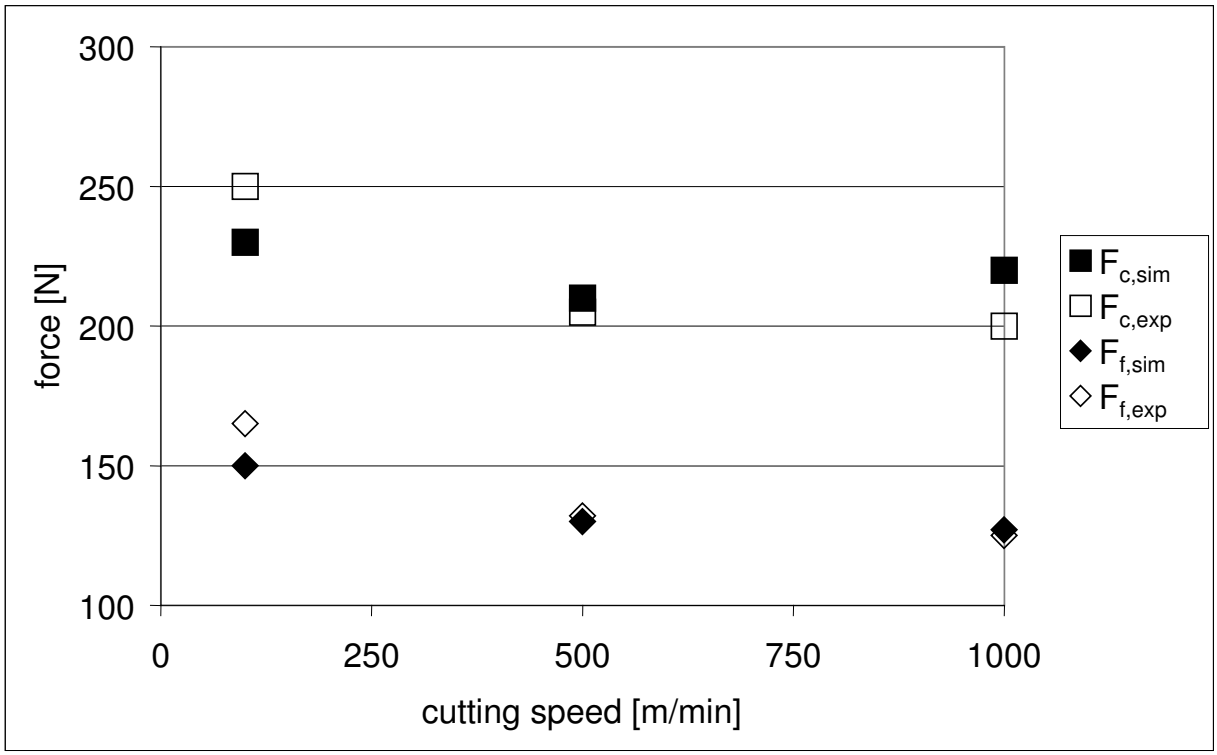


Figure 7.15: Simulated and measured cutting and feed forces (AISI 1045, material law: eq. 2.13, f = 0.1 mm, a_p = 1 mm)

7.6.2 Chip geometry in turning AISI 1045

As described above the chip geometry in the simulation and the experiment are not the same. This affects of course the values for the length of cut, chip radius and chip thickness. However, for low cutting speeds the error is less significant. Therefore, a comparison is done for low cutting velocities. **Figure 7.16** shows the results of the length of the contact zone measured from the external cutting $l_{k,ext}$ (figure 5.29), the in-situ photography $l_{k,in\text{-}situ}$ (figure 5.54) and the simulated one. The best agreement is found for the values of the external cutting. This can be explained as follows. The length of cut obtained from the insert analysis in the SEM can be assumed as a lower boundary. It always gives the value for the area of the contact length where an intensive shearing contact is found. In contrast, the in-situ measurement does not allow to distinguish between the plastic and elastic parts of the contact length. As the workpiece material is modeled ideally-plastically, no elastic behavior is considered and it is obvious that the error by the in-situ photo must lead to a higher deviation.

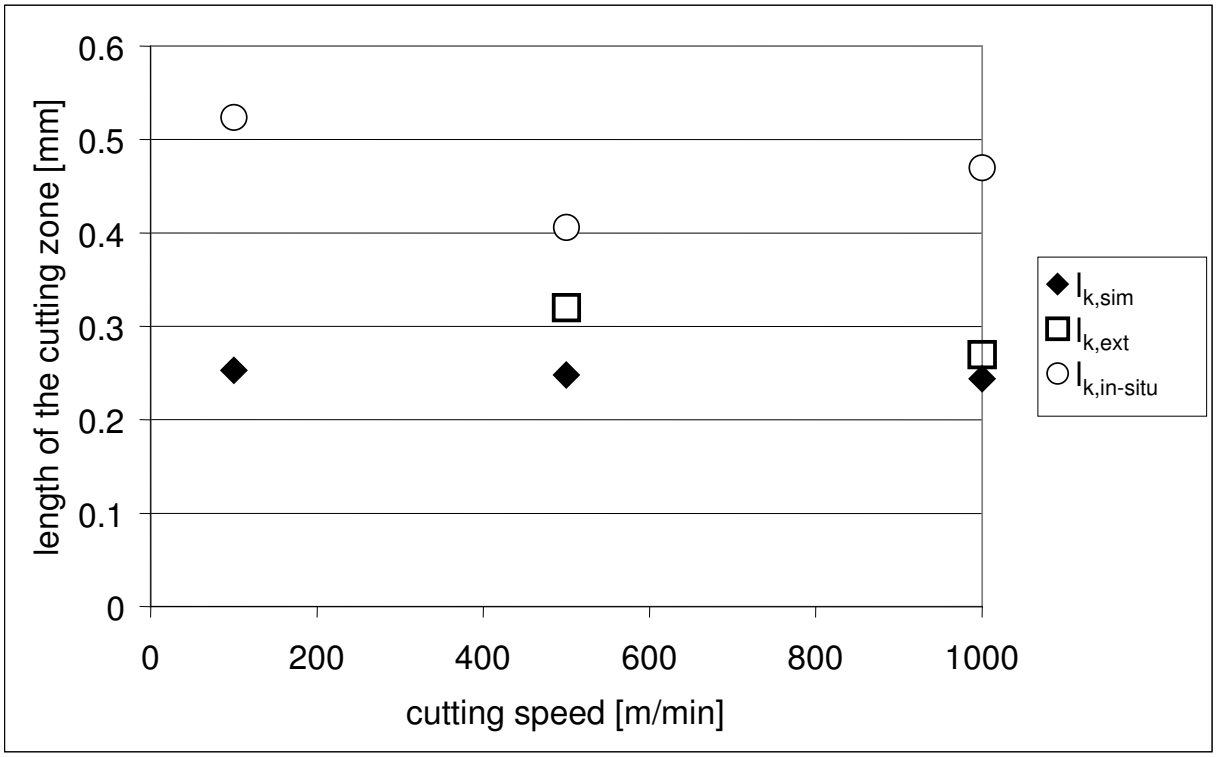


Figure 7.16: Simulated and measured length of contact zone at different cutting speeds (AISI 1045, material law: eq. 2.13, f = 0.1 mm, a_p = 1 mm)

The chip thickness is a value that allows to verify the chosen material law. As the chip formation is discontinuous even at low cutting speeds (figure 5.24) only a mean

value of chip thickness can be compared to the simulated continuous chip. The mean chip thickness obtained in external cutting tests as well as the in-situ results show a good agreement with the simulation, **figure 7.17**. Thus the applied material law is not too inaccurate. For the chip velocity only the data of the in-situ photography can be taken to verify the simulation results. If the chip formation is continuous it can be calculated by the ratio of the chip and uncut chip thickness obtained from external or orthogonal cuts. For segmented chip formation this is not possible. The comparison of simulated and measured chip velocity is given in **figure 7.18**. The agreement is very good. This is surprising as the difference of continuos (simulation) and discontinuous (experiment) should have an influence. The reasons for the good agreement are the high chip radii as well as the choice of the measurement spot. Latter is laid near to the secondary shear zone for the experiment as well as for the simulation. The chip movement in this area is similar for continuous and segmented chip formation (compare figure 5.56).

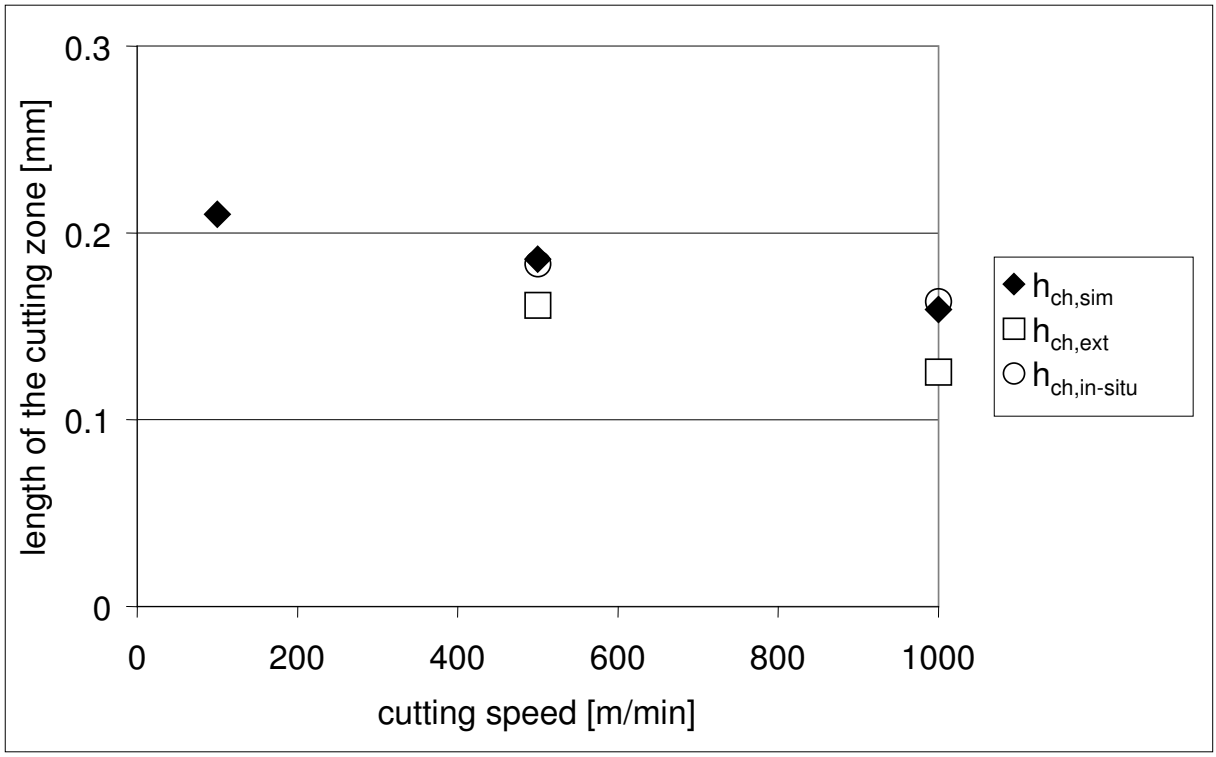


Figure 7.17: Simulated and measured chip thickness at different cutting speeds (AISI 1045, material law: eq. 2.13, f = 0.1 mm, a_p = 1 mm)

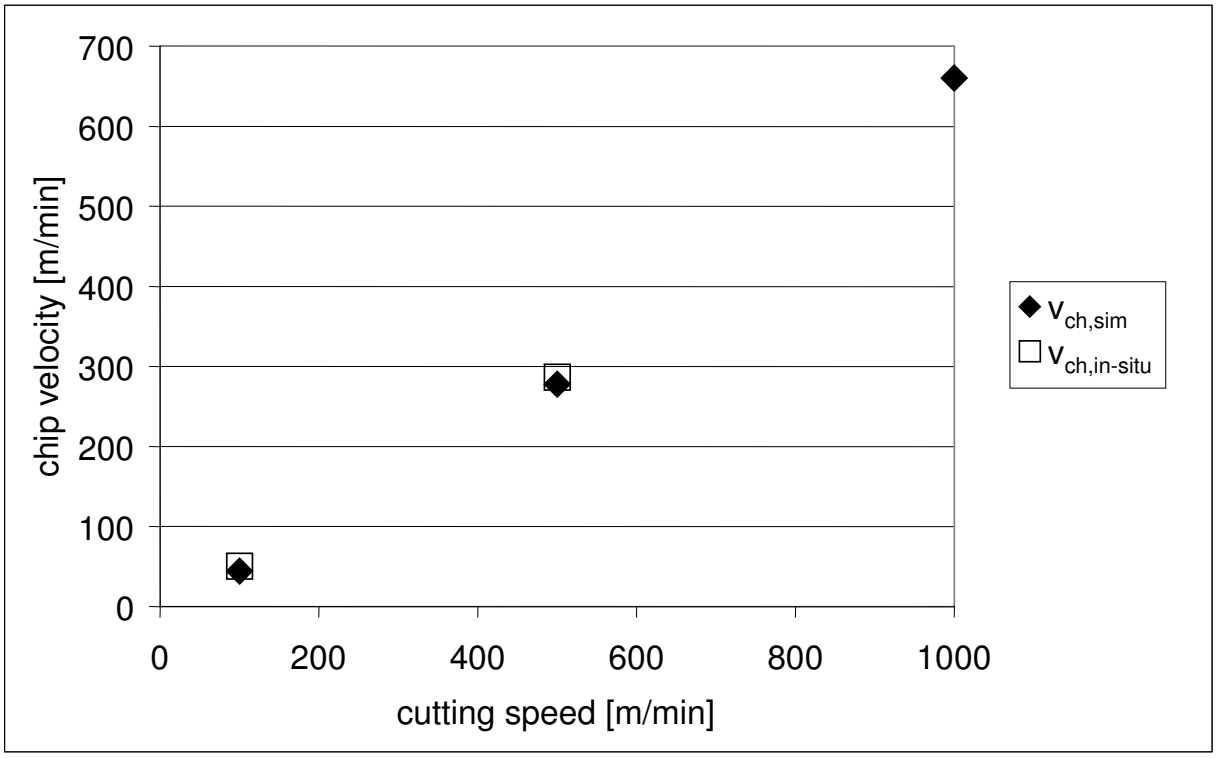


Figure 7.18: Simulated and measured chip velocities at different cutting speeds (AISI 1045, material law: eq. 2.13, f = 0.1 mm, a_p = 1 mm)

7.6.3 Chip temperature in turning AISI 1045

As mentioned above, the chip temperature depends on different inputs and their interactions. The results from the experimental design lead to an optimized combination of inputs. Conducting a simulation based on the results of the DOE a good result was achieved for moderate cutting speeds (**figure 7.19**). This is due to the fact that the measured chip temperatures approach a constant value, the melting temperature of the workpiece material (compare chapter 5).

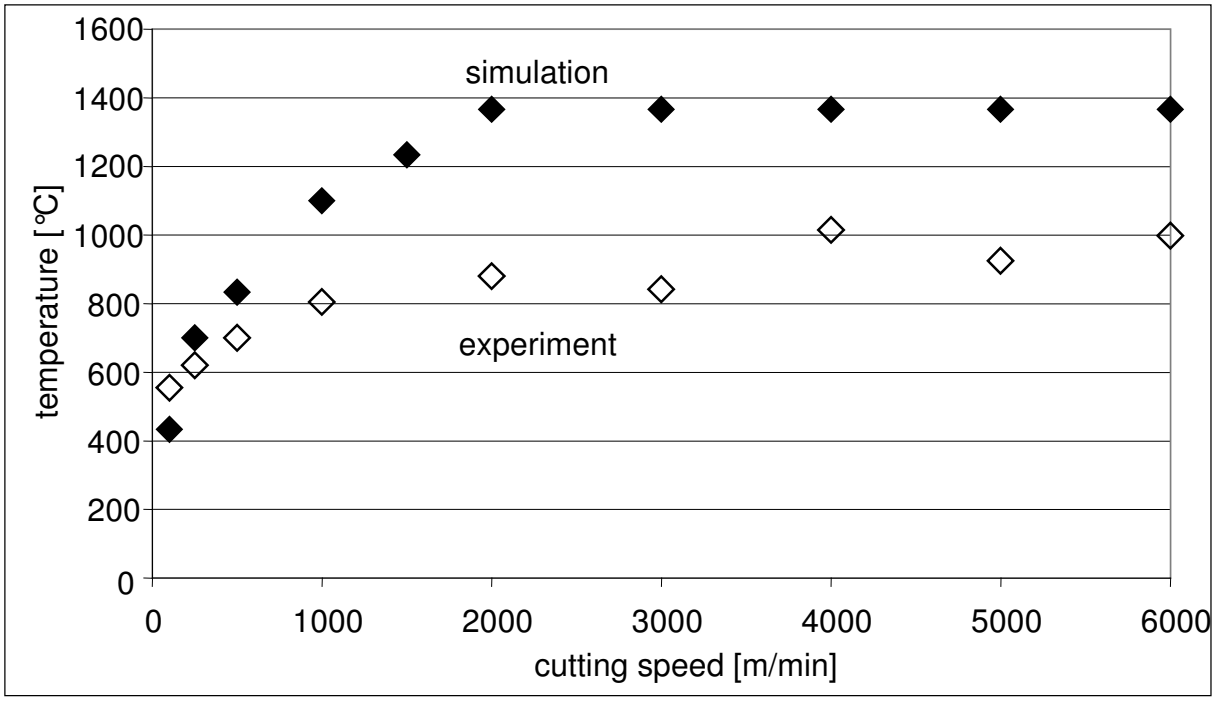


Figure 7.19: Simulated and measured chip temperatures at different cutting speeds (AISI 1045, material law: eq. 2.13, f = 0.1 mm, a_p = 1 mm)

As a consequence, the maximum temperature of the simulation is also limited by the melting temperature. This modification is necessary to prevent the simulation from calculating flow stresses for molten materials. The error caused by the temperature limit is low. This can be explained by the fact that the melting temperature in the cutting process will occur at the bottom of the chip near the end of the contact zone. The velocity of the chip and the pressures in this area push the molten material out of the cutting area. As a consequence the temperature of the bottom of the chip will always be limited by the melting temperature. The chip temperature was measured using the two-color pyrometer (chapter 5). The deviation of the measured and simulated chip temperature at high cutting speeds can be due to different influences. First of all the measurements do not take place in the hottest area of the cutting process. This is due to the short contact zone of chip and tool in cutting steel with a feed of f = 0.1 mm. Actual measurements where the fiber is located close to the tool tip show further increased temperatures /MUELx1, MUE04a, MUEL04/. Furthermore, if molten material is carried away, the temperature measurement will always lead to lower temperatures. Another possible reason are the differences of simulated and measured length of contact zone and chip radius. As a consequence it is not sure whether the measurement locations and diameters of the measurement spot are the

same in the experiment and the simulation. On the other hand it is not sure that, especially at very high cutting speeds, the fiber is completely covered by the chip. The boundaries of the chip are assumed to be colder than the center. A consequence is the measurement of lower temperatures.

7.6.4 Resultant forces in turning AA 7075

Beside modeling the chip formation in turning steel some simulations with aluminum were conducted, **figure 7.20**.

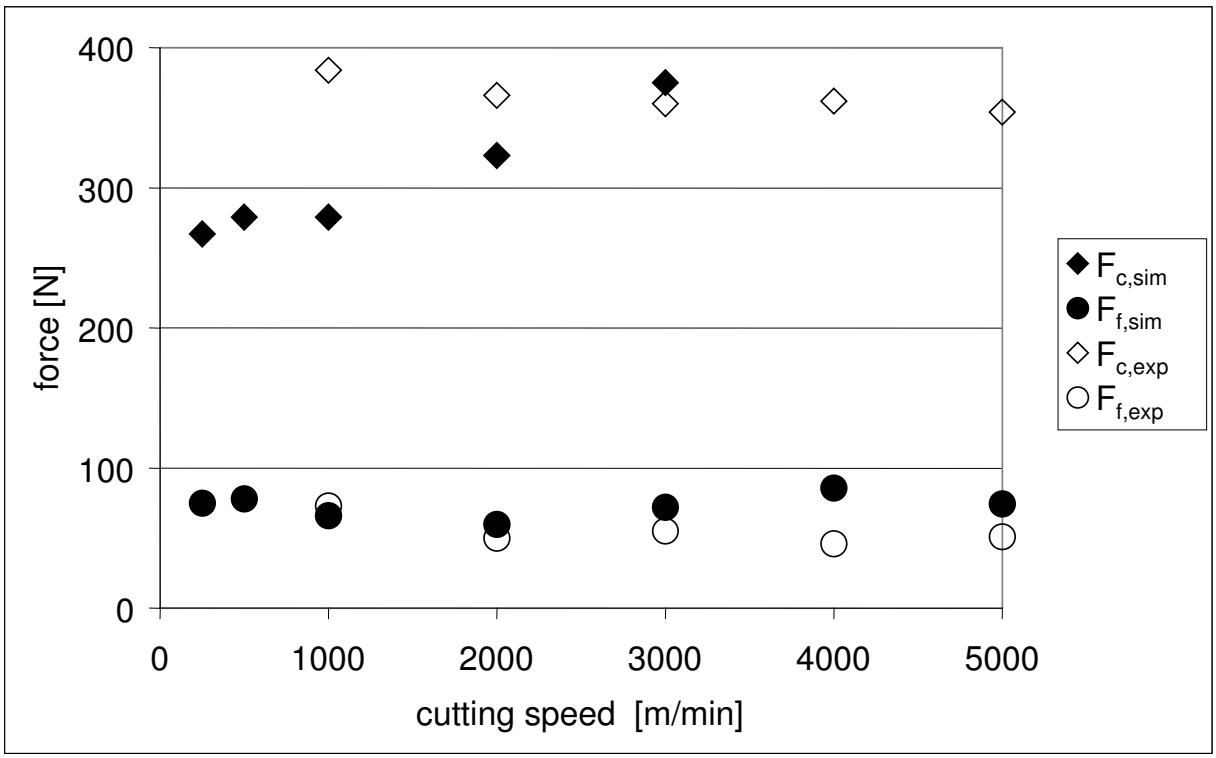


Figure 7.20: Simulated and measured cutting and feed forces (AA 7075, material law: eq. 2.14, f = 0.25 mm, a_p = 2 mm)

Examining the aluminum alloy AA 7075 it is found that applying the analytical constitutive material law (equation 2.14 and 2.15) allows a good prediction of the cutting forces for cutting speeds between v_c = 2000 and 3000 m/min. At low cutting speeds, the simulation underestimates the cutting forces. Increasing the speed above v_c = 3000 m/min, the simulation overestimates the forces. This is similar to the results of steel using equation 2.14. The stronger influence of the strain rate on steel compared to aluminum is due to the different values of the strain rate coefficient η. For aluminum the value is η_{al} = 0.004 MPa∗s while for steel η_{st} = 0.02 MPa∗s is

measured (compare table 2.5). A further reason may be the fact that in the simulation a continuous chip is found while the experiments, especially at high cutting speeds, show a strong chip breakage. The underestimation of the cutting forces at low speeds may also be due to the assumption of a constant coefficient of friction for all temperatures. As the chip formation, chip thickness, chip radius and length of the contact zone change in this area (compare chapter 5), an improvement of the input data is necessary.

7.6.5 Chip temperatures in turning AA 7075

The comparison of the simulated and measured cutting temperatures is given in **figure 7.21**. The poor agreement of measured and simulated cutting temperatures at low cutting speeds has the same reasons as explained for the cutting forces.

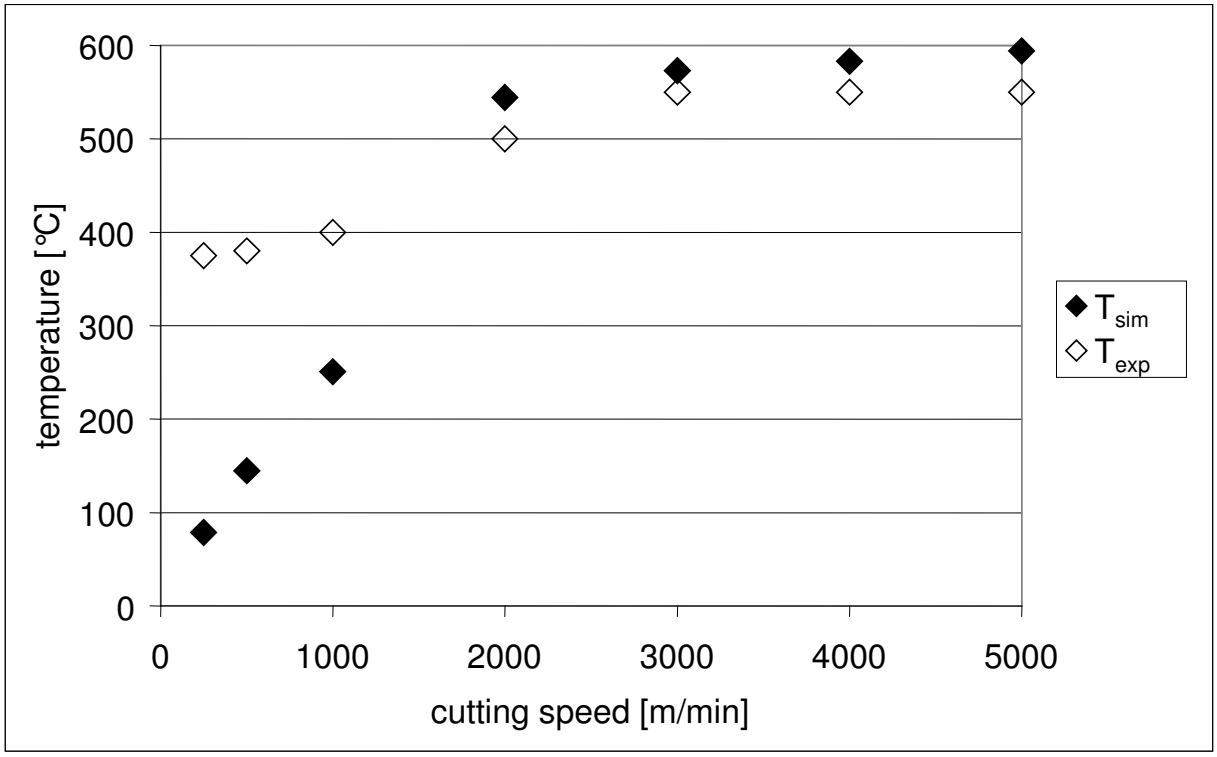


Figure 7.21: Simulated and measured chip temperatures at different cutting speeds (AA 7075, material law: eq. 2.14, f = 0.25 mm, a_p = 2 mm)

It is promising that the good agreement of predicted and measured cutting temperatures and forces is found in the same range of cutting speeds. In contrast to the results of the cutting forces a good agreement of the temperatures can be found at high cutting speeds. In this simulation the temperature was also limited by the

melting temperature. The reason why the agreement is better than for steel may be that the temperature measurement in cutting aluminum took place near to the contact zone. This was possible because of the higher toughness of the cemented carbide tool. Additionally the feed was f = 0.25 mm that enlarges the length of the contact zone and thus a temperature measurement in or near to the contact zone was possible.

8 Conclusions from cutting simulation

In chapter 7 the FE model of the cutting process was presented. Furthermore, the simulation results were compared to the experiments described in chapter 5. Several differences have been found and possible reasons were given. However, for machining AISI 1045 between a cutting speed of $v_c = 100$ m/min and $v_c = 1000$ m/min a good agreement of simulation and experiment was found. This agreement is achieved for the cutting forces as well as the cutting temperatures and even the chip geometry and speed. The presented model captures the thermo-mechanical mechanisms in cutting. As a consequence it can be used to describe the material behavior of the workpiece during the machining operation. Currently this is only valid if the influence of chip segmentation on the resultant forces and temperatures is neglected. The resultant error is low in cutting steel in the given range of cutting speeds.

8.1 Simulation of continuous chip formation

The steady state character of continuous chip formation allows an analytical modeling of the chip formation process. But, as described above, several assumptions have to be made for an analytical model. First of all, the process is reduced to the quasi two dimensional orthogonal cutting. Additionally, many parameters are assumed to be constant, e.g. the friction conditions at the tool rake face and the stress and temperature in the shear zones. Contrary, FE-method allows to consider variable temperatures and stresses in the shear zones. Moreover, even a three dimensional model of the process can be set up. Nevertheless, modeling of chip formation using FEM also needs the definition of several assumptions. The mechanism of chip formation has to be described in a way, that allows the creation of new surfaces, the secondary and the tertiary shear zone. Using currently available FEM codes, also the workpiece material has to be considered as homogenous and the friction between tool and chip has to be described.

To realize the creation of a new surface using the method of finite elements, two approaches exist. The first one is based on the classical theory of cutting that a fracture can be found in front of the tool tip. In the FEM such a fracture can be realized by the separation of two elements, by deleting an element or by substitution

of an element by two separated elements. The accuracy and numerical effects of these possibilities vary. For example, if the element in front of the tool tip is deleted, the information (stress, strain, strain rate, temperature) of this element is lost. This could lead to wrong results if the element density is low in that area. To delete or separate elements some kind of fracture law has to be formulated. In the most cases the fracture is started when the entering distance from the (very sharp) tool tip in an element exceeds a critical value. Other fracture criteria assume a critical strain or stress at which the new surface is generated /HUAN96/.

The second possibility to simulate the chip formation, which is applied in the current work, is to model the cutting process as a forming operation. The new surfaces are generated, similar to the fine blanking process, by shearing and forming processes. Also in this method, some information is lost. The reason is that in simulating the cutting process as a forming operation, the values for strain are very high and thus the mesh is highly distorted. To prevent the simulation from breaking down, a continuous remeshing has to take place. The information of the nodal points of the distorted mesh is transferred to a new, undistorted mesh by interpolation. Because of this interpolation some high gradients may be smoothed if the mesh density is to low.

The main advantages of the latter model are that no fracture or separation criterion in front of the tool tip are needed. Furthermore the theory of a fracture in front of the tool tip is not very likely when simulating cutting operations with a realistic, rounded tool tip. As mentioned above, a compression area can be found in front of the tool tip where the workpiece material moves very slow and also high compressive stresses occur.

8.1.1 Primary shear zone

In continuous chip formation, the shape and orientation of the primary shear zone are constant after the steady state is achieved. The distribution of the velocity in the direction of the cutting speed v_c can be used to define the location and shape of the primary shear zone, **figure 8.1**. Linking the tool tip and that point of the free surface where the material of the uncut chip thickness is transferred into the chip, the shear angle Φ can be found. In the area of the free surface and near to the tool tip, the orientation of the shear zone is well described by the shear angle. In front of the tool

tip the orientation of the primary shear zone and the shear angle differs. The primary shear zone is now divided into increments, each supplied with an own increment shear angle. Starting at the tool tip it can be found that the values for the increment shear angle rises from zero to the value of the shear angle Φ. In the area where the difference of shear angle Φ and increment shear angle Φ_i is not zero, the compression zone is located, figure 8.1.

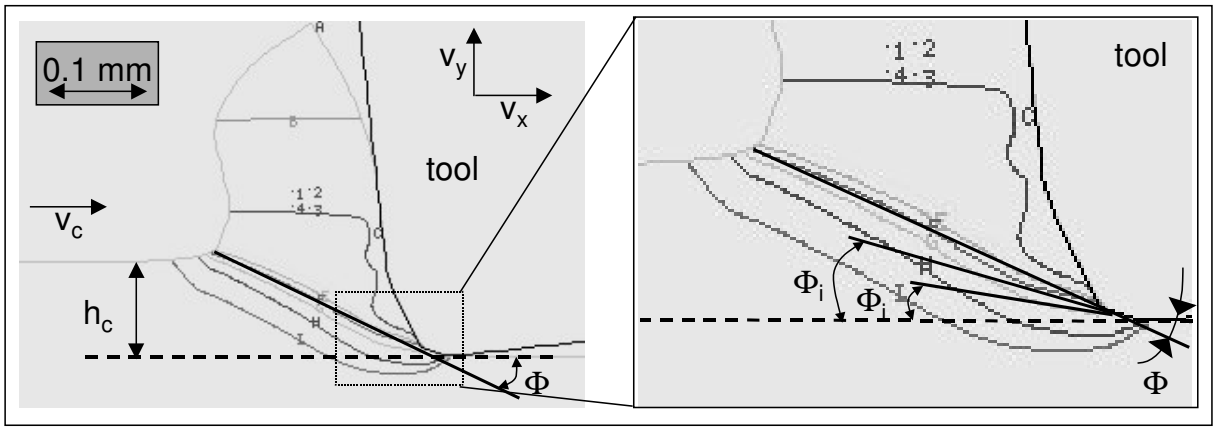


Figure 8.1: Location of the primary shear zone and the compression zone (AISI 1045)

The deformation and temperature history of the material which passes through the primary shear zone can be reported by conducting a point tracking for the interesting elements. In **figure 8.2** four areas in the uncut chip thickness are tracked (figure 8.2 right top). Before the workpiece material of the uncut chip thickness reaches the primary shear zone, a deformation takes place which was already described by Warnecke /WARN73/. The beginning of this low deformation zone is about half of the uncut chip thickness in front of the primary shear zone. In this area, an effective strain up to $\varepsilon_{,eff} = 0.2$ can be found and this deformation leads to a slightly increased uncut chip thickness. Thus the material entering the primary shear zone already has a forming history and will have a higher strength because of the strain hardening. Entering the primary shear zone, a strong increase of effective strain, effective strain rate and temperature is found. After the material has passed the primary shear zone, the shearing strain remains constant. Additionally, the relative position of the four points has changed (figure 8.2 right bottom).

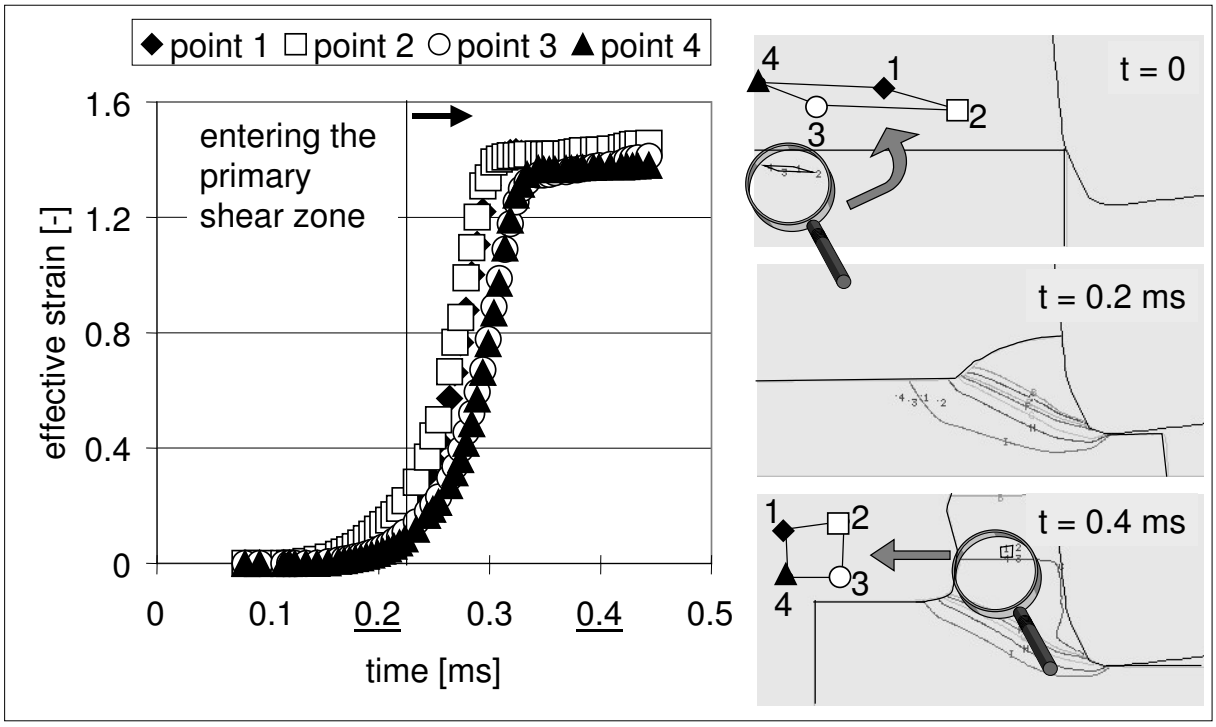


Figure 8.2: Point tracking of four points passing the primary shear zone (AISI 1045, material law: eq. 2.13, v_c = 1000 m/min, f = 0.1 mm)

The values for effective strain, stress, strain rate and temperature of the four points (figure 8.2) are given in **figure 8.3**. The effective stress is constant while the material passes the primary shear zone and afterwards decreases steadily to zero. The maximum value of the effective stress in the primary shear zone is equal for all points belonging to this shear zone while temperature, effective strain and effective strain rate are slightly higher for those points closer to the tool tip. These nearly constant conditions in the whole primary shear zone lead to continuous chip formation.

The values of one point (point 4 of figure 8.2) are plotted in **figure 8.4**. When the tracked element approaches the first deformation zone the strain rate and stress show an increase.

The temperature remains constant until the strain increases. The stress and temperature are constant until the element has passed the primary shear zone. The strain rate shows a maximum when the element is in the primary shear zone and decreases fast after passing through it.

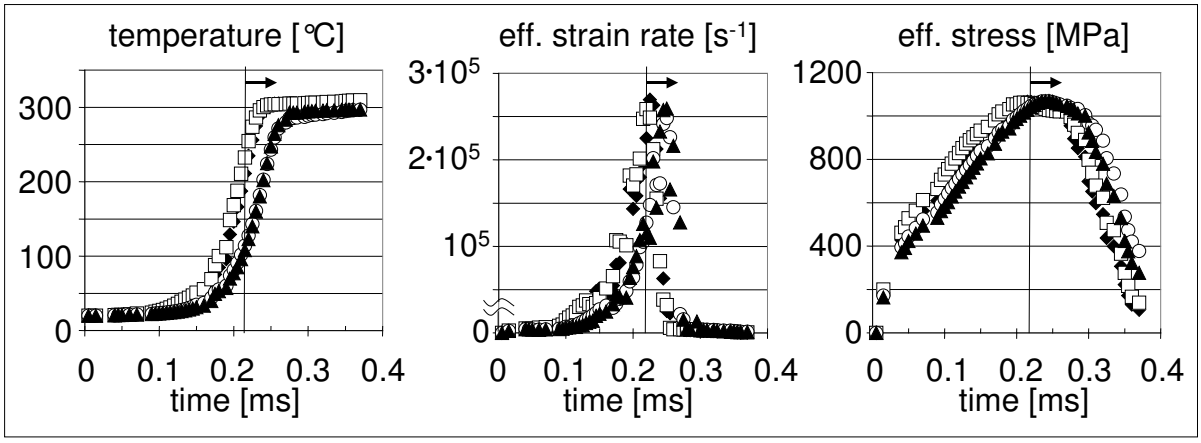


Figure 8.3: T, ε_v and σ_v for four points (figure 8.2) passing the primary shear zone (AISI 1045, mat. law: eq. 2.13, v_c = 1000 m/min, f = 0.1 mm)

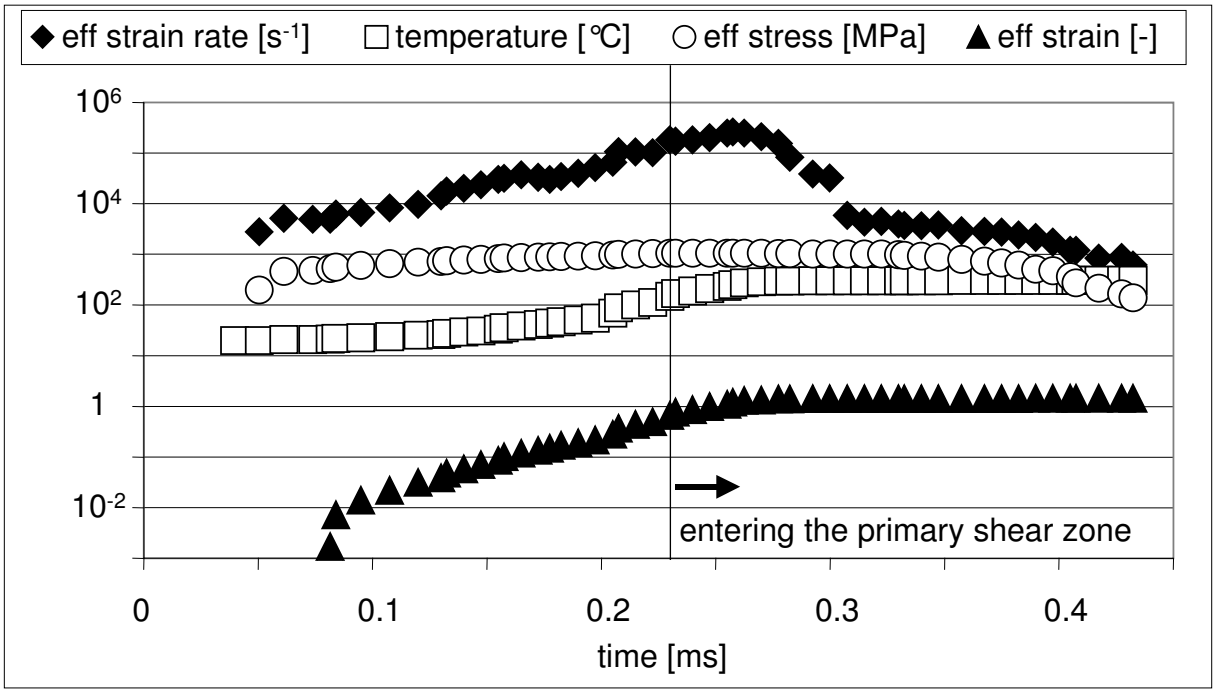


Figure 8.4: T, ε_v, $d\varepsilon_v/dt$ and σ_v for point 4 (figure 8.2) passing the primary shear zone (AISI 1045, mat. law: eq. 2.13, v_c = 1000 m/min, f = 0.1 mm)

8.1.2 Compression zone and build-up edge (BUE)

As described above, the area in front of the tool tip where the incremental shear angles are different from the shear angle is defined as the compression zone. This zone links the three shear zones and has a remarkable influence on the chip formation process. In this zone the workpiece material which approaches with the cutting velocity v_c is slowed down. **Figure 8.5** shows a point tracking for an element

located in the compression zone. At the beginning it passes the primary shear zone until the first maximum of the strain rate is obtained. At this time the stress, strain and temperature have obtained their maximum. These values do not change until the element leaves the compression zone in the chip and the stress decreases.

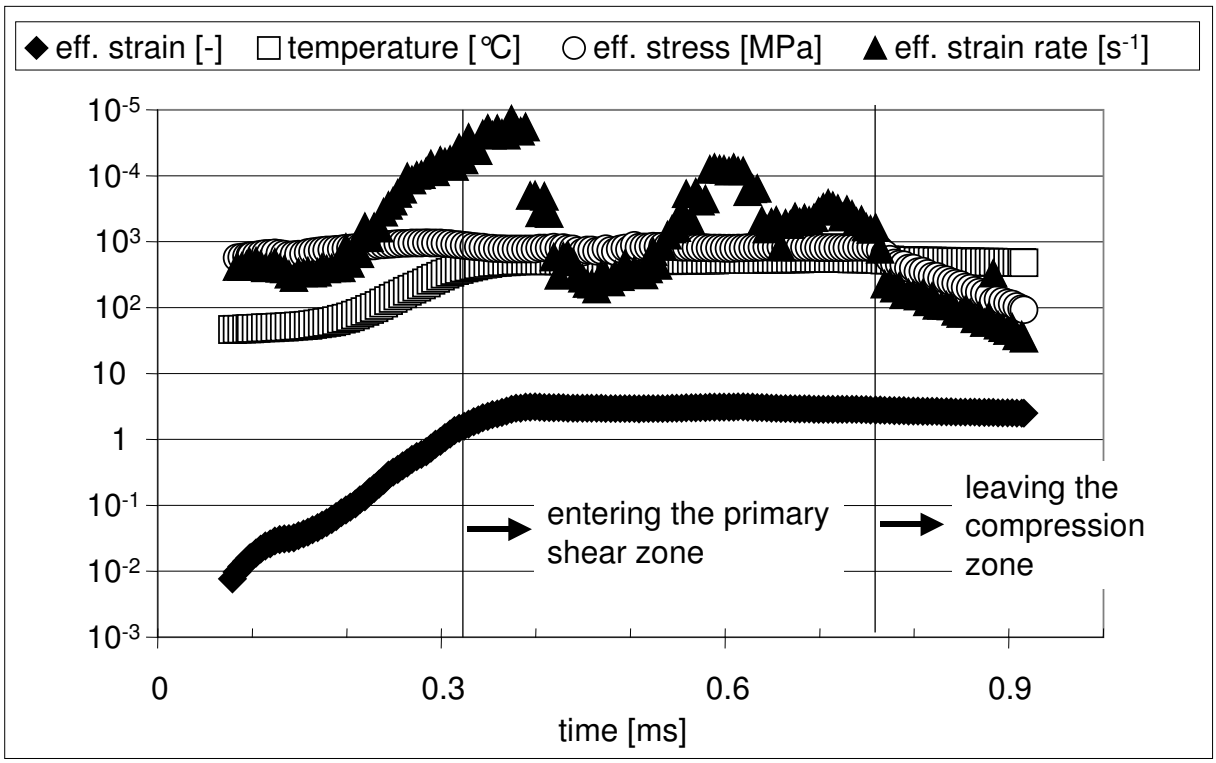


Figure 8.5: Point tracking of an element passing through the compression zone (AISI 1045, mat. law: eq. 2.13, v_c = 100 m/min, f = 0.1 mm)

In real cutting processes at low cutting speeds the presence of slow material in front of the tool tip leads to the occurrence of build-up edges (BUE) and therefore to increased tool wear and lower surface qualities. The influence of the build-up edge on the process quality is high and depends on several material dependent values such as the tribological conditions at the rake face, the tool surface quality and strain hardening behavior of the workpiece material. The simulation of the mechanism which leads to the occurrence of BUE would be very interesting for the design of cutting tools. Because of the unsteadiness of the BUE process and the unknown input data, a simulation of this process is currently impossible. Nevertheless, the current work will deliver the fundamental data to start investigations in this field.

In continuous chip formation without BUE the material which will be found at the bottom of the chip and on the machined surface has passed the compression zone.

This is quite important because this material will be in contact with the tool rake and flank face and is thus the tribological partner of the tool-workpiece contact which leads to tool wear. Monitoring and influencing the material which leaves the compression zone will offer new approaches to reduce tool wear and increase the workpiece quality.

8.1.3 Secondary shear zone and build-up layer (BUL)

The secondary shear zone is located at the rake face of the cutting tool. The transmission of the compression to the secondary shear zone is defined by the distribution of the chip velocity. In the area of the compression zone the components of the chip velocity which are orientated in feed direction change the sign. In the current simulation the beginning of the secondary shear zone is defined as the point where the chip velocity in feed direction (v_y) is higher than 30% (**figure 8.6**) of the maximum chip velocity in this direction. In figure 8.6 the isolines of the velocity components in x- and y-direction are given. The location of the three points 1 to 3 is important for the results of the following examinations.

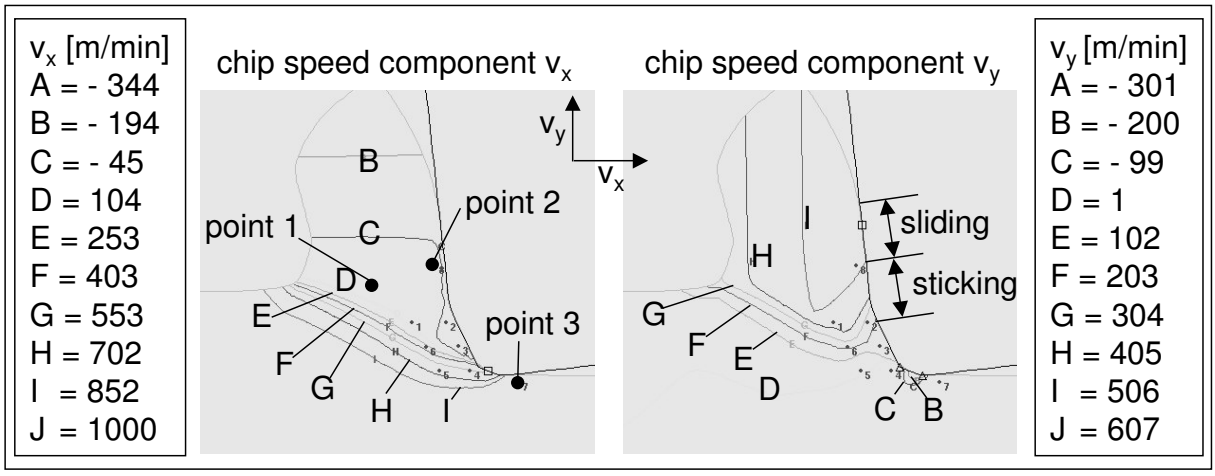


Figure 8.6: Definition of sticking and sliding zone by the velocity in feed direction (AISI 1045, mat. law: eq. 2.13, v_c = 1000 m/min, f = 0.1 mm)

In literature the secondary shear zone is further divided into a sticking and a sliding zone /ZORE66/. The idea behind this definition, which is also applied in the current work, is to obtain two areas with different friction conditions. In the sliding zone shear friction dominates. The chip velocity in feed direction is not constant. The chip material which is near or in contact with the rake face of the tool is slower than the

rest of the chip. In this work the chip material in the secondary shear zone with a speed below 80% (figure 8.6) of the chip velocity in feed direction belongs to the sticking zone. Because of the law of continuity and the constant chip thickness the velocity gradient has to be overcome by shearing of the chip. Therefore, shearing occurs in the sticking zone which can be visualized in the cross section of a chip. In literature, this shear zone is also called build-up layer (BUL) /SPAA71/ which must not be mixed up with the build-up edge (BUE). In the second part of the secondary shear zone, the sliding zone with a difference to the chip speed in feed direction of less than 20% (figure 8.6), no shearing occurs. In this area the chip is still in contact with the rake face of the tool, but the friction between the build-up layer and the rake face is of elastic nature and can be described by the Coulomb friction law. As mentioned above, the material of the secondary shear zone has passed the primary shear zone (**figure 8.7**).

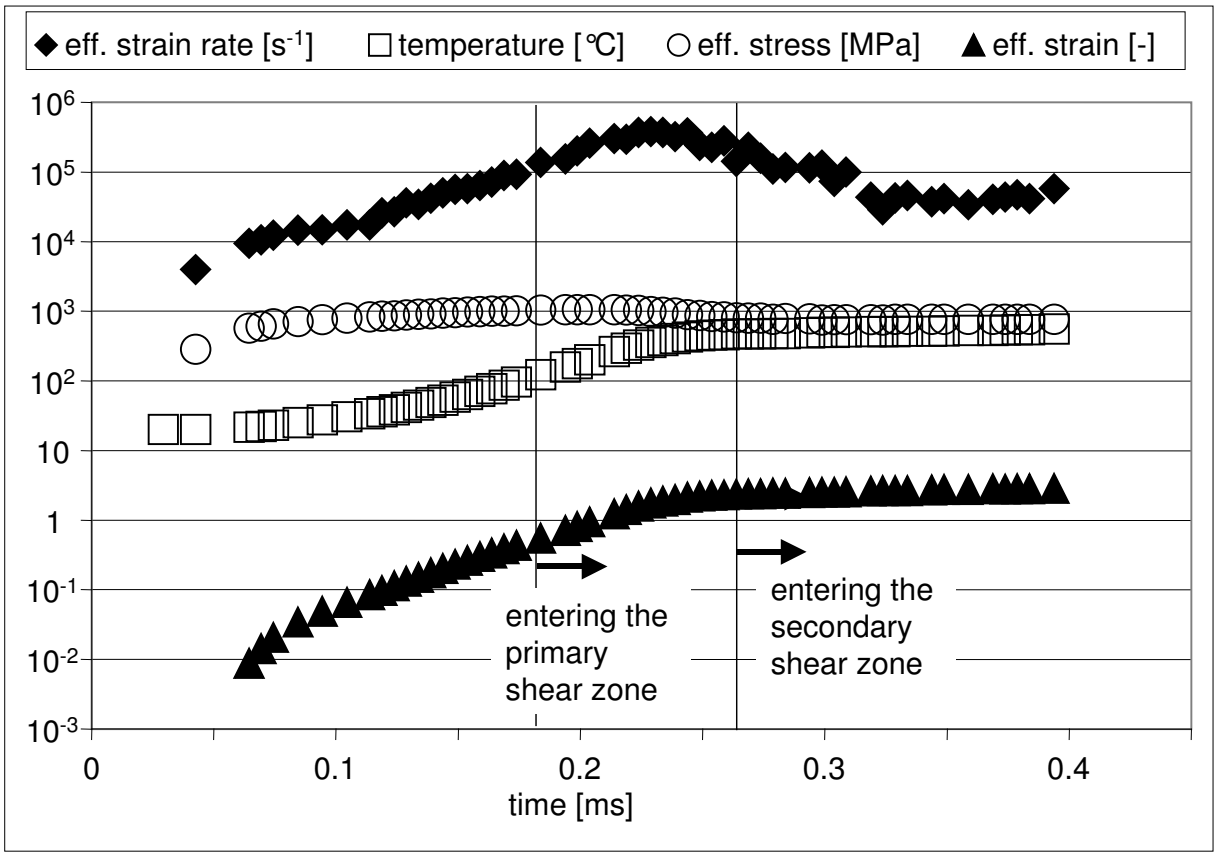


Figure 8.7: T, ε_v, $d\varepsilon_v/dt$ and σ_v for point 2 (figure 8.6) (AISI 1045, mat. law: eq. 2.13, v_c = 1000 m/min, f = 0.1 mm)

The effective strain summarizes from $\varepsilon = 0$ to $\varepsilon = 3.0$ and the temperature from room temperature up to 540 °C. The strain rate and stress are lower in the secondary shear zone.

8.1.4 Tertiary shear zone

The tertiary shear zone is the only one which does not belong to the chip but to the workpiece. Some of the material of the tertiary shear zone passes the primary shear zone, the rest the compression zone. The forming history of the material that has passed the primary shear zone and then enters the tertiary shear zone is similar to that in the secondary shear zone. The tertiary shear zone is also created by the gradient of workpiece velocity and can be separated from the compression zone by the change of velocity value from negative to positive in feed direction (**figure 8.8**).

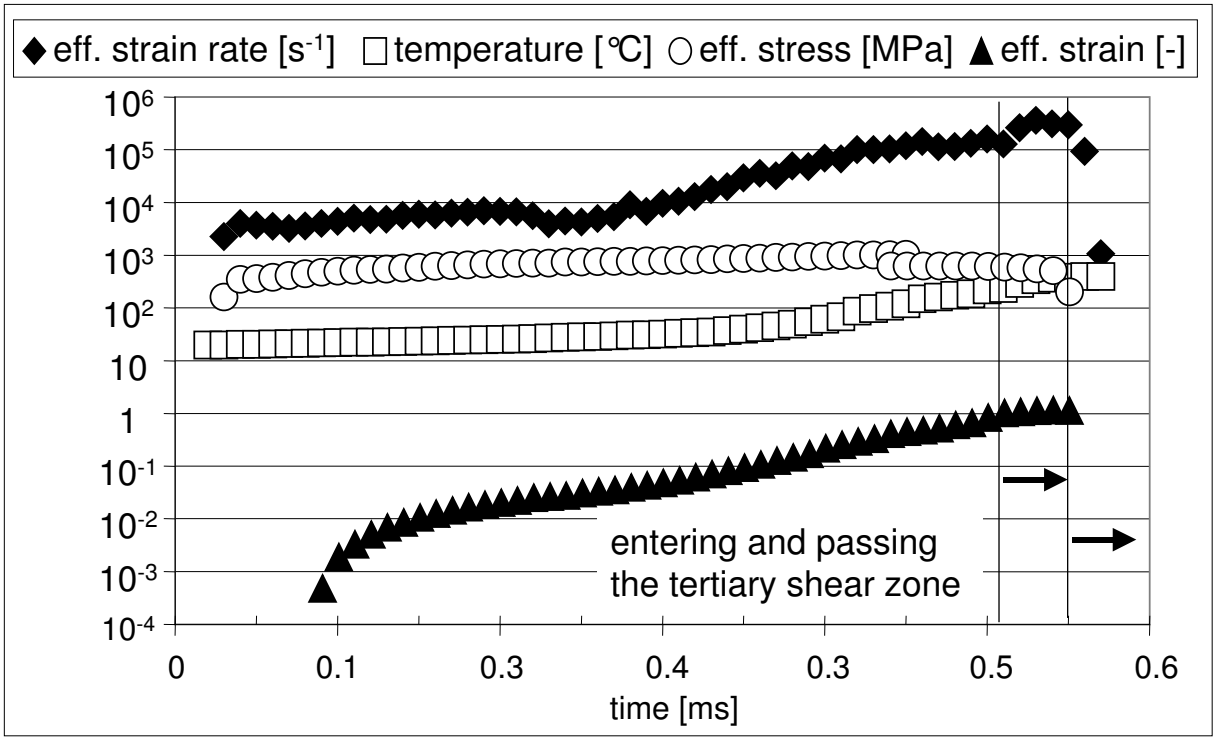


Figure 8.8: T, ε_v, $d\varepsilon_v/dt$ and σ_v for point 3 (figure 8.6) (AISI 1045, mat. law: eq. 2.13, v_c = 1000 m/min, f = 0.1 mm)

The length of the tertiary shear zone strongly depends on the tool geometry and the flank wear of the tool. When cutting with an unworn tool, the tertiary shear zone is dominated by the mechanisms in the compression zone. If the tool shows an increased flank wear, the contact zone between tool and surface increases. The

velocity gradient is high in the area of the whole tool-workpiece contact. Therefore, the shearing increases. Because of the already present deformation in the primary shear zone and the compression zone the forming ability is low.

This results in a thicker tertiary shear zone compared to that obtained with an unworn tool. The shearing which occurs in this area is very important for the further properties of the workpiece surface. It causes an increase of the temperature so that the workpiece could be annealed by the cutting process. This heat treatment of the workpiece can also influence the residual stresses and, when using coolant, the temperature gradient can lead to thermally introduced cracks.

8.1.5 Conclusions from simulating continuous chip formation

Comparing the maximum values of effective strain rate, strain, stress and temperature in the three shear zones for different cutting speeds the following results are found, **figure 8.9**:

- An increase of the cutting speed leads to a significant increase of the effective strain rate in all shear zones.
- The effective strain, stress and temperature are not affected in the same way.
- The effective stress is in the range of the flow stress and shows a low dependency on the cutting speed or the examined shear zones.
- The strongest deformation is found for all cutting speeds in the secondary shear zone. Its value is about $\varepsilon = 3$ which is twice the value of the other shear zones.
- The effective strain in the primary shear zone is high at low cutting speeds.
- In contrast to this, the effective strain in the tertiary shear zone rises if the cutting speed increases.
- The temperature shows a similar dependency on the cutting velocity. Its maximum value in the secondary shear zone is about $T = 700$ °C, the minimum value in the primary shear zone is $T = 300$ °C.

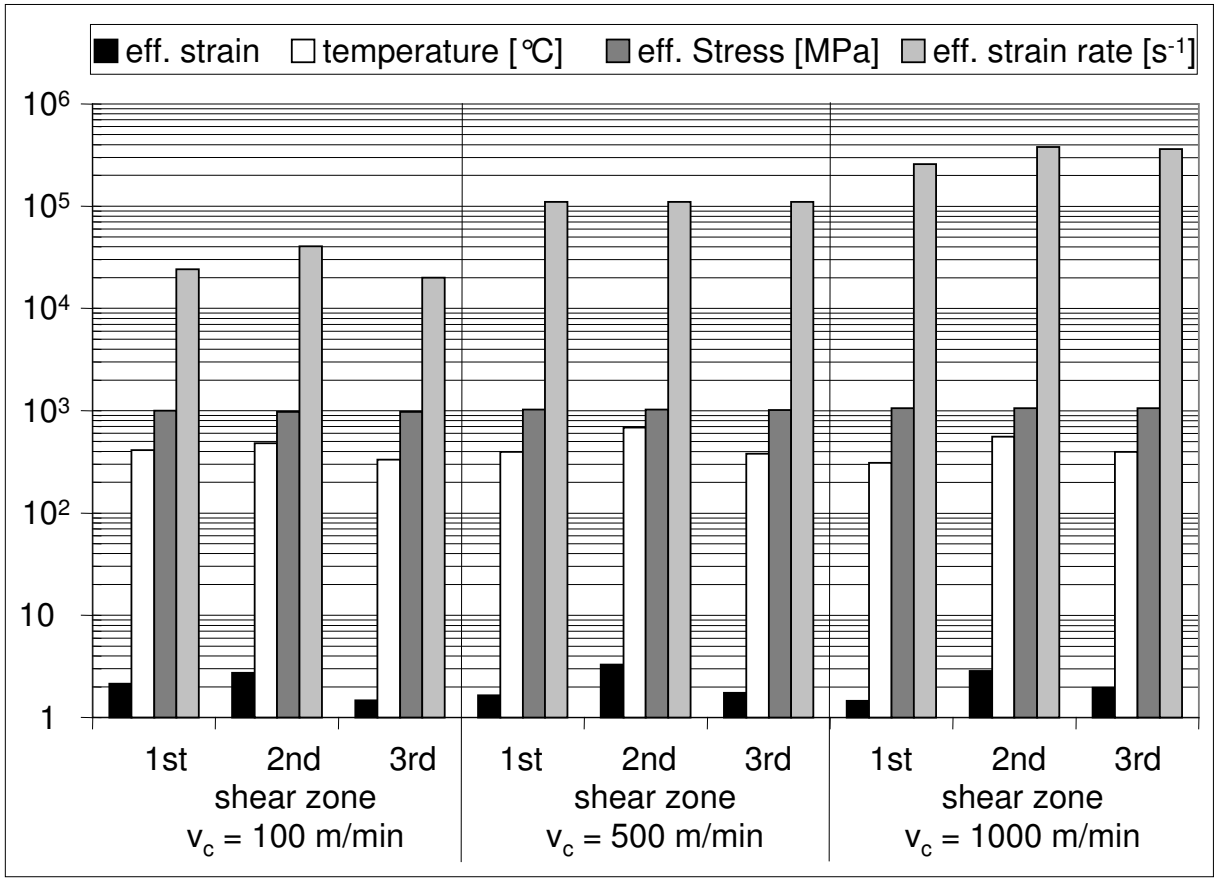


Figure 8.9: Influence of cutting speed on T, ε_v, $d\varepsilon_v/dt$ and σ_v in the three shear zones (points 1-3 in fig. 8.6, AISI 1045, mat. law: eq. 2.13, f = 0.1 mm)

These results are compared to the values Spaans obtained by applying the streamline theory /SPAA71/, **table 8.1**. It can be found that he underestimates the flow stress, the occurring temperature and strain. This conclusion is valid even though the compared cutting speeds are different. However, regarding the predicted strain rate at low cutting speeds a good agreement is found. The strong differences concerning the effective stress can be explained by the material data that was used in the different approaches.

Spaans assumed the damping factor (compare chapter 2) to be $\eta = 0.0017$ MPa•s. Based on the examinations by Treppmann /TREP01/ the damping factor in the simulation is $\eta = 0.02$ MPa•s and thus a magnitude higher. However, especially at low cutting speeds the agreement for effective stress, strain rate and temperature obtained by Spaans and the current FEM simulation is good. Both approaches predict a temperature decrease in the primary shear zone if the cutting speed is increased.

source	Spaans	FEM	Spaans	Spaans	FEM	FEM
cutting speed [m/min]	40	100	200	400	500	1000
effective stress [MPa]	500	998	540	560	1028	1061
max. temperature [°C]	350	413	330	320	395	309
max. eff. strain	3	2.13	3	3	1.6	1.45
max. eff. strain rate [s^{-1}]	$2.3 \cdot 10^4$	$2.4 \cdot 10^4$	$3.2 \cdot 10^4$	$3.5 \cdot 10^4$	$1.1 \cdot 10^5$	$2.6 \cdot 10^5$

Table 8.1: Comparison of data in the primary shear zone obtained by Spaans /SPAA71/ and FEM

8.2 Simulation of segmented chip formation

The most important shape in chip formation is the segmented chip. It can be found in cutting nearly all metallic materials, especially those with a high strength. Even for workpiece materials which show a continuous chip formation an increase in cutting speed, feed or a decrease of the rake angle leads to segmented chip formation. Additionally, for high performance cutting operations, where the chip has to be transported very fast out of the cutting area to prevent the tool or machined workpiece from damage, a segmented chip formation is preferred because of its advantageous chip breakage. Thus the segmented chip formation has to be simulated to allow the improvement of tools and parameters for high performance operations such as High Speed Cutting (HSC) and High Performance Cutting (HPC).

In the current work, the segmented chip and the serrated chip are referred to the expression segmented chip. This means, that the chip formation of cast iron, hardened steel, titanium alloys and of high speed cutting steel and aluminum alloys is described. The reason is, that the occurrence of segmented chip formation depends on mechanisms which influence the simulation results. In contrast to continuous chip formation, where the workpiece description by the flow stress data is sufficient, the simulation of segmented chip formation needs some kind of failure criterion. This can be modeled by different approaches described in this chapter.

The segmented chip is created by periodical compression and shearing. Therefore, the chip formation cannot be described by assuming a constant shear angle and a

time dependent modeling is needed. In the current model the assumption of adiabatic or catastrophic shearing is made. The mechanisms, which are also present in dynamical compression tests for aluminum (**figure 8.10**, compare chapter 2), can be described as follows: The uncut chip thickness or the specimen is compressed very fast. Because of the geometrical conditions in both setups, a shear localization occurs. The majority of the deformation energy is transformed into heat and thus a strong increase of temperature is found in this area. The heating rate is so high that the amount of heat decreased by thermal conduction can be neglected, the material softens and (adiabatic) shearing occurs, **figure 8.10**.

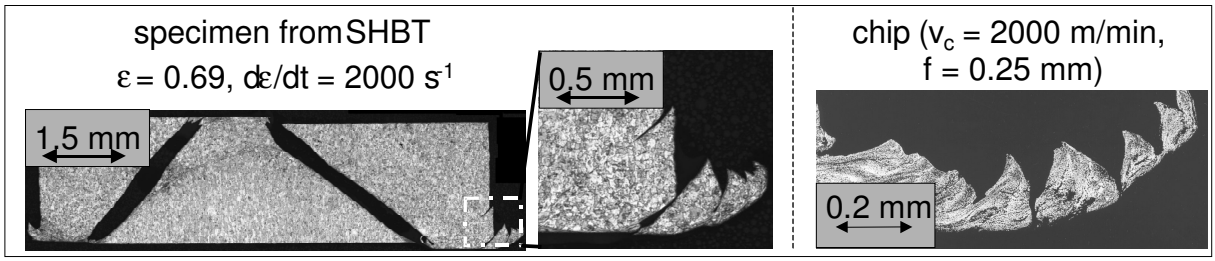


Figure 8.10: Comparison the specimen of a high speed compression test and a chip /TREP01/

In cutting, the short shearing period is stopped by the cold workpiece material which is found in front of the tool tip and the compression starts again. The adiabatic material behavior can be modeled by different means. One is to modify the flow stress curve. DEFORM uses the isothermal flow stress (compare chapter 2) curve to simulate the forming operation. This flow stress curve has a positive slope and therefore no instability caused by material softening at high strains occurs. If an adiabatic flow stress curve is used (compare chapter 2) the negative slope of the curve leads to an instability at high strains and thus a localization. However, applying an adiabatic curve within DEFORM is only correct if the Taylor-Quinney coefficient is set to zero. Otherwise the thermal softening would be twice, because the heat generated by the forming operation is still in the values of the adiabatic flow stress curve. On the other hand the Taylor-Quinney coefficient is also needed to calculate the heat generated by friction.

Because of these shortcomings a second approach is described. The adiabatic material behavior can also be modeled by modifying the specific heat coefficient and the thermal conductivity of the workpiece material. This method has the “advantage”

that the modification cannot evaluated experimentally. The heat transfer mechanism in chip formation takes place so quickly that no data can be obtained in measurements. However, the current available papers concerning segmented chip formation without the implementation of cracks use one of these criteria. Therefore, the results of both are presented.

8.2.1 Segmented chip formation based on a modified flow stress curve

The model described in chapter 7 leads to good results regarding the simulated resultant forces and chip thickness. However, the segmented chip formation is not realized. The reason for this error can be found in the available material data. As described above, the material properties have to be known over a wide range of temperature, strain and strain rate. Moreover, high gradients of strain rate and temperature have to be described. It may be possible that for those conditions the material test set-ups as dynamic pressure tests are not sufficient.

This is the reason why in the current simulation the calculated flow stress curve was modified. **Figure 8.11** shows the original and the modified curve. For high values of strain a decrease of the flow stress curve was assumed. The aim of this modification is to obtain a decrease of the workpiece stability which leads to catastrophic shearing. This approach is often used in simulating segmented chip formation /MARU01, KLOC01, BÄKE02/.

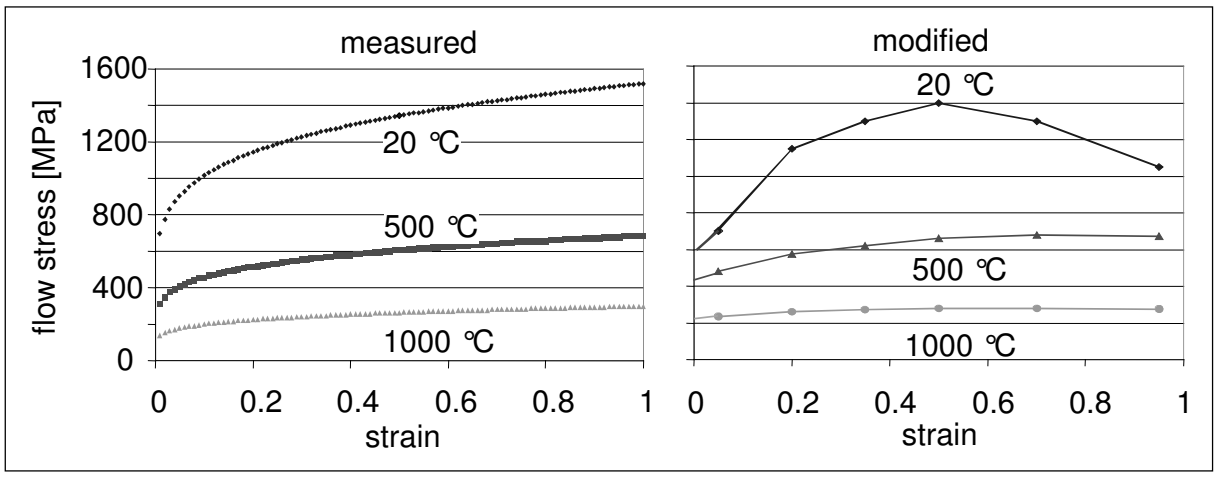


Figure 8.11: Measured and modified flow stress curve

The physical explanation of this would be, that the influence of the increased temperature generation on the workpiece stability is enforced. Up to $\varepsilon = 0.5$ the flow stress curves are not different. The strongest influence of the temperature generated by the high strain occurs at low temperatures. At high temperatures the influence of the strain generated heat is set small because a decrease of stability has already occurred.

This modification has a strong influence on the obtained chip formation, **figure 8.12**. A strong localization of the strain rate is observed. Because of the material softening in the areas of high strain a segmented chip formation occurs. The chip formation consists of two phases, the upsetting of the workpiece material and the shearing.

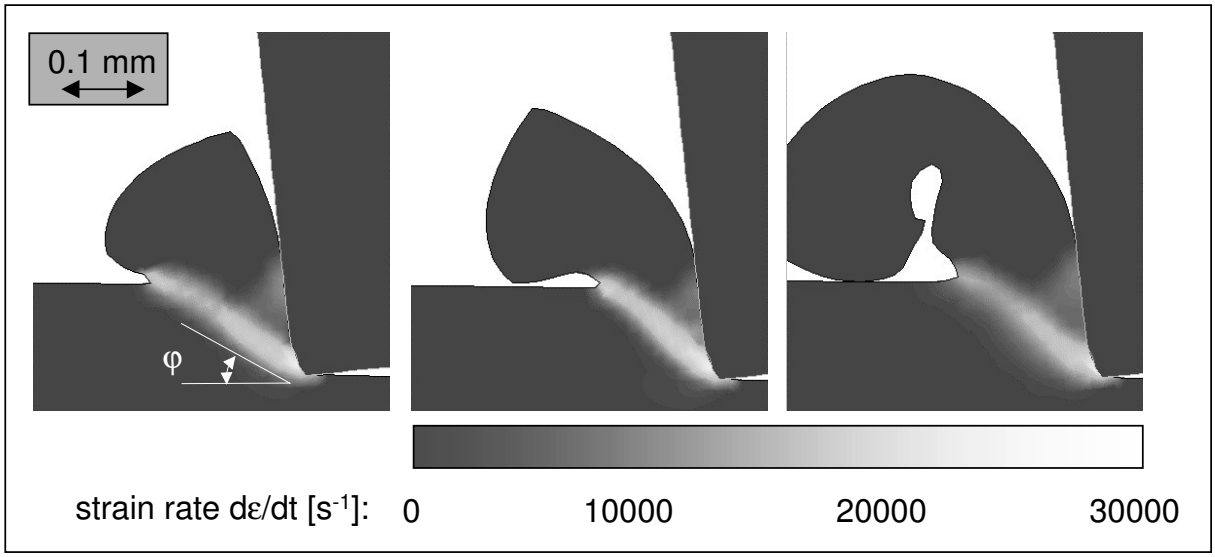


Figure 8.12: Strain rate distribution in segmented chip formation at $v_c = 3000$ m/min

Because of this process the angle φ is not constant. Furthermore the angle between the direction of the cutting speed and the plane between tool tip and free surface is no longer a shear angle. Latter is only valid in the shearing stage. This is the reason why the angle is not called shear angle ϕ but φ. The mechanism of alternating compression and shearing is known for the chip formation of titanium since 1973 /KREI73/. In Figure 8.12, the values for the angle φ vary between $\varphi = 29°$ and $\varphi = 36°$. The result is a varying chip thickness h_{ch} and a small radius of the chip. Unfortunately, the strong chip curling leads to the contact of chip and tool after only two lamellae. For a better description of the chip formation process, the cutting speed in the simulation is reduced to $v_c = 100$ m/min, **figure 8.13**, which leads to an

increased chip radius. The different states of the segmented chip formation can be seen. From the shearing of one lamellae (Figure 8.13 a) with a high angle of $\varphi = 35°$ the upsetting phase with a significant low angle of about $\varphi = 30°$ follows (Figure 8.13 b).The beginning of adiabatic shearing can be seen in Figure 8.13 c (arrow), followed by the adiabatic shearing Figure 8.13 d. The segmentation of the chip shown in Figure 8.12 and 8.13 is very smooth. This is due to the gradient of temperature decrease and the geometry of the used elements as described above.

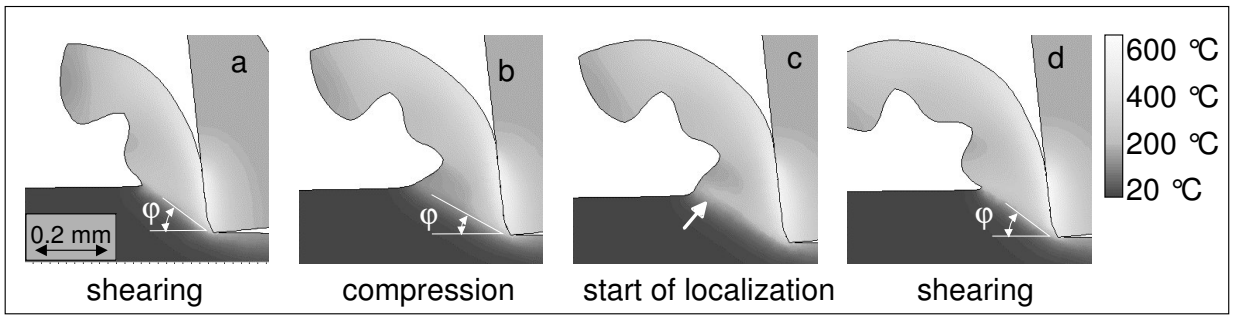


Figure 8.13: Temperature distribution in segmented chip formation at v_c = 100 m/min

8.2.2 Segmented chip formation because of modified thermal data

The simulation of adiabatic shearing can also be obtained by modifying the thermal input data. The distribution of the effective strain and the chip geometry of two simulations was shown in figure 7.9. A decrease of the thermal data lead to a quasi-adiabatic behavior. The result is a segmented chip with a strong shear localization between the lamellae. Compared to the modified flow stress curve the modification of the thermal data has the advantage that an isothermal flow stress can be used as well as a realistic Taylor-Quinney coefficient. Additionally the thermal input data cannot be measured at conditions as they occur in cutting. Therefore, a modification of the thermal data may be less critical than that of the flow stress curve /KLOC01, WEST02/. However, the modification influences the simulated forces. The adiabatic behavior leads to cutting forces that are about 25% lower compared to the experiment. To highlight the differences between a continuous and segmented chip formation a point tracking was conducted for elements in the lamellae and the three shear zones.

Because of the segmented chip formation the shearing in the primary shear zone is interrupted by the compression of the workpiece material. Therefore, this zone has to

be called “compression and shearing zone”. Nevertheless, to allow the comparison with the continuous chip formation the description “primary shear zone” is used for this area. The mechanism and the periodical character of this area can be described properly by the resultant force and the chip thickness. An increase in resultant forces and chip thickness can be found experimentally (compare figure 5.36) and in the simulation result. At the moment when the adiabatic shearing occurs the cutting forces drop and the chip thickness decreases, **figure 8.14**.

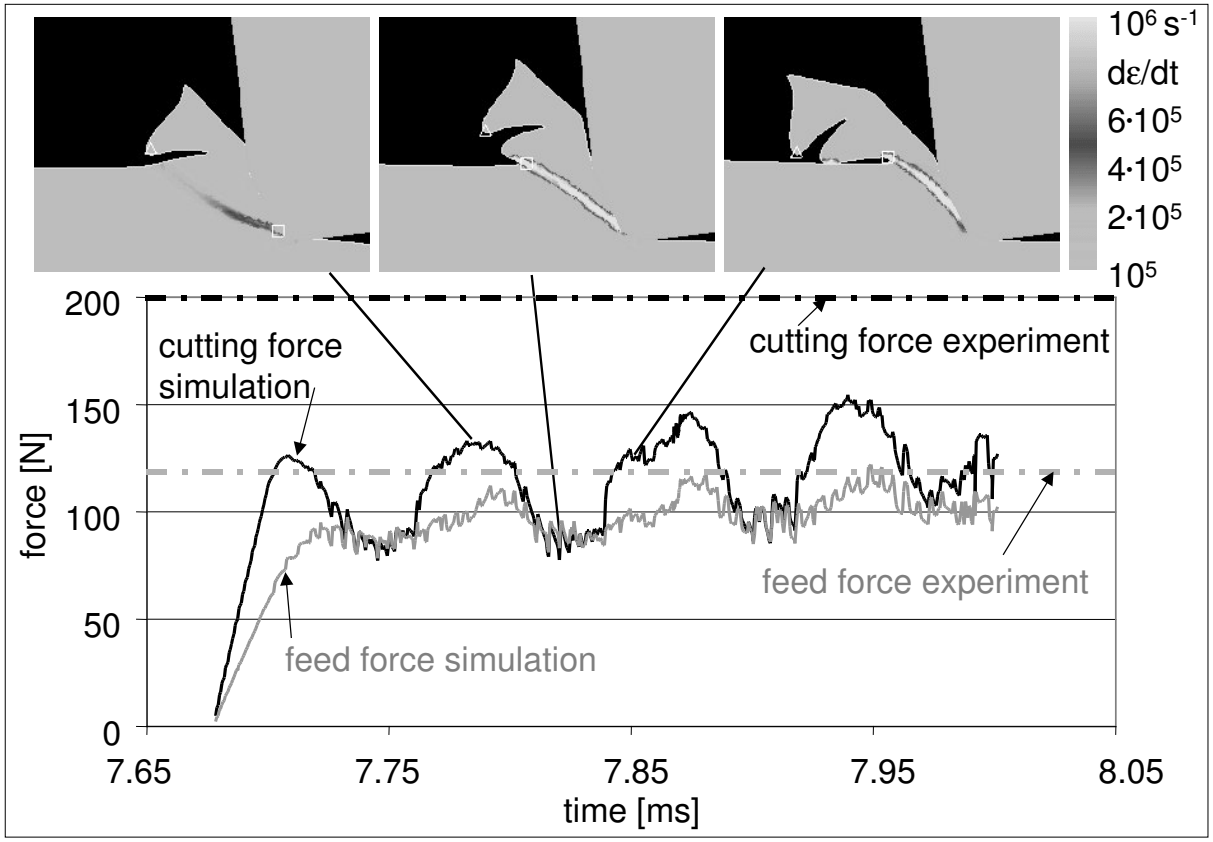


Figure 8.14: Cutting and feed forces in segmented chip formation (AISI 1045, material law: eq. 2.13, modified thermal data, v_c = 1000 m/min, f = 0.1 mm)

The segmented chip formation is therefore caused by an oscillating shear zone as it was described by Pekelharing (compare figure 7.4). The advantage of the FEM model is that information about the temperatures, relative velocities, strain, strain rate and resultant forces can be obtained. The temperature distribution in the lamellae and the shear zone is shown in **figure 8.15**. The elements in the lamellae and in a distance from the shear band (points 1 and 2) show a low and steady increase of the temperature. This is caused by the heat transfer in the lamella. The elements near to

the shear band (point 3 and 4) show a stronger increase. If an element is located in the shear zone (point 7 and 8) a strong increase is found. The temperature is higher than twice the one in the lamellae and three to four times higher than in continuous chip formation (compare figure 8.9 and table 8.1).

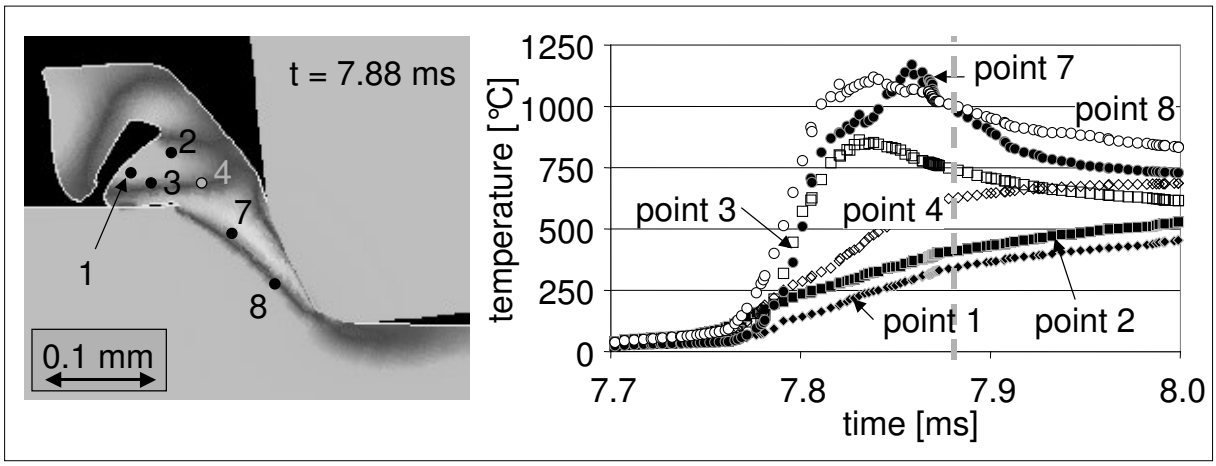


Figure 8.15: Temperature distribution in lamella and shear band during segmented chip formation (modified thermal data)

The values of effective strain show a similar dependency on the location in the chip as the temperature, **figure 8.16**. However, the maximum values in the primary shear zone of a segmented chip are twice as high as in continuous chip formation (compare figure 8.9 and table 8.1). This can also be found for the effective strain rate. The decrease of effective strain should not occur. It is due to the loss of material data because of the remeshing routine described earlier. The influence of the segmented chip formation on the secondary shear zone must be considered, because of the unsteady chip velocity. In the compression phase the chip velocity decreases but at the same time the length of the contact zone increases.

These conditions influence the shearing of the bottom of the chip. During the shearing period, which is shorter than the compression period, the speed of the chip segment is higher. Because of the law of continuity the shearing has to increase, too. This mechanism is also supported by the high temperature which is generated during the compression stage. The influence of the discontinuity can also be found in the cross section of the produced chips (compare figure 5.24). During the compression period, only the secondary shearing occurs which is one main difference to the

continuous chip. While the shearing of the chip segment happens, the two shear zones are linked.

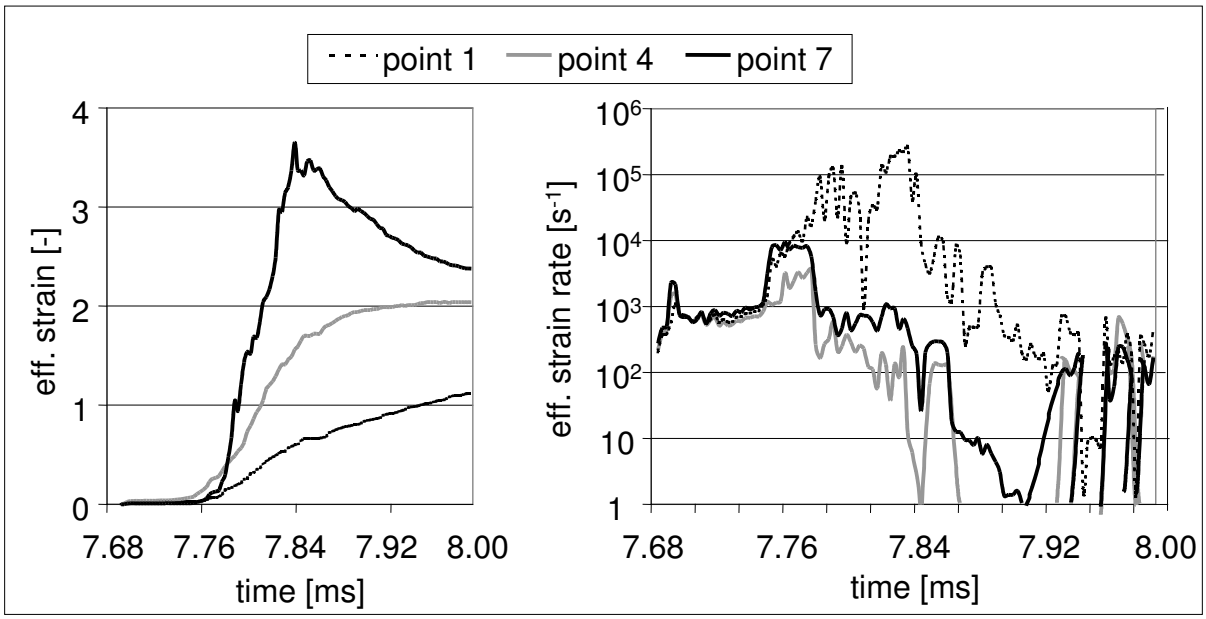


Figure 8.16: Distribution of ε_v and $d\varepsilon_v/dt$ in segmented chip formation for three points shown in figure 8.15

The heat generation by adiabatic shearing causes a strong increase of the temperature in the primary shear zone and the compression zone. As some material of the compression zone also flows into the tertiary shear zone a rise of the temperature can be found, **figure 8.17**. The corresponding curves for effective strain and strain rate are given in **figure 8.18**.

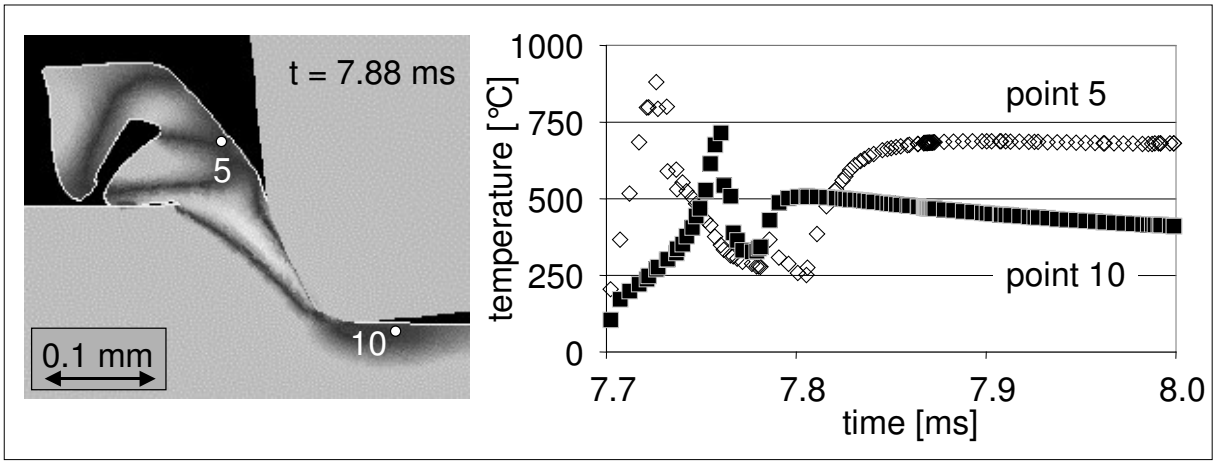


Figure 8.17: Temperature distribution in the secondary (point 5) and tertiary (point 10) shear zone in segmented chip formation

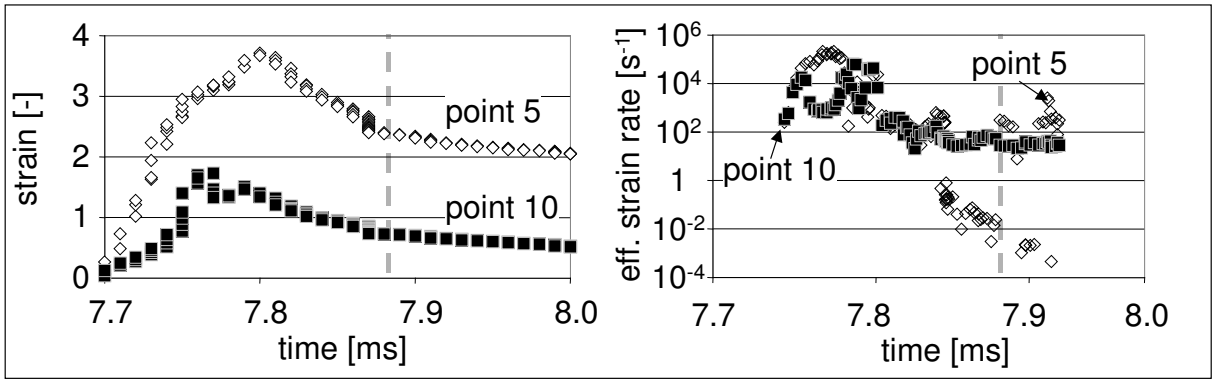


Figure 8.18: Effective strain and strain rate distribution in segmented chip formation in the secondary (point 5) and tertiary (point 10) shear zone

8.2.3 Segmented chip formation because of material damage

As already mentioned, a second reason for segmented chip formation can be the failure of the chip material. This theory, which is well established for cutting hardened steel and cast iron, can be implemented in the simulation in two ways.

On the one hand the damage can be implemented in the flow stress curve /BROD01/ and similar results compared to the simulation of adiabatic shearing will be obtained. On the other hand, a fracture can grow from the free surface into the primary shear zone. A fracture criterion is needed for the propagation and the end of propagation of the fracture. In the current simulation the following approach is used.

To allow the occurrence of fracture, tension stresses have to be found on the free surface. Only then the following shearing criterion is activated. These elements are deleted, if the maximum principle stress of elements in the primary shear zone is positive and higher than the tensile strength of the workpiece material, equation 8.1.

$$\sigma_1 > R_m \qquad \text{(eq. 8.1)}$$

This criterion can be easily applied to DEFORM by a user defined subroutine. Approaching the cutting edge the temperature in the primary shear zone shows an increase, therefore, the tensile strength in the elements increases and the criterion is no longer fulfilled. It must be noted that in the current version of DEFORM 7.2 an element deletion is the only possibility to apply a fracture criterion. This leads to a rough self contact of the workpiece in the primary shear zone. In the future a duplication of the nodes on both sides of the fracture would be preferred. The

obtained chip formation is shown in **figure 8.19**. At the beginning of the cut the lamellae is compressed. Than the criterion is hit and a fracture propagates through the primary shear zone and approaches the tool tip. After a distinctive distance the fracture stops, the lamella is pushed out of the cutting zone and a new compression will be started. Because of the missing ability to implement a fracture by a node duplication and the questionable validity of the simple fracture criterion no further simulations were conducted. However, to model the chip formation of cast iron, ceramics, plastics, stone and hardened steels, the described approach is promising.

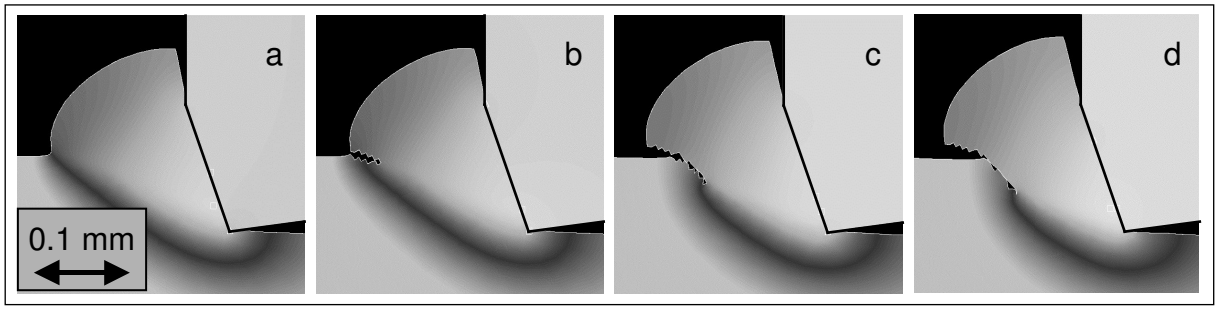


Figure 8.19: Chip formation by applying a fracture criterion

9 Conclusion and potential applications of the results

The performance of a metal cutting process is influenced by the machine tool, cutting process, tool material, tool coating, tool geometry, cooling strategy, cutting speed, feed, depth of cut and workpiece material. The change of one of these parameters may have a significant effect on tool life and workpiece quality. Consequently, the knowledge of these influences is important to obtain an optimized process.

In the current work the influence of a variation in cutting speed is investigated. The range is from low to very high cutting speeds. To describe the influence of the cutting speed on the process performance the current work has used state of the art and new developed setups in turning of three different workpiece materials. The results can be summarized as follows.

Because of low values for tool wear and cutting temperatures the maximum speed in cutting the wrought aluminum alloy AA 7075 (AlZnMgCu1.5) will be only limited by the machine tool. Although the fact that the resultant forces at high cutting speed (e.g. v_c = 6000 m/min) exceed those of low speeds will not limit the application of high speed or high performance cutting AA 7075. This increase of the resultant forces is caused by the workpiece material behavior at high values for strain rate.

On the other hand tool wear, process temperatures and resultant forces limit the cutting parameters of turning the titanium alloy Ti6Al4V. The main reason for the differences in machining aluminum and titanium are the occurring temperatures at the tip of the tool. For these materials, and also for turning AISI 1045 steel, the maximum temperature in the cutting process is limited by the melting temperature of the workpiece material. Currently the warm hardness and chemical stability of the tool material is too low to realize dry cutting processes at significant elevated cutting speeds. Furthermore, the low thermal diffusivity of titanium results in a significant thermal load on the tool. The result is an extensive tool wear. This is the reason why the realized cutting speeds in turning Ti6Al4V using ceramic or boron nitride tools are 100 times lower than for machining AlZnMgCu1,5 using uncoated cemented carbide.

Between these extremes the material steel is located. Turning AISI 1045 (C45E) the temperatures are lower than for titanium and significantly higher than for aluminum. The cutting speeds of aluminum cannot be reached. The reason is the severe wear of the ceramic tool caused by temperatures in the area of T = 1400 °C. It is proposed

that even if a new developed tool material would stand the wear attack, the very high resultant forces and poor surface properties will limit the technological cutting speed below $v_c = 2000$ m/min. The reason for the increased resultant forces is, similar to aluminum, the increase of material strength at high strain rates. The surface properties at high cutting speeds are downgraded by thermal softening and resulting plastic deformation of the rim zone.

However, for steel the mentioned technological limit of $v_c = 2000$ m/min is far beyond the applied cutting speeds. Thus new tool materials, coatings but also an optimized tool geometry or coolant strategy can increase the process performance and thus the productivity. To develop such improvements a very deep knowledge of the cutting process is necessary. It is demonstrated in the current work that modern setups allow to describe the chip formation process very accurately. On the other hand the remarkable expenditure to get and evaluate the data limits the range of variations concerning tool geometry, coatings and process parameters. Furthermore, the continuously improvement of existing steels as well as the development of new materials and tool coatings would result to an unrealistic number of experiments if the optimal parameters would be determined in this way.

One solution of this problem is to describe the cutting mechanism by a model and predict the influence of the mentioned variations. As small changes can have a strong influence on the process performance the number of simplifications to set up the model has to be minimized. Modeling the cutting process using the finite element method (FEM) fulfills this demand. Based on elastic-plastic and thermo-mechanical data the cutting process can be described. Even the influence of instationary mechanisms such as fracture and shearing may be considered. This is the main advantage compared to analytical models. Latter are based on several simplifications and show no advantage compared to the FEM.

Therefore, a FE model of the steel cutting process using the commercial FE software DEFORM was developed. To enable an intensive evaluation as well as a sensitivity analysis, the model is two dimensional. Based on input data by experts in the fields of material and thermodynamic science the simulated and experimental results show a good agreement in the range of $100 \text{ m/min} < v_c < 1000 \text{ m/min}$. To achieve this a constitutive material law dedicated to the special conditions in cutting is necessary. If

this description is not accurate, the simulation results are far from reality. Therefore, different approaches to model the material behavior are presented and the limitations are mentioned. A result of using one of these material laws was that, for the first time, a good agreement is found for cutting forces, cutting temperatures, chip velocity and chip thickness. The material parameters to setup the model are given in this work. The availability of this data and the experimental results can be used to set up and verify new models, e.g. by using a FE code different form DEFORM.

To allow the evaluation of cutting temperatures and chip geometry two newly developed experimental setups were used. One is a two-color pyrometer with a very high time and local resolution. It is a special development of the Institute of Heat Transfer and Air Conditioning (WÜK) at the RWTH Aachen. Furthermore, an in-situ setup to photograph the orthogonal cutting process was developed by the author. Based on the ideas of Warnecke and Childs in the 70th of the last century the chip formation can be photographed at industrial relevant cutting parameters. The information of both setups can be used to optimize the tool design and workpiece material to reduce tool wear and to improve the chip breakage. Furthermore, the verification by forces, temperatures and geometry ensures that the model is not fitted to one parameter but allows a good description and even prediction of the mechanisms in cutting.

This is the reason why it can be applied to optimize the cutting process in different areas. First of all, the model can be transferred to the third dimension and help to optimize tools with a complicated geometry such as mills, drills, threads, reamers and broaching tools. Additionally, the simulation delivers stresses, strains, strain rates, temperatures and local velocity distributions in cutting. This knowledge can be used to describe unknown effects such as the influence of coatings, coolants and even fracture mechanisms in cutting. A possible result is to prevent burr formation, annealing or tool breakage because of poor chip formation. Also the development of tools and coatings can be improved. The information of the simulation may lead to accurate tool wear laws and thus adapted tool materials.

To achieve all these aims it has to be considered that even the presented FE model consists of several simplifications. For example the workpiece is assumed to behave plastic instead of elastic-plastic, the description of friction is rough and the influence of the machine tool, coolants and coatings was not considered at all. However, the

existing model rated to be is superior to the analytical ones known by the author. As the latter were continuously improved for more than 70 years, the author is confident that the future research in modeling cutting processes using FEM will fill this gap.

This prognosis is based on the fact that commercially available FE-codes are already applied in industry /THIR03/. Furthermore, approaches such as a three-dimensional drilling and milling simulation are currently under investigation /KLOC02/. In two-dimensional simulations the influence of the cutting process on the machine tool, residual stresses and the prediction of tool wear is examined /KLO02a, KLO02b, KLOC03, YEN02/.

10 Literature

/ALTA00/ Altan, T.; Koppka, F.; Sartkulvanich, P.: Experimental determination of flow stress data for FEM simulation of machining operation. Engineering Research Center for Net Shape Manufacturing, The Ohio State University, Columbus, Ohio, 2000

/ALTA03/ Altan, T.: Simulation of cutting processes, CIRP January workshop, Paris, 2003

/ALVE70/ Alvelid, B.: Cutting temperature thermo-electrical measurement. Annals of the CIRP, (1970) 18, pp. 547-554

/ANDR58/ Andreev, G.S.: Photo-elastic study of stresses in a cutting tool using inématography. Vestnik Mashinostroeniya, 5, pp. 54-57, 1958

/ARCH53/ Archard, J.F. : Contact and rubbing of flat surfaces. Journal of Applied Physics, 1953 (1953) 24, pp. 981

/ARND72/ Arndt; G.: Ultra-high-speed machining. Annals of the CIRP, Vol 21/1 1972, pp. 3-4, 1972

/ARSE95/ Arsecularatne, J. A.; Mathew, P.; Oxley, P.L.B.: Prediction of chip flow direction and cutting forces in oblique machining with nose radius tools. Proceedings of the institution of mechanical engineers, 209, pp. 305-315, 1995

/ARSE96/ Arsecularatne, J. A.; Fowle, R.F.; Mathew, P.; Oxley, P.L.B.: Prediction of cutting forces and built-up edge formation conditions in machining with oblique nose radius tools. Proceedings of the institution of mechanical engineers, 210, pp. 457-469, 1996

/ASTA97/ Astakhov, V.P.; Shvets, S.V.; Osman, M.O.M.: Chip structure classification based on mechanics of its formulation. Journal of Material Processing Technology, 1997 (1997) 71, pp. 247-257

/BACC99/ Bacci da Silva, M.; Wallbank, J.: Cutting temperature: prediction and measurement methods - a review. Journal of Material Processing Technology, (1999), pp. 195-202

/BÄKE02/ Bäker, M.; Rösler, J.; Siemers, C.: A finite element model of high speed metal cutting with adiabatic shearing. Computers and Structures, 2002 (2002) 80, pp. 495-513

/BALA00/ Balaji, A.K.; Jawahir, I.S.: Variable tool-chip interfacial friction in 2-D and 3-d machining operations. International Workshop on Friction and Flow Stress in Cutting and Forming, ENSAM, Paris, 25.-26.01.2000, pp. 91-101

/BAY87/ Bay, N.: Friction Stress and Normal Stress in bulk metal-forming processes. Journal of Mechanical Working Technology, 1987 (1987) 14, pp. 203-223

/BAY00/ Bay, N.: Modeling and testing friction and lubrication in bulk metal forming. International Workshop on Friction and Flow Stress in Cutting and Forming, ENSAM, Paris, 25.-26.01.2000, pp. 5-15

/BEHR01/ Behrens, A., Westhoff, B.; Schulz, H. (Hrsg.): Fundamental aspects of investigating the hsc-chip formation process by FEM. Carl Hanser Verlag, München, pp. 53-65, 2001

/BENA02/ Ben Amor, Raouf: Thermomechanische Wirkmechanismen und Spanbildung bei der Hochgeschwindigkeitszerspanung, Dissertation, Universität Hannover, 2002

/BENO96/ Beno, J.: Untersuchungen zur Spanentstehungsstelle. wt Produktion und Management, 1996 (1996) 86, S. 462-467

/BLAN68/ Blankenstein, B.: Der zerspanungsprozess als Ursache für Schnittkraftschwankungen beim Drehen mit Hartmetallwerkzeugen. Dissertation, RWTH Aachen, 1968

/BRAI68/ Braiden, P.M.: The calibration of tool/work thermocouples. 8th int. MTDR conf. , Manchester, Sept 1967, pp. 653-666

/BRED59/ Bredendick, F.: Die Massenkräfte beim Zerspanvorgang. Werkstatt und Betrieb, Jahrg. 92, Heft 10, S. 739-742, 1959

/BROD01/ Brodmann, M.: Schädigungsmodell für schlagartige Beanspruchung metallischer Werkstoffe. Dissertation, RWTH Aachen, 2001

/BUDA68/ Buda, J.; Vasilko, K.; Stranava, J.: Neue Methoden der Spanwurzelgewinnung zur Untersuchung des Schneidvorganges. Industrie-Anzeiger, Jahrg. 90, Nr. 5, S. 24-27, 1968

/BUDA72/ Buda, J.: New methods in the study of plastic deformation in the cutting zone. Annals of the CIRP, (1972), pp. 17-18

/CERE00/ Ceretti, E.; Filice, L.; Micari, F.: Basic aspects and modeling of friction in cutting. International Workshop on Friction and Flow Stress in Cutting and Forming, ENSAM, Paris, 25.-26.01.2000, pp. 73-83

/CHIL00/ Childs, T.H.C.; Maekawa, K.; Obikawa, T.; Yamane, Y.: Metal machining - theory and application. Arnold, 2000

/CHIL71/ Childs, T.H.C.: A new visio-plasticity technique and a study of curly chip formation. International Journal of mechanical science, Vol 13, pp. 373-387, 1971

/CHIL98/ Childs, T.H.C.: Material property needs in modeling metal machining. Machining Science and Technology, 1998 (1998) 2, pp. 303-316

/CHOI85/ Choi, Z.: Temperaturmessung beim Schleifen. Industrie-Anzeiger, Nr. 79/80 v. 4.10.1985 / 107. Jg., S. 44-45, 1985

/DAMA90/ Damaritürk, H.: Temperaturen und Wirkmechanismen beim Hochgeschwindigkeitsfräsen von Stahl. Dissertation, TU Darmstadt, Hanser, 1990

/DAWE69/ Dawe, C.C.; Rubenstein, C.: Analysis of chip curvature. 10th M.T.D.R. Conference, Manchester, 1969

/DIML00/ Dimla, E.: Sensor signals for tool-wear monitoring in metal cutting operations - a review of methods. International Journal of Machine Tools & Manufacture, 40, pp. 1073-1098, 2000

/EISE00/ Eisenblätter, G.: Trockenbohren mit Vollhartmetallwerkzeugen. Dissertation, RWTH Aachen, 2000

/ELMA01/ Treppmann, C.; El-Magd, A.; Schulz, H. (Hrsg.): High speed quick-stop test with the Split-Hopkinson-Bar. Carl Hanser Verlag, München, pp. 199-201, 2001

/ELMA04/ El-Magd, A.; Korthäuer, M.: Experimentelle und numerische Untersuchung zum thermomechanischen Stoffverhalten, to be published in "Hochgeschwindigkeitsspanen metallischer Werkstoffe – Ergebnisse des SPP 1057 der DFG“, Tönshoff, K., Hollmann, F. (Hrsg.), Wiley-VCH Verlag

/ELWA01/ El-Wardany, T.I.; Elbestawi, M.A., Schulz, H. (Hrsg.): Effect of material models on the accuracy of high speed machining simulation. Carl Hanser Verlag, München, pp. 77-90, 2001

/FANG01/ Fang, N.; Jawahir, I.S.; Oxley, P.L.B.: A universal slip-line modell with non-unique solutions for machining with curled chip formation and a restricted contact tool. International Journal of mechanical science, 43, pp. 557-580, 2001

/FORM70/ Form, G.W.; Beglinger, H.: Fundamental considerations in mechanical chip formation. Annals of the CIRP, 1970 (1970) XVIII, pp. 153-167

/GENT02/ Gente, A.: Spanbildung von TiAl6V4 und Ck45N bei sehr hohen Schnittgeschwindigkeiten, Dissertation, TU Braunschweig, 2002

/GERS98/ Gerschwiler, K.: Untersuchungen zum Verschleißverhalten von Cermets. Dissertation, RWTH Aachen, Shaker-Verlag, Aachen, 1998

/GRON00/ Gronostajski, Z.: The constitutive equations for FEM analysis. Journal of Material Processing Technology, 106, pp. 40-44, 2000

/GRZE00/ Grzesik, W.: The influence of thin hard coatings on frictional responses in the orthogonal cutting process. International Workshop on Friction and Flow Stress in Cutting and Forming, ENSAM, Paris, 25.-26.01.2000, pp. 83-90

/HAFE01/ Haferkamp, H.; Niemeyer, M.; Henze, A.; Schäperkötter, M..; Schulz, H. (Hrsg.): Chip formation during machining of Ck45, in Scientific Fundamentals of HSC, Carl Hanser Verlag, München, pp. 32-42, 2001

/HAMO02/ Hamouda, A.M.: Effect of energy losses during an impact event on the dynamic flow stress. Journal of Material Processing Technology, 2002 (2002) 124, pp. 209-215

/HARD89/ Harding, J.: The development of constitutive relationships for material behavior at high rates of strain. Int. Conf. on Mech. Prop. of Mat. at High Strain Rates

/HEMM89/ Hemminger, W.F., Cammenga, H.K.: Methoden der Thermischen Analyse, Springer-Verlag Berlin, ISBN 3-540-15049-8

/HERB26/ Herbert, E.G.: The measurement of cutting temperatures. Proceedings of the institution of mechanical engineers, (1926) 1, pp. 289-329

/HIRA89/ Hirao, M.: Determining temperature distribution on flank face of cutting tool. Journal Mater. Shap. Technol., 3, pp. 143-148, 1989

/HÖHN96/ Höhne, G.; Hemminger, W.; Flammersheim, H.-J.: Differential Scanning Calorimetry, Springer-Verlag Berlin, ISBN 3-540-52381-2

/HOLL45/ Hollomon, J.: Tensile deformation. Transactions of the AIME, (1945) 162, pp. 268-290

/HU86/ Hu, R.S; Oxley, P.L.B.; Young, H.T.: Allowing for end cutting edge effects in predicting forces in bar turning with oblique machining conditions. Proceedings of the institution of mechanical engineers, 200, C2, pp. 89-99, 1986

/HUAN96/ Huang, J.M.; Black, J.T.: An evaluation of chip separation criteria for the FEM Simulation of machining. Journal of Manufacturing Science and Engineering, ASME, Vol 118 (1996), pp. 545-554, 1996

/IWAT76/ Iwata, K.; Ueda, K: The significance of dynamic crack behavior in chip formation. Annals of the CIRP, 25 (1976) 1, pp. 65-70

/JASP02/ Jaspers, S.; Dautzenberg, J.H.: Material behaviour in metal cutting: strains, strain rates and temperatures in chip formation. Journal of Material Processing Technology, 2002 (2002) 121, pp. 123-135

/JASP02a/ Jaspers, S.; Dautzenberg, J.H.: Material behaviour in conditions similar to metal cutting: flow stress in the primary shear zone. Journal of Material Processing Technology, 2002 (2002) 122, pp. 322-330

/JOCH01/ Jochmann, S.: Untersuchungen zur Prozess- und Werkzeugauslegung beim Hochpräzisionshartdrehen, Dissertation der RWTH Aachen, S. 82-90, 2001

/JOHN83/ Johnson, G.R.; Cook, M.W.: A constitutive model and data for metals subjected to large strains, high strain rates and high temperatures. 7th int. Symp. On Ballistics, The Hague, pp. 541-547

/KAHL79/ Kahles, J.F.; Field, M.; Harvey, S.M.: High-speed-machining. American Machinist, 1979

/KALH00/ Kalhori, V.: Modeling and Simulation of Mechanical Cutting. Ph.D. Thesis, Lulea University of Technology Schweden, 2000

/KATT57/ Kattwinkel, W.: Untersuchung an Schneiden spanender Werkzeuge mit Hilfe der Spannungsoptik. Dissertation, RWTH Aachen, 1957

/KECE58/ Kececioglu, D.: Shear-strain rate in metal cutting and ist effects on shear-flow stress. ASME, 80,1, pp. 158-168, 1958

/KECE58/ Kececioglu, D.: Force components, chip geometry and specific cutting energy in orthogonal and oblique machining of SAE1015 steel. ASME, 80, pp. 149-157, 1958

/KECE58/ Kececioglu, D.: Shear-zone temperature in metal cutting and its effects on shear-flow stress. ASME, 80, pp. 541-546, 1958

/KECE60/ Kececioglu, D.: Shear-zone size, compressive stress and shear strain in metal-cutting and their effects on mean shear-flow stress. ASME, 81, 1, pp. 79-85, 1960

/KHAR69/ Khare, M.K.: Untersuchungen des Reibungsverhaltens zwischen Span und Spanfläche sowie Prüfung der Scherwinkelbeziehungen durch Zersankraftmessungen beim Schnittuntersuchungsvorgang. Dissertation, TU Berlin, 1969

/KIEN52/ Kienzle, O.: Die Bestimmung von Kräften und Leistungen an spanenden Werkzeugen und Werkzeugmaschinen. VDI-Z, 94 (1952) 11/12, S. 299-305

/KLOC99/ Klocke, F.; Zinkann, V.: Hochgeschwindigkeit ändert die Spanbildung. VDI-Z, 141, Nr 3/4, S. 30-34, 1999

/KLOC00/ Klocke, F.; Hoppe, S.: „Experimentelle und numerische Untersuchungen zum Spanbildungsvorgang bei der Zerspanung mit geometrisch bestimmter Schneide mit hohen Schnittgeschwindigkeiten", in „Spanen metallischer Werkstoffe mit hohen Schnittgeschwindigkeiten“, Tönshoff K., Hollmann F. (Hsg), Verlag Universitat Hannover, 2000

/KLOC01/ Klocke, F.; Raedt, H.W.; Hoppe, S.: 2D-FEM Simulation of the orthogonal High Speed Cutting Process. Machining Science and Technology, vol. 5, issue 3, pp. 323-340, 2001

/KLOC01a/ Klocke, F.; Hoppe, S.: Schulz, H. (Hrsg.): Mechanism of chip formation in high speed cutting, in Scientific Fundamentals of HSC, Carl Hanser Verlag, München, pp. 1-10, 2001

/KLOC02/ Klocke, F.; Messner, G.; Hoppe, S.; Raedt, H.-W., Schmitz, R.: FEM Simulation of METAL forming and cutting operations, 7th ICTP in Japan, 2002

/KLO02a/ Klocke, F.; Markworth, L. Messner, G.: Modeling of Ti6Al4V machining operations, 5th CIRP Int. Workshop Modeling of Machining Operations, Purdue (USA), May 2002

/KLO02b/ Klocke, F.; Raedt, H.W.; Hoppe, S.; Messner, G.; Markworth, L.: Application of the FE-method to the machining process, CIRP modeling workshop, Paris, January 2002

/KLOC02c/ Klocke, F.; Hoppe, S.: High Speed Turning of the Aluminum Alloy AA7075, Production Engineering Research and Development, Annals of the German Society for Production Engineering, IX/1, pp. 21-24, 2002

/KLOC03/ Klocke, F.; Raedt, H.W.; Hoppe, S.; Messner, G.; Schmitz, R.: Simulation of machinability, CIRP modeling workshop, Paris, January 2003

/KOMA93/ Komanduri, R.: Machining and grinding: a historical review of the classical papers. ASME, 46, 3, pp. 80-132, 1993

/KOEN97/ König, W.: Fertigungsverfahren Drehen, Fräsen, Bohren. Springer-VDI-Verlag, Düsseldorf, 1997

/KRAG83/ Kragelsky, I.V.; Dobycin, M.N.; Kombolov, V.S.: Grundlagen der Berechnung von Reibung und Verschleiß. Carl Hanser Verlag, München, 1983

/KREI73/ Kreis, W.: Verschleißursachen beim Drehen von Titanwerkstoffen. Dissertation, RWTH Aachen, 1973

/KRIE01/ Krieg, T.: Eigenschaften von PVD-Werkzeugbeschichtungen für den Einsatz von umweltverträglichem Kühlschmierstoff beim Drehen und Bohren von Stahlwerkstoffen. Dissertation, RWTH Aachen, Shaker-Verlag, Aachen, 2001

/KRON61/ Kronenberg, M.: Gedanken zur Theorie und Praxis der Ultra-Schnellzerspanung. TZ f. prakt. Metallbearbeitung, Jahrg. 55, Heft 8, S. 443-510, 1961

/KUSN60/ Kusnetsov, V.D.; Polosatkin, G.D.; Kalashnikova, M.P.: The study of cutting processes at very high speeds. Sibirsk Physico-Technical Research Institute, 1960

/LANG72/ Langhammer, K.: Die Zerspankraftkomponenten als Kenngrößen zur Verschleißbestimmung an Hartmetall-Drehwerkzeugen. Dissertation, RWTH Aachen, 1972

/LARS72/ Larsen-Basse, J.; Oxley, P.L.B.: Effect of strain-rate sensitivity on scale phenomena in chip formation. Proceedings of the 13th int. Machine Tool Design and Research Conference, Birmingham, 18.-22.09.1972

/LATY63/ Latysheo, V.N.: Instrument for determining length of contact between chip and tool rake face. Machines and tooling, (1963) 5, pp. 37-39

/LEE51/ Lee, E.H., Shaffer, B.W.: The theory of plasticity applied to a problem of machining, Trans. ASME, J. Appl. Mech. 18, (1951), pp. 405-413

/LEE00/ Lee, W.-S.; Sue, W.-C.; Lin, C.-F.; Wu, C.-J.: The strain rate and temperature dependence of the dynamic impact properties of 7075 aluminium alloy. Journal of Material Processing Technology, 100, pp. 116-122, 2000

/LEE00a/ Lee, W.-S.; Lin, C.-F.; Chang, S.-T.: Plastic flow of tungsten-based composite under hot compression. Journal of Material Processing Technology, 100 (2000), pp. 123-130, 2000

/LEIT02/ Leitner, G.: Thermophysikalische Eigenschaften - Bewertungskriterien für Hochleistungswerkstoffe. www.ikts.fhg.de, 2002

/LENZ68/ Lenz, E.; Friedman, M.Y.: Tool-chip contact length as a parameter in metal cutting. A.S.M.E meeting, 1968

/LEOP80/ Leopold, J.: Modellierung der Spanbildung, Dissertation Technische Hochschule Karl-Marx-Stadt, 1/1980

/LEOP95/ Leopold, J.: Simulation sichert den Prozess der Hochgeschwindigkeitsbearbeitung. Maschinenmarkt, 101, S. 40-43, 1995

/LEOP01/ Leopold, J.; Hoyer, K.: Trennvorgang beim HSC-Fräsen simulieren und optimieren. Maschinenmarkt, 2001 (2001) 46, S. 32-36

/LEOP01a/ Leopold, J.; Hoyer, K.; Semmler, U.; Schulz, H. (Hrsg.): Simulation of chip forming process in high speed machining using eulerian finite element analysis, Carl Hanser Verlag, München, pp. 92-101, 2001

/LI95/ Li, X.; Kopalinsky, E.M.; Oxley, P.L.B.: A numerical method for determining temperature distributions in machining with coolant, part 1 modeling the process, part 2 calculation method and result. Proceedings of the institution of mechanical engineers, 209, pp. 33-52, 1995

/LIER97/ Liermann, J. : Hartdrehen wälzbelasteter Bauteile. Dissertation, RWTH Aachen, 1997

/LIN82/ Lin, G.C.I; Mathew, P.; Watson, A.R.; Oxley, P.L.B.: Predicting cutting forces for oblique machining conditions. Proceedings of the institution of mechanical engineers, 196, pp. 141-148, 1982

/MAEK96/ Maekawa, K.; Shirakashi, T.: Recent progress of computer aided simulation of chip flow and tool damage in metal machining. Proc. Instn. Mech. Engrs., Vol. 210, pp. 233-242, 1996

/MANY86/ Manyindo, B.M.; Oxley, P.L.B.: Modeling the catastrophic shear type of chip when machining stainless steel. Proceedings of the institution of mechanical engineers, 200, No C5, pp. 349-358, 1986

/MARU95/ Marusich, T.D.; Ortiz, M.: Finite element simulation of high-speed machining. Simulation of materials processing: theory, methods and applications, ISBN 9054105534, pp. 101-109, 1995

/MARU01/ Marusich, T.D.; Thiele, J.D.; Brand, C.J.: Simulation and analysis of chip breakage in turning processes, 3rd int. Conf. On Metal Cutting and HSC, Vol I, Oral Presentations, 27.-29.6.2002, pp. 83-92

/MATH82/ Mathew, P.; Oxley, P.L.B.: Predicting the Effects of very high cutting speeds on Cutting forces, etc., Annals of the CIRP, Vol. 31/1/1982, pp. 49-52, 1982

/MATW02/ www.matweb.com

/MERC45/ Merchant, M.E.: Mechanics of the metal cutting process. Journal Appl. Phys., 16, pp. 267-318, 1945

/MESL00/ Meslin, F.; Hamann, J.C.: Definition of constitutive equations and friction by inverse method and machining tests. International Workshop on Friction and Flow Stress in Cutting and Forming, ENSAM, Paris, 25.-26.01.2000, pp. 135-158

/MILM02/ Milman, Y.V.; Luyckx, S.; Goncharuck, V.A.; Northorp, J.T.: Results from bending tests on submicron and micron WC-Co grades at elevated temperatures. International Journal of Refractory Metals and Hard Materials, (2002) 20, pp. 71-79

/MOLI01/ Molinari, A.; Sutter, G.; Musquar, C.: Experimental study of orthogonal cutting in a large range of velocities. 3rd int. Conf. On Metal Cutting and High Speed Machining, Metz, France, 27.-29.7.2001, pp. 59-63

/MOLI02/ Molinari, A.; Nouari, M.: Modeling of tool wear by diffusion in metal cutting. Wear, 2002 (2002) 252, pp. 135-149

/MOLI02/ Molinari, A.; Nouari, M.: Modeling of tool wear by diffusion in metal cutting. Wear, 2002 (2002) 252, pp. 135-149

/MOLI97/ Molinari, A.; Sutter, G.; Delime, A.; Dudzinski, D.; Faure, L.: High speed machining experiments. 1. French and German Conference on High Speed Machining, Metz, Juni 1997

/MONT85/ Montgomery, D. C.: Statistical Quality Control, 2nd ed. John Wiley & Sons, New York (USA), 1985

/MOUF98/ Moufki, A.; Molinari, A.; Dudzinski, D.: Modeling of orthogonal cutting with a temperature dependent friction law. Journal of the mechanics and physics of solids, 46, pp. 2103-2138, 1998

/MUEL96/ Müller-Hummel, P.; Lahres, M.: Temperaturmessung an diamantbeschichteten Werkzeugen während der Zerspanung. Industrie Diamanten Rundschau, 1/96, S. 8-12, 1996

/MUE01a/ Müller, B.; Renz, U.: Temperature measurements with a fibber-optic two-colour-pyrometer, in "Scientific fundamentals of high speed cutting“, Schulz, H. (Hrsg.), Carl Hanser Verlag, München – Wien 2001, pp. 181-186

/MUE04a/ Müller, B.; Renz, U.: Experimentelle und numerische Untersuchungen zur Temperatur- und Wärmequellenverteilung beim Hochgeschwindigkeitsspanen, to be published in "Hochgeschwindigkeitsspanen metallischer Werkstoffe – Ergebnisse des SPP 1057 der DFG“, Tönshoff, K., Hollmann, F. (Hrsg.), Wiley-VCH Verlag

/MUEL00/ Müller, B.; Renz, U.: Temperaturmessung mit einem Zwei-Farben-Pyrometer, in „Spanen metallischer Werkstoffe mit hohen Schnittgeschwindigkeiten“, Tönshoff K., Hollmann F. (Hsg), Verlag Universitat Hannover, 2000

/MUEL01/ Müller, B.; Renz, U.: Development of a fast fiber-optic two-color pyrometer for the temperature measurement of surfaces with varying emissivities, Review of Scientific Instruments, American Institute of Physics, Vol. 72, No. 8, 2001, pp. 3366-3374

/MUEL02/ Müller, B.; Renz, U.: Thermographic measurements of high-speed metal cutting process, Proceedings of SPIE, Thermosense XXVI, Orlando, 2002, pp. 126-134

/MUEL03/ Müller, B.; Renz, U.: Time resolved temperature measurements in manufacturing, to be published in: Measurement, Elsevier Science Ltd., London, 34, 2003, pp. 263-370

/MUELx1/ Müller, B.; Renz, U.; Klocke, F., Hoppe, S.: Radiation thermometry at a high-speed turning process, to be published in: Journal of Manufacturing Science and Engineering, ASME

/MUEL04/ Müller, B.: Thermische Analyse des Zerspanens metallischer Werkstoffe mit hohen Schnittgeschwindigkeiten, Dissertation der RWTH Aachen, 2004

/NAKA58/ Nakayama, K.: Studies on the mechanism of metal cutting. Bulletin of the Faculty of Engineering, Yokohama National University, (1958) 7

/NAKA62/ Nakayama, K.: Chip curl in metal cutting. Bulletin Faculty of Engineering, Yokohama National University, 1962 (1962) 11

/OKAD01/ Okada, M.; Liou, N.-S.; Prakash, V.; Miyoshi, K.: Tribology of high-speed metal-on-metal sliding at near-melt and fully-melt interfacial temperatures. Wear, 2001 (2001) 249, pp. 672-686

/OKOS67/ Okoshi, M.; Kawata, K.: Effects of the curvature of work surface on metal cutting. Annals of the CIRP, 1967 (1967) XV, pp. 393-403

/OCUS61/ Ocusima, K.; Hitomi, K.: An analysis of hte mechanism of orthogonal cutting and ist application to discontinuous chip formation, Trans. ASME, J. Eng. Ind., (Nov. 1961), pp. 545-556

/OLOV00/ Olovsson, Lars: On the arbitrary Lagrangian-Eulerian Finite Element Method. Ph.D. Thesis, Linköpings Universitet, 2000

/ORTI95/ Ortiz, M.; Marusich, T.D.: Modeling and simulation of high-speed machining. International Journal for Numerical methods in Engineering, 38, pp. 3675-3694, 1995

/OXLE62/ Oxley, P.L.B.: An analysis for orthogonal cutting with restricted tool-chip contact. International Journal of mechanical science, Vol 4, pp. 129-135, 1962

/OXLE89/ Oxley, P.L.B.: Mechanics of machining, an analytical approach to assessing machinability. Halsted Press New York, 1989

/ÖZEL00/ Özel, T.; Altan, T.: Determination of workpiece flow stress and friction at the chip-tool contact for high-speed cutting. International Journal of Machine Tools & Manufacture, 2000 (1998) 40, pp. 133-152

/PALM59/ Palmer, W.B.; Oxley, P.L.B.: Mechanics of orthogonal cutting. Proceedings of the institution of mechanical engineers, Vol 173 No 24, pp. 623-654, 1959

/PETE97/ Petersen, S.B.; Martins, P. A. F.; Bay, N.: Friction in bulk metal forming: a general friction model vs. the law of constant friction. Journal of Material Processing Technology, 1997 (1997) 66, pp. 186-194

/PFEI93/ Pfeifer, T.: Qualtitätsmanagement. Carl Hanser Verlag München Wien, 1993

/PLÖG02/ Plöger, J. M.: Randzonenbeeinflussung durch Hochgeschwindigkeits-drehen, Dissertation Universität Hannover, S. 47-50, 2002

/PLÖG02a/ Plöger, J. M.: Randzonenbeeinflussung durch Hochgeschwindigkeits-drehen, Dissertation Universität Hannover, S. 86-95, 2002

/PRIM69/ Primus, I.-F.: Beitrag zur Kenntnis der Spannungsverteilungen in den Kontaktzonen von Drehwerkzeugen. Dissertation, RWTH Aachen, 1969

/RAED02/ Raedt, H.W.: Grundlagen für das schmiermittelreduzierte Tribosystem bei der Kaltmassivumformung des Einsatzstahles 16MnCr5. Dissertation, RWTH Aachen, 2002

/RAJA99/ Rajagopalan, S.; Irfan, M.A.; Prakash, V.: Novel experimental techniques for investigating time resolved high speed friction. Wear, 1999 (1999) 225-229, pp. 1222-1237

/RECH64/ Recht, R.F.: Catastrophic thermoplastic shear. Journal of Applied Mechanics, 1964 (1964) 6, pp. 189-193

/RICH88/ Richter, F.: Die physikalischen Eigenschaften der beiden Titanwerkstoffe Ti99,7 (3.7035) und Ti6Al4V (3.7165). Metall, 42, 6, S. 572575, 1988

/RICH91/ Richter, F.: Die physikalischen Eigenschaften von metallischen Werkstoffen. Metall, 45,6, S. 582-589, 1991

/ROSA00/ Rosakis, P.; Rosakis, A.J.; Ravichandran, G.; Hodowany, J.: A Thermodynamic internal variable model for the partition of plastic work into heat and stored energy in metals. Journal of the mechanics and physics of solids, 48 (2000), pp. 581-607, 2000

/ROSO03/ Rosochowska, M.; Balendra, R.; Chodnikiewicz, K.: Measurement of thermal contact conductance. Journal of Material Processing Technology, 2003 (2003) 135, pp. 204-210

/RUBE65/ Rubenstein, C.: A simple theory of orthogonal cutting. International Journal of mechanical science, Vol 4, pp. 123-156, 1965

/SAHM01/ Sahm, A.; Siems, S.; Schulz, H. (Hrsg.): Influence of chip segmentation on cutting force, Carl Hanser Verlag, München, pp. 151-160, 2001

/SAND03/ www.sandvik.com

/SARR01/ Sarrafi-Nour, G.R.; Coyle, T.W.: Temperature dependence of crack wake bridging stresses in a SiC-whisker-reinforced alumina. Acta Materialia, 2001 (2001) 49, pp. 3553-3563

/SATA63/ Sata, T.: Recent developments concerning cutting mechanics. Int. Prod. Eng. Res. Conf. A.S.M.E, Pittsburgh, Sept. 1963, pp. 18-25

/SCHÄ99/ Schäpermeier, E.: Hilfe zur Lösung von Zerspanungsproblemen beim Drehen. ZwF-Zeitschrift für wirtschaftlichen Fabrikbetrieb, 94, S. 624-627, 1999

/SCHE88/ Schedler, W.: Hartmetall (für den Praktiker). VDI Verlag, Düsseldorf, 1988

/SCHI65/ Schiffer, F.: Spanungskräfte bei sehr hohen Schnittgeschwindigkeiten. Wissenschaftl. Zeitschrift der Uni Dresden, 14, Heft1, S. 109-122, 1965

/SCHN98/ Schneibel, J.H.; Sabol, S.M.; Morrison, J.; Ludemann, E.; Carmichael, C.A.: cyclic thermal shock resistance of several advanced ceramics and ceramic composites. Journal American Ceramic Society, 81, 7, pp. 1888-1892, 1998

/SCHU00/ Schugger, Ch.; Meingast, U.; Renz, U.: Time-Resolved Velocity Measurements in the Primary Breakup Zone of a High Pressure Diesel Injection Nozzle. 16th Annual Conference on Liquid Atomization and Sprays Systems, ILASS-Europe 2000, Darmstadt, Germany, 11.-13.09.2000

/SCHU01/ Schulz, H.; Sahm, A.: Influence of heat treatment and cutting parameters on chip formation and cutting forces in high speed machining. WGP Annalen, (2001)

/SCHU01a/ Schulz, H.; Abele, E.; Sahm, A.: Material Aspects of Chip Formation in HSC Machining. Annals of the CIRP, 50/1/2001, pp. 45-48, 2001

/SHAT00/ Shatla, M.; Altan, T.: Flow stress measurement and applications in metal cutting. International Workshop on Friction and Flow Stress in Cutting and Forming, ENSAM, Paris, 25.-26.01.2000, pp. 127-124

/SHAT99/ Shatla, M.; Yen, Y.C.; Castellanos, O.; Menegardo, L.; Altan, T.: Prediction of cutting forces, temperatures and stresses from flow stress data and cutting conditions - research in progress. CIRP International Workshop on Modeling of Machining Operations, pp. 1-22

/SHAT99/ Shatla, M.; Kerk, C.; Altan, T.: Process modeling in machining. Internal Report of the ERC/NSM, Ohio State University, (1999), pp. 1-58

/SHAW53/ Shaw, M.C.; Cook, N.H.; Finnie, I.: The shear-angle relationship in metal cutting. Transactions of the ASME, (1553), pp. 273-288

/SHAW84/ Shaw, M.C.: Metal cutting principles. Oxford University Press, 1984

/SÖHN01/ Söhner, J.; Schulz, H. (Hrsg.): Simulation of the high speed milling process, Carl Hanser Verlag, München, pp. 66-76, 2001

/SPAA71/ Spaans, C.: The fundamentals of three-dimensional chip curl, chip breaking and chip control. Ph.D. Thesis, TH Delft, NL, 1971

/STEV70/ Stevenson, M.G.; Oxley, P.L.B.: An experimental investigation of the influence of speed and scale on the strain-rate in a zone of intense plastic deformation. Proceedings of the institution of mechanical engineers, 184, Pt 1, No 31, pp. 561576, 1969-70

/STEV97/ Stevenson, R.: Study on the correlation of workpiece mechanical properties from compression and cutting tests. Machining Science and Technology, 1 (1), pp. 67-79, 1997

/STRE85/ Strenkowski, J.S.; Carroll, J.T: A Finite Element Model of Orthogonal Metal Cutting. Journal of Engineering for Industry, 1985 (1985) 107, pp. 349-354

/SUTT03/ Sutter, G.; Faure, L.; Molinari, A.; Ranc, N.: An experimental technique for the measurement of temperature fields for the orthogonal cutting in high speed machining. International Journal of Machine Tools & Manufacture, 2003 (2003) 43, pp. 671-678

/SUTT97/ Sutter, G.; Faure, L.; Molinari, A.; Delime, A.; Dudzinski, D.: Experimental analysis of the cutting process and chip formation at high speed machining. Journal de physique, 7, C3, pp. 33-38, 1997

/SWIF52/ Swift, H.W.: Plastic instability under plane stress. J. Mech. Phys. Solids, 1 (1952) 18

/TAYL34/ Taylor, G.I.; Quinney, H.: The latent energy in a metal after working. Proc. R. Soc. London, A413, (1934), pp. 307-326

/THIR03/ 1st European ThirdWave Users` Conference, 14./15.05.2003, Fraunhofer IPT, Aachen

/TÖNS99/ Tönshoff, H.K.; Ben Amor, R.: Schnittunterbrechung bei hohen Schnittgeschwindigkeiten. Kolloquium des SPP 1057 der DFG, Bonn, 18.11.1999

/TÖNS01/ Tönshoff, H.K.; Friemuth, T.; Ben Amor, R.; Plöger, J.; Schulz, H. (Hrsg.): Characterizing the HSC-range, material behaviour and residual stresses, Carl Hanser Verlag, München, pp. 103-112, 2001

/TOUN00/ Tounsi, N.; Otho, A.: Dynamic cutting force measuring. International Journal of Machine Tools & Manufacture, 40, pp. 1157-1170, 2000

/TREP01/ Treppmann, C.: Fließverhalten metallischer Werkstoffe bei Hochgeschwindigkeitsbeanspruchung. Dissertation, RWTH Aachen, 2001

/TROO80/ Troost, : Einführung in die allgemeine Werkstoffkunde metallischer Werkstoffe. Wissenschaftsverlag Zürich, 1980

/UEDA01/ Ueda, K; Hosokawa, A.; Oda, K.; Yamada, Keiji: Temperature on flank face of cutting tool in high speed milling. Annals of the CIRP, Vol. 50/1/2001, pp. 37-40, 2001

/UEDA98/ Ueda, T.; Sato, M.; Nakayama, K.: The Temperature of a Single Crystal Diamond Tool in Turning. Annals of the CIRP, 47/1/1998, pp. 41-44, 1998

/UEDA99/ Ueda, T.; Huda, Mahfudz Al; Yamada, Keiji; Nakayama, K.: Temperature measurement of CBN tool in turning of high hardness steel. Annals of the CIRP, Vol. 48/1/1999, pp. 63-66, 1999

/VAN 77/ van Luttervelt, C.A.: The split shearzone - mechanism of chip segmentation. Annals of the CIRP, 1977 (1977) 25/1/1977, pp. 33-38

/VAN 98/ van Luttervelt, C.A.; Childs, T.H.C.; Jawahir, I.S.; Klocke, F.; Venu Vinod, P. K.: Present Situation and Future Trends in Modeling of Machining Operations. CIRP STC Cutting, (1998)

/VIER70/ Vieregge, G.: Zerspanung der Eisenwerkstoffe. Verlag Stahleisen, Düsseldorf, 1970

/WARN73/ Warnecke, G.: Spanbildung bei metallischen Werkstoffen. Dissertation, Universität Hannover, 1973

/WEBE91/ Weber, Dieter; Nau, Matthias: Elektrische Temperaturmessung. M.K. Juchheim, 1991

/WEST02/ Westhoff, B.: Modellierungsgrundlagen zur FE-Analyse von HSC-Prozessen. Dissertation, Universität der Bundeswehr Hamburg, 2002

/WEUL00/ Weule, H.; Schmidt, J.; Söhner, J.: Simulation of the high speed milling process. Production Engineering, VII/2, pp. 23-26, 2000

/WIDD00/ Widdermann, S.: FEM-Aktivitäten der deutschen Schmiedeindustrie. Schmiede-Journal, 9/2000 (2000)

/XIE96/ Xie, J.Q.; Bayoumi, A.E.; Zbib, H.M.: A study on shear banding in chip formation of orthogonal machining. International Journal Tools Manufacturing, Vol 36, No7, pp. 835-847, 1996

/YEN02/ Yen, E.; Söhner, J.; Altan, T.; Weule, H.: Estimation of tool wear in metal cutting with the finite element method. 5th CIRP International Workshop on Modeling of Machining Operations, West Lafayette, USA, 20-21 May 2002

/YOUN87/ Young, H.T.; Mathew, P.; Oxley, P.L.B.: Allowing for nose radius effects in predicting the chip flow direction and cutting forces in bar turning. Proceedings of the institution of mechanical engineers, 201, Nr.C3, pp. 213-226, 1987

/ZERI87/ Zerilli, F.j.; Armstrong, R.W.: Dislocation-mechanics-based constitutive relations for material dynamic calculations. Journal of Applied Physics, 1987 (1987) 61, pp. 1816-1825

/ZHAN03/ Zhang, S.; Hodgson, P.D.; Cardew-Hall, M.J.; Kalyanasundaram, S.: A finite element simulation of micro-mechanical frictional behaviour in metal forming. Journal of Material Processing Technology, 2003 (2003) 134, pp. 81-91

/ZIEB96/ Ziebeil, F.: Mechanische und thermische Belastung von Zerspanwerkzeugen. Dissertation, Universität Hannover, 1996

/ZITZ95/ Zitz, U.: Abschätzung der Rissentstehung bei der Kaltmassivumformung. Dissertation, RWTH Aachen, Shaker-Verlag, Aachen, 1995

/ZORE66/ Zorev, N.N.: Metall cutting mechanics. Pergamon, 1966

Curriculum vitae

	Stefan Hoppe
	Born on 29.03.1973 in Gladbeck/Westfalen (Germany)
	Married, 1 daughter
1980 – 1984	Lamberti Grundschule Gladbeck
1984 – 1992	Leibniz Gymnasium Gelsenkirchen-Buer, Abitur
1992 – 1993	Military service
1993 – 1999	Study of mechanical engineering at the RWTH Aachen
1996 – 1999	Student worker at the Chair of Manufacturing Technology of Prof. Dr.-Ing. F. Klocke at the Laboratory of Machine Tools and Production Engineering (WZL) in Aachen
since 1999	Member of the scientific staff of the Chair of Manufacturing Technology of Prof. Dr.-Ing. F. Klocke at the Laboratory of Machine Tools and Production Engineering (WZL) in Aachen